

COMPUTATIONAL AND MODELING APPROACHES TO MULTI-SCALE ANATOMICAL DESCRIPTION OF NEURONAL CIRCUITRY

Linus Manubens-Gil

TESI DOCTORAL UPF / ANY 2017

DIRECTOR DE LA TESI

Dra. Mara Dierssen i Dr. Jordi Garcia-Ojalvo

Biologia de sistemes - Centre de Regulació Genòmica.

DEPARTAMENT CEXS-UPF-PHD PROGRAMME IN BIOMEDICINE



A qui dorm en CIEs, a la família, a les amistats, al laboratori i a l'Irene

"Intellectual work is an act of creation. It is as if the mental image that is studied over a period of time were to sprout appendages like an ameba—outgrowths that extend in all directions while avoiding one obstacle after another—before interdigitating with related ideas."

Santiago Ramón y Cajal, Recuerdos de mi vida

Agraïments

En primer lloc voldria agraïr a la Mara i al Jordi la codirecció d'aquesta Tesi. A la Mara, la oportunitat material de fer-la, amb el seu equip, el seu laboratori i els seus recursos. També el guiatge, amb contribucions conceptuais que a vegades m'han sigut difícils d'encaixar a primer cop d'ull però que al final sempre han acabat sent ingredients genuïns i necessaris per a la Tesi. Al Jordi, la seva contribució sempre ben mesurada, just als punts i moments necessaris, i amb la visió analítica que permet fer d'aquesta Tesi un treball entre la línia experimental del laboratori de la Mara, i l'obertura d'un camí nou en estudis de neurociència computacional en el seu context. Als dos, la infinita dedicació i paciència, sempre tenyida d'una passió per les preguntes que intentem respondre que, com tot el que és essencial, és difícil de veure amb els ulls. Sé que no he sigut un estudiant que els ho hagi posat fàcil. Agraeixo les seves correccions en dies i hores intempestives, i sempre la millor predisposició per a intentar millorar la feina que he anat fent. Però sobre tot, els voldria agraïr la gran oportunitat que ha estat per a mi aprendre de la interacció diària, i totes les subtilitats que acompanyen al què és "fer ciència", a través del contacte amb dues persones que tenen una trajectòria científica excel·lent com la seva.

Des del principi hem sabut que el meu projecte tenia un caràcter "massa ambicios". Els agraeixo el feedback constant, que amb el temps ha permés que anem aconseguint construir un cos consistent de desenvolupaments conceptuels i ànalisis que vagin formant part de la resposta a aquella pregunta general de "why the brain is wired as it is?", i alhora mantinguin un lligam ferm amb la feina feta per la comunitat neurocientífica des de múltiples punts de vista (com ara els de la neurociència computacional, de la neurociència del comportament, de la neurobiologia molecular i de la biologia de sistemes). I és que fa uns dies la Mara em comentava que un dels aprenentatges que he tret d'aquesta Tesi ha sigut que, com deia el Santiago Ramón y Cajal, "Observar sin pensar es tan peligroso como pensar sin observar". Haver-ho après, entre molts altres aprenentatges, és només gràcies a ells dos.

Vull agraïr, també, el suport i seguiment del meu comitè de Tesi, format per el James Sharpe, el Jaume Casademunt i l'Andrés Ozaita, destacant el seguiment proper del James. També les contribucions en Data Clubs i simposis del Mathieu Louis i el Ben Lehner.

En segon lloc vull agraïr a les companyes i companys de viatge del laboratori. Especialment al "mini-lab", format per estudiants d'estiu o en pràctiques, que al llarg dels anys han anat

ajudant-me amb contribucions durant períodes d'alguns mesos a la meva feina. Les primeres reconstruccions, amb l'ajuda de la Mihaela Didu; els experiments amb cultius cel·lulars amb la Queralt Serra Camprubí i en col·laboració amb el Jordi Soriano i el Lluís Hernández. També agraeixo a ells, especialment al Jordi, l'oportunitat d'intentar els experiments d'imaxe de calci en cultius al seu laboratori; els experiments innovadors per a immunoen cervells sencers amb el Burak Kizil; la inestimable aportació de l'Irene Puig Parnau en l'anàlisi de transparència i fluorescència en el CLARITY, el seu interès i contribució, també, en el desenvolupament dels mètodes d'anàlisi morfològic de poblacions, amb una menció especial al algoritme d'interpolació; les contribucions als desenvolupaments per a l'anàlisi de projeccions axonals amb tensors estructurals al Malav Shah; la contribució ajudant en experiments i anàlisi del protocol del CLARITY primer, i després en la imatge i reconstrucció de neurones de CA1 de la Gemma Comas Armangué; la participació impagable en reconstrucció de neurones tant del Maxim Telle, com de l'Ariadna Corredora i el Mario García Ureña; les contribucions en mesures d'anisotropia per a l'anàlisi d'arbres dendrítics del Maxim Telle i el Seyi Latunde-Dada; la contribució als estudis d'esterologia de l'Álvaro Fernández; la petita col·laboració amb el Ruggero Bettinardi en el desenvolupament del càlcul de vectors normals a capes neuronals pel model generatiu en 3D; les contribucions en les primeres proves en el món de la dinàmica molecular amb el Pratik Mandal; i, per acabar, agrair la profunda contribució del Marcin Gorny a l'obtenció de datasets del CLARITY, al desenvolupament de parts de codi per al preprocessat d'aquests, i el desenvolupament de petits fragments de codi que contribueixen al model generatiu en 3D.

Vull agrair també, la contribució durant el primer any del projecte de la Belén de Sancristóbal. La seva visió en aquell moment va ajudar a encaminar el projecte en una direcció que finalment ha sigut útil, especialment amb el desenvolupament del model de la capa II/III del cortex.

Vull agrair les contribucions a través de les col·laboracions amb el Jordi Soriano, el Gianni de Fabritiis i la Inma Ballesteros. Especialment, la contribució, també importantíssima, de la Inma Ballesteros amb les injeccions de Lucifer Yellow a CA1. L'aportació tant conceptual com pràctica en les análisis de dinàmica molecular del Gianni de Fabritiis i el Gerard Martínez. També la cessió de mostres, a més de la sempre constructiva aportació científica, de l'Andrés Ozaita.

Voldria fer una menció especial a la col·laboració per a fer possible la imatge de cervells sencers amb el Jim Swoger i el James Sharpe. Ha sigut un camí complicat, però aviat podrem treure profit de tantes hores i recursos dedicats. També un especial agraïment al Jim per la seva actitud sempre de suport, i la confiança i les oportunitats que m'ha donat. La escriptura, amb ell, del projecte IAME (amb el suport de la Mara entre bastidors) ha sigut l'experiència més fluïda que he tingut en el disseny d'un projecte científic. Vull agraïr també, en aquest sentit, la col·laboració del Rodrigo Rocamora a la Unitat d'Epilèpsia de l'Hospital del Mar, i al Francesc Alameda de l'unitat d'Anatomia Patològica pel seu interès i contribució al projecte.

Vull agraïr, també, les contribucions del grup de la Victòria Puig de l'IMIM (incloent la Victòria, el Thomas Gener i la Maria Alemany) i l'intent de col·laboració en el projecte NEM4O. Igualment, vull agraïr les mostres enviades i l'intent de col·laboració amb la Hannah Monyer.

Tot i que no va ser possible fer-ho realitat, vull agraïr al professor Hanchuan Peng la bona predisposició i l'esforç fet per organitzar una estada per a col·laborar amb ell i la seva invitació a hackathons de BigNeuron.

També m'agradaria agraïr les discussions i projectes compartits amb el Pau Clusella en l'àmbit del mapejat entre topologia i dinàmica de circuits neuronals.

Per últim en l'àmbit professional, voldria agraïr a la Maria Martínez de Lagrán les seves inacabables aportacions tant en coneixements en el món de l'estudi de malalties mentals en ratolins, com el suport personal en totes les etapes del projecte. A la Júlia Albaigès Ràfols l'ajuda en mil aportacions petites en la feina del dia a dia com genotipacions i control de la colònia. I a l'Ilario de Toma i el Ricardo Gómez, juntament amb la Maria Martínez de Lagrán, els aprenentatges que va suposar escriure el projecte REMBRANDT amb ells. I ara sí, finalment, a l'Ilario l'oportunitat d'ajudar-lo en la publicació del review en neuroepigenètica.

En l'àmbit personal m'agradaria agraïr tots els moments que hem compartit amb companyes i companys de laboratori. El suport mutu, i les vivències que tenyeixen tot el doctorat de

bons records. El viatge a l'Alberca, el congrés de la SENC a Granada, els retreats, i tants i tants cafès a la terrassa i (no tants) sopars per Barcelona. Recordaré tenir-vos colze a colze a: Maria Martínez de Lagrán, Júlia Albaigès Ràfols, Marta Fructuoso, Mireia Ortega, Marcos Quevedo, Belén de Sanchristóbal, Jose Espinosa, Ilario de Toma, Edu Domínguez, Silvina Catuara, Laura Xicota, Marcin Gorny i Cèsar Sierra.

Sé que amb el cap ple com el tinc probablement hauré oblidat algú, mil disculpes per avançat!

Vull fer una menció especial a la relació d'amistat que hem anat teixint durant aquests quatre anys amb la Júlia i la Maria Alemany. El suport mutu que ens hem donat i les mil estones de cafès, sopant o fins i tot viatjant han sigut una part maquísima del Doctorat. Espero que ho sigui molt temps més.

En la mateixa línia les estones compartides amb tu, Miquel, i tots els cafès i passejades per la terrassa parlant de ciència i de les nostres vides.

Vull agraïr el suport i les estones compartides amb la comunitat de doctorands del CRG i tots els doctorands de la nostra promoció, incloent una menció especial al Sebastian, el Reza, la Hana, l'Andrea, la Laura, el Joan, la Hima, la Marta, el Marcos i la Juna. Encara que no mencioni a tothom, “un saludu” a totes les persones que amb els creuaments als passadissos li donem la xispa de la vida al CRG. Una menció especial al sector experimental del Toni Gabaldón (Ester, Ewa i Susana), de tant a prop heu sigut també un suport important. També, encara que no hagi estat mai al CRG, agraïr la contribució personal de l'Aina a l'hora de començar amb tot aquest projecte.

Agraïr també el suport i la comprensió amb el meu enclaustrament al pis que compartim, Genís i Sebastian un altre cop.

A família i amics de Santpedor (tu també Bordes) no cal que us digui fins a quin punt heu sigut un suport important per mi. Aviat tornaré a aparèixer. Heu sigut aquell fonament que cal per, quan tot tremola, “posar un peu a terra i aixecar el cap cot del sot”.

Pau i Oriol, sou quasi família. Que vagi per totes les braves i buenas olas que hem fet, i les que farem a partir d'ara!

Conjuntament amb el grup dels físics, heu sigut els aliats a l'àrea metropolitana. Gràcies per ser-hi.

I, per acabar, un agraïment molt profund a l'Irene Comellas. El teu suport durant tota la gestació d'aquesta Tesi ha sigut inigualable. Mai oblidaré els últims moments abans de dipositar-la. Espero que, amb el temps, et pugui tornar tota la dedicació, suport i energia que m'has donat.

Linus Manubens-Gil has been funded by a personal fellowship from La Fundació Privada Centre de Regulació Genòmica (CRG; NIF **G62426937**) during the period 2013-2017.

The work has received financial help from the Spanish Ministry of Innovation and Economy (SAF2013-49129-C2-1-R), Jerome Lejeune Foundation, FRAXA Foundation, Spanish Ministry of Health, PI11/00744 and the Spanish Ministry of Economy and Competitiveness, Centro de Excelencia Severo Ochoa 2013-2017', SEV-2012-0208.

ABSTRACT / RESUM

Abstract

During the last century the nervous system has been mainly studied from a reductionistic approach, based on the hypothesis that understanding in depth single neurons or limited neuronal populations would lead to general conclusions on brain function. However, to what extent anatomical details of single neurons can affect the wiring of the networks they form is a largely overlooked question. Intellectual disability provides an excellent opportunity to explore the relevance of fine structural details, because many disorders show specific architectural alterations that correlate with cognitive performance.

In this Thesis, I aimed to study how the network topology of neuronal circuits is affected by dendritic architectural features in a mouse model of intellectual disability, namely Down's syndrome, and upon the rewiring effect of pro-cognitive treatment. I did so from three points of view:

1. The exploration of a 2D minimal computational model of cortical layer II/III parameterized by experimental data on dendritic tree architecture of healthy mice and two Down syndrome mouse models.
2. The study of within-region morphological variations of hippocampal CA1 pyramidal neurons and their dependency of spatial embedding in healthy mice and a Down syndrome mouse model.
3. The development of an experimental and computational framework for whole brain multiscale analysis and modeling.

My work revealed that the dendritic tree architecture and the distribution of synaptic contacts have significant implications on how optimal single neurons are for information processing efficiency and storage capacity, and suggests that those single-neuron features permeate to the network level, determining the computational capacities of neural ensembles.

Also, I found position-dependent neuromorphological inhomogeneities in CA1 pyramids along with variations of neuronal cell density, suggesting that intrinsic properties of CA1 can vary across its extension. Those inhomogeneities were different in healthy and TgDyrk1A mice, possibly affecting emergent functional aspects.

In my Thesis I faced challenges to bridge structural descriptions at the cellular and networks scales and to study morphological inhomogeneities in cell populations. To solve those challenges, I developed computational tools for analyzing and modeling the anatomy of neuronal circuits while bridging the microscopic and mesoscopic scales. The analysis tools I developed and validated allow population-based analyses of cellular and dendritic density. Those, combined with the optimized CLARITY whole-brain clearing technique I implemented, will allow tackling the relationship between neuromorphology and the computational capacities of neural ensembles from a systems perspective.

Resum

Durant l'últim segle, el sistema nerviós s'ha estudiat des d'un punt de vista reduccionista, basant-se en la hipòtesi que entendre en profunditat neurones individuals o fraccions petites de poblacions neuronals portaria a conclusions generals sobre la funció del cervell. De totes maneres, fins a quin punt detalls anatòmics de neurones individuals poden afectar la connectivitat de les xarxes que formen, és una qüestió que en gran part s'ha passat per alt. Les discapacitats intel·lectuals proporcionen una oportunitat excel·lent per explorar la rellevància de detalls estructurals, perquè molts trastorns cognitius mostren alteracions arquitectòniques específiques que correlacionen amb habilitats cognitives.

En aquesta Tesi, pretenia estudiar com la topologia dels circuits neuronals és afectada per característiques arquitectòniques en un model murí de discapacitat intel·lectual, en concret de síndrome de Down, i per tractaments pro-cognitius amb efectes de remodelació de la xarxa. Ho he fet des de tres punts de vista:

1. L'exploració d'un model computacional 2D mínim de la capa cortical II/III parametritzat amb dades experimentals d'arquitectura dendrítica en ratolins sans i en dos models murins de síndrome de Down.
2. L'estudi de variacions morfològiques en neurones piramidals dins d'una mateixa regió en la capa CA1 de l'hipocamp i la seva dependència en la localització espacial en ratolins sans i en un model murí de síndrome de Down.
3. El desenvolupament d'un marc experimental i computacional per a l'anàlisi i model·lització del cervell del ratolí des d'una perspectiva multi-escala.

La meva feina mostra que l'arquitectura dendrítica i la distribució de contactes sinàptics tenen implicacions significatives en l'optimalitat de neurones individuals per a l'eficiència en el processat d'informació i per a la capacitat d'emmagatzemar memòries, i suggerix que aquestes dues quantitats permeen al nivell de xarxa, determinant les capacitats computacionals de conjunts de neurones.

També, he trobat variacions neuromorfològiques a CA1 dependents de la posició en neurones piramidals, acompanyades per variacions en densitat cel·lular, apuntant que propietats intrínseqües de CA1 poden variar al llarg de la seva extensió. Aquestes

inhomogeneitats eren diferents en ratolins sans i TgDyrk1A, possiblement tenint efectes en aspectes funcionals emergents concrets.

En la meva Tesi he afrontat reptes en lligar descripcions estructurals a escales cel·lular i de xarxes i en l'estudi de propietats morfològiques inhomogènies en poblacions cel·lulars. Per superar aquests reptes, he desenvolupat eines computacionals per a l'anàlisi i el modelat de l'anatomia de circuits neuronals lligant l'escala microscòpica i mesoscòpica. Aquestes eines, combinades amb l'optimització de la tècnica de clarejat de cervells sencers CLARITY que he implementat, permetrà afrontar l'estudi de la relació entre la neuromorfologia i les capacitats computacionals de conjunts de neurones des d'una perspectiva de sistema.

PREFACE

Preface

Despite being far from a complete description of the nervous system, the cellular architecture of neurons has an important role in determining how the structural properties of neuronal networks give rise to neural functions or dysfunctions. However, how anatomical details of single neurons affect the wiring of the networks they form, and consequently their function, is a largely overlooked question. Given that many pathological conditions, such as Alzheimer's disease, intellectual disability, epilepsy or chronic stress present aberrant dendritic morphologies, those scenarios provide an excellent opportunity to explore how fine structural alterations have an impact on cognitive performance.

This Thesis originates from the interest of the Cellular and Systems Neurobiology group at the Center for Genomic Regulation in understanding the mechanisms underlying the neuropathology of intellectual disability. Pioneering studies in our lab discovered a distinctive cellular pathology in Down syndrome characterized by microstructural alterations in the cerebral cortex and the hippocampus. These brain regions are critical for high cognitive functions, which are disturbed in individuals with DS. The most characteristic feature of those regions is their rich connectivity, based predominantly on excitatory connections in the dendritic spines of pyramidal neurons. The aberrant microanatomy detected in Down syndrome mouse models could be partially rescued upon pro-cognitive treatments that correct the overdosage of a DS candidate gene, *DYRK1A*, which encodes for a member of the Dual-specificity tyrosine phosphorylation-regulated kinase (DYRK) family and is sufficient and necessary to recapitulate some of the Down syndrome phenotypes. Although it is not yet known whether this rescue has an impact on the network, a clinical trial in humans with the same treatment found increased cortical functional connectivity in fMRI studies.

Thus, a key hypothesis in my Thesis is that dendritic architecture changes in intellectual disability may have a strong impact on neuronal network topologies, which would explain the subsequent changes in connectivity. To examine that hypothesis, I first had to gain a more systematic view, to understand the variation in the normal dendritic arborization and the pathological deviations in intellectual disability by profiling dendritic trees in different mouse strains and Down syndrome models. This was done through the analysis of existing datasets. To define the optimal wiring scenario, I applied scaling laws derived in the literature

and Pareto optimality for understanding the contribution of various architectural features of dendritic trees in single cells to maximizing routing efficiency and storage capacity

However, those concepts and features do not apply to the circuit level, thus making impossible to directly extrapolate the extent to which dendritic aberrations at the single level could affect network functionality. To this aim I had to build my own computational models to explore how local network topology is affected by alterations in single-neuron morphostructural features in mouse models of intellectual disability, and by neuronal reformatting and network rewiring upon pro-cognitive treatments known to partially rescue the cognitive phenotypes in DS. In order to do so, I explored the morphospace of dendritic trees, generated instantiations of the local horizontal connectivity of cortical pyramidal layer II/III and studied their topology using graph theoretical. Specifically, I took routing and storage capacity as the principal variables for defining an “efficiency morphospace”.

In the second part of my Thesis, I wanted to experimentally explore within-class variability in a well-defined canonical population of neurons, namely CA1 pyramidal neurons, as a function of their spatial location. Previous models are derived assuming certain simplifications such as homogeneity and isotropy. My experiments provided initial population level descriptions that revealed an unexpected position-dependent level of microanatomical variability that suggests continuous heterogeneity to be an important feature of neural circuits.

To achieve the goals described above, during my Thesis I implemented a variety of analytic frameworks and theoretical perspectives, keeping in mind the challenge of using brain samples and datasets at different spatial scales (microscopic to mesoscopic), and of developing theoretical frameworks to test my hypotheses. The outcomes of my Thesis have set the basis for further research lines in Dierssen’s lab involving new computational modeling to interrogate the structure-function relationship. This theoretical and Systems Neuroscience approach was also supervised by Prof. Jordi García-Ojalvo (University Pompeu Fabra), co-director of my work.

In the final part of my Thesis, I made some steps towards obtaining whole brain structural information with microscopic resolution using state-of-the-art brain clearing techniques.

Those will serve to explore how micro-connectomic disturbances in local networks may impact large-scale connectivity and can induce specific topology alterations and suboptimal computational capacities at the systems level. Charting cellular localizations, arborizations, and projections throughout the whole brain is a mandatory step to understand network properties, but the tools for combining these levels of description are not available yet. I started filling this gap by providing software to construct multiscale structural maps from brain-clearing experiments, and to use them for the computational instantiation of neuronal circuit contact topology on a brain-wide scale. The set of tools I developed offer a first step towards a systems-perspective description of neuronal circuits' microscopic structural and population-based properties. Finally, I also propose a new method for selecting clearing media, based on the use of molecular modeling (**Annex III**).

During the present Doctoral Thesis, I had the opportunity to be part of several international and national scientific collaborations with renowned research groups in the systems neuroscience. For applying the concept of optimality, I had the opportunity to discuss directly with Prof. Hermann Cuntz. I also discussed directly with Prof. Inmaculada Ballesteros the study of cortical basal trees. To perform whole-brain imaging I have established a long-term collaboration with the lab of Dr. James Sharpe. For the implementation of the 2D model I had the opportunity to discuss directly with Prof. Jordi Soriano and Dr. Javier Orlandi. Finally, for the molecular-dynamics study of fluorescent protein quenching I had the assessment of the group of Dr. Gianni De Fabritiis.

During this Doctoral Thesis, I presented my work in four national and two international meetings, and I have participated also in local simposia (CRG Christmas symposium, CRG PhD Symposium etc.), and outreach and teaching activities of the laboratory.

Publications of this Thesis

Where environment meets cognition: a focus on two developmental intellectual disability disorders.

De Toma I., Manubens-Gil L., Ossowski S., and Dierssen M. *Neural Plasticity*, 2016.

Articles in preparation:

Exploration of the morphospace in a minimal model of local cortical layer II/III: neuromorphological alterations in DS mouse models and their impact on computational capacities. Manubens-Gil L., Garcia-Ojalvo J. and Dierssen M., in preparation.

Environmental enrichment effects on neuromorphological alterations in the TgDyrk1A DS mouse model and its mesoscopic implications on the trisynaptic circuit. Pons-Espinal M.*[,] Manubens-Gil L.* et al., in preparation (Co-first author).

CLARITY technique optimization through fluorescent protein molecular dynamics and docking simulations. Manubens-Gil L., Swoger J., Sharpe J., Garcia-Ojalvo J. and Dierssen M., in preparation.

Systems-perspective analysis pipeline for whole-organ fluorescence microscopy teravoxel-sized datasets

Manubens-Gil L., García Ojalvo, J. and Dierssen M. in preparation.

Multi-scale morphological effects on neuronal network contact topology: Pareto optimality in the TgDyrk1A DS mouse model

Manubens-Gil L., García Ojalvo, J. and Dierssen M. in preparation.

INDEX

Index

ABSTRACT	xvii
PREFACE	xxv
INDEX.....	xxxiii
LIST OF FIGURES	xxxvii
LIST OF TABLES	xli
GENERAL INTRODUCTION.....	5
HYPOTHESIS AND OBJECTIVES	17
1. CHAPTER I. NEUROMORPHOLOGY IMPLICATIONS ON LOCAL NETWORK CONNECTIVITY IN A MINIMAL MODEL OF CORTICAL LAYER II/III	21
1.1. Introduction.....	25
1.2. Methods.....	37
1.2.1. Optimal dendritic wiring of cortical pyramidal neurons of Ts65Dn and Dyrk1A+/-	37
1.2.2. A 2D minimal model to determine the impact of dendritic wiring features on network properties.....	45
1.2.3. Network topology characterization using graph theory	50
1.3. Results.....	53
1.3.1. Single-neuron wiring optimality in models of intellectual disability	53
1.3.2. Network computational capacities.....	71
1.3.3. Dendritic rewiring effects on network computational capacities	82
1.3.4. Pareto optimality for computational capacities.....	82
1.4. Discussion and conclusions.....	84
2. CHAPTER II. IMPACT OF SINGLE-NEURON STRUCTURAL DIVERSITY IN HIPPOCAMPAL CA1 POPULATIONS	93
2.1. Introduction.....	97
2.2. Methods.....	106
2.2.1. Single-cell analysis	106
2.2.2. Population-based analysis: morphological within-class variability of CA1 pyramidal neurons along the antero-posterior hippocampal axis in wild-type and TgDyrk1A	110
2.2.3. Development of a customized pipeline for population-based analysis in histological sections	114
2.3. Results.....	122

2.3.1. Morphological properties of TgDyrk1A CA1 pyramidal neurons.....	122
2.3.2. Cellularity and volume variations along the antero-posterior axis of dorsal CA1 in TgDyrk1A.....	129
2.3.3. Development of computational tools for generative modeling of 3D neuronal circuits.....	138
2.4. Discussion and conclusions.....	142
3. CHAPTER III. RECONSTRUCTING AND MODELING THE TRANSPARENT WHOLE BRAIN	149
3.2. Methods.....	157
3.2.1. Brain clearing technique (CLARITY).....	157
3.2.2. CLARITY Whole-brain imaging and data preprocessing	160
3.2.3. Statistical analysis.....	162
3.3. Results and discussion	163
3.3.1. Cost-effective optimization of tissue clearing techniques	163
3.3.2. Computational pipeline for CLARITY based whole-brain structural interrogation	167
3.4. Discussion and conclusions.....	175
GENERAL DISCUSSION	183
CONCLUSIONS	195
BIBLIOGRAPHY	201
ANNEX	215
ANNEX I: Supplementary Figure	217
ANNEX II: Number of afferents and dendritic tree area correlation.....	219
ANNEX III: Computational and experimental approaches for optimizing cleared whole- brain fluorescence microscopy imaging.....	221
ANNEX IV: Publications of this Thesis.....	233

List of Figures

Figure 1. Camera lucida reconstruction of a pyramidal neuron from a rat neocortex.	6
Figure 2. Sagittal view of the rat brain indicating the different brain areas.	29
Figure 3: Schematic representation of a pyramidal neuron and analysed neuromorphological metrics.	39
Figure 4: Schematic representation of the workflow for single neuron reconstruction and morphometric analysis.	40
Figure 5: Schematic representation of the circuit building process.	47
Figure 6: Dendritic and spine numbers dependency on the dendritic tree radius in wild-type C57BL/6J mice.	50
Figure 7: Camera lucida drawings of the basal dendritic trees of layer II/III motor cortex pyramidal neurons of Ts65Dn, Dyrk1A +/- and their respective controls.	53
Figure 8: Dendrograms for four representative neurons.	55
Figure 9: Overview of the neuromorphological metrics obtained in the statistical analysis with the Trees Toolbox.	56
Figure 10: Boxplots of single-neuron morphological metrics.	58
Figure 11: Principal component analysis.	60
Figure 12: Power law relations between total dendritic length and branch number for layer II/III basal tree reconstructions of Ts65Dn and Dyrk1A+/- neurons, and their respective controls.	62
Figure 13: Power law relations between total dendritic length and arbor radius for layer II/III basal tree reconstructions of Ts65Dn and Dyrk1A+/- neurons, and their respective controls.	63
Figure 14: $L \sim bp^\alpha$ and $R \sim L^\alpha$ power law relations between the number of branch points and total dendritic length, and total dendritic length and arbor radius for a morphospace exploration of layer II/III basal tree reconstructions.	65
Figure 15: Implications of the morphospace exploration on the computational capacities of the cortical layer II/III single-neuron dendritic trees.	66
Figure 16: Morphospace principal component analysis.	67
Figure 17: 2D projections of the morphospace exploration.	70

Figure 18: Implications of the morphospace exploration on the computational capacities of the cortical layer II/III local network model.....	72
Figure 19: Implications of the morphospace exploration on topological properties of the cortical layer II/III local network model.....	75
Figure 20: Normalization of dendritic radial distributions to the C57BL6/J strain wild-type data	79
Figure 21: Dendritic and spine radial distributions normalized to wild-type C57BL6/J mice.	80
Figure 22: Overview of the morphospace exploration in the cortical layer II/III local network model.....	81
Figure 23: 3D rendering of the mouse hippocampus.....	103
Figure 24 : Overview of the imaging, stitching, alignment and segmentation procedure ..	115
Figure 25: Overview of the cell density mapping procedure.....	117
Figure 26: Overview of the dendritic density mapping procedure.....	118
Figure 27 : Schematic representation of interpolation method developed.	119
Figure 28: Schematic representation for the MDA procedure to the generation of anatomical templates.	121
Figure 29: Genotype-dependent dendritic tree architectural modifications.....	122
Figure 30: Principal component analysis (PCA) of the neuromorphological and geometric variables of the dendritic tree.....	124
Figure 31: Power law relations between total dendritic length and branch number for layer II/III basal tree reconstructions of wild-type and TgDyrk1A neurons.....	125
Figure 32: Storage capacity estimations for wild-type and TgDyrk1A CA1 apical dendritic trees.....	126
Figure 33: CA1 along the proximal-distal axis.	127
Figure 34: Genotype-dependent differences in neurite path length and branch order in TgDyrk1A.	128
Figure 35: Stereological estimations for volume (left) and cellular density of Thy1-labeled (middle) and NeuN immunostained (right) neurons in CA1 pyramidal layer.....	130
Figure 36: Volume and cellular density quantifications of CA1 pyramidal layer with the computational methods for population analysis.	131

Figure 37: Bland-Altman plots of differences between the computational method and stereology vs. the mean of the two measurements.....	132
Figure 38: Cell density and dendritic occupancy in CA1 and CA3.....	133
Figure 39: Comparison between single-cell and population-based Sholl analyses.....	134
Figure 40: VBM analysis of dendritic density in CA1 from wild-type vs. TgDyrk1A mice.....	136
Figure 41: Dendritic density plot for distal CA1.....	137
Figure 42: Our aim is to use population-based structural properties to parametrize a generative model leading to realistic network templates.....	138
Figure 43: 3D model for the instantiation of biologically realistic neuronal circuitry.	141
Figure 44: 3D structural analysis of whole mouse brains.	153
Figure 45: Schematic representation of CLARITY protocol basis.....	155
Figure 46: Comparison of transparency of RIM candidates.....	163
Figure 47: Comparison Sharpness ratio for RIM media candidates.....	164
Figure 48: Stereomicroscope images for the assessment of sample transmittance under the different RIM media candidates.....	165
Figure 49: Comparison of fluorescence intensity in Thy1-YFP brain samples.	166
Figure 50: Contrast to Noise Ratio of the fluorescence microscope images obtained from slices under exposure to each of the four RIM media candidates.	166
Figure 51: Deformation of the samples under 2 days (2d) and 4 days (4d) of incubation in RIM media candidates: Chung (diatrizoic acid solution), TDE83 (TDE 83% solution), Gly (glycerol 87% solution) and FC (FocusClear).....	167
Figure 52: Maximum-value projections (inverted contrast) through one hemisphere of a B6.Cg-Tg(Thy1-YFP)HJrs/J mouse brain scanned at 5x magnification (scale bar = 1000 μ m).....	168
Figure 53: Snapshots of 3D views of whole brain imaging datasets in different imaging media.....	169
Figure 54: Multi-resolution imaging in a cleared whole mouse brain.	170
Figure 55: Deformation-based morphometry.	171

Figure 56: Registration to a common template for automatic segmentation.....	172
Figure 57: Structural tensor for axonal tracking.....	173
Figure 58: Overview of the whole-brain analysis and modeling workflow.....	174
Figure 59. Dendritic architecture heterogeneity throughout cortical layer II/III.	189

List of Tables

Table 1: Brain alterations in Down syndrome.....	10
Table 2: Neuromorphological metrics.....	40
Table 3: Neuromorphological parameter set for the instantiation of the 2D model.....	49
Table 4: Statistical comparisons between single-neuron morphological metrics.. ..	59
Table 5: Sholl analysis average values for Ts65Dn, Dyrk1A+/- cortical layer II/III basal trees and their wild-type counterparts.....	77
Table 6: Average synaptic densities along the radius of Ts65Dn, Dyrk1A+/- cortical layer II/III basal trees and their wild-type counterparts.....	78
Table 7: FDR analysis of the VBM dendritic density in CA1 comparison between wild-type vs. TgDyrk1A mice.....	136

GENERAL INTRODUCTION

GENERAL INTRODUCTION

There is consensus among neuroscientists that the cellular architecture of neurons, despite not providing a complete description of the nervous system, has an important role determining the function of neuronal networks. Key properties of these cells are the spatial organization of the afferent structures (dendrites), and the topology of the synaptic connections, which constrains the dynamics of a neural circuit, shaping the repertoire of collective activities that gives rise to neural functions or dysfunctions. This is studied by a new discipline called micro-connectomics, which deals with the analysis of organizational principles in neuronal connectivity at the cellular scale. A growing body of data on the anatomical microcircuitry at the cellular and synaptic level, in the form of ‘micro-connectomes’, has shed light on information processing in simplified neural systems. However, for complex structures such as the mammalian neocortex, which is related to many high-level computational processes such as sensory processing, planning, motor control, perception and language, detailed micro-connectomes may still be years away. An alternative approach has been to statistically characterize connectivity patterns between different cell types (Hill, Wang, Riachi, Schürmann, & Markram, 2012), but few studies have been devoted to analyze connectivity patterns that could uncover complex network topologies. Thus, both approaches leave a gap between cellular architecture and the understanding of fundamental properties governing the emergence of cognitive function.

Basic elements of neuronal architecture and their role in neuronal computation

My work is centered in the main intercellular communication apparatus in the neuron: the dendritic tree. A typical neuron may be divided into three distinct parts (**Figure 1**): a cell body or soma, an axon, and dendrites. The latter two are specialized extensions of membrane that constitute the neuron’s communication interfaces. Dendrites are membranous protoplasmatic projections branching from the body of a neuron. They are usually extensively subdivided, forming a dense arborization surrounding the neuron, called a dendritic tree. The area occupied by the dendritic tree is larger than the soma, and consequently the dendritic membrane covers a much greater surface. The main function of the dendrites is to get information from other cells and deliver that information to the cell body. On the dendrites we find dendritic spines, membranous protrusions that actually synapse with the axon’s terminal bulbs (axo-dendritic synapses), or with another dendrite

(dendro-dendritic synapses). A single dendritic tree can have tens of thousands of dendritic spines, e.g. of excitatory inputs of information.

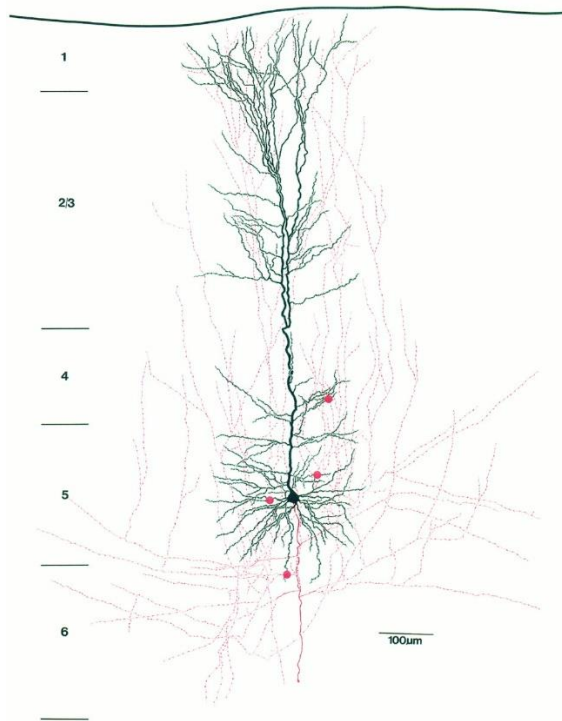


Figure 1. Camera lucida reconstruction of a pyramidal neuron from a rat neocortex. The reconstruction shows a thick-tufted layer 5 pyramidal neuron. Dendritic morphology of the neuron is drawn in black, and axonal arborization in red. The red dots indicate contacts established onto basal and oblique dendrites by the axon. Note the extensive vertical axonal collaterals, some of which could be followed up to layer 1 (2.5 mm from the soma). (Lübke, Markram, Frotscher, & Sakmann, 1996).

Most neurons also have an axon, a tube-like extension that carries information as an electrochemical impulse to the terminal boutons (buttons), or endfeet, located on the receiving cell. The influence of the structure of this information apparatus (dendrites and axon) on neuronal function has been largely demonstrated in experimental studies. Regarding the axonal morphology, Ramon et al. showed already in the 1970s action potential modifications at sites of abrupt increase in axonal diameter (Ramón, Moore, Joyner, & Westerfield, 1976). Branching is also an important factor. For example, high frequency current modulations in unbranched axons lead to abnormal patterns such as fragmented trains, quasi-periodic, and chaotic responses (Smith, 1977). Measurements along axonal branching points with two different radii exhibited different temporal responses in the two daughter branches (Sasaki, Matsuki, & Ikegaya, 2012). Stockbridge showed that if branching

consisted of short and long daughter branches, only the first of adjacent spike pair invades the long branch, while the two spikes propagate along the short one (Stockbridge & Stockbridge, 1988). Sasaki et al. examined changes in action potential width caused by modulations of axonal length and branching order (Sasaki, Matsuki, & Ikegaya, 2011).

In this Thesis I have focused in the study of the dendrites, this is because their microanatomical details are accessible, which is not the case for the axon, but also because of their prominent role in information acquisition and processing. Mammalian dendrites have a rich repertoire of electrical and chemical dynamics, making individual neurons capable of very sophisticated information processing (Yuste & Tank, 1996). Experimental and computational studies have shown a strong interdependence between morphology and electrical dynamics at the single-cell level (Segev and Rall 1998; Van Elburg and van Ooyen 2010; Eyal et al. 2014), although the underlying mechanisms are poorly understood, and the impact of morphology on electrical activity at the network level remains elusive.

Neuronal design: the concept of optimality

At the end of the 19th century, Ramón y Cajal proposed the idea that dendrites optimize connectivity by minimizing conduction time in a tradeoff with total cable length cost^[1]. During the last decades, the interest for the concept of optimality in neuronal cells and networks has been growing (Chen, Hall, & Chklovskii, 2006; Chklovskii, 2004; Chklovskii, Schikorski, & Stevens, 2002; Cuntz, Mathy, & Häusser, 2012). It has been proposed that dendritic trees grow to fill optimally a target space. Two power laws relating the total length and the number of dendritic branches, and the dendritic tree radius in single neurons respectively have been derived from Cajal's principle for conservation of cytoplasm and conduction time (Cuntz et al., 2012; Wen & Chklovskii 2009). Since these optimal wiring scaling laws for single neurons were derived, some studies have used the concept to describe specific neuronal populations (Iyer et al., 2013; Polavaram, Gillette, Parekh, & Ascoli, 2014), and neuronal diversity in specific layers or regions (Leguey et al., 2016) or throughout development (Lefebvre, Sanes, & Kay, 2015). There is a wide variety of different neuronal morphologies in the brains of different animal species (Bullock & Horridge, 1965; Nieuwenhuys & Nicholson, 1998; Strausfeld, 2012), in different brain regions of the same species (Shepherd et al., 1998), or even in the same brain region (Markram et al., 2004), but all follow the optimal wiring scaling law derived by Cuntz et al. (Cuntz et al., 2012). Even so,

the high structural variability among neuronal classes, and among brain regions and genetics for the same cell type makes it difficult to define an optimal range of variance. This may be achieved by capitalizing on the scenario provided by neuropathological models, using comparative analysis of micro-connectomics (Schröter, Paulsen, & Bullmore, 2017).

Intellectual disability as a model of suboptimal networks

Abnormalities in dendritic structure are a characteristic feature of many brain disorders. One clear example are individuals with intellectual disability that present reduced dendritic branching patterns, shortened dendritic lengths, loss of spines, and changes in spine shape and size (Kulkarni & Firestein, 2012). Since the discovery in the 1970s that dendritic abnormalities in cortical pyramidal neurons are the most consistent pathologic correlate of intellectual disability, research has focused on how dendritic alterations are related to reduced intellectual ability. The recent identification of the genetic bases of some mental-retardation-associated alterations, and the introduction of powerful sophisticated tools in the field of microanatomy has led to a growth in the studies of the alterations of pyramidal cell morphology in these disorders. Most probably these alterations may have strong implications on single-neuron wiring and its optimality. Additionally, dendritic rewiring via pro-cognitive treatments tackling neuronal architecture provides a unique opportunity to establish causal links between neuronal morphology and wiring, and cognitive function. However, while in healthy phenotypes the studies assessing optimality questions are still limited (Schröter et al., 2017), the analysis of intellectual disability models has not even been started. Thus, our study constitutes a first step towards the identification of fundamental properties for optimal wiring through the comparative analysis of intellectual disability (Huttenlocher, 1970; Huttenlocher, 1974; Purpura, 1974).

Our laboratory has extensively studied Down syndrome (DS) mouse models to understand the microanatomical changes driven by specific genetic perturbations. Such studies require a varied repertoire of approaches in DS and to investigate phenotype/genotype relationships given by an increased dosage of HSA21 genes in mice (see Cairns 2001; Galdzicki and Siarey 2003 for review). The analysis of the relationships between cognition, genotype and brain microanatomy are possible in: (1) transgenic animals overexpressing single or combinations of genes, (2) mouse models that carry all or part of MMU16, which has regions of conserved

homology with HSA21 and (3) chimeric mice that carry a fragment of human chromosome 21 (Tomizuka et al., 1997).

In this Thesis I focused on a well validated model of partial trisomy and two models with dosage changes of a candidate gene for DS: the Ts65Dn mouse model (Davisson, Schmidt, & Akeson, 1990), which contains three copies of mouse chromosome 16 (MMU16 from *Afp* to *Mx1*), and the TgDyrk1A and Dyrk1A+/- mouse models, over-expressing and under-expressing respectively *Dyrk1A* (Dual specificity tyrosine phosphorylation-regulated kinase 1A). DYRK1A is possibly the most extensively studied chromosome 21 gene during the last decade, due to the remarkable correlation of its functions in the brain with important DS neuropathologies, such as neuronal deficits, dendrite atrophy, spine dysgenesis, and cognitive and behavioral deficits.

We were the first in reporting that by modulating its dosage of activity, we could specifically manipulate important properties of the dendritic trees, thus providing a suitable scenario for our questions

However, understanding the implications of such detailed alterations and modifications in neuronal wiring, requires bridging the gap between cellular architecture and the emergence of cognitive function from a whole-brain perspective. At the macroscopic scale, the adult DS brain has a characteristic morphology that includes reductions in overall brain weight and volume, with disproportionate volume reductions in the frontal and temporal lobes (**Table 1**). In addition, the brain is brachycephalic, with disproportionately small cerebellar volumes, a simplified gyral appearance, and a narrow superior temporal gyrus. Conversely, the parahippocampal gyrus is larger than normal in DS, although greater gray matter reductions have been described in the frontal lobe, the hippocampus and at the level of cerebellum (Menghini, Costanzo, & Vicari, 2011; Pinter, Eliez, Schmitt, Capone, & Reiss, 2001; Rigoldi et al., 2009). No abnormalities in pattern of brain asymmetry have been noted (Pinter et al., 2001).

Structural neuroimaging studies have confirmed the findings of post-mortem studies showing reduced volume of the hippocampus system and disproportionately smaller frontal lobe in adults with DS (Beacher et al., 2010; Jernigan, Bellugi, Sowell, Doherty, & Hesselink, 1993; White, Alkire, & Haier, 2003). Neuroimaging investigations have also shown that such

individuals have decreased volume of grey matter tissue in the cerebellum, frontal lobe, right middle–superior temporal gyrus, and the left CA2–CA3 region of the hippocampus, and have highlighted that these brain areas have major roles in the specific mnestic alterations that are exhibited in this disorder (Krasuski, Alexander, Horwitz, Rapoport, & Schapiro, 2002; Raz et al., 1995; Teipel et al., 2004).

In contrast to cortical regions, subcortical regions show relatively preserved volumes in DS (Jernigan et al., 1993; Pinter et al., 2001). In the context of significantly smaller overall cerebral volumes, the relatively large size of these latter structures, suggests that there is a dissociation of the development of cortical versus subcortical regions, which will affect neurological development with some functions being compensated for while others are not. Along with these structural alterations, atypical patterns of brain activation have been demonstrated in DS (Jacola et al., 2011), allowing predictions on structural–functional maps in this disorder (Colom, Karama, Jung, & Haier, 2010). For example, the poor performances of individuals with DS in linguistic tasks could be partially explained in terms of impairment of the connectivity of frontocerebellar structures that are involved in articulation and verbal working memory (Fabbro, Libera, & Tavano, 2002), whereas the reduced long-term memory capacities may be related to the frontotemporal lobes and, specifically, to hippocampal dysfunction (Pennington, Moon, Edgin, Stedron, & Nadel, 2003).

Table 1: Brain alterations in Down syndrome. Alterations found in Down syndrome subjects shown by brain area and age (newborns, adults between 20 and 50 years old, and individuals aged over 50).

Brain alterations in Down syndrome			
Brain region	Newborns	Adults (20-50)	Aged individuals (> 50)
Whole brain	Almost normal weight	Reduction in weight; brachicephalic	Smaller overall cerebral volumes
Prefrontal cortex	Reduction in volume	Reduction in volume	Reduction in volume
Parietal cortex	Normal or reduction in volume	Reduction in volume	Unknown

Temporal cortex	Narrow superior temporal gyrus	Reduction in volume of right middle or superior temporal gyrus	Decreased gray matter volume in posterior cingulate and entorhinal cortex
Hippocampus	Unknown	Reduction in volume	Early degeneration
Parahippocampal region	Unknown	Increase in size of the parahippocampal gyrus	Reduction in volume
Cerebellum	Reduction in volume	Reduction in volume	Reduction in volume
Brain stem	Reduction in volume	Increase in gray matter volume	Degeneration of locus coeruleus
Subcortical areas	Almost normal size	Normal	Degeneration of basal prosencephalon cholinergic nuclei (nucleus of Meynert); reduction in amygdala volume

Understanding the impact of suboptimally wired networks

While many correlational studies have found that neuromorphological architectural changes at the microscopic scale accompany cognitive impairments, the understanding of the impact of specific alterations on the organization and function of neuronal networks is still not understood. This is due to some fundamental limitations usually found in the approaches taken in the field of Neuroscience. First, the gap between the descriptions of alterations found at the single-cell level and the assessment of the organization and function of neuronal circuits from a network perspective. Second, the tendency to overlook spatial inhomogeneity and subtle variations on the organization and composition of neuronal circuits, which usually are assumed to be highly stereotypical. And third, the lack of a systems' perspective that allows taking into account the role of specific brain regions or neuronal layers in the context of the whole brain, considering that their impact on cognitive functions is limited. These limitations vertebrate the structure of this Thesis and each of the Chapters aims to contribute conceptual frameworks and approaches towards overcoming them.

One of the concepts that seems to permeate through multiple scales of description of neuronal networks is wiring optimality. As mentioned above, single neuron dendritic trees have been shown to grow to fill optimally a target space while minimizing conduction time and at a low cost. At the same time, whole-brain connectomes have been proposed to be shaped by an economic trade-off between wiring cost and the emergence of topological patterns valuable for cognitive demands (Bullmore & Sporns, 2009). I interpret single-neuron wiring optimality studies as a first step towards a generic framework for understanding fundamental properties of the nervous system, and I propose that graph-theoretical analyses of neuronal circuits at the cellular scale will allow (1) to disentangle the implications of multi-scale morphological properties on neuronal wiring, (2) to bridge the single-cell and network levels of description, (3) to identify neuronal subcircuits involved in specific functions, and ultimately, (4) to identify the rules governing neuronal wiring.

To explore those concepts, I compared the brain of wild-type mice with those of mice with suboptimal cognitive function. Since in most cases the experimental tools to link microstructural properties with network topology do not exist, I first analyzed the architectural properties of single dendritic trees, including their wiring optimality, and took a computational modeling approach to assess their effect on network topological patterns. I developed a framework that allows to quantitatively explore the neuromorphological space and assess its implications on the optimality for signal processing and storage capacity, linking single cell architecture with network contact topology. In the second part of the Thesis, I obtained single neuron morphology and population-based experimental data in a brain region responsible of specific cognitive functions, and analyzed how architectural features vary along the topography of a neuronal layer and how morphological alterations relate to cognitive impairment in intellectual disability. To assess the effect of those multiscale architectural features on network wiring, I developed a computational model able to instantiate the connectivity of neuronal circuits based on the obtained experimental data. And, finally, I gathered multi-scale experimental data and developed an extensible computational modeling framework that allows a systems perspective analysis of the link between neuromorphology and network connectivity.

HYPOTHESIS AND OBJECTIVES

HYPOTHESIS AND OBJECTIVES

During the last century the nervous system has been studied from a reductionistic approach based on the conviction that understanding in depth single neurons or limited neuronal populations would lead to general conclusions on brain function. However, to what extent anatomical details of single neurons can be affecting the wiring of the networks they form is a largely overlooked question. This is especially challenging when acknowledging for the unexpected morphological variety, and the structural inhomogeneities along each brain region. A prevailing alternative approach has been to statistically characterize subpopulations of a canonical cell type, which has already uncovered traces of complex network topologies. Considering that dendritic morphology can undergo significant changes in many pathological conditions, such as Alzheimer's disease, intellectual disability, epilepsy, schizophrenia or chronic stress, those scenarios provide an excellent opportunity to explore the relevance of fine structural details. Pioneering studies in our lab indicate that Down syndrome (DS), the most frequent genetic cause of intellectual disability is characterized by specific architectural alterations in pyramidal neurons that correlate with defective cognitive performance. In some cases, the neuronal structure and connectivity damage characteristic of this disorder may potentially be reversed by treatments with pro-cognitive effects. Specifically, we found that structural deficits can be partially rescued upon pro-cognitive treatment in DS, which corrects the over-dosage of a candidate gene, *DYRK1A*.

Hypothesis

We hypothesize that dendritic neuromorphological alterations of single neurons in intellectual disability lead to suboptimal signal integration and connectivity that (1) have significant implications on the network topology resulting in suboptimal computational capacities in intellectual disability, and (2) can explain specific pathological impairments.

Objectives

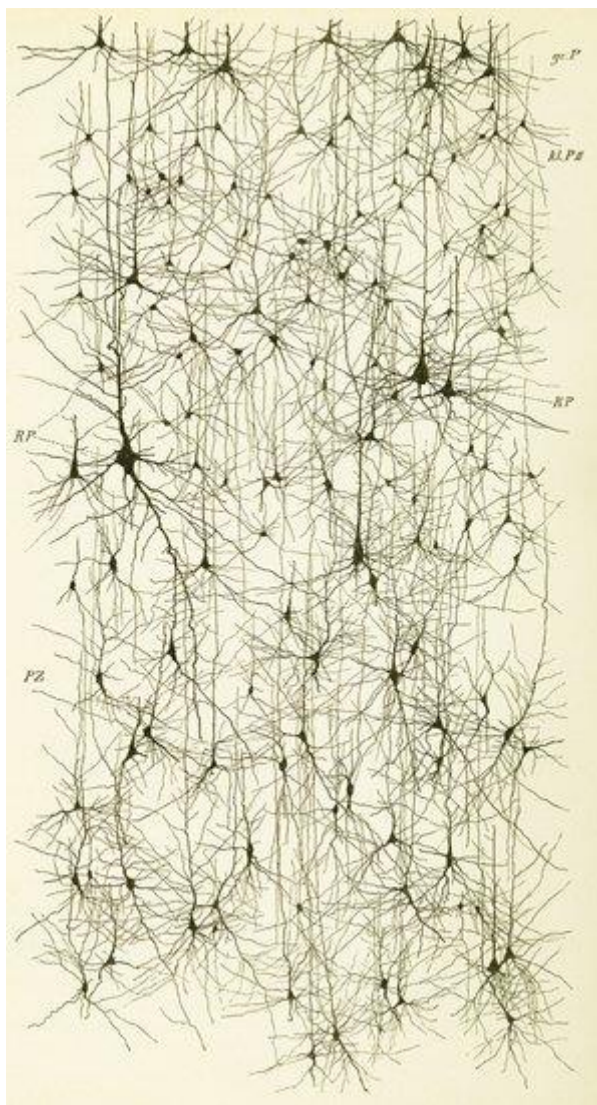
To prove the hypothesis above, the specific aims of this Thesis are:

Objective #1/ To investigate how alterations in single-neuron morphostructural features in mouse models of intellectual disability sculpt local network topology, through *in-silico* exploration of the resulting morphospace.

Objective #2/ To assess the neuronal reformatting and network rewiring effect of proven pro-cognitive treatments known to rescue the cognitive phenotypes in DS.

Objective #3/ To develop new tools that will allow us to (1) explore how micro-connectomic disturbances in local networks may impact on large-scale connectivity, and (2) determine whether micro-connectomic aberrations imply specific topology alterations and suboptimal computational capacities at the systems level.

1. CHAPTER I. NEUROMORPHOLOGY IMPLICATIONS ON LOCAL NETWORK CONNECTIVITY IN A MINIMAL MODEL OF CORTICAL LAYER II/III



*Cortical pyramids reconstructions and drawings by Cajal.
From. Cajal's Butterflies of the Soul.
Science and Art. Javier DeFelipe.*

"To know the brain—we said to ourselves in our idealistic enthusiasm—is equivalent to discover the material course of thought and will. [. . .] Like the entomologist hunting for brightly coloured butterflies, my attention was drawn to the flower garden of the grey matter, which contained cells with delicate and elegant forms, the mysterious butterflies of the soul, the beating of whose wings may some day (who knows?) clarify the secret of mental life."

Santiago Ramón y Cajal, Recuerdos de mi vida.

1.1. Introduction

The study of brain architecture was originally taken from a descriptive perspective (Ramón y Cajal, 1995). The seminal works of Lapicque (Lapicque, 1907), Hodgkin & Huxley (Hodgkin & Huxley, 1952) and Morris & Lecar (Morris & Lecar, 1981) implied a paradigm shift towards quantitative mathematical modeling of neuronal function at the single-cell level. The advent of mechanistic models accounting for the computations performed by networks of neurons, pioneered by David Marr (Marr, Willshaw, & McNaughton, 1991), required an assessment of the connectivity among populations of neurons. The advancements in computational neuroscience, combined with the emergence of whole-brain imaging techniques (such as magnetic resonance imaging; MRI), has led to a perspective centered on the network connectivity that is generally dissociated from the original detailed anatomical studies. Thus, computational neuroscience has advanced on the exploration of the function of neuronal networks relying on (low resolution) whole-brain imaging experimental data or single-cell statistical estimates of connectivity. This implied the development of a robust mathematical framework, mainly contributed by graph theory, to assess the architecture of neuronal circuits in terms of network connectivity. Such a framework has unraveled organizational principles of brain connectivity and provided insight on the implications of altered connectivity in brain pathologies (Bullmore & Sporns, 2009). However, the low resolution of whole-brain imaging techniques hinders a wealth of anatomical detail, and the implications that microscopic architectural traits have on brain connectivity are not well understood (Schröter, Paulsen, & Bullmore, 2017). At the single-cell level, biophysical models of single neurons have been refined to understand the interplay between architecture and dynamical activity (London & Häusser, 2005), but a robust mathematical framework to assess the implications of neuromorphology on the suitability for neuronal computation, or on the connectivity of brain circuits is missing. Relatively recent studies on dendritic wiring optimality (Cuntz, Mathy, & Häusser, 2012; Wen, Stepanyants, Elston, Grosberg, & Chklovskii, 2009) can allow us to generalize from architectural features towards impaired function. Still, such a generalization requires bridging the single-cell and network levels of description.

As mentioned in the **General Introduction**, in this Thesis I focus on the contribution of dendritic tree architecture on the wiring of neuronal circuits. Dendritic geometry has been

shown to be an important factor modulating the pattern of neuronal firings (action potentials) (Mainen, Sejnowski, & Others, 1996). In addition, the size of dendritic arbors modulates the shape of the action potential onset, which determines the capability of the axonal spikes to encode rapid changes in synaptic inputs (Ilin, Malyshev, Wolf, & Volgushev, 2013), being accelerated in neurons with larger dendritic surface area (Eyal, Mansvelder, de Kock, & Segev, 2014). Interestingly, dendritic morphology is dynamic and can undergo significant changes in many pathological conditions. Using computational models of neocortical pyramidal cells (van Elburg & van Ooyen, 2010), it has been shown that not only the total length of the apical dendrite but also the topological structure of its branching pattern markedly influences inter- and intra-burst spike intervals and even determines whether or not a cell exhibits burst firing. In fact, there is only a range of dendritic sizes that supports burst firing, and that this range is modulated by dendritic topology. Either reducing or enlarging the dendritic tree, or merely modifying its topological structure without changing total dendritic length, can transform a cell's firing pattern from bursting to tonic firing. Thus, it should be expected that variations on the morphological properties of neuronal trees (i.e. tree size, branch and synaptic contact densities or the morphology of dendritic branches) can have an impact both on the integration of signals in single neurons, and the wiring and signal processing at a population level.

While the importance of morphological properties for the wiring and computation of neuronal networks is clear, a general understanding of the laws governing how healthy brains are wired (and which of those are broken in brain pathologies) is missing. To obtain such a general understanding, one possible approach is to link the local properties of neuronal arborisations to network computation. This could be attained by embodying morphological reconstructions in computational simulations. However, most computational models have commonly disregarded fine morphological features involved in network connectivity given that often a general understanding of the wiring or the dynamics of the studied circuits is pursued.

As an example that is close to the modeling I used in this work, Orlandi et al. (Orlandi, Soriano, Alvarez-Lacalle, Teller, & Casademunt, 2013) simulated the connectivity and dynamics of 2D networks formed by neuronal cultures on plates and found that the emergence of bursts of activity in those networks can be explained by the summation of

noisy spontaneous synaptic currents that given the structure of the networks focus on specific sites and initiate waves of activity. However, even though the structural connectivity was explicitly modelled, the impact of neuron architectural features on the studied phenomena was not addressed. This exemplifies how simple models are generally used to explain fundamental phenomena observed in neuronal networks but still miss the connection between fine morphological properties and the wiring and function of neuronal networks. Another work using similar modeling by Voges et al. (Voges, Schüz, Aertsen, & Rotter, 2010) addressed how the existence of patchy connections could be accounted for in network models of horizontal connectivity in cortical layer II/III. In this case, while approaches to account for morphological properties in the models are proposed, their effect on the network connectivity is not assessed. Few studies have advanced on bridging the microscopic (single-neuron) and the network levels of description. A step in this direction has been done recently by Vegué et al. (Vegué, Perin, & Roxin, 2017), who have studied how small-sized samples accounting for connectivity statistics of neurons are representative of the topology of whole neuronal networks. However, again, a systematic analysis of how neuronal architecture constrains the network topology is not addressed. These studies exemplify that existing computational models of simplified neuronal networks pursue a general understanding of the dynamics of neuronal networks, and only some have focused on either the implications of detailed neuromorphological properties for network wiring.

Very few studies have simulated connectivity based on neuronal reconstructions with micrometric detail in specific layers or regions (Reimann et al., 2017), or whole organisms (Szigeti et al., 2014). A relevant example is the Blue Brain Project, which simulated cell to cell connectivity in a portion of rat cortex taking into account a wealth of multi-scale biological features (Markram, 2006). The results obtained in that project are now starting to be used to study the topological properties of neuronal networks (Reimann et al., 2017). However, while those last examples have increased the level of detail used to parameterize the simulations, an exploration of the relevance of microscopic neuromorphological architecture for the network connectivity is still missing.

Our model system: basal dendritic trees of neocortical pyramidal cells

Even though studying the wiring of whole-brain realistic circuits (micro-connectomes) involved in specific functions will ultimately provide novel insights into network connectivity fundamental laws, it is reasonable to first assess the relationship between diverse neuromorphological features and network connectivity in a manageable simplified framework. Here I specifically selected the pyramidal cells of layers II and III of the motor cortex and the local horizontal circuitry they form, so that the framework of the study is simplified to a 2D plane homogeneously populated by neurons spanning dendritic trees around them and sending quasi straight axons that form a local network. By taking into account some of their architectural properties, I aim to assess their impact on the connectivity of the network and its capacities for processing and storing information.

The cerebral cortex: stereotypical architecture for cognitive processing

The cerebral cortex is the brain zone (2-3 mm thick) that consists of an outer region of neural tissue (grey matter) and covers the two hemispheres. The primary cortices are defined as the cortical regions that present somewhat simpler functions. These include areas that directly receive the sensory input (vision, hearing, and somatic sensation) or that are involved in the display of limb or eye movements. The association cortices perform more complex functions (**Figure 2**).

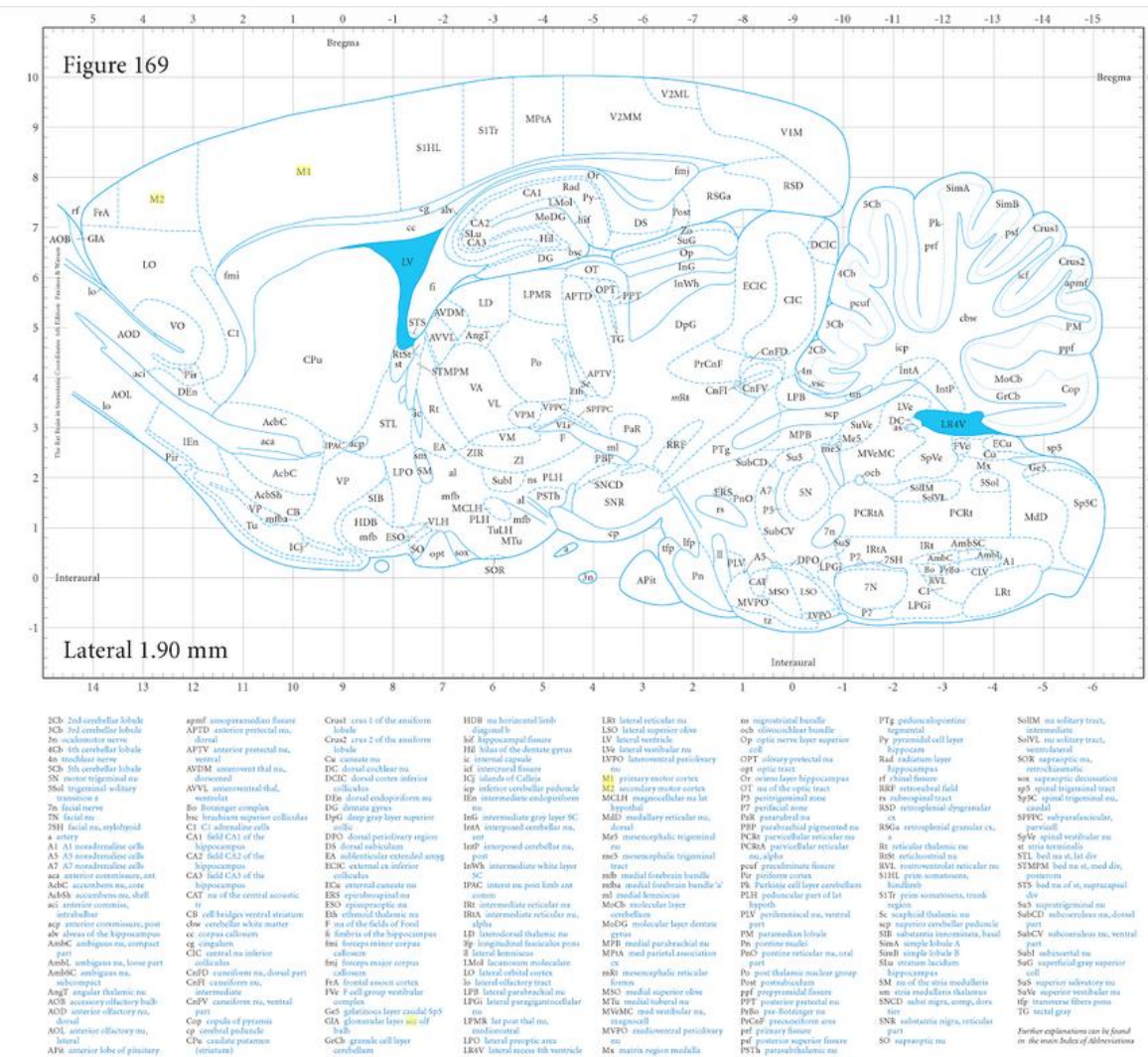


Figure 2. Sagittal view of the rat brain indicating the different brain areas. Motor cortices (M1 and M2) are highlighted in yellow. From The Rat Brain in Stereotaxic Coordinates (Paxinos, Watson, Pennisi, & Topple, 1985).

The great majority of the cerebral cortex is represented by the neocortex. It is morphologically divided in six layers and holds from 10 to 14 billion neurons of the human brain (Herculano-Houzel, 2009). These six layers are numbered with Roman numbers from the surface to the inner part. The molecular layer (layer I) contains very few neurons; layer II is the external granular; layer III the external pyramidal; layer IV the internal granular; layer V the internal pyramidal; and layer VI the multiform, or fusiform layer. Each cortical layer involves different neuronal shapes, sizes and densities as well as different distributions of nerve fibres.

Functionally, the layers of the cerebral cortex can be divided into three parts:

1. **The supragranular layers:** They involve layers I to III. They both send and receive intracortical connections, which can be either associational (i.e., with other areas of the same hemisphere), or commissural (i.e., connections to the opposite hemisphere, through the corpus callosum). The supragranular region of the cortex is highly developed in humans and allows communication between one portion of the cortex and the other regions.
2. **The internal granular layer:** Contains layer IV, receives thalamocortical connections from specific thalamic nuclei and innervates the other cortical layers. Thus, its role is the reception of sensory information, being the most prominent layer in the primary sensory cortices with greater thickness and neuronal density.
3. **The infragranular layers:** Formed by layers V and VI, they primarily connect the cerebral cortex with subcortical regions. These layers are mainly developed in motor cortical regions. The motor areas present significantly small or non-existent granular layers and are often called "agranular cortex". Layer V provides all of the principal cortical efferent projections to basal ganglia, brainstem and spinal cord. Layer VI, the multiform or fusiform layer, projects primarily to the thalamus.

Here, I focused on the supplementary motor area (MII, superiomedial part of area 6), is a part of the premotor cortex that extends onto the medial side of hemisphere. This area shows projections to the primary motor cortex, basal ganglia, thalamus, brainstem and also to the contralateral supplementary motor area. This area is active before movement and is thought to be involved in initiation of motion. It consists of local circuit neurons, with short axons that exert their effects in the local region of their cell bodies and dendrites. They are located in brain areas innervated by long-axedon principal neurons and perform integrative and modulating functions in local brain regions (Paxinos & Franklin, 2004).

The pyramidal neuron as the fundamental processing unit

There are several identifiable cell types in the cerebral cortex. Pyramidal neurons are the most abundant cell type in the cerebral cortex of mammals, birds, fish and reptiles, indicating an adaptive value for the organism, and are found in most mammalian forebrain structures

associated with cognitive functions, including the cerebral cortex, the hippocampus and the amygdala. The lone axon of each pyramidal neuron typically emanates from the base of the soma and branches profusely, making many excitatory glutamatergic synaptic contacts along its length. Of interest to my work, current research demonstrates that in the case of cortical neurons, about 98% of the synapses are axodendritic and only 2% synapse with the soma (Barrett et al., 2010).

The dendritic tree of a pyramidal neuron has two distinct domains: the basal and the apical dendrites, which descend from the base and the apex of the soma, respectively. Usually, one large apical dendrite connects the soma to a tuft of dendrites. This main apical dendrite bifurcates before giving rise to the tuft at a variable distance from the soma. In some cases the resulting ‘twin’ apical dendrites each bifurcate again. Oblique apical dendrites emanate from the main apical dendrite at various angles. All pyramidal neurons have several relatively short basal dendrites. Pyramidal neurons are covered with thousands of dendritic spines that constitute the postsynaptic site for most excitatory glutamatergic synapses. The number of spines represents thus a minimum estimate of connectivity of a neuron.

Basal dendritic trees of neocortical pyramidal cells in DS mouse models

Using intracellular injections with Lucifer Yellow to visualize the whole basal dendritic tree, Dierssen et al. found that pyramidal cells are smaller, less branched and 24% less spinous in Ts65Dn mice than those in controls (M Dierssen et al., 2003). These effects on pyramidal cell structure parallel those found in humans, and the structural changes in Ts65Dn mice are mimicked by Dyrk1A^{+/−} and TgDyrk1A mice, to a similar and a lower extent respectively. The three mouse models show motor impairments (Fotaki, Martínez De Lagrán, Estivill, Arbones, & Dierssen, 2004; Kida, Rabe, Walus, Albertini, & Golabek, 2013; Martínez de Lagrán et al., 2004), and TgDyrk1A mice also show lower performance in the puzzle box task (Ruiz-Mejías et al., 2016), which involves the ability to obtain and remember a motor repertoire.

From a modeler perspective, the neuromorphological alterations, together with the behavioral phenotype of those mouse models, provide an excellent opportunity to parameterize empirically the modeled neuronal networks, assess the relevance of the network morphospace dimensions proposed to be accountable for cognitive function (processing

efficiency and storage capacity in this case), and provide predictions of the cognitive performance of those mouse models in untested tasks (e.g. puzzle box in Ts65Dn and Dyrk1A^{+/−}), or upon pro-cognitive treatments.

Environmental enrichment as a model of dendritic rewiring

The morphological and physiological characteristics of the central nervous system are the result of a combination of genetic and environmental factors (Bartoletti, Medini, Berardi, & Maffei, 2004). Several studies report anatomical and physiological consequences of exposure to a sensory enriched environment (EE) (Diamond, Krech, & Rosenzweig, 1964; Volkmar & Greenough, 1972). Many studies report the effects of EE on synaptic transmission in the hippocampus (Artola et al., 2006; Duffy, Craddock, Abel, & Nguyen, 2001; Foster & Dumas, 2001; Irvine & Abraham, 2005) as well as in the prefrontal cortex (Kolb & Gibb, 1991) and in the parietal cortex (Leggio et al., 2005).

EE has been reported to increase synaptic plasticity that has been proposed as the cellular substrate of information processing and memory formation, consolidation, retrieval and extinction. These processes are probably dependent on structural modification of synaptic connectivity, with long-term potentiation (LTP) and long-term depression (LTD) initiating structural modifications in dendritic spines. This is especially interesting in DS, since abnormalities in synaptic plasticity (that is, LTP) are seen in DS mice (see Mara Dierssen, Herault, & Estivill, 2009 for review). A key finding in DS mouse models has been the imbalance of the excitation–inhibition at the network level (Belichenko et al., 2009; Kurt, Davies, Kidd, Dierssen, & Flórez, 2000; Kurt, Kafa, Dierssen, & Davies, 2004), over inhibition being observed that may explain the LTP and LTD disturbances (R J Siarey, Stoll, Rapoport, & Galdzicki, 1997; Richard J Siarey et al., 1999). In adult trisomic mice, treatment with a GABA_A receptor antagonist normalized NMDA-type glutamate receptor-mediated currents and induction of LTP was restored (Nambu, Lewis, Wharton, & Crews, 1991). Regarding *in vivo* studies, experience-dependent neural plasticity is of time-critical nature (Escorihuela, Fernandezteruel, et al., 1995). The main problem in DS is the lack of stability of the effects, probably due to alterations in the translation of transient synaptic changes into stable structural modifications. Understanding the effect of EE at the network level could not only explain the behavioural improvement seen in those mouse models, but also point at alternative pro-cognitive treatments that could increase wiring optimality more effectively.

Linking single-neuron neuromorphological properties with network architecture and computational capacities

In this Chapter I explore the link between neuromorphology and network connectivity by analysing the architecture of single dendritic trees and instantiating 2D local neuronal networks. To assess how optimal the wiring of single neurons is, I used both the existing scaling laws proposed to account for such an optimality already mentioned in the **General Introduction**, and a novel adaptation of the concept of multi-objective optimality.

Cajal's law for conservation of cytoplasm and conduction time suggests that there is a trade-off between material cost and signal integration efficiency in single neurons. This concept is the foundation of the wiring optimality definitions obtained by Cuntz and Chklovskii (Cuntz et al., 2012; Wen et al., 2009). However, in both cases, the derived mathematical expressions relating neuromorphological metrics when assuming optimality implicitly account for various functional aspects, mainly signal integration efficiency and connectivity repertoire (through the balancing factor in the scaling law defined by Cuntz et al.). This is, to define neuromorphological laws implying optimal wiring, a mixture of integration efficiency and connectivity maximization rationales are used. This implies that when using the derived scaling laws to assess wiring optimality of dendritic trees, the explicit variables accounting for connectivity maximization become implicit (the balancing factor defined by Cuntz and the dendritic repulsion defined by Chklovskii), hindering the relative contribution of each functional aspect to putative suboptimal dendritic architecture. Moreover, the fact that optimality is measured by fitting scaling laws, implies that the statistical significance of studies with small numbers of neurons is difficult to assess.

To overcome these limitations I here propose to assess wiring optimality through morphospace explorations and the quantification of well-differentiated functional aspects, namely routing efficiency and storage capacity, so that dendritic tree wiring optimality is given by the maximization of those while preserving material cost. The concept of maximizing more than one property simultaneously (multi-objective optimality) is not novel and was first tackled by Vilfredo Pareto in the scope of economic sciences (Pareto, 1963). Following his definition, a Pareto-optimal configuration of a system implies that no change can be made to improve any aspect (i.e. increasing routing efficiency or storage capacity, or reducing the

material cost) without deteriorating another one. Those configurations define the Pareto front, a boundary in the morphospace that implies multi-objective optimality. Thus, a Pareto-suboptimal system can undergo a Pareto improvement by improving an aspect without deteriorating any other (e.g. by a rearrangement of its branches, a dendritic tree could have higher routing efficiency without increasing its cost). Only one study, to my knowledge, has applied this concept to human tractography data, and explored how genetic algorithms can modulate the capacities of whole-brain networks and displace them towards Pareto-optimal configurations (Avena-Koenigsberger et al., 2014). Here I aimed to use it in order to test whether the architecture of single neurons, or the networks they form, are Pareto-optimal and, if they deviate in brain pathology, to dissect how differential neuromorphological properties contribute to such deviations.

To bridge the single-neuron and network scales of description, I have applied the graph theory conceptual framework (generally used in the neuroimaging field) to micro-connectome topology. Mixed theoretical and experimental studies have found fundamental properties in macroscopic neuronal networks such as their clustered, hierarchical organization (Bullmore & Sporns, 2009; Sporns, Chialvo, Kaiser, & Hilgetag, 2004) that have been observed across organisms and along evolution. Assessing the existence of those properties while accounting for cell-to-cell connectivity has still not been done to my knowledge, and can be a powerful environment to investigate to what extent single-cell architectural properties can have an impact on the connectivity of specific neuronal circuits. Thus, I propose to study neuronal networks as graphs formed by the neurons (nodes) and the connections among them (directed edge) (Artzy-Randrup, Fleishman, Ben-Tal, & Stone, 2004). I think that the comparative analysis of intellectual disability neuronal networks in this conceptual framework can shed light on the relative contribution of the multi-scale architectural alterations to cognitive function.

As mentioned above, the selection of the metrics used to quantify and analyze structural traits in a single neuron or a network defines a morphospace, which allows to assess structural properties relevant for their performance, and to define fitness as a function of the quantified metrics (Avena-Koenigsberger, Goñi, Solé, & Sporns, 2015). A series of studies have explored topological properties of neuronal networks mainly relevant for their information processing capabilities. Routing efficiency defined as the average shortest path length in the

network emerges as a structural trait accounting for the information processing (Avena-Koenigsberger et al., 2014). Experimental data from whole-brain connectomes has shown that routing efficiency is maximized while maintaining the cost of wiring the network, thanks to the aforementioned clustering and hierarchical organization (Bullmore & Sporns, 2009). While a neuronal network's routing efficiency is a well-established metric that seems to be optimized, the conceptual framework of the network morphospace can be extended to account for other structural traits relevant for cognitive performance. Besides processing information, another important function performed in the brain is storing memories in the form of firing patterns susceptible to be recovered upon experience. The storage capacity of single neurons has been approximated at the single-cell level by Poirazi & Mel (Poirazi & Mel, 2001), providing a quantitative upper bound to the combinatorial amount of firing patterns that a neuron could differentiate based on the amount of synaptic connections received and the number of afferent neurons providing them. This definition of storage capacity was shown to correlate with the amount of firing patterns that a simple network can store and retrieve below a given error (Poirazi & Mel, 2001). To quantify the storage capacity of neuronal networks, I chose to obtain its average based on the connection topology of instantiated circuits.

Once the dimensions of the morphospace have been defined, empirical networks can be quantified and the morphospace can be computationally explored either by rewiring networks or using generative models of network growth (Avena-Koenigsberger et al., 2015). Existing studies have generally used whole-brain MRI experimental data (Goñi et al., 2014) or generative modeling based on the idea of introducing nodes and connections based on the existing network and pursuing specific topologies (Albert & Barabási, 2002; Hilgetag & Kaiser, 2004). Only a few works, such as the microconnectomic mapping of the *C. elegans* brain and the Blue Brain project, have studied the topological properties of networks based on biologically realistic generative modeling (Markram, 2006; J. G. White, Southgate, Thomson, & Brenner, 1986). In this Thesis, I develop a computational framework able to do so while introducing single neuron architectural properties as parameters. Thus, I obtain the network morphospace dimensions by measuring topological metrics of network graphs instantiated while taking into account the neuromorphology. By doing so, an approximation of the effects on processing efficiency and storage capacity produced by neuromorphological architecture can be obtained.

In my work, as mentioned above, I chose to study local horizontal connections of cortical layer II/III. The reasons for this choice are: (1) The abundance of horizontal recurrent connectivity in this layer (Voges et al., 2010), which justifies the simplification of the layer to a 2D homogeneous neuronal mosaic, (2) the stereotypical connectivity patterns found in the neocortex, which are conserved among cortical areas devoted to very diverse processing roles¹, and (3) the fact that DS-related intellectual disability mouse models show dendritic alterations in cortical layers II/III in the M2 cortex implies that our computational modeling results can be contextualized by experimental data providing a link between our computational study and the biological reality.

¹ Understanding the role of subtle neuromorphological properties on the network connectivity and its computational capacities in a subsampled cortical area can be reasonably extrapolable to other areas in the neocortex

1.2. Methods

In this first part of the Thesis I took a mixed experimental and computational modeling approach for analyzing the repercussion of single-cell neuromorphological properties on the neuronal network. Computational models allow the exploration of theoretical relationships between morphology and connectivity; however, the physiological relevance of the findings is not always clear. In this regard, mouse models showing different alterations of the dendritic morphospace along with cognitive impairment provide a convenient scenario for testing those findings.

First I extracted functional properties (dendritic wiring optimality) from specific neuromorphological metrics that I obtained from neuronal reconstructions of two mouse models (Ts65Dn and a Dyrk1A heterozygous) showing DS-like neuronal structure abnormalities and cognitive deficits. In order to explore the impact of dendritic architectural properties on the horizontal connectivity of cortical layer II/III, I implemented a computational model to explore and instantiate 2D homogeneous neuronal networks based on an existing model (Orlandi et al., 2013). I used this model to explore how the modification of dendritic tree size, its complexity and the density of synaptic contacts modulates the network topology and computational capacities. Finally, using published experimental data from our lab, I instantiated networks recapitulating the neuromorphological alterations found in DS mouse models.

1.2.1. Optimal dendritic wiring of cortical pyramidal neurons of Ts65Dn and Dyrk1A+/-

To identify how neuromorphological changes may affect dendritic wiring optimality, I used published neuronal reconstructions of single pyramidal neurons manually selected and injected with Lucifer Yellow (LY) (Elston & Rosa, 1997; Elston, Benavides-Piccione, & DeFelipe, 2001). Briefly, pyramidal neurons of layers II/III of motor cortices (M2) in 150 μm vibratome sections tangential to the cortical surface that contain whole basal dendritic trees are filled with LY by continuous current injection. A camera lucida microscope

attachment was used to draw the basal dendritic arbor, and those drawings are the actual information I used.

I used reconstructions of mouse models that show relevant genotype-specific dendritic arbor abnormalities along with cognitive deficits:

- (1) The first dataset (M Dierssen et al., 2003) were neuronal reconstructions of Ts(1716)65Dn (Ts65Dn) a DS mouse model and wild-type (wild-type) mice. The chromosomal rearrangement in B6EiC3Sn a/A-Ts (1716)65Dn (Ts65Dn) female was originally generated by radiation inducing a spontaneous reciprocal translocation of the telomere proximal region of Mmu16 to the centromere and pericentromeric region of Mmu17 (1716) and mice derive crossings of a B6EiC3Sn a/A-Ts (1716)65Dn (Ts65Dn) female to B6C3F1/J males (The Jackson Laboratory). Euploid littermates were used as controls.
- (2) For the second dataset (R Benavides-Piccione et al., 2005) neuronal reconstructions were obtained from heterozygous *Dyrk1A* mice (C57BL/6J-129Ola mixed genetic background, Harlan Ibérica, S.L.), a candidate gene for DS. Wild-type littermates were used as controls.

Of note, the controls of these two strains have different genetic backgrounds, and thus the study was separated in four different experimental groups, so that I could also compare non-pathological variations in dendritic structure.

Neuromorphological analysis

From the 82 neuronal reconstructions published in (M Dierssen et al., 2003) (Ts65Dn) and (Benavides-Piccione et al., 2005) (*Dyrk1A*+/-), I selected six pyramidal neurons from two mice per genotype. In the published work, metrics obtained included dendritic length and dendritic complexity obtained by the Sholl analysis. Even though the original datasets also include spine density measurements, I have focused here on the dendritic branching phenotype. These measures were obtained manually for the Ts65Dn experiment and using the Neurolucida package for the heterozygous mice. However, Neurolucida morphology files (*.asc; <http://www.mbfbioscience.com/neurolucida>) were not available. I re-analyzed the original data to obtain measurements that were comparable across models and that are needed for estimating dendritic wiring optimality.

I used the Simple Neurite Tracer plugin (Longair, Baker, & Armstrong, 2011) (available via http://fiji.sc/Simple_Neurite_Tracer as part of the package Fiji) to obtain *.swc format morphology files from the original camera lucida dendritic tree drawings. The software semi-automates the reconstruction procedure by finding the highest intensity path between manually selected points in an image. The obtained paths can be saved in standard neuronal reconstruction formats and subsequently analyzed. **Figure 4** shows a schematic overview of this procedure.

Simple Neurite Tracer morphological files for Ts65Dn, Dyrk1A+/- and their wild-type littermates were then exported to Trees Toolbox in *.swc format to obtain morphological metric statistics using the *stats_tree* function (Cuntz, Forstner, Borst, & Häusser, 2010). Briefly, the function provides a set of measurements that describe in detail morphological properties of the dendritic tree: total length, maximum and mean path length, mean branch length, dendritic spanning area, number of branch points, maximum and mean branching order, dendritic area (surface occupied by dendrite), mean straightness of dendritic branches, mean branching angle, mean asymmetry, center of mass in different directions and the ratio between width and height (see **Figure 3** and **Table 2**).

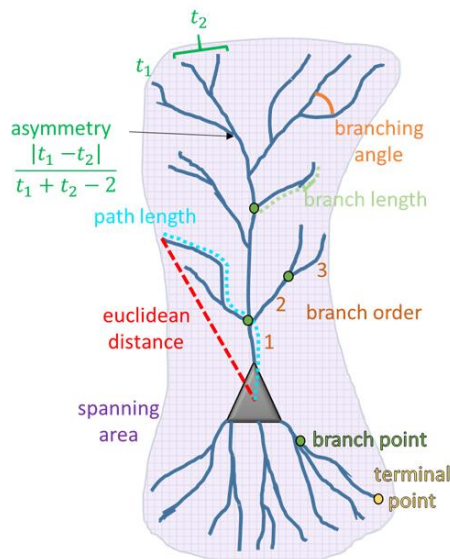


Figure 3: Schematic representation of a pyramidal neuron and analysed neuromorphological metrics.
The represented morphological metrics include: asymmetry (green), path length (light blue), euclidean distance (red), spanning area (purple), branching angle (orange), branch length (light green) and branch order (brown). Branch points are represented in green and terminal points in yellow.

Table 2: Neuromorphological metrics. Summary of the studied neuromorphological metrics used in this Thesis, with their units and a short description.

Name	Unit	Description
Total length	μm	Total length of dendrite, including all the branches of the dendritic tree
Path length	μm	Length from a terminal point to the root of the tree
Branch length	μm	Length of a single branch, including dendritic segments between branch points
Spanning area	μm^2	Area covered by the tree
Number of branch points	-	Number of branches in a tree
Branch order	-	Property of every branch. Starts from value 0 at the root of the tree and increases by 1 after every branch point
Dendritic area (density)	μm^2	Area occupied by dendritic segments
Straightness	-	Ratio between the path length and the euclidean distance between a terminal or branch point and the root of the tree
Branching angle	rad	Angle between two daughter branches at any branch point
Asymmetry	-	At any branch point, the ratio between the number of terminal points of the less complex and the more complex daughter branch
Center of mass	μm	Center of mass of the tree in a single dimension
Width vs Height ratio	-	Ratio between the width of a tree (size in x) and its height (size in y)

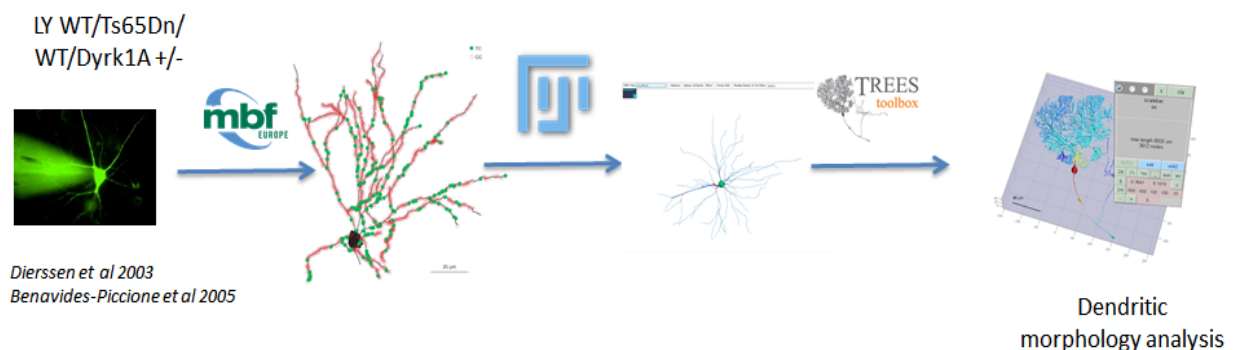


Figure 4: Schematic representation of the workflow for single neuron reconstruction and morphometric analysis. LY injections were performed and camera lucida drawings obtained as part of previous studies in our lab. 2D reconstructions were obtained using Simple Neurite Tracer in Fiji. A statistical analysis of the morphological metrics summarized in Table 1 was done using the Trees Toolbox.

Sholl analyses were done in the mutant models by quantifying the number of branches intersecting circles at equispaced radii from the soma with a radius step = 25 μm (dendritic branches smaller than 25 μm might not be counted) in the camera lucida drawings (M Dierssen et al., 2003). High magnification imaging (x100 Zeiss immersion lens) was used to quantify spine densities by counting the number of spines per 10 μm increments of 20 randomly selected dendritic segments (M Dierssen et al., 2003).

To visualize schematically the complexity of reconstructed dendritic trees, dendograms of the trees were obtained by using the *dendrogram_tree* function of Trees Toolbox. A dendrogram is a schematic tree diagram representing the branches and their relative order of appearance in 2D, branching points appear in increasing y coordinates. Branches of the same order are arranged in parallel along the x axis. The y-value at which a branch starts or terminates in the plots is given by the metric path length of the branches.

Principal Component Analysis

To identify the metrics that better separate the Ts65Dn, Dyrk1A +/- and their respective controls, I performed a Scaled Principal Component Analysis (Wold, Esbensen, & Geladi, 1987) (PCA) of dendritic tree architectural metrics using the PCA function of R. Plots were constructed in R (version 3.4.1) using ggplot2 (version 2.2.1) to reduce the number of variables into a smaller number of principal components (artificial variables) that account for most of the variance.

The purpose of this analysis was to identify which morphological variables explain most of the variance in the analyzed neurons, and to what extent combinations of those variables explain the differences between genotypes. All metrics were statistically tested for their variance among groups using ANOVA (ggpubr implementation, version 0.1.5). Pairwise comparisons were performed using two-way unpaired t-tests. Shapiro-Wilk tests were used to check whether the distributions are normal.

Optimal dendritic wiring

Cuntz found that dendritic trees optimally wired to connect to sets of points (synapses) in space following a power law between the total tree length and the amount of branch points (Cuntz et al., 2012). The power law was derived mathematically based on Cajal's law for conservation of cytoplasm and conduction time (Ramón y Cajal, 1995). Here I explored whether trisomic and heterozygous neurons were optimally wired, and also if the differences in morphological metrics between the controls of the trisomic and heterozygous strains detected in the PCA, affected wiring optimality. This is important since there is a strain-dependent motor behaviour difference.

Wiring optimality was assessed by fitting a power law to the relation between total tree length and amount of branch points (described in detail in Cuntz et al., 2012). The code used for the analysis, including reconstruction datasets, the morphological metric statistical analysis and the power law fit to the reconstructed trees can be found at https://bitbucket.org/linusmg/2d_model_bitbucket.

Single neuron morphospace exploration and Pareto optimality

To extend on the existing work assessing dendritic wiring optimality, I defined a morphospace with three variables putatively accounting for computational capacities: the cost of wiring the tree, the efficiency in routing information towards the soma and the capacity of the tree for identifying different input patterns (storage capacity). Subsequently I computationally generated synthetic dendritic trees to explore how neuron architecture (e.g. dendritic tree size, complexity and density of synaptic spines) affects their computational capacities.

I defined the variables of the morphospace (cost, routing efficiency and storage capacity) in function of single-neuron architectural properties as follows.

Routing efficiency

While this quantity is well-defined at the network level (see **Section 1.2.2.**) and even though the wiring optimality definition explored by Cuntz implicitly accounts for it, a consistent definition at the single-neuron level is missing. I propose a simplistic definition contributed

by the average straightness of the dendritic tree branches, the coefficient of variation of dendritic branch lengths and the amount of synaptic contacts normalized by the span of the tree:

$$e_{rout} = \frac{s}{A} \cdot \frac{\bar{d}_b}{l_b} \cdot \frac{1}{c.v.(l_b)} \quad (1)$$

Where s is the number of synaptic spines, A the dendritic tree span (area), d_b the Euclidean distance between the two extremes of a branch b , l_b the path length of a branch b and $c.v.$ stands for coefficient of variation.

Accounting for the spine density and dendritic straightness is justified by electrophysiological experiments showing higher synaptic current transmission when spine density is increased and longer time delays (Chklovskii, Schikorski, & Stevens, 2002; Wen & Chklovskii, 2005) and greater attenuation of synaptic signals (Zador, Agmon-Snir, & Segev, 1995) with longer path length.

Storage capacity

I estimated the storage capacity of a single neuron as the total number of non-redundant possible states for a given neuron receiving s synapses provided by d presynaptic neurons as previously defined by Poirazi and Mel (Poirazi & Mel, 2001). Briefly, assuming that the dendritic location of inputs (synapses) does not affect the integration of the signal in a given neuron (linear model), the combinatorial “n choose k” quantification of possible states for a post-synaptic neuron expressed in bits (basic unit of information) is given by:

$$b_L = 2 \log_2 \binom{s+d-1}{s} \quad (2)$$

Where s is the number of received synaptic connections and d is the number of unique afferents providing them. The number of afferents was estimated based on the modeling of section 1.3.2. (see **Annex II**).

Cost

To account for the material cost of wiring a dendritic tree I simply used its total length:

$$c = \sum l_b \quad (3)$$

Where l_b is the path length of a branch b .

The exploration of the defined morphospace was done through the generation of synthetic trees using the Trees toolbox (Cuntz, Forstner, Borst, & Häusser, 2011). Based on the wild-type group of the Ts65Dn experiment, clones of those trees were obtained using the *clone_tree* function, which connects points distributed randomly in the spanning fields of the original tree group using a minimum spanning tree (MST) algorithm. Variations in the straightness of dendritic branches can be introduced by adjusting the value of the balancing factor, which accounts for the trade-off between material cost and conduction time (Cuntz et al., 2010). Variations in branch density were introduced by scaling the amount of points used to generate cloned trees in the *clone_tree* function (the modified source code can be found at https://bitbucket.org/linusmg/2d_model_bitbucket/ in the folder single_tree_analysis/branch_density). Variations in tree size were assessed by scaling the dendritic tree radius of the control group using the *scale_tree* function. Additionally, a MATLAB script to distribute spines along the dendrites of the reconstructions following experimental distributions of spine densities was used to quantify the total number of spines in each tree. This also allowed to obtain quantifications for the spine reach area (all the surface reachable by the spines in a given tree) and to measure the ratio between dendritic span area and spine reach area. 10 synthetic trees were generated with each parameter set and the morphospace metrics accounting for computational capacities were obtained. Additionally, optimal wiring power law fits were obtained for all the groups of trees by using the total length, radius and number of branch points of each reconstruction and using the *nls* function in R (v 3.4.1).

Pareto optimality

In this work, I define an efficiency space given by the routing efficiency, storage capacity and cost metrics defined above, and assess optimality by identifying Pareto fronts in 2D

projections of the efficiency space and by measuring the distance of specific groups of neurons to the Pareto front for each functional maximization at a minimum cost.

1.2.2. A 2D minimal model to determine the impact of dendritic wiring features on network properties

The next question was if single cell neuromorphological properties (namely dendritic tree size, its variability, dendritic complexity and synaptic density) had an effect on network connectivity. To this aim I used a 2D minimal computational model, that allowed us an *in silico* exploration of the most important neuromorphological variables and an instantiation of the DS networks.

The model mimics the growth process of a homogeneous network (Orlandi et al., 2013) providing a synthetic instantiation of a 2-dimensional homogeneous neuronal population. The assumption of a bi-dimensional homogeneous local cortical network (Orlandi et al., 2013) is justified given that our experimental data derive from “mosaic-like” basal dendritic trees. This computational model allows to explore the changes in the morphospace driven by the dendritic properties (in this case of different mouse models), and determine the topological properties of the instantiated “mutant” networks, relating them to computational capacities of neuronal networks.

I used the numerical values derived from the neuromorphological analysis performed in datasets of the previously described models (Ts65Dn and Dyrk1A +/-) and a transgenic mouse model over-expressing *DYRK1A* (TgDyrk1A) (Altafaj et al., 2001). In this model the full-length rat *DYRK1A* sequence is under the control of an inducible sheep metallothionein-Ia promoter in a C57BL6/SJL background. Littermates not expressing the transgene were used as controls. This third dataset was obtained from (Martínez de Lagrán et al., 2012).

Finally, to test dendritic rewiring effects I used environmental enrichment. Briefly, after weaning (21 days of age), TgDyrk1A and wild-type mice were randomly reared under non-enriched (NE) or enriched (EE) conditions. The NE mice were reared in conventional Plexiglas cages (20 x 12 x 12 cm height) in groups of two to three animals. EE mice were reared in spacious (55 x 80 x 50 cm height) Plexiglas cages with toys, small houses, tunnels, and platforms. The arrangement was changed every 3 days to maintain the novelty of the

environment. To stimulate social interactions, six to eight mice were housed in each EE cage. Both groups were maintained under the same 12 h (8:00 to 20:00) light-dark cycle in controlled environmental conditions of humidity (60%) and temperature ($22 \pm 1^\circ\text{C}$), with free access to food and water. In both experiments, only females were used given that transgenic male mice showed hierarchical behavior, as similarly seen in Ts65Dn mice (Martínez-Cué et al., 2005).

Computational model

A family of models with similar assumptions to ours have been used to explore spontaneous activity generation in primary neuronal cultures (Orlandi et al., 2013), horizontal connectivity in the mammalian cortex (Voges et al., 2010) and basic features of cortical networks (Feldt, Bonifazi, & Cossart, 2011). Here I implemented and refined a computational generative model developed by (Orlandi et al., 2013) (originally devised for neuronal cultures) in order to simulate the local horizontal connectivity of cortical layers II/III in which I then introduce detailed dendritic tree neuromorphological properties (dendritic tree size, its variability, dendritic complexity and spine density). **Figure 5** schematically shows the circuit building process.

All the software development and computational analysis was performed in an HP-Z620 Workstation (equipped with an Intel Xeon E5-2620, 64GB RAM, Nvidia Quadro K4000 and 1TB SSD drive) running Ubuntu 16.04. In order to introduce the dependence on neuromorphological metrics and to have an efficient instantiation, I implemented the model in C++. Random number generators and optimization of the compiled code required the libraries GSL (Gough, 2009) and BOOST (Sieck, Lee, & Lumsdaine, 2001). The source code can be found at https://bitbucket.org/linusmg/2d_model_bitbucket.

Our implementation homogeneously locates somata (defined as circles with diameter d_s) in a synthetic 2D space. Subsequently, from each soma emerges a quasi-straight path (axon) given by a biased random walk (10 μm segments are subsequently located forming an angle with previous segments given by a uniform distribution). The average length of the axons is and each single axon length is obtained from a Rayleigh distribution with mean and scale parameter σ_a . Dendritic trees for each soma are generated as circles with radii given by a

Gaussian distribution with mean \bar{r}_d and sigma σ_d (See *Parametrization of the 2D minimal model* and **Table 3** for an overview of the parameters from the literature used).

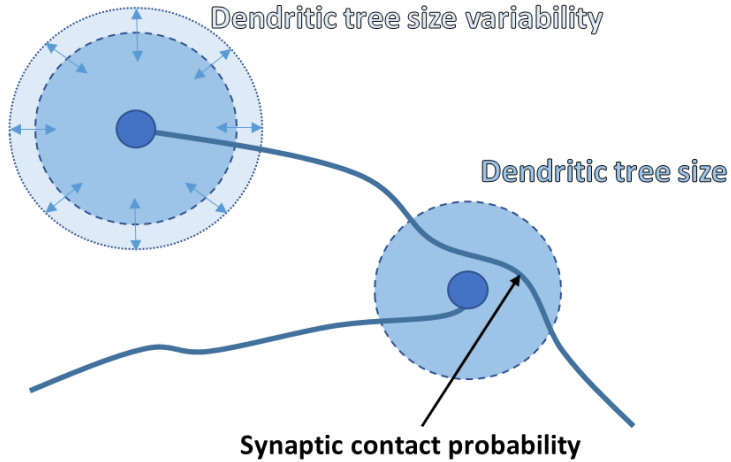


Figure 5: Schematic representation of the circuit building process. Circles with diameter d_s representing somas are located randomly in a synthetic 2D space. From the somas emerge quasi-straight paths representing axons. Each single axon length is obtained from a Rayleigh distribution with mean \bar{l}_a and scale parameter σ_a . Dendritic trees are circles with radius \bar{r}_d and sigma σ_d . In every point of the synthetic 2D space having an overlap between an axon and a dendritic tree, a new connection between the two neurons is added with probability α .

A connection between the two neurons is obtained in every point of the 2D space where a dendritic tree and an axon overlap, with a probability α that has been assumed to be constant in existing models (see **Figure 5**). However, this does not take into account fine neuromorphological aspects such as dendritic complexity and spine density that are relevant since they determine the spatial distribution of synaptic contacts in neuronal trees. In order to introduce those in the model, I assumed that the probability of finding a spine at a specific radius of the tree overlapping with an axon is equivalent to the probability of a synaptic contact. I defined the probability for a synaptic contact $\alpha(r)$ at a given radius r from the soma as the probability of finding a dendrite at r , and a spine in a dendritic fragment of length Δl . This probability is given by the spine $sd(r)$ and dendritic $bp(r)$ densities at r :

$$\alpha(r) = \frac{bp(r) \cdot w}{2\pi r} \cdot sd(r) \cdot \Delta l \quad (4)$$

Where w is the diameter of a dendrite (set as $1\mu\text{m}$ in our model), and $\Delta l = 1\mu\text{m}$ is determined by the spatial discretization of the model.

Thus, the synaptic contact probability in our modified 2D model depends on the radial distributions of both dendritic branches and spine densities. Interestingly, using the wild-type experimental data for spine and dendritic densities, the mean synaptic contact probability $\overline{\alpha(r)}$ is approximately 0.3. This proved to be anatomically correct by being close to estimated connection probability values in the mammalian cortex (Markram, 2006; Orlandi et al., 2013). Once all the neurons have been positioned, scanning all the points in the 2D space, and calculating the synaptic contact probability in each axon overlapping a dendritic tree, allows to obtain pairwise connections between all the neurons in the network. Taking into account that redundant synapses can occur between a pair of neurons leads to the generation of a weighted adjacency matrix.

Parameterization of the 2D minimal model

To study the implications of single-neuron morphology on network connectivity, it has been necessary to perform a systematic revision and selection of existing data. I parameterized generic neuronal properties with data from previously published articles (Ballesteros-Yáñez, Benavides-Piccione, Elston, Yuste, & DeFelipe, 2006; Komulainen et al., 2014; Orlandi et al., 2013) accounting for cortical layer II/III morphological properties including soma diameter, axonal length and tortuosity, and synaptic contact probability in wild-type mice. The values and sources used are summarized in **Table 3**.

Among the generic properties introduced in the model it is worth mentioning the neuronal density and axon parameterization chosen. Using a realistic neuronal density is not possible due to computational limitations (Orlandi et al., 2013; Voges et al., 2010). Thus, I subsampled to a reduced neuron density by, instead of assuming a projection of the complete layer II/III, simulating a thin sublayer of the width of a single soma diameter. This subsampling leads to a neuron 2D density of 1350 neurons/mm², obtained by multiplying the neuronal density in the 3D layer by the width of the thin layer modeled. Based on this assumption, I located randomly 3037 neurons in the area of the synthetic circuit, set to 2.25mm² (1.5mm sided square with periodic boundary conditions). The axonal mean length used is 500μm in order to simulate only local horizontal connections (given by the local axonal tree in layer II/III) following experimental data in the mouse M2 cortical layer II/III (Voges et al., 2010), and

disregarding horizontal patchy connections, connections between cortical layers and interhemispheric projections.

Table 3: Neuromorphological parameter set for the instantiation of the 2D model. Values and units for each parameter are specified along with the literature reference they were obtained from.

Variable	Description	Value	Units	Reference
d_s	Soma diameter	15	μm	(Komulainen et al., 2014)
\bar{r}_d	Dendritic mean radius	150	μm	(Ballesteros-Yáñez et al., 2006)
σ_d	Sigma of the dendritic radius Gaussian distribution	40	μm	(Orlandi et al., 2013)
α	Synaptic contact probability	0.3	-	(Markram, 2006; Orlandi et al., 2013)
\bar{l}_a	Axon mean length	500	μm	(Voges et al., 2010)
σ_a	Scale parameter of the axonal length Rayleigh distribution	100	μm	(Orlandi et al., 2013)
dl	Axonal biased random walk segment length	10	μm	(Orlandi et al., 2013)
σ_θ	Sigma of the axonal biased random walk angle Gaussian distribution	6	$^\circ$	(Orlandi et al., 2013)

To introduce dendritic morphology information in the model, I need to include the synaptic contact probability, which is defined by **Equation 4**. I obtained the $bp(r)$ and $sd(r)$ distributions for cortical layer II/III basal trees of wild-type C57BL/6J mice based on data from the literature (Ballesteros-Yáñez et al., 2006) (see **Figure 6**). To obtain mathematical expressions, I performed polynomial regressions on the dendritic and spine density distributions. Fitting was done using the lm function in R, and 5th and 6th degree polynomial expressions were obtained. The obtained polynomials were introduced in **Equation 4** to calculate the synaptic contact probability at any radius of the modeled dendritic trees.

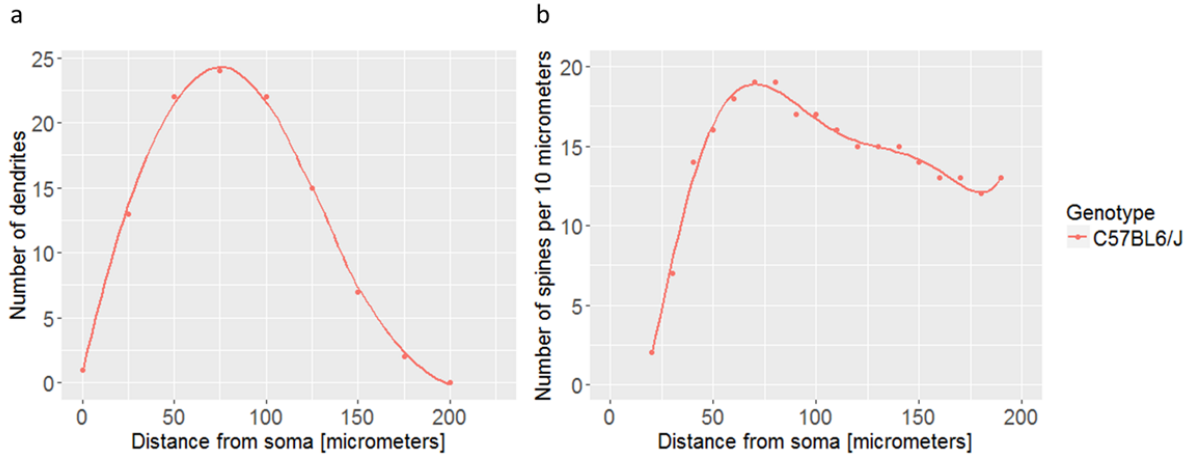


Figure 6: Dendritic and spine numbers dependency on the dendritic tree radius in wild-type C57BL/6J mice. Distributions of dendrite (a) and spine (b) numbers in function of the distance from the soma. Mean values obtained from the literature characterizing basal dendritic trees of M2 in the layer II/III of the cortex (Ballesteros-Yáñez et al., 2006).

1.2.3. Network topology characterization using graph theory

I analyzed the adjacency matrices (square matrices that represent all the vertices of a graph and the connections among them) of the instantiated networks using graph theory. Due to the properties of the model, I expect the generated networks to be close to random, but to deviate slightly from purely random (Erdős-Rényi) networks by the fact that neurons close to each other have higher probability of connection. Previous studies have shown that expected consequences of the distance-dependent connection probability on topological properties of the network are: an *excess of reciprocal connections* (if neuron i is an afferent of j, the probability of j being an afferent of i increases), an increased *clustering coefficient* (probability to find a connection between adjacent neurons to a given neuron i) (Vegué, Perin, & Roxin, 2017), the existence of neurons with high values in the *degree distribution* (with the degree of a node being the amount of connections received and sent by that neuron) (Girvan & Newman, 2002) and increased *small-worldness* (ratio between the clustering coefficient and the path length of a network) (Bassett & Bullmore, 2006). Those metrics were obtained using the iGraph package in R.

To study properties of the network as proxies of behavior, I focused on three topological metrics that can be related to computational capacities of networks processing information: routing efficiency, storage capacity and cost, that have been previously defined for whole-

brain tractography-based networks (Avena-Koenigsberger et al., 2014) or single cells (Poirazi & Mel, 2001) and defined what I call the efficiency space.

Routing efficiency

Routing efficiency is the shortest path length φ_{ij} between any pair of nodes (neurons) i and j . φ_{ij} is inversely proportional to the amount of intermediate nodes separating i and j . Thus, when two neurons in the network are closely connected or have more synapses, the efficiency gets higher. The shortest path length matrices were obtained using the “distances” function in iGraph (<http://igraph.org/r/doc/distances.html>), which computes pairwise distances taking into account weighted connections using the Dijkstra algorithm (Ahuja, Mehlhorn, Orlin, & Tarjan, 1990).

Then, the formal definition for the routing efficiency is as follows:

$$E_{rout} = \sum_{i,j} \frac{1/\varphi_{ij}}{N(N-1)}, i \neq j \quad (5)$$

Where φ_{ij} is the graph path length between the nodes i and j , and N is the total number of nodes in the graph.

Storage capacity

I estimated the storage capacity of the instantiated network as the total number of non-redundant possible states for a given neuron receiving s synapses provided by d presynaptic neurons as previously defined by Poirazi and Mel (Poirazi & Mel, 2001). Briefly, assuming that the dendritic location of inputs (synapses) does not affect the integration of the signal in a given neuron (linear model), the combinatorial “n chose k” quantification of possible states for a post-synaptic neuron expressed in bits (basic unit of information) is given by:

$$\mathbf{B}_L = \sum_i \mathbf{b}_{L,i} \quad (6)$$

Where b_L is given by **Equation 2**.

Cost

The cost of the network is given by the product of the number of synapses and the physical distance between any pair of neurons. Thus, the cost is proportional to the connection weight (amount of synapses to be maintained) and physical distance between any pair of neurons. This measure quantifies the cost of making and maintaining anatomical connections between neurons (Avena-Koenigsberger et al., 2014). The cost of a connection between neurons i and j can be expressed as the product between the amount of synapses connecting them (synaptic weight w_{ij}) and the physical distance separating them (l_{ij}). Then, the total wiring cost of the whole network is:

$$\text{cost} = \sum_{i < j}^N w_{ij} l_{ij} \quad (7)$$

Where w_{ij} is the number of synaptic connections between neurons i and j , and l_{ij} the physical distance between them.

Pareto optimality

In **Section 1.2.1.** I proposed using Pareto optimality to study the multi-objective suitability of single-neuron dendritic architecture for signal integration and storage capacity at expenses of the cost of wiring the tree. I here propose that a similar trade-off exists between the cost of wiring a network and its routing efficiency or storage capacity, so that that neuronal networks are optimally wired to maximize routing efficiency and storage capacity while preserving material cost. Similarly, I define an efficiency space given by the routing efficiency, storage capacity and cost metrics defined above, and assess optimality by identifying Pareto fronts in 2D projections of the efficiency space and by measuring the distance of specific groups of networks to the Pareto front for each functional maximization at a minimum cost.

1.3. Results

1.3.1. Single-neuron wiring optimality in models of intellectual disability

In order to assess putative implications of dendritic alterations for signal integration I obtained and analyzed basal dendritic tree reconstructions of LY stained neurons of Ts65Dn and Dyrk1A +/ - and compared them with their respective wild-type littermates (6 neurons from 2 animals per group, **Figure 7**). The studies previously performed in our laboratory showed morphological alterations in the basal dendritic trees of layer II/III motor cortex pyramidal neurons in intellectual disability mouse models. Specifically, dendritic tree spanning area and complexity, and synaptic density were reduced in the Ts65Dn (M Dierssen et al., 2003), and Dyrk1A+/- (R Benavides-Piccione et al., 2005) models.

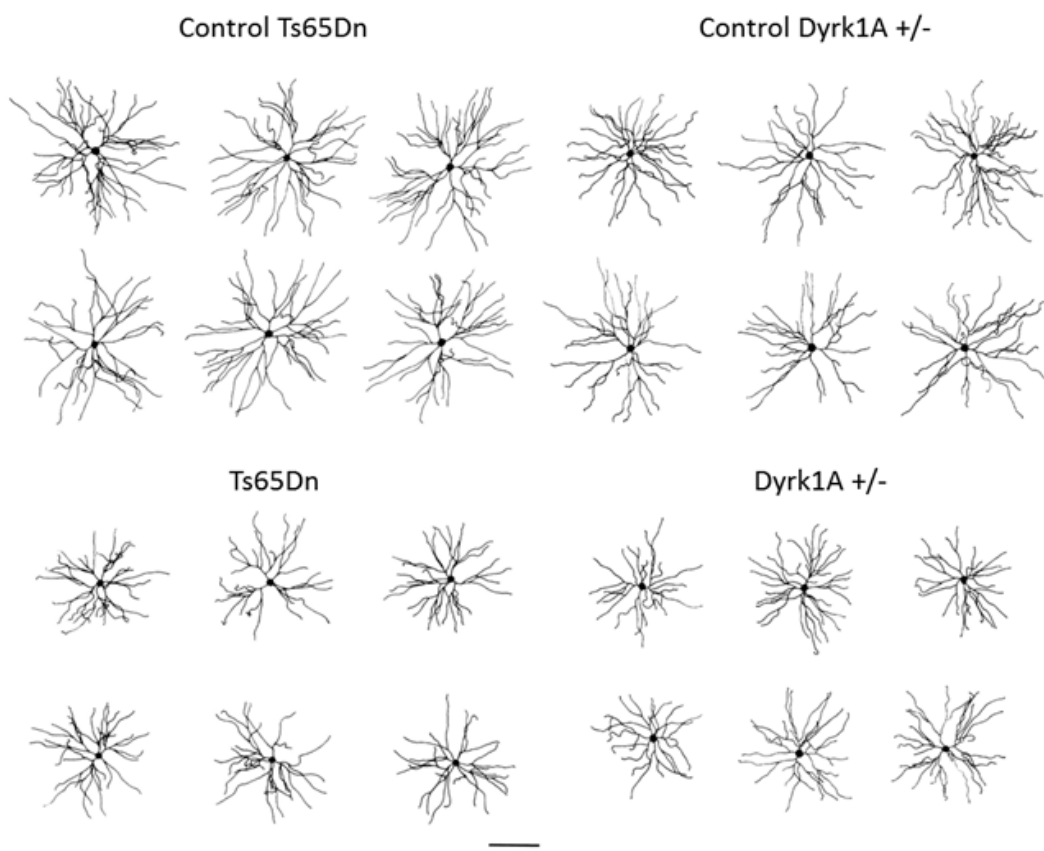


Figure 7: Camera lucida drawings of the basal dendritic trees of layer II/III motor cortex pyramidal neurons of Ts65Dn, Dyrk1A +/ - and their respective controls. The drawings represent a 2D projection of the basal tree seen in the tangential plane to the cortical layers. Qualitatively, Ts65Dn and Dyrk1A+/- appear to be smaller and less complex than their wild-type counterparts. Scale bar = 100 μ m.

Here I used camera lucida drawings (**Figure 7**) to evaluate dendritic tree morphological features and performed a statistical analysis using Trees Toolbox. An overview of metrics summarizing the analysis can be seen in **Figure 9**. A Trees Toolbox workspace with all the reconstructions can be found at https://bitbucket.org/linusmg/2d_model_bitbucket.

Dendrograms of representative trees provide an overview of the morphological differences between the two mouse models and their controls. Regarding the impact of genetic background, the comparison of wild-type mice of two strains (B6EiC3Sn and C57BL/6J-129Ola) showed similarly long dendrites reaching a maximum length close to 200 μm . However, dendritic complexity for those single trees was higher in the Ts65Dn control, with 44 branches, and slightly lower in the Dyrk1A $^{+/-}$ control, with 36 branches. Both Ts65Dn and Dyrk1A $^{+/-}$ neurons show reduced branch length, reaching maximum dendritic lengths close to 125 μm for Ts65Dn neurons and slightly below 120 μm in Dyrk1A $^{+/-}$ and reduced dendritic complexity (31 branches in Ts65Dn neurons and 25 branches in Dyrk1A $^{+/-}$ neurons, respectively).

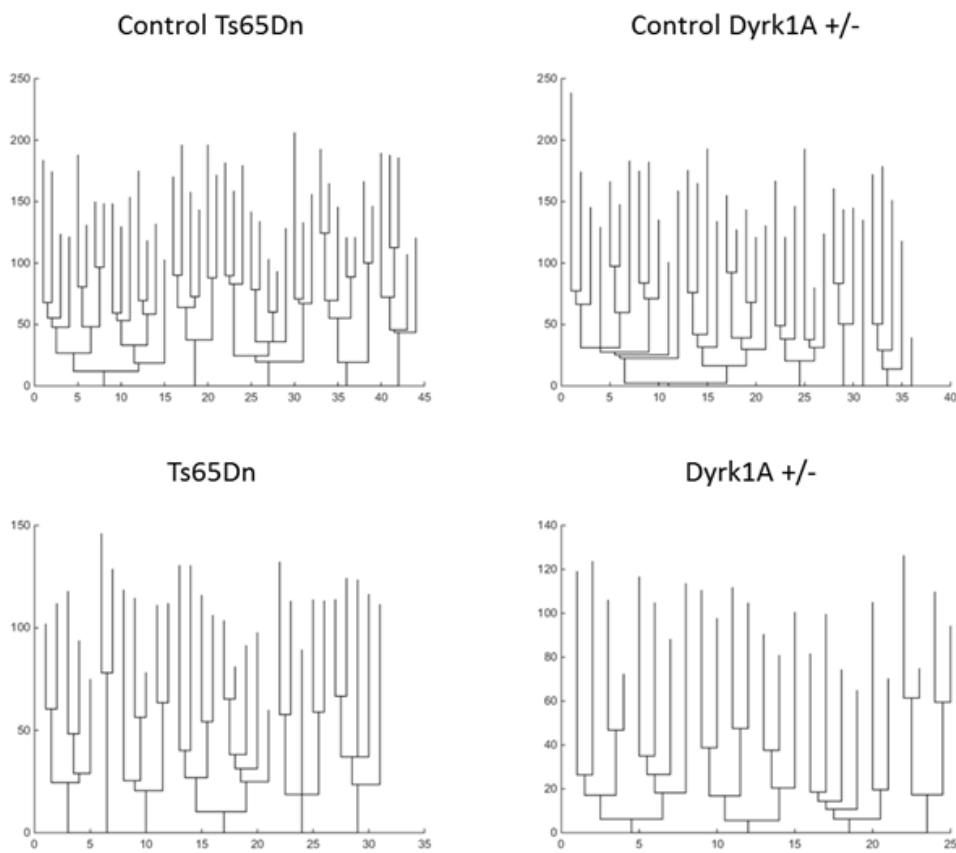


Figure 8: Dendrograms for four representative neurons. The plot represents the amount of branches versus their length. Ts65Dn and Dyrk1A $^{+/-}$ neurons show reduced dendritic complexity and shorter dendritic segments than controls.

To assess the morphological differences in detail, I used the series of metrics described in **Table 4**. Those provide a complete description of the dendritic tree size, complexity and morphological properties of the dendrites (length, straightness and branching angle). First, I performed a one-way ANOVA test to identify significant differences among the four conditions and two-way unpaired t-tests with post-hoc Bonferroni corrections to identify pairwise significant differences.

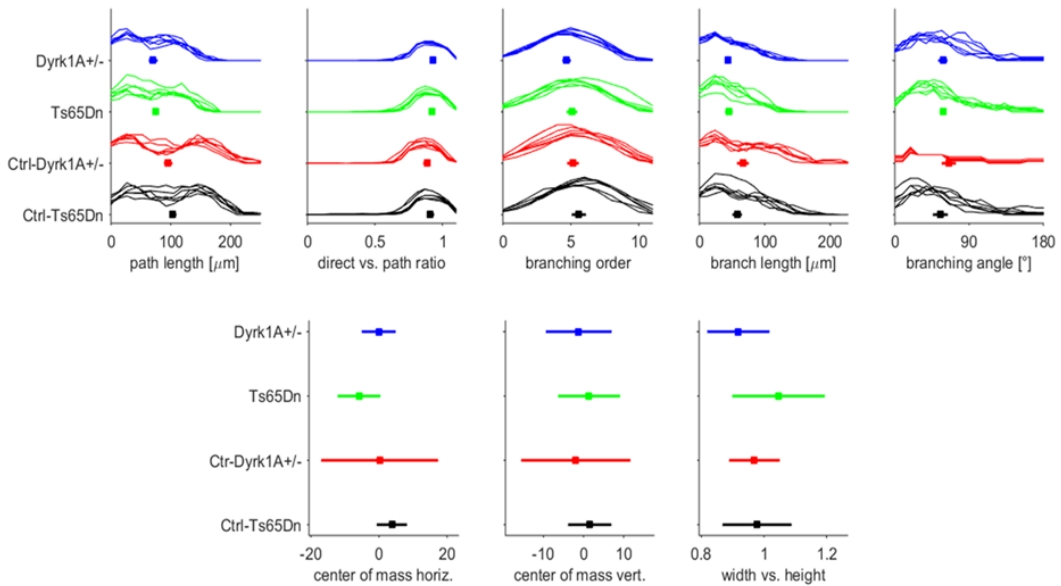


Figure 9: Overview of the neuromorphological metrics obtained in the statistical analysis with the Trees Toolbox. Each panel shows series of distributions of morphological metrics for Ts65Dn control (black), Dyrk1A+/- control, Ts65Dn and Dyrk1A+/- mice. Each line is a density plot of a single metric for all the branches of a single neuron. The square colored dots and lines indicate the mean and standard deviation of the distributions.

The total dendritic length (sum of the lengths of dendritic segments) is severely reduced in both mutant models ($F_{(3,20)} = 46.357$, $p = 3.44 \times 10^{-9}$; **Figure 10** upper left panel) as compared to their controls. Ts65Dn neurons show a statistically significant reduction respect to their controls ($2251 \pm 99 \mu\text{m}$ versus $3954 \pm 403 \mu\text{m}$, respectively, Bonferroni *post-hoc* correction; $p = 7.10 \times 10^{-8}$). In a similar trend, Dyrk1A+/- neurons have reduced dendritic length than their wild-type controls ($2143 \pm 334 \mu\text{m}$ and $3415 \pm 352 \mu\text{m}$ respectively; Bonferroni-corrected $p = 6.34 \times 10^{-6}$). Finally, the comparison between the two control groups (B6EiC3Sn and C57BL/6J-129Ola) show a tendency to have trees with less dendritic material (sum of the lengths of dendritic segments: $3954 \pm 403 \mu\text{m}$ and $3415 \pm 352 \mu\text{m}$ respectively; Bonferroni-corrected $p = 0.051$) in the C57BL/6J-129Ola strain. Spanning area (**Figure 10** bottom left panel), maximum path length (**Figure 10** upper middle panel) and mean density (**Figure 10** middle right panel) follow similar trends, with a marked reduction in both mutant mouse models and subtle differences between control strains, if any (see **Table 4**).

Interestingly, the number of branch points (**Figure 10** middle left panel), which provides an estimation of tree complexity, shows also significant overall differences ($F_{(3,20)} = 7.39$, $p = 1.60 \times 10^{-3}$). Specifically, it is reduced in Ts65Dn neurons compared to their controls ($27.8 \pm$

2.6 and 37.3 ± 5.9 respectively; Bonferroni-corrected $p = 7.35 \times 10^{-3}$), but also in C57BL/6J-129Ola versus B6EiC3Sn neurons (28.5 ± 4.3 and 37.33 ± 5.9 respectively; Bonferroni-corrected $p = 0.014$). This trend is also observed for the mean branch order (see **Table 4**), indicating that less complex dendritic trees tend to have reduced branching hierarchies.

Our analysis shows that both Ts65Dn and Dyrk1A+/- neurons have reduced mean branch length (**Figure 10** upper right panel) compared to controls ($F_{(3,20)} = 29.85$, $p = 1.39 \times 10^{-7}$). There are significant differences between Ts65Dn and their controls ($45.2 \pm 3.9 \mu\text{m}$ and $57.8 \pm 5.2 \mu\text{m}$ respectively; Bonferroni-corrected $p = 1.53 \times 10^{-3}$), and between Dyrk1A+/- and their controls ($43.2 \pm 2.7 \mu\text{m}$ and $66.5 \pm 6.9 \mu\text{m}$ respectively; Bonferroni-corrected $p = 4.79 \times 10^{-7}$). The neurons from mixed background C57BL/6J-129Ola mice have longer segments than B6EiC3Sn neurons ($66.5 \pm 6.9 \mu\text{m}$ versus $57.8 \pm 5.2 \mu\text{m}$ respectively; Bonferroni-corrected $p = 0.039$). The mean density is also lower in both Ts65Dn and Dyrk1A+/- versus their controls, and increased in C57BL/6J-129Ola versus B6EiC3Sn (see **Table 4**).

Finally, straightness (**Figure 10** bottom middle panel) and the mean branching angle (**Figure 10** bottom right panel) show similar values in Ts65Dn, Dyrk1A+/- and the C57BL/6J-129Ola control groups. However, ANOVA revealed significant overall differences $F_{(3,20)} = 10.35$, $p = 2.53 \times 10^{-4}$ for straightness and $F_{(3,20)} = 3.52$, $p = 0.034$ for mean branching angle mainly driven by the different phenotype of the B6EiC3Sn control neurons. Specifically, compared to the B6EiC3Sn strain, C57BL/6J-129Ola wild-type neurons show reduced straightness (0.884 ± 0.017 and 0.911 ± 0.017 respectively; Bonferroni-corrected $p = 0.023$), and increased mean branching angle ($0.96 \pm 0.13 \text{ rad}$ and 1.14 ± 0.12 respectively; Bonferroni-corrected $p = 0.031$).

One-way ANOVA tests among the four groups did not show significant differences for the center of mass of the trees, the maximum branch order, the width vs. height ratio and the mean asymmetry (data not shown).

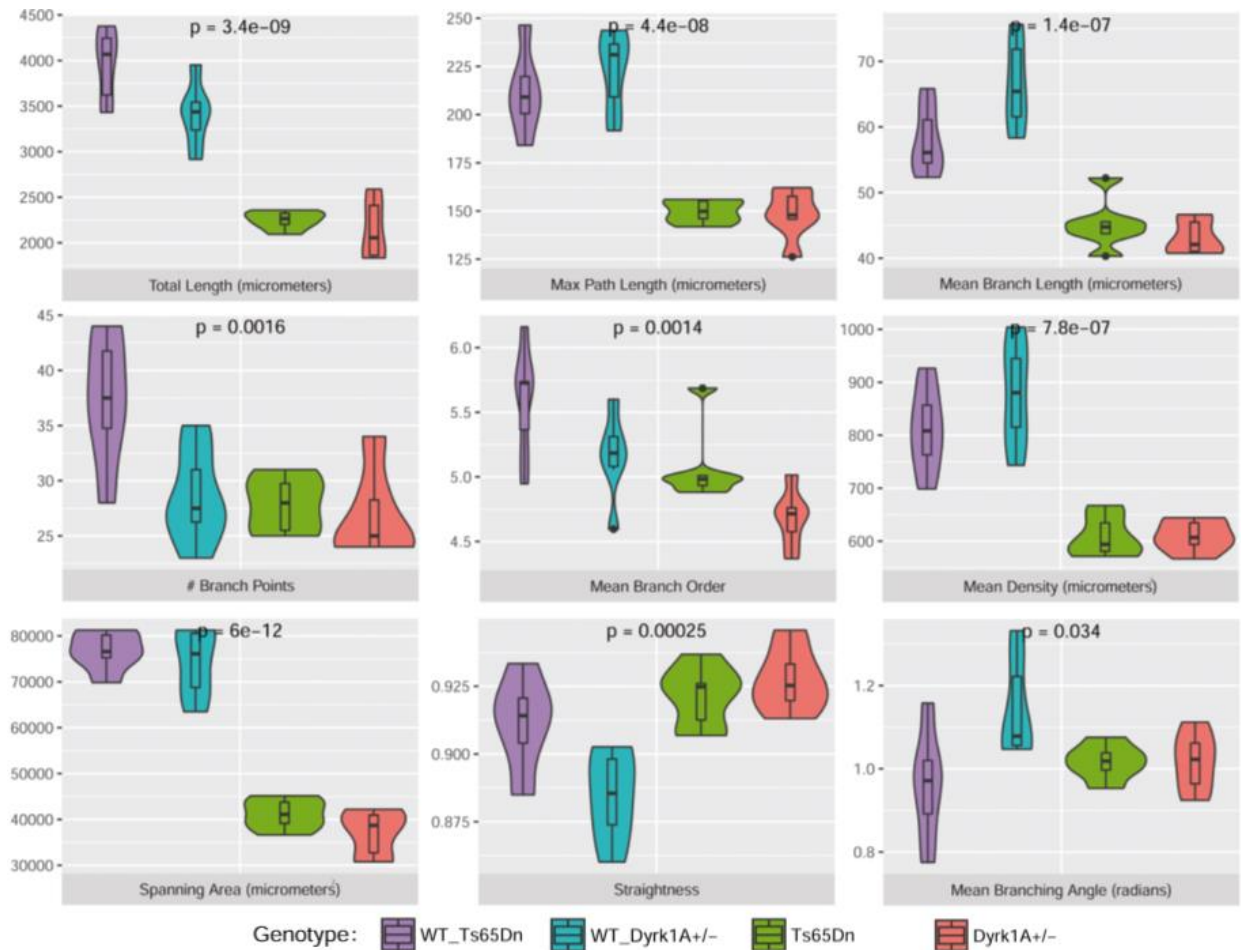


Figure 10: Boxplots of single-neuron morphological metrics. Each panel shows violin and boxplots for metrics having significant differences in one-way ANOVA tests between the Ts65Dn, Dyrk1A+/- and their respective controls, the p-value of the test is shown on top of each panel. Each metric units are specified in the panel label. Each colored box/violin plot represents the distribution of the metric for each group. Spanning area, mean and maximum path length, mean branch length and dendritic area are reduced in both Ts65Dn and Dyrk1A+/- mice. Dyrk1A+/- control littermates show decreased total length and branch points, increased mean branch length (accompanied by reduced straightness), increased mean branching angle and increased mean density.

Table 4: Statistical comparisons between single-neuron morphological metrics. The table summarizes both the mean and standard deviation values for controls and mutant mouse models, the t-values, degrees of freedom and Bonferroni-corrected p-values for pairwise t-tests between each mutant mouse model and its respective control. The three last columns show Bonferroni corrected p-values for comparisons between wild-type strains, the variation between sample means F and the one-way ANOVA test p-value.

Metric	Study	Control		ID model		t-value	degrees of freedom	ID model comparison Bonferroni-corrected p-value	WT comparison Bonferroni-corrected p-value	ANOVA F	ANOVA p-value
		Mean	SD	Mean	SD						
Total length	Ts65Dn	3953.67	403.03	2250.97	98.87	10.05	5.60	7.10E-08	0.05	46.36	3.44E-09
	Dyrk1A+/-	3415.15	352.24	2142.93	334.03	6.42	9.97	6.34E-06			
Max path length	Ts65Dn	211.63	21.34	149.88	5.98	6.82	5.78	1.64E-05	1	34.32	4.43E-08
	Dyrk1A+/-	222.98	21.02	148.32	12.91	7.41	8.30	1.03E-06			
# Branch points	Ts65Dn	37.33	5.92	27.83	2.56	3.61	6.81	7.35E-03	1.36E-02	7.39	1.60E-03
	Dyrk1A+/-	28.50	4.32	26.83	4.02	0.69	9.95	1			
Straightness	Ts65Dn	0.91	0.02	0.92	0.01	-1.16	8.81	1	2.26E-02	10.35	2.53E-04
	Dyrk1A+/-	0.88	0.02	0.93	0.01	-5.13	8.98	3.02E-04			
Max branch order	Ts65Dn	9.33	0.52	8.83	1.17	0.96	6.88	1	1	2.81	0.07
	Dyrk1A+/-	9.17	0.75	8.00	0.89	2.44	9.72	0.18			
Branching angle	Ts65Dn	0.96	0.13	1.02	0.04	-0.95	6.01	1	3.18E-02	3.52	3.38E-02
	Dyrk1A+/-	1.14	0.12	1.02	0.07	2.16	8.01	0.24			
Branch length	Ts65Dn	57.85	5.20	45.21	3.92	4.75	9.30	1.53E-03	3.87E-02	29.85	1.39E-07
	Dyrk1A+/-	66.51	6.91	43.15	2.70	7.71	6.50	4.79E-07			
Path length	Ts65Dn	103.66	3.68	75.40	3.07	14.46	9.69	2.38E-09	2.80E-02	80.58	2.42E-11
	Dyrk1A+/-	95.70	5.00	70.52	5.23	8.53	9.98	1.73E-08			
Branch order	Ts65Dn	5.59	0.43	5.08	0.30	2.40	8.99	0.08	0.21	7.61	1.39E-03
	Dyrk1A+/-	5.16	0.33	4.69	0.22	2.90	8.66	0.13			
Width vs. Height	Ts65Dn	0.98	0.11	1.05	0.14	-0.94	9.21	1	1	1.42	0.27
	Dyrk1A+/-	0.97	0.08	0.92	0.10	1.02	9.57	1			
Center of mass horiz.	Ts65Dn	3.80	4.07	-5.90	5.92	3.31	8.87	0.54	1	1.08	0.38
	Dyrk1A+/-	0.18	16.83	-0.09	4.63	0.04	5.75	1			
Center of mass vert.	Ts65Dn	1.54	5.07	1.39	7.40	0.04	8.84	1	1	0.24	0.87
	Dyrk1A+/-	-1.95	13.31	-1.18	7.87	-0.12	8.12	1			
Spanning area	Ts65Dn	76751	4288	41192	3310	16.08	9.40	1.59E-09	1	93.69	6.00E-12
	Dyrk1A+/-	74224	7634	37133	5101	9.90	8.72	7.55E-10			
Asymmetry	Ts65Dn	0.38	0.02	0.38	0.03	0.11	7.67	1	1	0.77	0.52
	Dyrk1A+/-	0.37	0.01	0.39	0.02	-1.71	7.54	0.92			
Dendritic area	Ts65Dn	810.42	81.29	608.55	39.52	5.47	7.24	6.17E-04	1	19.75	3.40E-06
	Dyrk1A+/-	877.94	100.42	609.71	30.12	6.27	5.89	1.42E-04			

Principal component analysis

To identify metrics that explain the differences found in those intellectual disability models or account for the strain-dependent neuromorphological variability, I performed a Principal Component Analysis (PCA) of the mutant and wild type mice. The two first principal components explain 59.7% of the variance in the data (**Figure 11**). Principal Component 1 (PC1, 45.7% explained variance) is mainly contributed by measures that account for the size of the tree: the dendritic spanning area, the total length of the tree and the maximum and mean path length. Following those metrics, straightness, branch order and density show considerable contributions to PC1. Principal Component 2 (PC2, 14.0% explained variance)

is mainly contributed by the mean branching angle, followed by the number of branch points, the horizontal center of mass and the mean branching asymmetry.

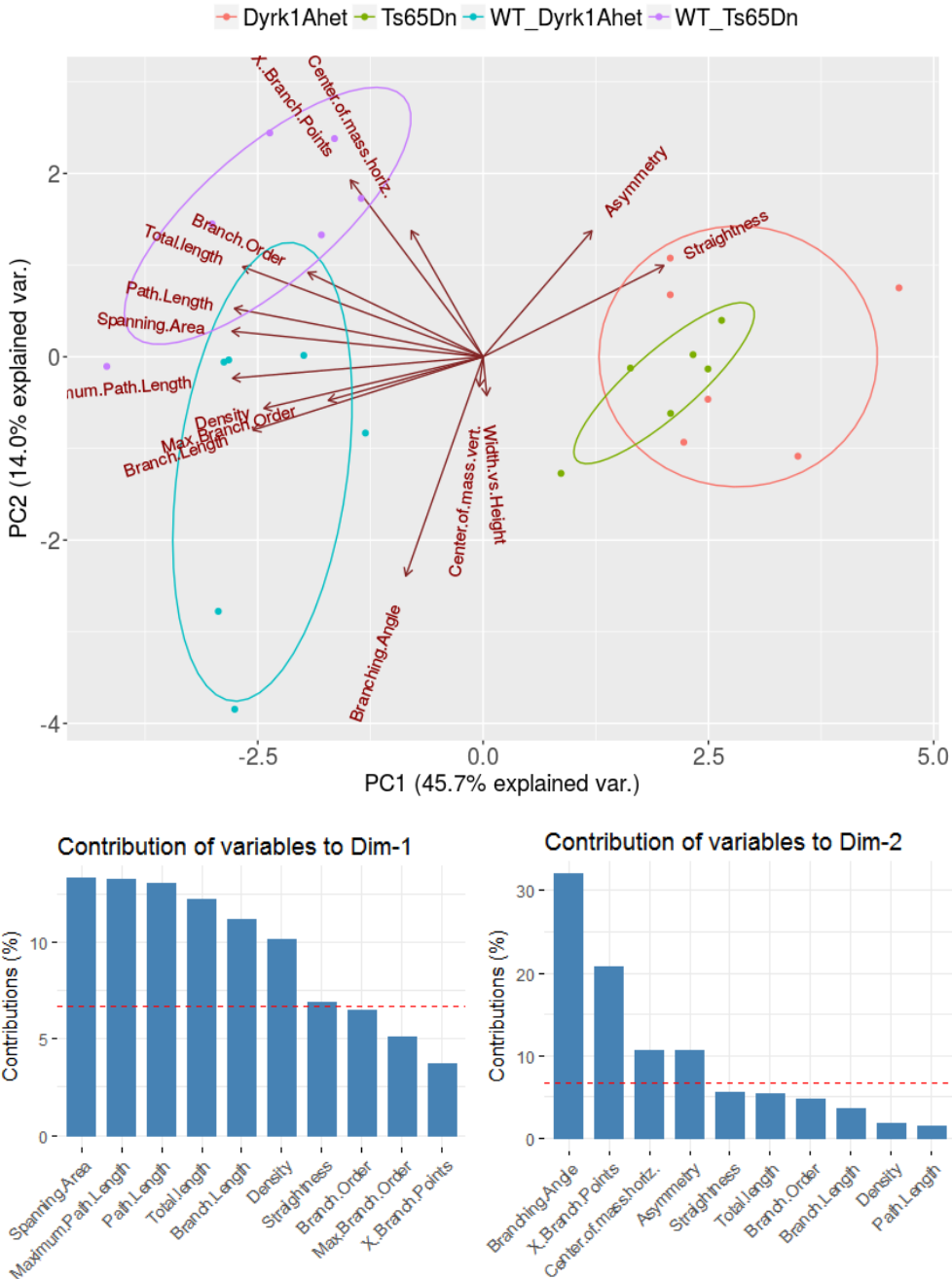


Figure 11: Principal component analysis. PCA of the variables, where arrows represent the direction of each variable in the PCA space. Longer arrows belong to variables that are well represented by the two principal components. Each of the points represents one neuron, colored by the group they belong to. 68% confidence normal data ellipses for each group are drawn with solid lines. Bottom Bar plots showing the percentage of explained variance for each principal component. Bars represent the contribution (%) of each variable and the red dashed lines indicate the expected average contribution. The first principal component is a composite variable accounting for the dendritic tree size and the total dendrite length. The second principal component is a composite variable accounting for other morphological measurements, mainly the branching angle, the number of branch points and the horizontal center of mass and mean asymmetry.

A 2D projection overview of those principal components shows that the neurons clustered by genotype, being the wild-type and mutants mainly separated in PC1, while the different genetic background by PC2. Thus genetic background dependent neuromorphological differences are mainly related to mean branching angle and number of branch points. Instead, the variables contributing more to the difference between wild-types and mutants are mostly related to the tree span, its complexity and the straightness of the branches, being the most relevant metrics for dendritic wiring optimality. These results suggest that intellectual disability mouse models could have an excess of branches in small trees.

Wiring optimality

Cuntz el at. (Cuntz, Mathy, and Häusser 2012) demonstrated using a large set of morphological reconstructions from the NeuroMorpho.org database, that dendrites of the various neuronal classes balance wiring costs differently, but the relationships between key features in their morphology followed scaling laws that could be predicted by models based on wiring minimization principles. If a set of n points is distributed in 2D with a density $d = n/S$, the average surface occupied by a single point is $s' = d^{-1}$, and the average minimal distance between points is proportional to the square root of s' : $r = c \cdot d^{-1/2}$ with proportionality constant c . If the average distance between connected points is minimal, the total length of dendrite connecting the n points is proportional to S and given by $L = c \cdot S \cdot d \cdot d^{-1/2} = c \cdot S \cdot d^{1/2}$. Assuming a constant ratio between the number of contact points and the number of branch points (Cuntz, Mathy, and Häusser 2012), the total dendritic length scales with the number of branch points following a $1/2$ power law in any optimally wired 2D tree. I thus asked whether the differences in dendritic arborization that I detected in behaviorally affected mouse models (Ts65Dn and Dyrk1A $+$ / $-$) and between two different strains could affect wiring optimality.

In our reconstructions, I assumed branch points as the target points of the dendrites, since those can unambiguously be counted. Thus, to test the optimality, I fitted a power law to the total dendritic length vs. number of branch points, both normalized by the dendritic tree spanning area. I found that the B6EiC3Sn Ctrl-Ts65Dn trees follow a close-to-optimal space fitting a power law of 0.45 s.e.=0.13, while both the Ts65Dn and Dyrk1A $+$ / $-$ neurons deviate from the 0.5 optimal value, with power laws of 0.74 s.e.=0.15 and 0.75 s.e.=0.16,

respectively. Interestingly, the Ctrl-Dyrk1A $^{+/-}$ group (C57BL/6J-129Ola), present an intermediate phenotype, with a power fit of 0.65 s.e.=0.11 indicating slightly suboptimal tree wiring.

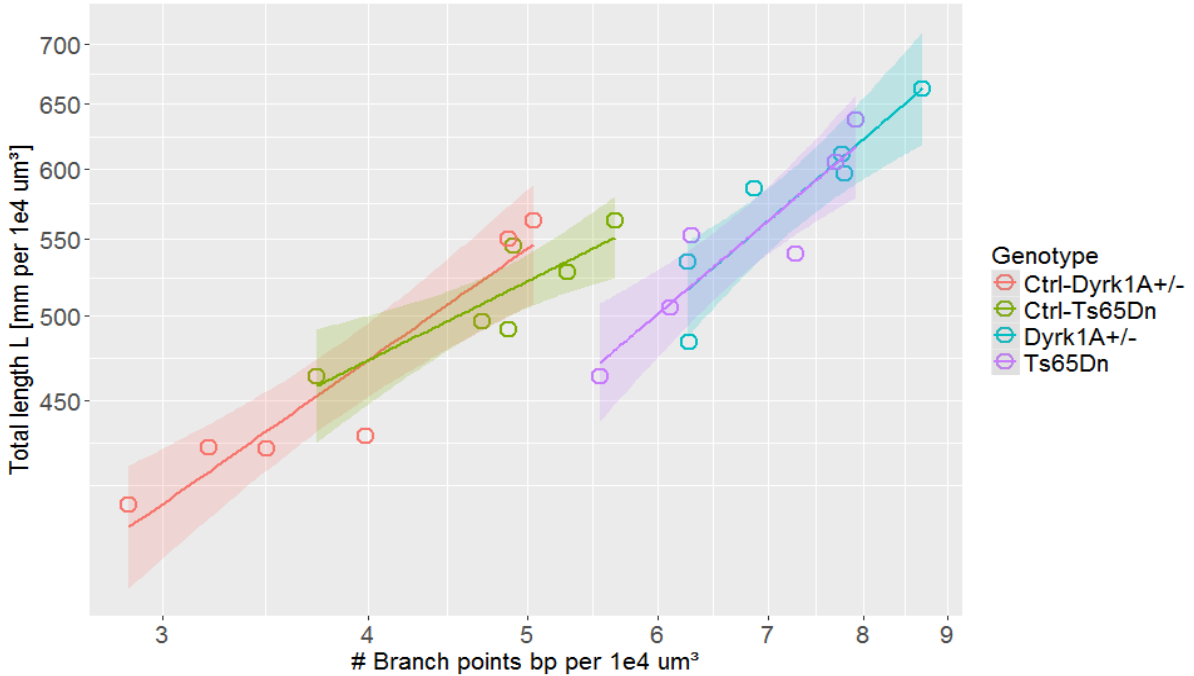


Figure 12: Power law relations between total dendritic length and branch number for layer II/III basal tree reconstructions of Ts65Dn and Dyrk1A $^{+/-}$ neurons, and their respective controls. The $\frac{1}{2}$ optimal power for 2D trees is only followed by the B6EiC3Sn Ts65Dn control trees (power = 0.45 ± 0.13), while both Ts65Dn (0.74 ± 0.15) and Dyrk1A $^{+/-}$ (0.75 ± 0.16) show a strong deviation, and C57BL/6J-129Ola Dyrk1A $^{+/-}$ controls (0.65 ± 0.11) slightly deviate. The number of branch points and total length were normalized by the dendritic surface ($S=10.000 \mu\text{m}^2$). Shaded regions indicate 95% confidence level interval of the power law fit.

From an alternative point of view, Wen and Chklovskii concluded that optimal wiring implies that the path length the radius of the trees and its total length should satisfy a power law relation with exponent 0.43 for layer II/III basal dendritic trees (Wen & Chklovskii 2009). I fitted power laws to the data points given by the DS mouse model reconstructions and their respective controls. I found that the four conditions present high variability in their fits. B6EiC3Sn Ctrl-Ts65Dn trees follow a power law of 0.20 s.e.= 0.09. Ts65Dn trees follow a negative power law, with power -0.63 s.e. = 0.32. Dyrk1A $^{+/-}$ neurons and their controls have powers 0.33 s.e. = 0.16 and -0.02 s.e.= 0.25, respectively. Given the measured errors, the fitted powers differ significantly from the optimal value found by Wen and Chklovskii for the case of Ts65Dn neurons and their controls. Even though these results point at the fact that Ts65Dn trees are suboptimally wired, the observed variations in the scaling power,

and specially the deviation from optimality in Ts65Dn controls are difficult to interpret, being probably due to the small numbers of samples in the analysed groups.

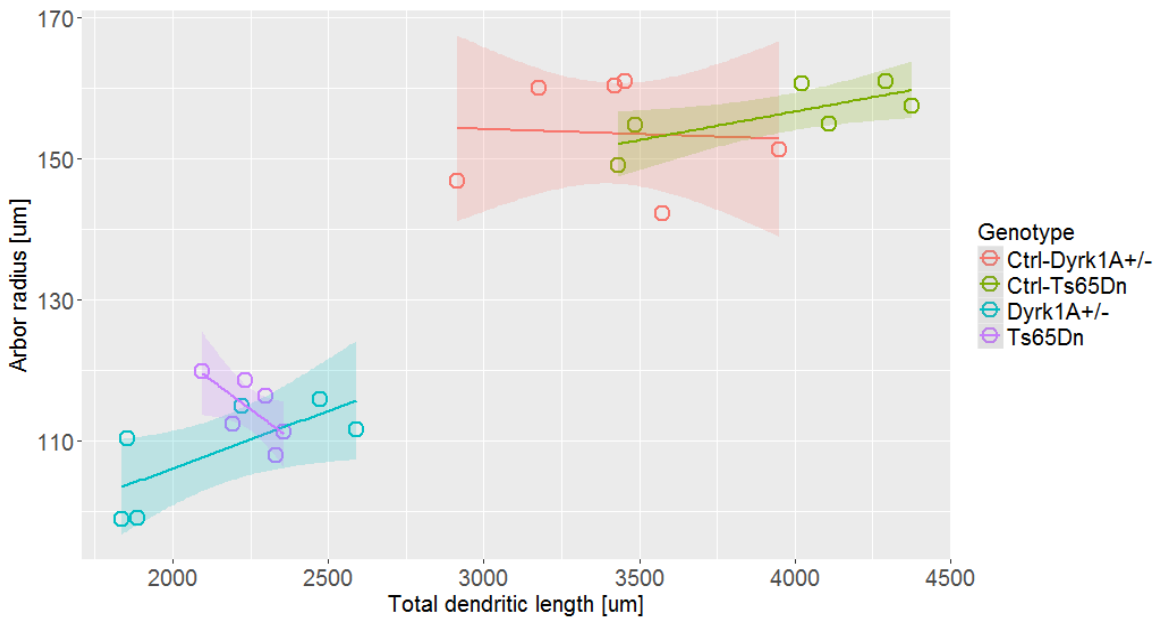


Figure 13: Power law relations between total dendritic length and arbor radius for layer II/III basal tree reconstructions of Ts65Dn and Dyrk1A+/- neurons, and their respective controls. The 0.43 optimal power for 2D trees is only followed by the B6EiC3Sn Ts65Dn control trees (power = 0.20 ± 0.09), while both Ts65Dn (-0.63 ± 0.32) and Dyrk1A+/- (0.33 ± 0.16) show a strong deviation, and C57BL/6J-129Ola Dyrk1A+/- controls (-0.02 ± 0.25) slightly deviate. Shaded regions indicate 95% confidence level interval of the power law fit.

Wen and Chklovskii also found that wild-type layer II/III basal dendritic trees have an occupation ratio of 0.3. Given that the trends around the scaling law between total length and radius are hard to interpret, I asked whether the dendritic trees of DS mouse models present differences in the occupation ratio.

Morphospace exploration and single-neuron Pareto optimality

While the scaling of branch numbers and total length of dendritic trees points at suboptimal space filling in both DS mouse models and the C57BL/6J-129Ola control mice, the description obtained with the scaling of the radius with total dendritic length is contradictory. Moreover, the implications of the neuromorphological alterations observed in each condition for the function of single neurons (i.e. their ability to integrate signals and store information) is not clear from the interpretation of the scaling laws. By using the definitions

of cost, routing efficiency and storage capacity mentioned above, I assessed how various neuromorphological properties contribute to them, and how they correlate with the optimality indicators given by the powers of the scaling laws. Dendritic tree size, branch density, and the balancing factor ($b\beta$) of the MST algorithm were scaled below and above the wild-type values (from 0.5 to 1.5 times the original value with a step of 0.1 in the case of dendritic tree size and branch density and for values from 0 to 2 with a step of 0.2 for the balancing factor). After generating groups of cloned trees with modified morphological properties, I quantified their cost, routing efficiency, storage capacity, occupancy ratio and the power of the scaling laws discussed above.

The exploration of the morphospace shown that the scaling law power differs upon morphological variations, indicating deviations from optimality (e.g. excessive number of branches for a given dendritic length) (see **Figure 14**). Increasing dendritic tree size (this is, increasing dendritic tree radius with constant branch number) obviously implies a reduction in the power of the scaling law $L \sim bp^\alpha$, while it does not change significantly for $R \sim L^\alpha$. Increasing branch density implies a reduction in the power of both scaling laws. When dendritic segments are less tortuous (increased balancing factor) the power of the $L \sim bp^\alpha$ scaling law increases and the power of the $R \sim L^\alpha$ scaling law decreases.

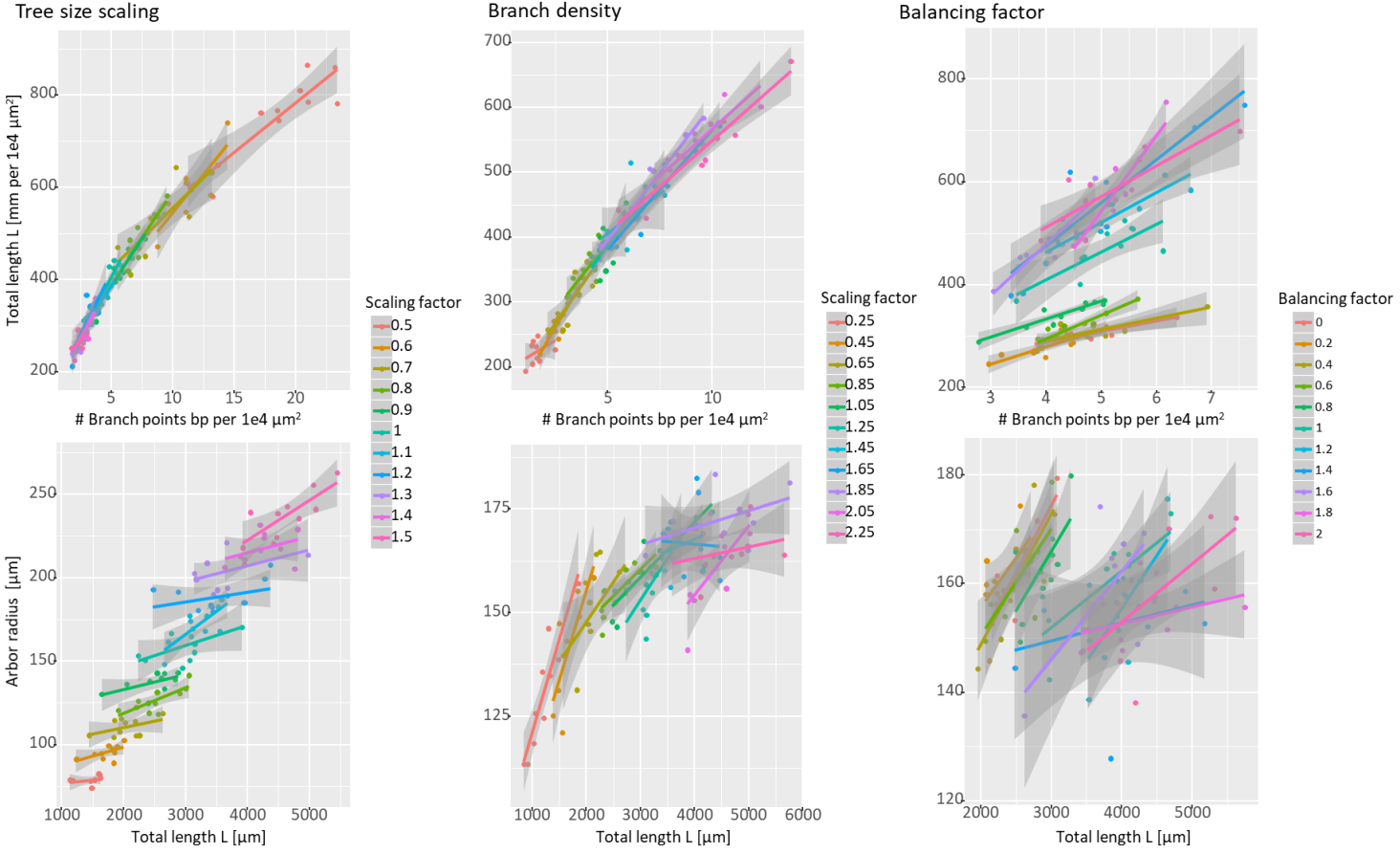


Figure 14: $L \sim bp^\alpha$ and $R \sim L^\alpha$ power law relations between the number of branch points and total dendritic length, and total dendritic length and arbor radius for a morphospace exploration of layer II/III basal tree reconstructions. The left column shows the variation on the scaling law fits for increasing tree size. The central column shows the variation in the scaling law fits for increasing dendritic branch density. The right column shows the variation on the power law fits with increasing balancing factor. Each fit was obtained from a group of 10 computationally generated tree structures. The colors and legends indicate the scaling factors applied to the neuromorphological parameters.

Similarly, cost, routing efficiency and storage capacity vary in the morphospace exploration as shown in **Figure 15**. Increased spine density (first column) does not affect the cost of wiring because we assumed that the cost is given by the dendritic length, but increases linearly routing efficiency and asymptotically storage capacity. Increased branch density (second column) linearly increases cost and routing efficiency, the latter having smaller slope and less impact than spine density. Storage capacity is also increased asymptotically, having an impact of the same magnitude than scaling spine density. Increased tree size (third column) implies a linear increase in cost that has higher slope than branch density. Routing efficiency is decreased linearly due to lower spine density in the dendritic tree span. Storage capacity

shows a superlinear increase, having higher impact than the other morphological properties explored. Trees having increased balancing factor (less tortuous branches and higher number of branches; fourth column), show a linear increase in cost and routing efficiency, while not having any effect on storage capacity.

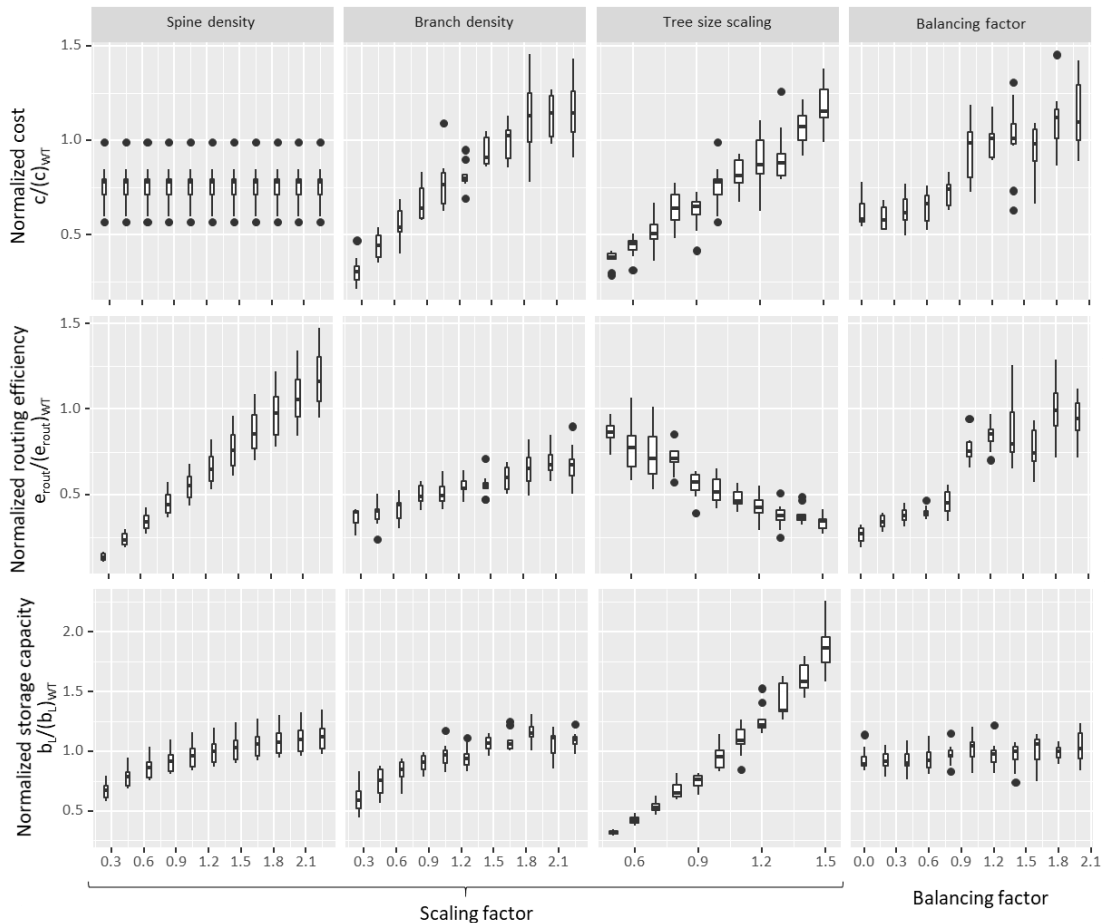


Figure 15: Implications of the morphospace exploration on the computational capacities of the cortical layer II/III single-neuron dendritic trees. Box plots for normalized cost (1st row), routing efficiency (2nd row) and storage capacity (3rd row) in the 2D model upon the variation of the spine density (1st column), branch density (2nd column), dendritic tree size (3rd column) and balancing factor (4th column). Each box plot represents 10 neurons obtained with a given parameter set.

To have an overview of the contribution of each morphological metric for the functional capacities I defined and how they relate to the wiring optimality scaling powers defined previously, I performed a PCA including my definitions for cost, routing efficiency and storage capacity; the powers of the $L \sim bp^\alpha$ and $R \sim L^\alpha$ scaling laws, and the morphological metrics that contribute to those variables (**Figure 16**).

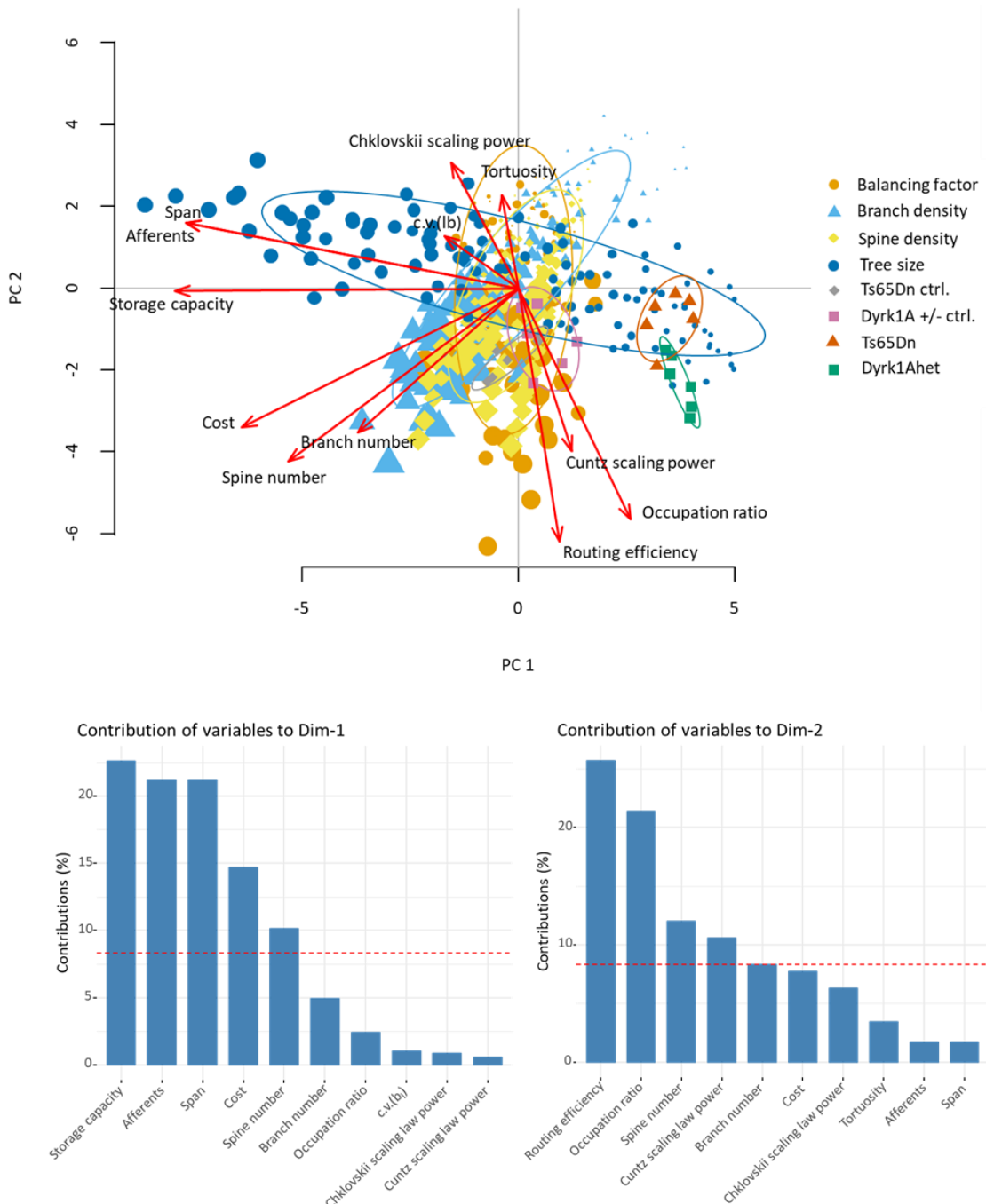


Figure 16: Morphospace principal component analysis. PCA of the morphospace variables explored, where arrows represent the direction of each variable in the PCA space. Longer arrows belong to variables that are well represented by the two principal components. Each of the points represents one neuron, colored by the parameter that was being modulated when it was generated. The size of the points indicates the scaling factor applied to the modulated parameters. 68% confidence normal data ellipses for each group are drawn with solid lines. Bottom Bar plots showing the percentage of explained variance for each principal component. Bars represent the contribution (%) of each variable and the red dashed lines indicate the expected average contribution. The first principal component is a composite variable mostly accounting for storage capacity and the dendritic tree span. The second principal component is a composite variable mainly accounting for routing efficiency, the occupation ratio and the spine number.

The three first principal component found in the analysis explain 72.3% of the variance. Principal Component 1 (PC1, 35.3% explained variance) is mostly contributed by storage capacity, followed by metrics accounting for the size of the trees, the dendritic tree span and the total dendritic length (cost). To a lower extent, the total number of spines also contributes to PC1. Principal component 2 (PC2, 25.2% explained variance) is mostly contributed by routing efficiency, followed by the occupation ratio and the spine number and the power of the scaling law $L \sim bp^z$ contributing to a lower extent. Even though contributing still less, the power of the scaling law $R \sim L^x$ also mostly contributes to PC2. The total dendritic length, and the numbers of branches and spines, contribute to a similar extent both to PC1 and PC2. Given that PC1 is mostly contributed by storage capacity and PC2 is mostly contributed by routing efficiency, the analysis highlights that the functional metrics chosen are mainly orthogonal, and that the variations in the scaling laws obtained by Cuntz and Chklovskii are directly and inversely proportional to routing efficiency respectively. Indicating that even though both derivations implicitly account for the connectivity repertoire, they end up accounting mostly for the efficiency in signal integration (as given by the definition proposed here).

By locating in the PCA the groups of DS model trees experimentally obtained, the analysis shows that DS trees separate from their controls mostly along PC1, and that there is almost no separation along PC2. This indicates that the defined optimality scaling laws are not able to account for the differences observed in the trees I analysed, while the calculation of the storage capacity does. Thus, this analysis points out that explicitly accounting for the connectivity repertoire when assessing neuron wiring optimality might be necessary.

To define a framework able to account for both routing efficiency and storage capacity and assessing how optimal neurons are to integrate and store information, I have used the concept of multi-objective, or Pareto, optimality. From this perspective, optimal neurons will maximize routing efficiency and storage capacity while preserving minimum wiring cost. To assess to what extent the dendritic architectures explored are Pareto optimal, I defined two 2D spaces given by routing efficiency and cost, and storage capacity and cost. By plotting the average routing efficiency, storage capacity and cost for each of the groups of neurons in the morphospace exploration I performed, Pareto fronts given by specific parameter explorations can be identified. When plotting routing efficiency versus cost, the data points

provided by the exploration of different balancing factors, provides maximum routing efficiency at a given cost. Tree size and branch density explorations are outperformed by the values obtained in the experimental groups. This is explained by the fact that the reconstructed trees have higher balancing factor than 0.85 (as this value was not known, it had to be estimated based on the literature; Cuntz et al., 2010). By taking the data points of the balancing factor exploration, the routing efficiency versus cost Pareto front of layer II/III basal dendritic trees can be approximated well by a linear fit. Points being closer to the Pareto front are closer to optimality for routing efficiency, dendritic trees with suboptimal architecture will have excessive cost for a given level of routing efficiency.

The morphospace exploration shows that the relation between cost and routing efficiency (**Figure 17**, left) is well approximated by a linear fit for the scaling of branch density, and by an exponential curve for tree size scaling. This implies that either increasing dendritic tree size or increasing branch density does not entail an advantageous configuration towards routing efficiency. Conversely, the slope of the linear increase in routing efficiency as a function of the wiring cost for increased balancing factor, shows that increasing the balancing factor is the most efficient strategy towards maximizing routing efficiency. For high routing efficiency values, high balancing factor neurons have the lowest cost, which justifies choosing the exploration of this parameter as the Pareto front in this study. Then, the distance between the points given by reconstructed groups of trees (or single neurons) and the Pareto front accounts for their optimality. The lower the distance to the front, the closer to optimal the dendritic architectures are. The fact that the balancing factor used in the morphospace exploration appears to be lower than the real value implies that the wild-type dendritic trees are more efficient than groups of trees in the defined Pareto front. To account for this, I considered distances for data points with higher efficiency than the Pareto front as negative. Thus, the distance to the front (d_p) shows that C57BL/6J wild-type neurons are the most efficient routing information at a given cost ($d_p=-0.10 \pm 0.14$). The mixed background C57BL/6J-129Ola wild-type neurons have 20% lower routing efficiency and 10% lower cost, with a distance $d_p=-0.07 \pm 0.15$ to the Pareto front. While Ts65Dn and Dyrk1A+/- neurons have similar routing efficiency than C57BL/6J-129Ola wild-types (74%, 82% and 80% of the C57BL/6J wild-type respectively), they also show higher cost per unit of area (115%, 111% and 90%, respectively). Their distance to the Pareto front, ($d_p=0.15 \pm 0.13$ for the Ts65Dn and $d_p=0.05 \pm 0.16$ for the Dyrk1A+/-), summarizes the situation and predicts that

Ts65Dn cortical layer II/III basal dendritic trees could be less efficient in routing information than Dyrk1A^{+/−} trees.

The right panel of **Figure 17** shows the relation between storage capacity and cost. In this case, the Pareto front is given by the dendritic tree size scaling for high storage capacity values, showing a linear dependency between storage capacity and cost with a slope of 1.63; and by the branch density scaling at low storage capacity values, which is fitted well by an exponential function with exponent 1.06. While Ts65Dn and Dyrk1A^{+/−} neurons show decreased storage capacity with respect to their wild-type counterparts (50% and 54% respectively) they also have lower material cost (53% and 55% respectively). However, the distance between both controls and both DS mouse model neurons to the Pareto fronts defined by the tree size and branch density respectively indicates that neither the C57BL/6J or the C57BL/6J-129Ola wild-type ($d_p=0.35 \pm 0.12$ and $d_p=0.20 \pm 0.11$ respectively) nor both DS models dendritic trees ($d_p=0.28 \pm 0.10$ for the Ts65Dn and $d_p=0.25 \pm 0.04$ for the Dyrk1A^{+/−}) are wired to optimize storage capacity. The morphospace exploration suggests that a small balancing factor combined with big tree size would be optimal for maximizing storage capacity at a given cost. However, as seen above, decreasing the balancing factor would imply a dendritic architecture less advantageous for signal integration efficiency.

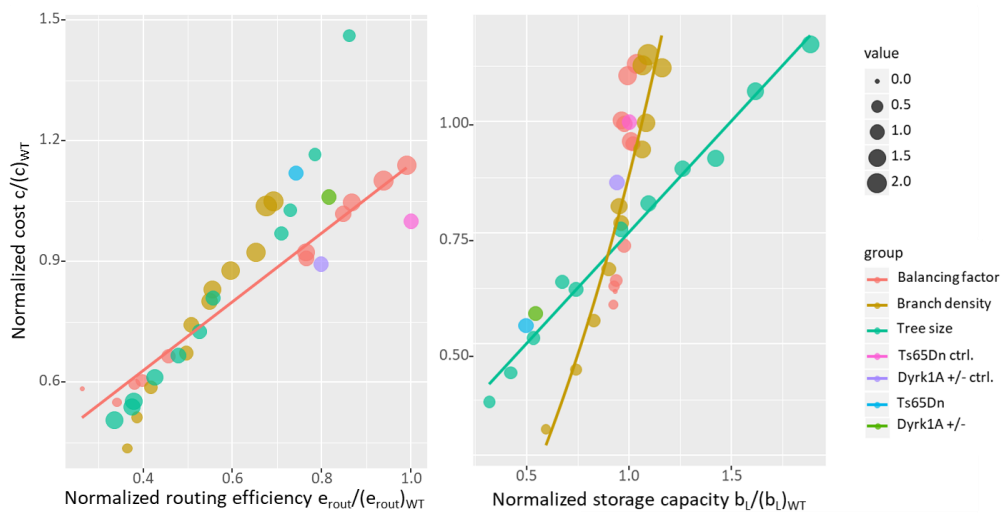


Figure 17: 2D projections of the morphospace exploration. Each point represents the mean value for normalized cost, routing efficiency and storage capacity of the groups of neurons analysed ($n=10$ for the computationally generated groups of neurons and $n=6$ for the experimentally obtained reconstructions). The color indicates the group the reconstructions belong to. The size of the points represents the scaling factor applied to the modulated parameter. The solid lines show linear and exponential fits to the explorations that have been used as Pareto fronts. Given that the routing efficiency is normalized by the tree spanning area by definition, the cost was also normalized to the spanning area for the routing efficiency plot.

This analysis, together with the morphological analysis of the trees, shows that while DS mouse models and C57BL/6J-129Ola mixed background mice have lower routing efficiency than C57BL/6J wild-type mice, only the DS models show suboptimal architecture for routing efficiency. This suboptimality is contributed mainly by smaller dendritic trees in the case of the Dyrk1A +/- model and both by reduced tree size and branch density in Ts65Dn trees. On the side of storage capacity, only the DS models show a clear impairment, while both wild-type strains have very similar storage capacity abilities. Dendritic architecture is suboptimal for memory storage in all the cases, either due to excessive branch density (both wild-type strains) or to reduced dendritic tree size (DS models). Interestingly, the reduced straightness and branch density of the mixed background C57BL/6J-129Ola mice imply that their architecture is closer to the Pareto front for storage capacity obtained in our exploration. Altogether, the analysis also suggests that layer II/III healthy basal dendritic trees have architectural characteristics prioritizing signal integration efficiency rather than memory storage.

1.3.2. Network computational capacities

Synaptic contact probability and dendritic tree size modulate routing efficiency and storage capacity

First, inspired by already existing similar models of local 2D networks, I explored the morphospace by assuming that the synaptic contact probability is constant along the dendritic trees (**Figure 18**; blue symbols). After, I introduce a synaptic contact probability extracted from experimental data. In the constant synaptic contact probability condition, the cost of wiring the network grows linearly when increasing synaptic contact probability. c The superlinear growth network cost detected when increasing dendritic tree size, suggests that the amount of contacts in the network depends less of the radius and more of the spanning area of the neuron. As compared to those parameters, increasing dendritic tree size variability only produces a slight linear increase of the cost (see **Figure 18**, upper panel).

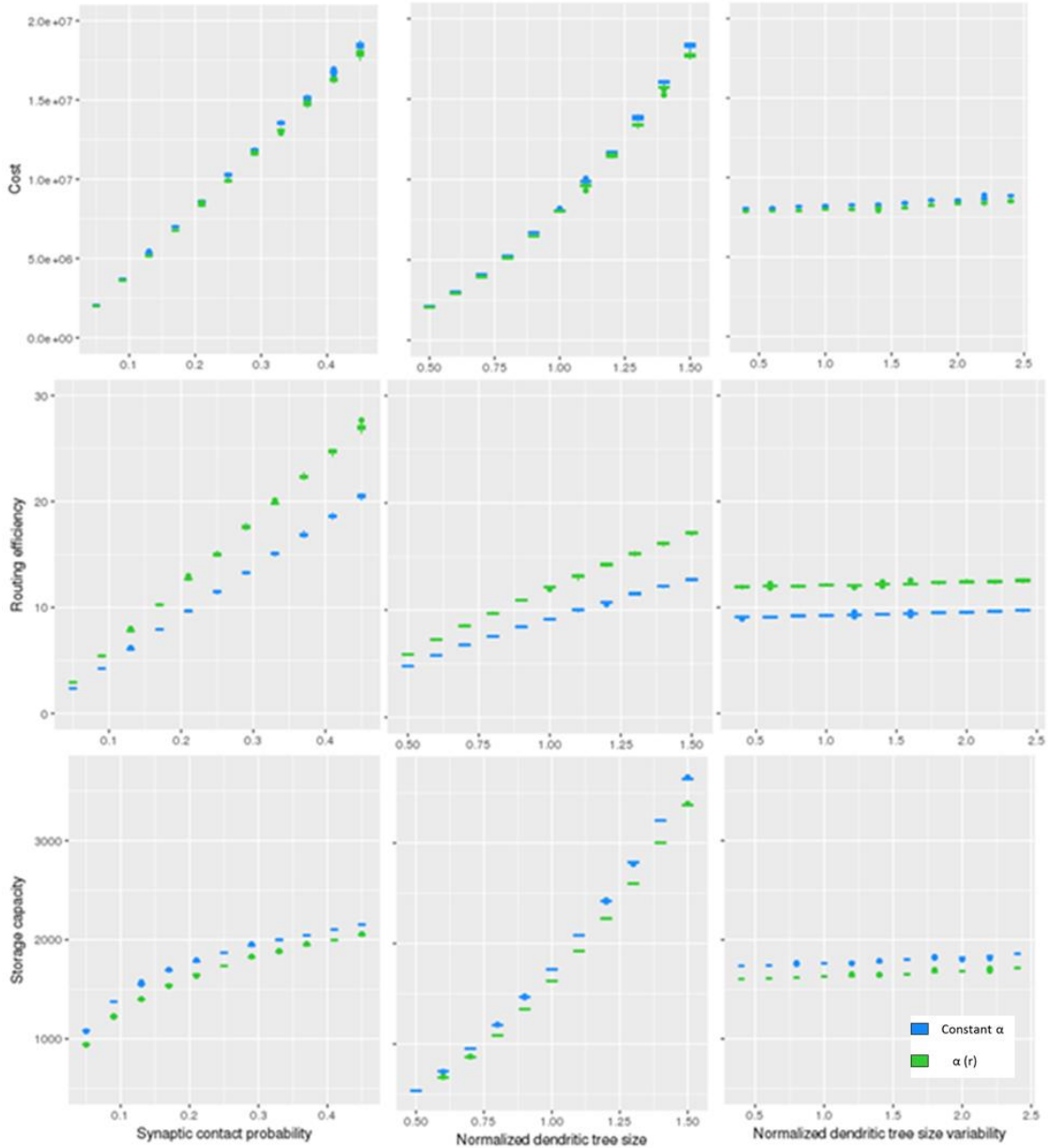


Figure 18: Implications of the morphospace exploration on the computational capacities of the cortical layer II/III local network model. Box plots for routing efficiency (1st row), storage capacity (2nd row) and cost (3rd row) in the 2D model upon the variation of the synaptic contact probability (1st column), normalized dendritic tree size (2nd column) and dendritic tree size variability (3rd column). In blue, instantiations of the network with a constant synaptic probability α , in green instantiations with synaptic contact probability dependent on the radius $\alpha(r)$ (Equation 4). Each boxplot represents 10 simulations with the same parameterization.

Both increases in dendritic tree size and synaptic contact probability (contributed by dendritic complexity and synaptic density), increase linearly the network routing efficiency (**Figure 18**, middle panel). However, the impact of increasing synaptic or dendritic densities is stronger

than that of increasing dendritic tree size. A similar effect was encountered when increasing dendritic tree size variability, which only slightly increases the network routing efficiency.

Our results also show that the storage capacity of the network increases superlinearly by increasing dendritic tree size and asymptotically with synaptic contact probability (**Figure 18**, lower panel). The superlinear increase with dendritic tree size suggests that the storage capacity is proportional to dendritic tree area (see **Annex II**). Again, increasing dendritic tree size variability only slightly increases storage capacity. Interestingly, I observed that storage capacity gets to a plateau for synaptic contact probability values of the magnitude reported in the mammalian cortex (0.3-0.4) (Markram, 2006, Wen & Chklovskii 2009). This might be counterintuitive, since it would suggest that if assuming that synaptic contact probability is constant along the dendrite, then storage capacity would be saturated with the architectural properties of the layer II/III dendritic trees in basal conditions. To assess whether a more realistic assumption for synaptic contact probability could imply changes on the capacities of the network, in a second round of simulations, I explored the same morphospace while introducing the radial dependence on the synaptic contact probability (see **Section 1.2.3** **Figure 18**; green symbols).

In fact, even considering its radial dependence, the mean synaptic contact probability gets to the same plateau as above (disregarding radial dependency), for synaptic contact probability values (0.3-0.4), I found that in this case the amount of connections is similar, only slightly smaller for high synaptic densities, than in the case of constant synaptic probability (α_c), as shown by the shape of the curve of the network cost, which is directly proportional to the number of connections (**Figure 18**, lower panel). Even though the number of connections is the same, the radius-dependent synaptic contact probability implies slightly decreased (~10%) storage capacity and a relevant increase (~30%) in routing efficiency (**Figure 18**, upper and middle panels). It should be noted that storage capacity starts to saturate for $\alpha(r)$ values for which the amount of synaptic contacts (cost) is still growing. This implies that the saturation is not produced because the trees are not making new contacts, but because those are coming from the same afferents. This defines a “sweet spot” around the wild-type values, where routing efficiency is maximally increased in comparison to the constant synaptic contact probability instantiations, while preserving the cost of wiring the network and having small amounts of redundant contacts.

Finally, when the dendritic tree size is increased, the higher amounts of contacts (cost) introduced by the radial dependency also grows superlinearly, and the increasing dendritic tree size variability again produced a slight linear increase in both cost, storage capacity and routing efficiency.

To test if the explored morphospace could also be constraining topological properties such as deviations from randomness, promoting higher clustering in the network and a small-world organization. I obtained mean degree distributions, small-worldness ratios and reciprocities. The analysis shows that log degree distributions do not deviate from exponential, implying that the networks have a random network topology (data not shown). Low synaptic contact probability values (~ 0.1) imply a decrease in reciprocity (**Figure 19** upper panel). When taking into account the radial dependency, reciprocity is slightly smaller ($\sim 5\%$) than for constant α . In both approximations it saturates for α above ~ 0.15 , indicating that each neuron in the network is connected with all the afferent axons crossing their spanning area. Bigger dendritic trees imply a sublinear increase in reciprocity, while increased dendritic tree size variability implies a linear decrease in reciprocity.

Regarding clustering (**Figure 19** middle panel), its behaviour has some similarities with reciprocity. Its increase upon higher synaptic contact probability is similarly saturating for $\alpha \sim 0.15$, even though in this case, its value is the same for both constant and radius-dependent α . When taking into account the radial dependency, the decrease in clustering for small α is more relevant. With increasing dendritic tree size, clustering increases asymptotically, with similar values for α and $\alpha(r)$. However, for increasing dendritic tree size variability, shows a slight linear increase, in contraposition to the trend shown by reciprocity. This indicates that with increased dendritic tree size variability some neurons in the network are reaching other neurons that were further apart from them in the graph, thus increasing its clustering, but that the amount of reciprocal connections is reduced due to the fact that also there are more small neurons unable to reach the axons of other neurons they are projecting to.

Finally, the small-worldness (**Figure 19** lower panel) is shown to be reduced asymptotically with increasing synaptic contact probability. Interestingly, in all the instantiations, when introducing the radial dependency, the small-worldness ratio of the network increases slightly ($\sim 5\%$). This means that even though having a similar number of contacts (as mentioned

above), the radial dependency slightly favours a small-world configuration. With increased dendritic tree size the small-worldness ratio decreases asymptotically indicating that the network is more densely and homogeneously connected, as shown by the increase in reciprocity and clustering. Dendritic tree size variability in this case does not affect the small-worldness ratio.

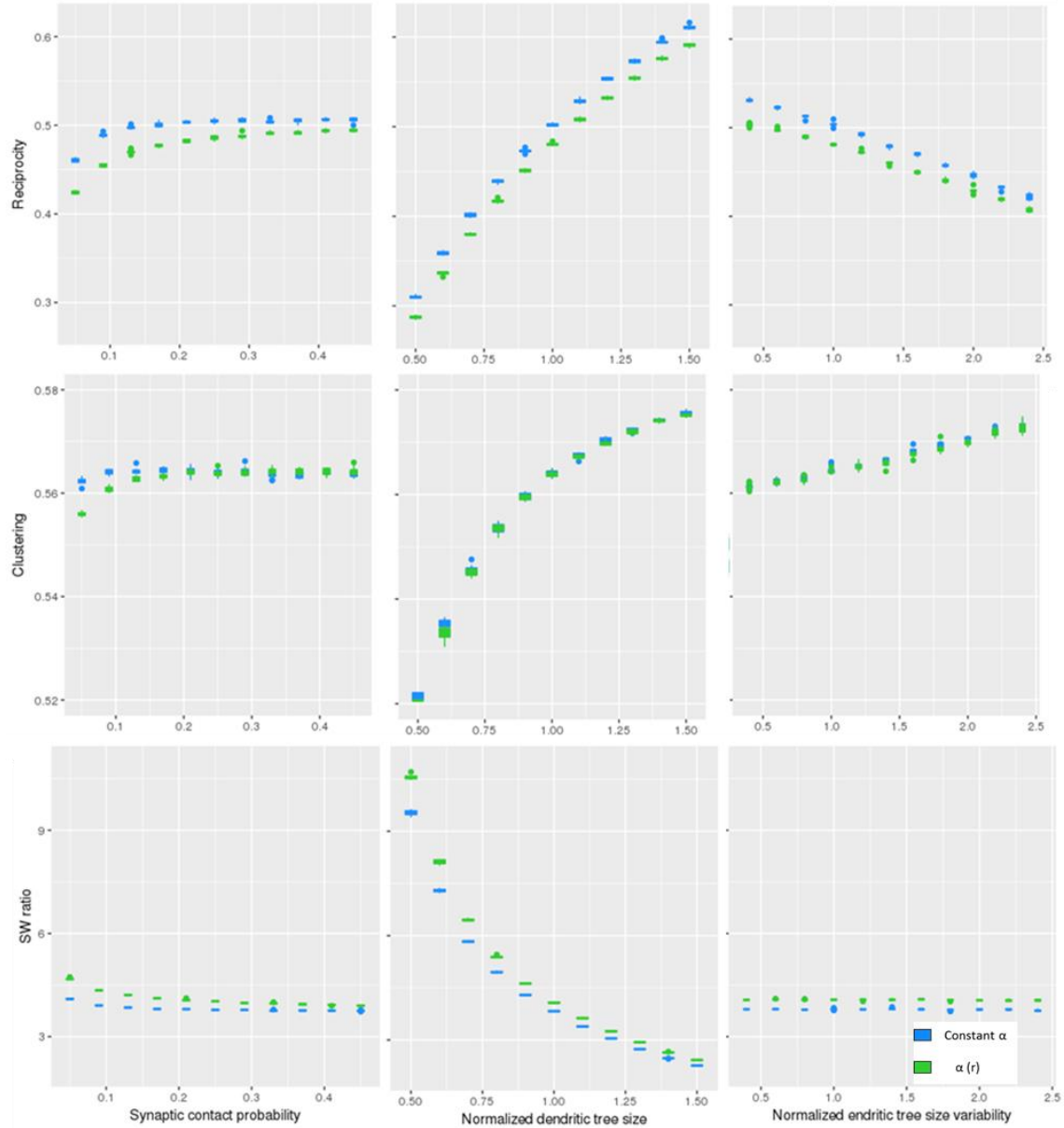


Figure 19: Implications of the morphospace exploration on topological properties of the cortical layer II/III local network model. Box plots for clustering (1st row), small-worldness ratio (2nd row) and reciprocity (3rd row) in the 2D model upon the variation of the synaptic contact probability (1st column), normalized dendritic tree size (2nd column) and dendritic tree size variability (3rd column). In blue, instantiations of the network with a constant synaptic probability α , in green instantiations with synaptic contact probability dependent on the radius $\alpha(r)$ (Equation 4). Each box plot represents 10 simulations with the same parameterization.

Dendritic abnormalities of mutant mouse models lead to reduced computational capacities

Our computational model allows to directly incorporate the neuromorphological metrics obtained previously in our laboratory, allowing us to also incorporate in the analysis a mouse model overexpressing *DYRK1A*, the TgDyrk1A published neuromorphological data (de Lagran et al., 2012) along with the Ts65Dn and Dyrk1A+/- . This provided the opportunity to explore subtle gene dosage effects and the influence of slightly different genetic background on dendritic arborization. To do so, I used the published Sholl and spine density quantifications of our models but since I had no access to the cell density, axonal length and axon tortuosity, I used published control values. For this reason, in our instantiation of mutant networks I focus on dendritic architecture and do not assess the putative contributions of these other morphological properties on the network connectivity.

The published Sholl analysis data for all the models and their wild-type counterparts are listed in **Table 5** and **Table 6**. Those parameters provide a description of the dendritic complexity and synaptic densities in all the biological conditions that I aim to assess in our simulations.

Table 5: Sholl analysis average values for Ts65Dn, Dyrk1A+/- cortical layer II/III basal trees and their wild-type counterparts. Mean numbers of dendritic branches intersecting radii at increasing 25 μ m steps of distance to the soma for the Ts65Dn and Dyrk1A+/- DS mouse models and their respective controls. The last row indicates the references from which those values were obtained.

	Ctrl-Ts65Dn	Ts65Dn	Ctrl-Ts65Dn-EE	Ts65Dn-EE	Ctrl-TgDyrk1A	TgDyrk1A	Ctrl-Dyrk1A+/-	Dyrk1A+/-
Distance from soma (μ m)	Number of dendrites (Sholl analysis)							
25	12	16	13	16	26	19	17	17
50	22	23	25	23	39	25	26	22
75	24	16	27	13	33	22	27	18
100	21	7	22	5	22	14	22	10
125	15	2	13	2	9	5	13	4
150	7	0	5	0	2	1	5	1
175	3	0	1	0	0	0	2	0
200	0	0	0	0	0	0	1	0
Reference	Dierssen et al. 2003				Martinez de Lagran et al. 2012		Benavides-Piccione et al. 2005	

Table 6: Average synaptic densities along the radius of Ts65Dn, Dyrk1A+/- cortical layer II/III basal trees and their wild-type counterparts. Mean numbers of spines in 10 μ m segments (see **Section 1.2.1**) in function of the distance to the soma for the Ts65Dn and Dyrk1A+/- DS mouse models and their respective controls. The last row indicates the references from which those values were obtained.

	Ctrl-Ts65Dn	Ts65Dn	Ctrl-Ts65Dn-EE	Ts65Dn-EE	Ctrl-TgDyrk1A	TgDyrk1A	Ctrl-Dyrk1A+/-	Dyrk1A+/-
Distance from soma (μ m)	Number of spines							
10	0	0	0	0	0	1	3	1
20	1	7	6	6	5	5	9	6
30	5	15	14	14	12	10	13	11
40	9	17	20	17	16	14	15	12
50	12	19	25	20	17	15	15	12
60	15	19	25	20	18	15	17	11.5
70	15	18	24	20	19	16	16	11
80	17	19	24	19	19	15	15	12
90	16	17	22	19	15	13	15	11.5
100	16	15	23	17	-	-	14.5	11
110	15	15	21	17	-	-	14	11
120	15	13	21	16	-	-	13.5	10.5
130	14	18	21	17	-	-	13	9
140	15	-	19	12	-	-	13	11
150	14	-	18	12	-	-	11	12
160	14	-	17	-	-	-	9	10
170	13	-	20	-	-	-	14	-
180	14	-	19	-	-	-	13	-
190	13	-	10	-	-	-	13	-
200	12	-	9	-	-	-	15	-
210	13	-	-	-	-	-	-	-
220	14	-	-	-	-	-	-	-
230	14	-	-	-	-	-	-	-
Reference	Dierssen et al. 2003				Martinez de Lagran et al. 2012		Benavides-Piccione et al. 2005	

Even though the experimental conditions and procedures were very similar in the three published experiments, the cross comparison among experimental controls showed variations in the amount and radial distributions of dendrites and spines (**Figure 20 a**), but to ensure a meaningful comparison between experimental conditions, and even though these differences may be biologically relevant and possibly represent genetic background-dependent differences, I curated the data as follows: all the dendritic and spine density distributions were normalized to their respective control values for each single experiment and, in order to compare experimental conditions, I scaled the normalized distributions to a common control curve obtained from the literature data of layer II/III basal trees in M2 for B6EiC3Sn wild-type mice (**Figure 20 b** and **Table 5** and **Table 6**).

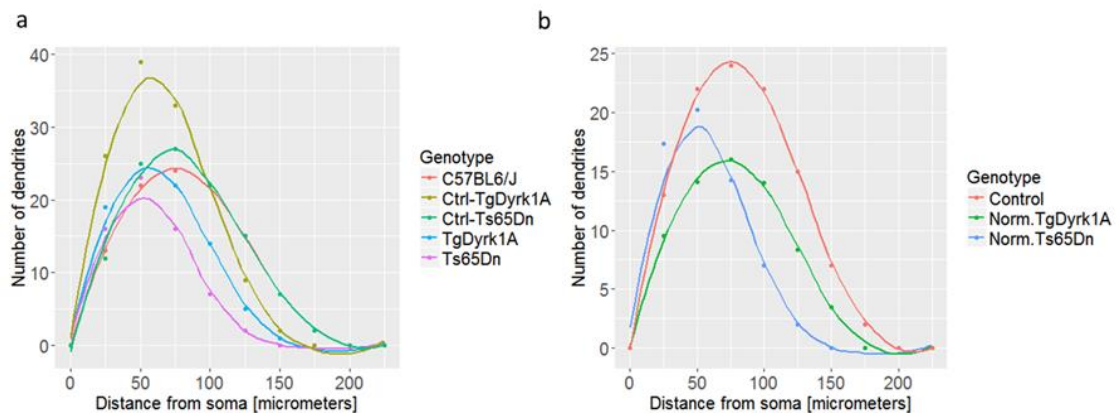


Figure 20: Normalization of dendritic radial distributions to the C57BL6/J strain wild-type data. (a) Distributions of dendrite numbers in function of the distance from the soma obtained from experimental data of different experiments. Each colored set of points shows the mean values obtained in the experiments, each line is a polynomial fit to those data points: in red, the common control used in our 2D computational model (C57BL6/J strain); in brown, the TgDyrk1A control; in green, the Ts65Dn control; in blue, the TgDyrk1A DS mouse model; and in purple, the Ts65Dn mouse model. Mean values obtained from the literature specified in the main text, characterizing basal dendritic trees of M2 in the layer II/III of the cortex. (b) Distributions of dendrite numbers along the radius of the tree for the Ts65Dn and TgDyrk1A DS mouse models normalized to a common control (C57BL6/J strain).

I obtained analytic expressions for dendritic and spine density distributions by performing polynomial regressions on the normalized distributions. Fitting was done using the lm function in R as described in **Section 1.2.2**. Normalized experimental data and polynomial regressions are shown in **Figure 21**. The obtained polynomials were directly introduced in the model in order to compute the synaptic contact probability in function of the distance from the soma as explained in **Section 1.2.2**.

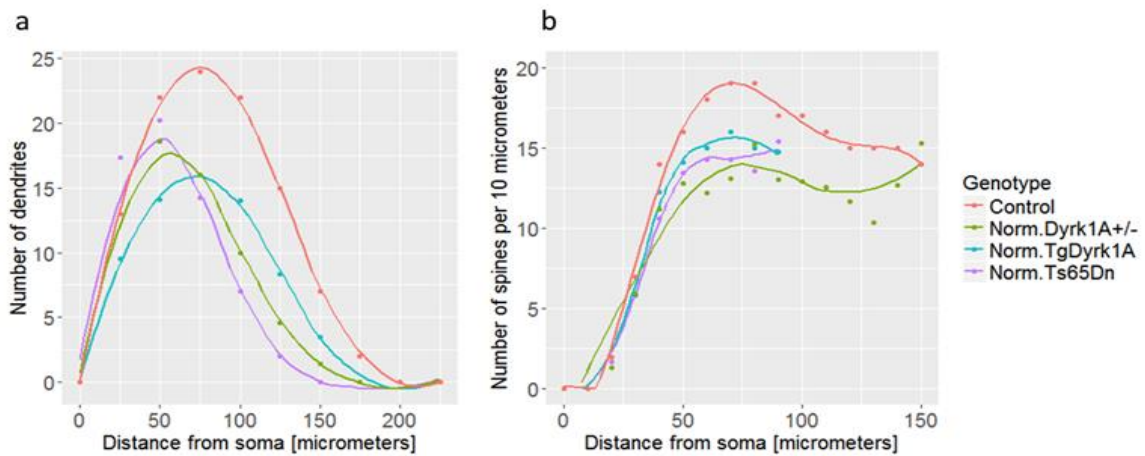


Figure 21: Dendritic and spine radial distributions normalized to wild-type C57BL6/J mice. Distributions of dendrite (a) and spine (b) numbers along the radius of the tree for the Dyrk1A $^{+/-}$ (green), TgDyrk1A (blue) and Ts65Dn (purple) DS mouse models normalized to a common control (C57BL6/J strain: in red).

I then introduced experimental dendritic and synaptic spine distributions from the DS mouse models (Ts65Dn, TgDyrk1A and Dyrk1A $^{+/-}$) and generated 10 networks using the normalized distributions. These normalized distributions were used to assess the impact of the specific alterations found in the different DS mouse models on the topology and computational capacities of the modeled network.

I performed a one-way ANOVA test to identify significant differences among all the groups, and two-way unpaired t-tests with post-hoc Bonferroni corrections to identify pairwise significant differences. The three studied mouse models show reduced routing efficiency ($F_{(5,54)} = 7681, p = 1.07 \times 10^{-75}$) and storage capacity ($F_{(5,54)} = 8202, p = 1.83 \times 10^{-76}$). Storage capacity is strongly reduced, in Ts65Dn (-54%; Bonferroni-corrected $p = 2.69 \times 10^{-75}$) and Dyrk1A $^{+/-}$ (-42%; Bonferroni-corrected $p = 6.58 \times 10^{-74}$) networks, and to a lower extent in TgDyrk1A (-26%; Bonferroni-corrected $p = 4.83 \times 10^{-70}$) as compared to the C57BL/6J control. Routing efficiency is also reduced in Ts65Dn (-61%; Bonferroni-corrected $p = 1.27 \times 10^{-106}$), TgDyrk1A (-49%; Bonferroni-corrected $p = 2.94 \times 10^{-89}$) and Dyrk1A $^{+/-}$ (-57%; Bonferroni-corrected $p = 2.26 \times 10^{-100}$) networks in comparison to the wild-type. From the position of the different models in the efficiency space, I can infer that while the three models deviate from the computational capacities of the wild-type, the one with worse implications in our simulations is the Ts65Dn that shows 39% routing efficiency and 46% storage capacity of the control group. The comparison between the Ts65Dn and the TgDyrk1A is worth

mentioning; while they show similar levels of routing efficiency (39% and 51% of the control group respectively), the Ts65Dn shows much less storage capacity (46%) than the TgDyrk1A (74%). This difference is caused mainly by the reduced tree size of the trisomic mice. At the same time, the fact that Dyrk1A^{+/−} mice have slightly bigger dendritic tree size than Ts65Dn mice, implies slightly higher storage capacity for Dyrk1A^{+/−} networks versus Ts65Dn (+12%), having stronger impact than the reduced synaptic contact probability found in the Dyrk1A^{+/−} neurons (**Figure 22 b**).

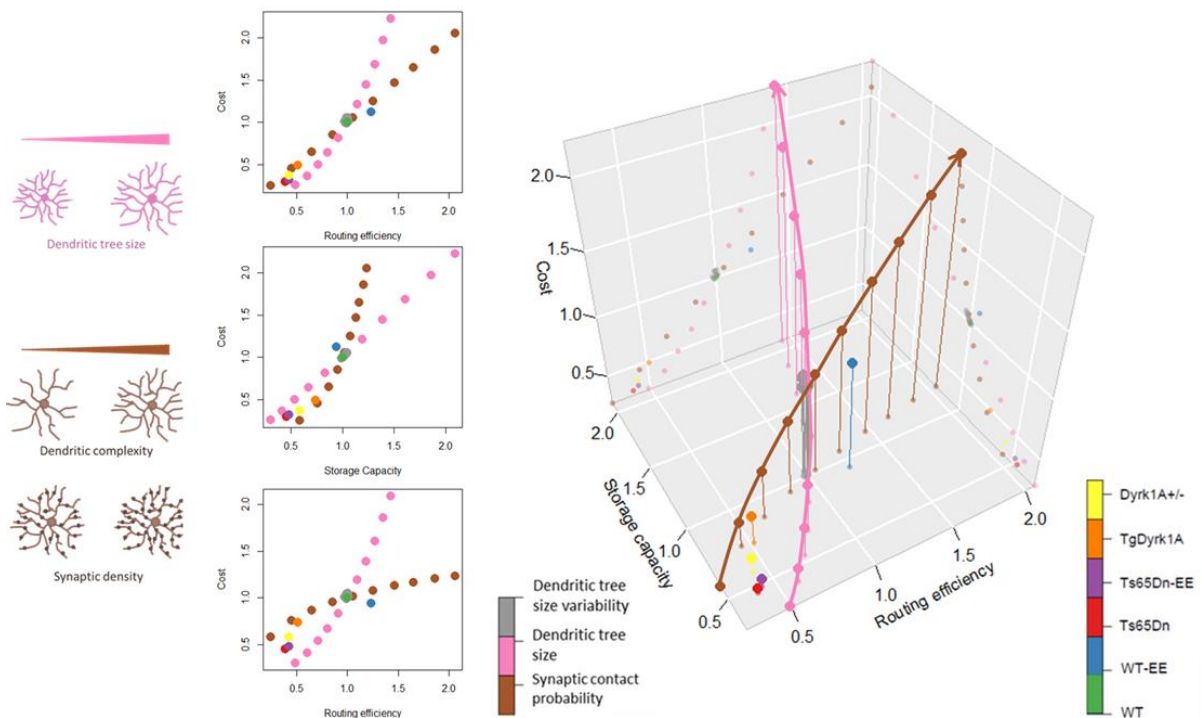


Figure 22: Overview of the morphospace exploration in the cortical layer II/III local network model. 3D representation of the data points for routing efficiency, storage capacity and cost normalized to the wild-type value, for (1) the morphospace exploration of our computational 2D model shown in Figure 13 and Figure 14, and (2) the different mouse models instantiated. The pink points were obtained by scaling the dendritic tree size; in brown, the synaptic contact probability; in grey, the dendritic tree size variability; in green, the C57BL/6J wild-type control; in blue the environmentally enriched control; in red the Ts65Dn mouse model, in purple the environmentally enriched Ts65Dn; in orange the TgDyrk1A mouse model and in yellow the heterozygous Dyrk1A ^{+/−} mouse model. The left panel shows 2D projections of the morphospace: routing efficiency vs cost (top), storage capacity vs cost (middle) and routing efficiency vs storage capacity (bottom).

1.3.3. Dendritic rewiring effects on network computational capacities

I investigated how neuromorphological variations detected upon treatment with environmental enrichment, which has shown beneficial effects in Ts65Dn and wild-type mice (M Dierssen et al. 2003; Martínez-Cué et al. 2002), affect the routing efficiency and storage capacity of our model cortical layer II/III networks.

As expected by the mild effect produced by environmental enrichment at the morphological level, the Ts65Dn mice only show a modest (yet significant) increase in storage capacity versus the non-enriched situation (9%; Bonferroni-corrected $p = 4.34 \times 10^{-13}$). A similar change is seen in routing efficiency (5%; Bonferroni-corrected $p = 3.08 \times 10^{-13}$).

In the case of wild-type mice reared in environmental enrichment conditions, the routing efficiency shows a relevant increase by a 24% with respect to non-enriched conditions (Bonferroni-corrected $p = 3.33 \times 10^{-53}$) while storage capacity is mildly reduced by a 6%. From this exploration, I can hypothesize how putative treatments could imply a rescue of the computational capacities in the network. While an increase in synaptic density reaches storage capacity saturation at a high cost, an increase in dendritic tree size (even subtle) would efficiently rescue the studied capacities and provide a stronger therapeutical effect.

1.3.4. Pareto optimality for computational capacities

By focusing on the two dimensions of the efficiency space given by the cost and the routing efficiency, I can link conceptually our single-neuron wiring optimality study with the exploration made at the network level, as described in the Methods section (**Section 1.2**). The fact that for small trees the dendritic tree size exploration defines a Pareto front for routing efficiency, and the synaptic contact probability exploration defines another Pareto front for storage capacity, indicates that at the network level there is a Pareto optimum given by single cell morphological properties. The networks parameterized with the TgDyrk1A mouse model data, with a distance to the Pareto front of $d_P=0.12$, are the less optimal for routing efficiency given their cost (even though they have higher routing efficiency than the parameterizations of the other DS mouse models). The environmentally enriched Ts65Dn is the closest to the Pareto front, $d_P=0.08$, indicating that it is the most optimal configuration

for routing efficiency and that the environmental enrichment (while having a small impact) favours a rewiring of the network towards a configuration more suitable for processing information. Both Ts65Dn ($d_p=0.09$) and Dyrk1A +/- ($d_p=0.10$) show a very similar situation, being slightly less optimal than the environmentally enriched Ts65Dn. The environmentally enriched wild-type networks show higher routing efficiency than networks generated with the synaptic contact probability exploration, indicating high optimality for processing information ($d_p=-0.05$).

Regarding storage capacity, the location of the various mouse models is the opposite. Networks instantiated based on the morphological properties of TgDyrk1A neurons are the closest to an optimal configuration for storage capacity ($d_p=0.03$). They are followed by Dyrk1A +/- parameterized networks ($d_p=0.07$), and by both environmentally enriched Ts65Dn ($d_p=0.10$) and non-enriched Ts65Dn ($d_p=0.10$) parameterized networks. Again the environmental enrichment implies a slight improvement versus the non-enriched condition in the Ts65Dn case. In the environmentally enriched wild-type networks the optimality for storage capacity is lost ($d_p=0.11$), indicating that the improvement in routing efficiency implies a functional imbalance. It is important to note that given that the only source of variability in the model is given by the introduced dendritic tree size variability, the comparison between the efficiency space metrics are highly precise, given that those are at least three orders of magnitude lower than the obtained mean values, I did not specify the standard deviations of the obtained distances.

In comparison with the results from the Pareto optimality exploration for single neurons, it can be seen that both the Ts65Dn and Dyrk1A +/- models are suboptimal for routing efficiency both at the single-neuron and at the network level. However, while single-neuron routing efficiency optimality seems to be higher for Dyrk1A +/- rather than Ts65Dn neurons, at the network level Ts65Dn parameterized networks show a slightly closer position to the Pareto front given by the dendritic tree size exploration. In the case of storage capacity, both the single-neuron and network level optimality exploration indicate a very similar situation for both mouse models, being only the case of the Dyrk1A +/- model a bit closer to optimality at the network level. Thus, while overall the suboptimal wiring seems to permeate from one level to the other, a detailed connection between both levels of description regarding routing efficiency might not be straightforward.

1.4. Discussion and conclusions

Single-neuron wiring optimality

Our morphological analysis of Ts65Dn, Dyrk1A+/- mice and their respective controls has confirmed previous observations. The original studies (Benavides-Piccione et al., 2005; Dierssen et al., 2003) already pointed in the direction of a similar phenotype for both models. Here I confirmed that both Ts65Dn and Dyrk1A+/- neurons show reduced dendritic length and complexity, and higher amount of branches per normalized dendritic length. A substantial number of studies have associated morphological differences in ID mouse models with cognitive impairment measured by performance indices in cognitive tasks (Escorihuela, Fernández-Teruel, et al., 1995; Sago et al., 1998). Lesion and activation/inactivation studies in the M2 cortex have been shown to affect motor function (Manita et al., 2015). Ts65Dn mice show hyperactivity in various behavioral tests: open field lighting or open arms of the raised cross-shaped maze; being also hyperactive when surrounded with plenty of new stimuli, as with environmental enrichment (Coussons-Read & Crnic, 1996). Conversely, Dyrk1A +/- mice show marked hypo-activity (Martínez de Lagrán et al., 2007). In fact Dyrk1A+/- neurons have more marked alterations than Ts65Dn in the case of the mean branch order and spanning area being significantly smaller in heterozygous mice. Thus, our morphological analysis does not explain the opposite behavioral phenotypes

Interestingly, 129Ola genetic background mice show motor impairments in their flexibility and motor coordination (Royle, Collins, Rupniak, Barnes, & Anderson, 1999). Our analysis suggests that those could be driven by the strain differences between B6EiC3Sn and C57BL/6J-129Ola wild-type mice. Among those differences, the reduced number of branch points and straightness and higher dendritic area and mean branching angle versus the B6EiC3Sn wild-type. In fact, those are relevant features for signal integration that could be involved in the mild behavioral impairment observed in this strain.

Until now these structural differences have been assumed to determine functional changes in these mutant strains. Here I decided to analyze if those differences of dendritic branching patterns still fit to the optimal dendritic wiring laws derived by Cuntz et al. (Cuntz et al. 2012) and Wen & Chklovskii (Wen & Chklovskii 2009). The scaling between the total dendritic length and the number of branches shows that cortical layer II/III basal trees are sub-optimally wired in the Ts65Dn and Dyrk1A+/- mouse models and in C57BL/6J-129Ola

wild-type mice. Alternatively, the scaling between the total dendritic length and the dendritic tree radius shows that Dyrk1A+/- neurons and their controls could follow optimal scaling while both Ts65Dn and their controls deviate from an optimal scaling. However, the latter measurements show strong variability, indicating an important limitation of this approach to assess optimality. The fact that the radius of the reconstructed trees is very similar within the analyzed groups, implies that the scaling law fit. Thus, even though I consider that the analyses are informative (especially in the case of the total dendritic length versus number of branch points scaling), any conclusions drawn from them must be taken cautiously.

The alternative Pareto optimality assessment I propose could help relaxing the need of bigger samples, given that the definition of Pareto fronts is performed *in-silico* and the optimality is quantified as a distance in the morphospace. This implies that optimality can be quantified for single cells, and that a careful definition of the morphospace variables could increase the statistical power of the analysis.

Moreover, both scaling laws have implicit variables accounting for the maximization of the connectivity repertoire. While Cuntz et al. (Cuntz et al. 2012) explored how variations in the balancing factor would affect the scaling law power, Wen & Chklovskii (Wen & Chklovskii 2009) provided an approximation for cortical layer II/III basal dendritic trees and discussed it through multiple potential synapse avoidance. The fact that Cuntz et al. saw that the variations induced in the scaling law power by changes in the balancing factor were small could explain the lower variability observed when fitting it and provides robustness to this analysis. However, in both cases there is a free parameter that can vary among neuronal cell types depending on their functional specialization. Those variations would emerge naturally as a consequence of the morphospace exploration I propose. As an example, the architectural suboptimality of both Ts65Dn and Dyrk1A+/- neurons appears to affect both routing efficiency and storage capacity, while the mixed background C57BL/6J-129Ola wild-type neurons show suboptimal architecture mostly for routing efficiency (as compared to the B6EiC3Sn wild-types) and B6EiC3Sn wild-type suboptimality exclusively for storage capacity.

Additionally, overall the analysis presented shows that the architecture of layer II/III basal trees favors routing efficiency rather than storage capacity for a given wiring cost. It can be expected that other cell types such as Purkinje cells in the cerebellum, or CA3 neurons in the hippocampus will have architectures favoring storage capacity rather than routing efficiency.

However, testing the suitability of this framework for identifying such functional specializations remains to be done.

While the Pareto optimality framework used provides advantages, its most important limitation is the fact that the generation of the Pareto fronts is not analytical. While the explorations performed here allowed me to assess the relevance of morphological changes in biologically meaningful ranges and compare the experimental groups I analyzed, there is the possibility that the Pareto front of the system is not defined by the explorations I performed. Thus, other strategies such as the exploration of the morphospace using genetic algorithms, as performed by Avena-Koenigsberger et al. (Avena-Koenigsberger et al., 2014), could provide more reliable estimates of “absolute” Pareto fronts. Additionally, while the definition of routing efficiency used was defined by taking care of avoiding any dependence with the dendritic tree size (neither the straightness, the branch length coefficient of variation nor the normalized synaptic density should depend) a more detailed definition could be obtained by adjusting the weights of each contribution. Similarly, the storage capacity at the single cell level was obtained as directly proportional to the dendritic tree area, disregarding dendritic complexity, a refined estimation of storage capacity, thus, remains necessary.

Based on our single-neuron morphology and wiring optimality studies, I could speculate that the Ts65Dn and TgDyrk1A mouse models could have altered signal integration efficiency at the single cell level and over-represented connections from the same afferent neurons (optimal wiring, **Figure 17**). This hypothesis could be tested functionally by checking whether neurons deviating from optimality have increased synaptic response to groups of neurons innervating the region (e.g. thalamic or cortical projections from other sensory areas) (Grillner, 2015). This scenario could ultimately lead to an over-activation of M2 contributing to the hyperactive phenotype of those mouse models. In fact, unpublished data from our laboratory showed increased excitability in the motor cortex of DS patients (Principe et al, unpublished) using functional studies analysing motor evoked potentials upon transcranial magnetic stimulation.

In contrast, the reduced straightness found in the C57BL/6J-129Ola strain, suggests that afferent synaptic signals could have delayed integration, possibly altering their response and introducing alterations in the activity dynamics of the region upon activation. Nevertheless, this explanation does not stand for all the behavioral phenotypes. While the dendritic

architecture of the Dyrk1A^{+/−} neurons is very similar to the Ts65Dn phenotype, behaviorally Dyrk1A^{+/−} show marked hypo-activity (in contrast with the hyperactivity of Ts65Dn mice). This could be explained by other aspects accompanying *Dyrk1A* under-expression. Previous work in our lab (de Lagran et al., 2007), showed decreased striatal dopamine levels and a reduced number of dopaminergic neurons in the substantia nigra pars compacta, that certainly contribute to the final motor behavior phenotype in this strain. Thus, understanding the hyper/hypo-activity phenotype also requires disentangling the morphological and functional contributions at the higher-order network level. Even so, instantiating local networks in a systematic way can provide interesting information about the emergent functional phenotypes.

As the main limitation of this analysis, it should be noted that the numbers of neurons used in this study are very small, and thus in my opinion should not be generalized to the whole population. Even so, the important morphological differences among wild-type and mutant neurons, imply statistically significant differences. However, increasing the number of biological replicates, reproducing the study and complementing this knowledge with other models of intellectual disability in cortical layer II/III remains a necessary task. Additionally, the design of studies combining behavioral information of single animals and their morphological characterization, even though not allowing a full prediction as discussed above, would provide interesting correlations between the architectural traits and behavioral differences.

In conclusion, single-cell reconstructions have been extensively used to understand the relationship between dendritic morphology and the computations performed by neurons. However, the impact of neuronal geometry on the network properties is much less understood even though a wealth of knowledge about the physiology and morphology of some of these neurons is established. I here took a computational approach that can serve as a “hypothesis tester”. For example, I can ask if the morphologies of the optimized neurons resemble the mutant neurons, or it can also be used in an exploratory manner, in which case the model neurons are used to identify the morphological parameters of theoretical interest. In this way, my approach can serve as a “hypothesis pump”.

Network exploration

Our first goal was to disentangle the differential contributions of various neuromorphological features to the network computational capacities. Our *in-silico* exploration suggests that the density of synaptic contacts has less impact than dendritic tree size on the connectivity of the network and its computational capacities. Routing efficiency grows linearly with synaptic contact probability and superlinearly with dendritic tree size. Storage capacity grows asymptotically with synaptic contact probability and, with a smaller slope, with dendritic tree size. Of note are the facts that taking into account the radial dependency in synaptic contact probability does not change the number of contacts made by the neurons, and increases the small-worldness ratio of the network. Thus, contributing to the deviation from purely random topologies in neuronal networks (Vegué et al., 2017) and showing that taking the radial dependency into account in simple neuronal models can be contributing significantly to the network properties (concept not underlined in existing approximations to my knowledge).

The cortical layer II/III network instantiation parameterized with experimental data from our DS mutant models shows slightly differential affectations at the network level, given by small differences in their dendritic and spine radial distributions (see **Figure 21**). I first discuss the implications of those differences for wiring optimality, and second their connection with behavioral studies.

The analysis of the network routing efficiency seems to accompany the optimal wiring proposed by Cuntz et al. (derived from Cajal's laws for cytoplasm and conduction time; Cuntz et al. 2012), showing that morphologically altered neurons lead to suboptimal network connectivity. The mutant networks have excessive material in regards of the routing efficiency reached, while wild-type optimal morphologies lead to network topologies that are Pareto-optimal for routing and material efficiency. Alternatively, the morphospace exploration and Pareto-optimality analysis at the single neuron level shows that layer II/III basal dendritic trees have optimal architecture for signal integration and that more branching and lower straightness would favor storage capacity at the same cost. Those differences are explained by the fact that the definitions of cost and routing efficiency do not account exactly for the same properties at both levels. While I chose to use the amount of contacts as the cost at the network level, in the case of single neurons it was reasonable to choose the amount

of dendritic material. Our exploration shows that to some extent wiring optimality at the single neuron level permeates to the network level, a revised selection of the morphospace metrics at both levels (for example defining the network cost including a contribution given by dendritic material) can provide further insight on the relationship between both levels of description.

While our results appear to be consistent regarding the single-neuron and network optimality, associating them with the behavioral perspective does not clarify the doubts raised by the comparison between hyper/hypo-activity behavioural data and the wiring optimality study. However, they suggest testing whether the network stimuli processing efficiency (and its dynamics) could be impaired differentially in Ts65Dn and Dyrk1A+/- mice, possibly linking the single-neuron description with the network dynamics through altered intercolumnar communication.

By taking into account that the M2 local connectivity participates into a larger network involved in the learning of motor repertoire (Barthas & Kwan, 2017), the impairment in storage capacity for the DS mouse models can be discussed in relation to executive function tasks. In this case, the literature available only consists in a single study assessing the Puzzle Box task performance in TgDyrk1A mouse model. Their impairment suggests that the reduction in storage capacity seen in our model can be associated with the behavior. To test whether the relationship between architectural features and storage capacity follows the relationship I assumed, behavioral experiments comparing the executive function and/or motor repertoire acquisition capabilities of the different DS mouse models are needed.

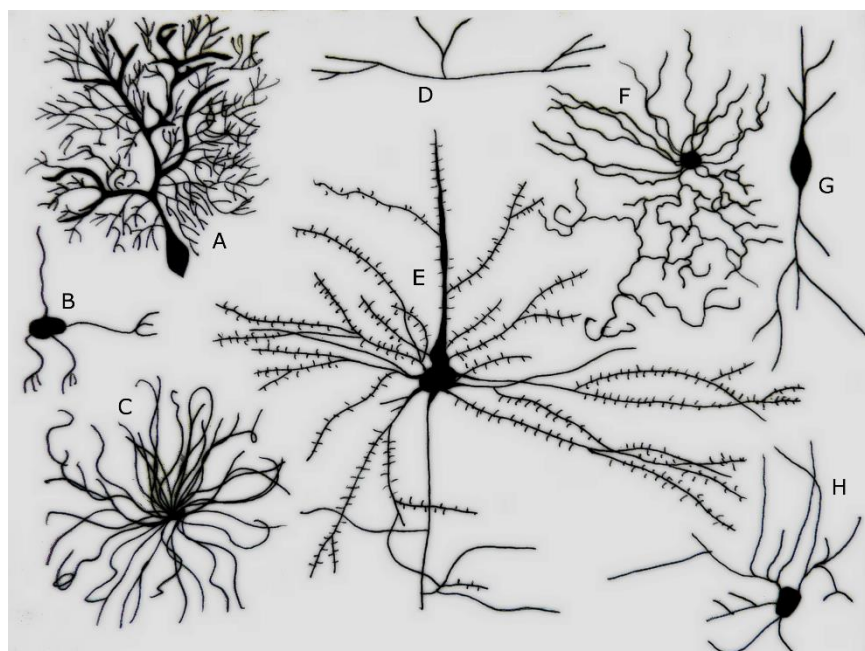
The parameterization of data obtained from mice undergoing pro-cognitive treatment tackling dendritic rewiring can also contribute to the comparative analysis between neuromorphological conditions and cognitive capacities. In the case of environmental enrichment, an increase in spine densities in both wild-type and Ts65Dn mice has been shown (M Dierssen et al., 2003). In the case of wild-type mice the treatment also improved cognitive performance in the Puzzle Box task (O'Connor, Burton, Leamey, & Sawatari, 2014). The subtle increase in storage capacity (9%) and routing efficiency (5%) for Ts65Dn in our computational model should undergo behavioral testing. The increase in routing efficiency (24%) and slightly increased routing efficiency (6%) obtained with the

environmentally-enriched wild-type parameterization accompanies the improved Puzzle Box performance (20 to >50% reduction in the time taken to solve the task) of C57BL/6J wild-type mice. The increase in routing efficiency originates in the increased spine density of environmentally-enriched wild-type mice versus their controls (M Dierssen et al., 2003) and is magnified by the high sensitivity of routing efficiency towards synaptic contact probability. While experimental data in the hippocampus shows a clear increase in dendritic tree size (Beauquis, Roig, De Nicola, & Saravia, 2010), additional experiments in cortical layer II/III to corroborate spine densities observed in the dataset I used is lacking. To assess whether the definition of storage capacity used is meaningful, a better estimate could be obtained by training neuronal networks with the instantiated topologies to store combinations of connectivity patterns and assessing their reliability in function of the morphospace exploration I have done (Poirazi & Mel, 2001).

Additionally, an important limitation of our model is the assumption of homogeneity, which forces a strong constraint hindering the modular and hierarchical organization of neuronal circuits (Bassett & Bullmore, 2006). Similarly, I have not explored other questions of interest, such as the subpopulation of abnormal neurons needed to impair significantly the network computational capacities, how neuronal densities could be affecting the obtained results, how detailed branching patterns could be modulating the network connectivity or how dynamical activity patterns emerging from different network topologies would differ. However, I consider it as a manageable test scenario for a conceptual framework that I aim to apply to whole circuits involved in specific cognitive functions (e.g. entorhinal cortex - hippocampal circuit and its involvement in spatial/single item recognition learning). In fact, the first steps needed in this direction are assessed in depth in Chapter II.

Altogether, I think that the work presented can be a useful founding piece for comparative micro-connectomics in the frame of intellectual disabilities.

2. CHAPTER II. IMPACT OF SINGLE-NEURON STRUCTURAL DIVERSITY IN HIPPOCAMPAL CA1 POPULATIONS



Different Types of Neurons. A. Purkinje cell B. Granule cell C. Motor neuron D. Tripolar neuron E. Pyramidal Cell F. Chandelier cell G. Spindle neuron H. Stellate cell (Credit: Ferris Jabr; based on reconstructions and drawings by Cajal).

"Unfortunately, nature seems unaware of our intellectual need for convenience and unity, and very often takes delight in complication and diversity."

Santiago Ramón y Cajal, in his 1906 Nobel lecture. The structure and connexions of neurons.

2.1. Introduction

The results presented in Chapter I, showed that relatively subtle morphological alterations in single cells are relevant for the network topology and that wiring suboptimality at the single-cell level permeates to the network level in DS mouse models. Such wiring suboptimality might be specific to the M2 cortex, or might be present throughout all the affected brain regions in DS. Thus, I decided to study a different brain region to probe the optimality concepts that, at the single cell level, have been proposed to apply to all cell types.

In fact, as detailed in the **General Introduction**, DS presents structural and functional abnormalities in various brain regions, and, as such, provides interesting opportunities to approach my question. I decided to focus on the hippocampal formation, which is known to have abnormal cellular architecture in DS that has been related to cognitive impairments in spatial and contextual memory formation and retrieval. In this region the architecture of the pyramids is quite different to that found in the neocortex. Even though each type of pyramidal neuron has basal and apical dendrites and an apical tuft, they can vary considerably between different layers, cortical regions and species. For example, the basal dendrites of layer II/III pyramidal neurons are smaller, simpler and have a lower spine density in the primary visual cortex than in higher visual cortical areas. Basal dendrites are especially large, complex and spiny in the prefrontal cortex. In the hippocampus, the apical dendrites of hippocampal CA3 pyramidal neurons branch closer to the soma than those of CA1 pyramidal neurons, which typically have a more distinctive main apical dendrite and tuft. This raises two interesting questions: do pyramidal neurons with subtle morphological differences change network topologies? If not, how is network optimality maintained at the same level?

The comparison of wiring optimality in brain regions such as the cortex and the hippocampus enable to understand better the impact of single neuron deviations at the network emergent topological properties. Besides, a systematic analysis of wiring optimality in circuits affecting different cognitive domains could help understanding which topological aspects are necessary for healthy brain function. Interestingly, architectural heterogeneity does not just appear throughout the mammal brain, but within subregions and neuronal layers. This has been largely overlooked in the literature, and required the development of an analysis and modeling framework able to account for local structural variations

The hippocampus as a model system

The hippocampus is part of the phylogenetically older areas of cortex termed the allocortex. These more primitive areas are located in the medial temporal lobes and are involved with olfaction and survival functions such as visceral and emotional reactions. In turn, the allocortex has two components: the paleocortex and archicortex. The paleocortex includes the piriform lobe, specialized for olfaction, and the entorhinal cortex. The archicortex consists of the hippocampus, which is a three-layered cortex.

The hippocampal formation has long been recognized as necessary for the integrity of memory in mammals and other vertebrates, and relatively limited disturbances of the hippocampal circuitry have been reported to produce serious memory impairment. The anatomical basis of this system is the so called trisynaptic circuit formed by the perforant path arising in the entorhinal cortex, which terminates onto the dendrites of the granule cells of the dentate gyrus. The axons of the dentate gyrus granule cells form the mossy fibers that make synaptic contact with the pyramidal cells of the CA3. The axons of CA3 pyramidal cells form the Schaffer's collaterals that make synaptic contact with the pyramids of CA1.

Despite involving only three layers of processing, the hippocampus has been shown to be fundamental for encoding declarative memory and spatial information (Marr et al., 1991). Sensory information is received in the dentate gyrus, that has been proposed to perform pattern separation (Hasselmo & Wyble, 1997; Marr et al., 1991; McNaughton & Morris, 1987; O'reilly & McClelland, 1994; Treves & Rolls, 1994). Axonal projections from the dentate gyrus innervate CA3 (Perforant Path), which has extensive recurrent connectivity and has been proposed to form associations between encoded memory patterns (Hasselmo, Schnell, & Barkai, 1995; Hasselmo & Wyble, 1997; Norman & O'reilly, 2003; Treves & Rolls, 1992, 1994). Finally, CA1 receives input from both CA3 (Schaffer collaterals, innervating the *stratum pyramidale* sublayer) and the entorhinal cortex (Perforant Path, innervating the *stratum lacunosum* sublayer), and has been suggested to behave as a comparator between the stored memories in CA3 and the sensory input from the entorhinal cortex (Gray, 1982; Hasselmo & Schnell, 1994; Hasselmo & Wyble, 1997).

Down syndrome presents hippocampal structural and functional abnormalities

Hippocampal pathology is likely to contribute to cognitive disability in DS, yet the neural network basis of this pathology and its contributions to different facets of cognitive impairment remain unclear. In DS mouse models, and specifically the Ts65Dn model, significant learning deficits in various behavioral tasks that are putatively hippocampal-dependent (Demas, Nelson, Krueger, & Yarowsky, 1998; Hunter, Bimonte, & Granholm, 2003; Stasko & Costa, 2004). Also, significantly lower numbers of neurons in the dentate gyrus of Ts65Dn mice compared to control animals have been reported (Insausti et al., 1998). The presence of these ‘hippocampal phenotypes’ in Ts65Dn mice has acquired renewed importance with the finding that, in persons with DS, hippocampal function may be disproportionately affected in the general context of their cognitive disabilities (Pennington, Moon, Edgin, Stedron, & Nadel, 2003). In fact a significant reduction in the number of neurons has been reported in the granule cell layer of the dentate gyrus in Ts65Dn. This may well lead to a concomitant decrease in the number of synaptic sites available in the dentate gyrus for receiving information through the perforant path; it may provide the morphologic basis of spatial memory impairment since fewer granule cells would decrease the total number of mossy fibers that could make synapses onto CA3 neurons. Furthermore, stereological studies have revealed a significant increase in the number of CA3 neurons in Ts65Dn mice. This result may be explained as an attempt to compensate for the loss of mossy fiber synaptic terminals by making available a larger postsynaptic territory.

Similarly, TgDyrk1A mice partly recapitulate the DS phenotype, showing impaired spatial (Altafaj et al., 2001) and single item recognition memory (De La Torre et al., 2014), alterations in adult neurogenesis in the dentate gyrus including reduced cell proliferation rate, abnormal dendritic architecture and reduced survival of newly born cells (Pons-Espinal, Martínez de Lagrán, & Dierssen, 2013), and shifts in both long-term potentiation and long-term depression (Ahn et al., 2006). Interestingly, it has also been reported that both cognitive and microstructural defects can be reversed with extrinsic factor treatment, such as environmental enrichment or administration of the drug epigallocatechin-3-gallate (EGCG) (Pons-Espinal, Martínez de Lagrán, & Dierssen, 2013).

Within-cell type variation in the brain

The brain atlases obtained by Paxinos et al. have been widely used in the study of both human, rat and mouse brains (Mai & Paxinos, 2011; Paxinos, 2014; Paxinos & Franklin, 2004). Paxinos extensively reviewed microanatomical studies characterizing the composition of the brain region subdivisions mainly defined by Ramón y Cajal (Ramón y Cajal, 1995) and Lorente de Nó (de Nó, 1934), including the spatial distribution of cell-types, dendritic trees and axonal projections. While original brain region subdivisions were aimed to the functional subdivision of neuronal circuits, in some cases studies performed during the 20th century already account for spatial inhomogeneities inside such subdivisions. As an example, in the context of the description of the hippocampal formation, Paxinos states: “The packing density and thickness of the granule cell layer varies somewhat along the septotemporal axis of the dentate gyrus (Gaarskjaer, 1978). The packing density of granule cells is higher septally than temporally. Because the packing density of CA3 pyramidal cells follows an inverse gradient, the net result is that at septal levels of the hippocampal formation, the ratio of granule cells to CA3 pyramidal cells is something on the order of 12:1, whereas at the temporal pole the ratio drops to 2:3. Since the CA3 pyramidal cells are the major recipients of granule cell innervation, and the number of mossy fiber synapses is roughly the same along the septotemporal axis, contact probability is much lower septally than temporally.”

Similarly, Ishizuka et al. (David G Amaral, Ishizuka, & Claiborne, 1990) demonstrated dendritic architecture inhomogeneities throughout CA3 and CA2, with smaller and less complex dendritic trees in the limbs of the dentate gyrus, increased contact probability with granule cells, and bigger and more complex cells in distal regions, promoting the influence of synaptic inputs from entorhinal cortex projections. These examples suggest that structural inhomogeneities can impact the network topology. Such inhomogeneities inside the originally described subdivisions have been largely overlooked, and only partly accounted for in models of the organization of neuronal circuits (C. Bernard & Wheal, 1994). However, the most frequently regarded paradigm to address the organization of neuronal circuits has been a reductionist approach based on cell types, according to which discrete cell types are assumed to be homogeneous in terms of structure and function. Given the network topology differences produced by small changes in dendritic architecture seen in Chapter I, added to the complexity emerging from the existence of a wide variety of cell types and afferent projections in single neuronal layers, the impact of such inhomogeneities on network

topology could define subcircuits involved in differential computations (Mizuseki, Diba, Pastalkova, & Buzsáki, 2011).

However, the most frequently regarded paradigm to address the organization of neuronal circuits has been a reductionist approach based on cell types, according to which discrete cell types are assumed to be homogeneous in terms of structure and function. Neurons in the brain are commonly grouped into discrete cell types based upon morphology, marker-gene expression, electrophysiology, and location within their respective circuit motifs. Each of those cell classes has been assumed to retain constant properties, and thus they have been used in computational models as “clonal” stereotypic elements. For example pyramidal neurons, the most abundant type of neuron in the neocortex, display notably similar dendritic arborization patterns among different areas of the brain and between different cortical layers, in spite of their broad functional range. Dense arborizations of basal dendrites with multiple proximal branches wreath the cell bodies of pyramidal neurons, with a single apical dendrite projecting towards the pial surface, which eventually branches as it enters layer I (Mason & Larkman, 1990). This conserved shape has justified the application of systematic morphological analyses without considering morphologic peculiarities of individual neurons. Although the effects of such peculiarities on the function of pyramidal neurons are not known, apical and basal dendrites likely correspond to different circuit inputs producing specific contributions to pyramidal cell excitability and long term synaptic plasticity (Caulier, Clancy, & Connors, 1998; Dudman, Tsay, & Siegelbaum, 2007).

A number of studies have demonstrated that differences in organizational principles may also be present, wherein within-class variability may be an important aspect of neuronal systems (Solstez, 2006). This question has been systemically investigated using microanatomical and gene-expression studies of pyramidal cells. Several lines of anatomical and physiological evidence have identified differences in CA1 in each of the dorsal-ventral (D G Amaral & Witter, 1989; Dougherty et al., 2013; Dougherty, Islam, & Johnston, 2012; Malik, Dougherty, Parikh, Byrne, & Johnston, 2016), proximal-distal (Graves et al., 2012; Igarashi, Ito, Moser, & Moser, 2014; Jarsky, Mady, Kennedy, & Spruston, 2008), and superficial-deep (S.-H. Lee et al., 2014; Mizuseki et al., 2011; Slomianka, Amrein, Knuesel, Sørensen, & Wolfer, 2011) axes of the hippocampus.

Similar variations have been reported also for other brain regions, such as the cerebral cortex (De Felipe, González-Albo, Del Río, & Elston, 1999) or the striatum (Cossette, Lecomte, & Parent, 2005) that may account for the well-established extensively reported notorious functional variability among different neurons. Actually, the cerebral cortex is characterized by regional variations in its structure across different spatial planes. (J L Conel, 1967; J LeRoy Conel, 1941, 1947, 1955, 1959; Jesse LeRoy Conel, 1963) thoroughly examined these regional differences by quantifying cell structure variation in several cortical areas in the cortex of a developing human brain. However, even though there have been great advances in characterizing the detailed patterns and statistical structure of cortical variability (Ecker et al., 2014; Feng, Zhao, & Kim, 2015; Goris, Movshon, & Simoncelli, 2014; Kohn & Smith, 2005), it has mainly been considered as pure noise or nuisance (Carandini, 2004; Moreno-Bote et al., 2014; Shadlen & Newsome, 1998; Tolhurst, Movshon, & Dean, 1983), and only recently some authors have suggested that such structural variability underlies functional aspects such as the representation of perceptual uncertainty (Sanristóbal, Rebollo, Boada, Sanchez-Vives, & Garcia-Ojalvo, 2016). In fact, during neocortex development, the molecular specification cues exhibit smooth, graded profiles that span multiple cortical areas, suggesting the evolution of graded cell properties within the same cell class (Sansom & Livesey, 2009). Also, in adult primates (A. Bernard et al., 2012) and humans (M. J. Hawrylycz et al., 2012) spatial proximity correlates with gene-expression similarity for neocortical regions and continuously variable immunohistochemical (Kondo, Hashikawa, Tanaka, & Jones, 1994; Xu, Tanigawa, & Fujita, 2003), morphological (Elston, 2002), and anatomical (Freese & Amaral, 2005) neocortical properties have been found, suggesting that continual variation may be a general feature of repeated, spatially extended circuit motifs in the brain.

In this chapter, I focused on the dorsal CA1 given the existing information regarding its anatomical and functional proximal-distal inhomogeneities (Cembrowski et al., 2016; Graves et al., 2012; Igarashi et al., 2014; Jarsky et al., 2008). In the rodent, area CA1 of the hippocampus has a C shape that extends millimeters in the anterior-posterior, medial-lateral, and dorsal-ventral axes (**Figure 23**).

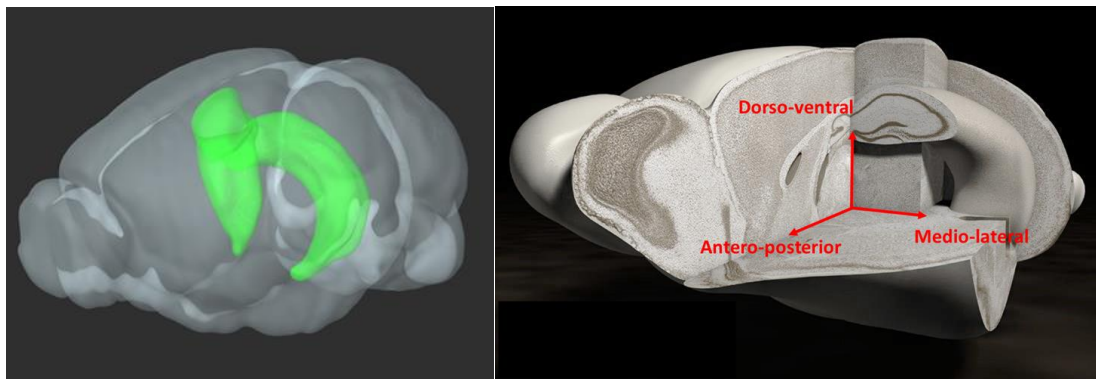


Figure 23: 3D rendering of the mouse hippocampus. (Left) 3D view of a whole mouse brain (gray) and its hippocampus (green) obtained from Allen Brain Explorer (Jones, Overly, & Sunkin, 2009). (Right) 3D rendering of a brain showing its anatomical axes.

As viewed in coronal sections, near its most rostral point, CA1 occupies approximately the top half of the continuous CA field. More caudally, the full dorsal-ventral extent of the CA1 region can be visualized; here, the most lateral band of cells comprises CA1. Conventionally, this 3D structure is described by three axes: the most prominent axis (dorsal-ventral) is typically referred to as the long axis and spans the length of CA1. Two-dimensional cross-sections perpendicular to the long axis reveal the proximal-distal axis (spanning from the CA2/CA1 “proximal” border to the CA1/subiculum “distal” border) and the superficial-deep axis (spanning from “superficial” cell bodies located closest to *stratum radiatum* to “deep” cell bodies located closest to *stratum oriens*).

Those subregions define functionally relevant differences. The dorsal hippocampus has been related to spatial and contextual memories, while the ventral region has been suggested to be involved in fear conditioning and anxiety (Fanselow & Dong, 2010). Additionally, recent studies have shown functional segregation along the proximo-distal axis of the dorsal hippocampus, being the proximal part more related to spatial memories and the distal one to contextual memories (stronger/weaker place cell firing) (Igarashi et al., 2014). A wealth of evidence has illustrated that there is profound functional segregation across the long hippocampal axis (Moser & Moser, 1998; Strange, Witter, Lein, & Moser, 2014), with both input to (Dolorfo & Amaral, 1998) and output from (Gibble, Kishi, & Peake, 2006; Groenewegen, te der Zee, Te Kortschot, & Witter, 1987; Risold & Swanson, 1996) the hippocampus exhibiting graded topographical mapping across the long axis. In this part of

my work, I hypothesize that DS mouse models have alterations affecting specific cognitive domains in the hippocampus, having a differential effect on spatial and contextual memory.

Population-based analyses

Until now, we only have incomplete descriptions of the within-class variation in neuronal networks, and most studies neglect the underlying spatial structural variation that shapes connectional topology. To address this, efforts are being done to atlasing individual neurons, from their molecular phenotype to generating complete morphological reconstructions of individual neurons from datasets of whole mouse brains imaged at sub-micron resolution (<https://www.janelia.org/project-team/mouselight>) or obtaining complete subanatomical descriptions (i.e. Electron Microscopy) of tissue volumes containing big populations of neurons. However, this is still an important challenge given the low throughput of the technique (Zheng et al., 2017) and the fact that it is difficult to identify what subcellular structures correspond to bona-fide neurons.

Single-neuron reconstructions provide enough anatomical detail to explore such within-class variability. However, until now, the reductionistic cell-type specific perspective taken in most neuroanatomical studies has left an empty gap regarding its study. For example, the most complete single-neuron morphology database (<https://neuromorpho.org>, Ascoli, Donohue, & Halavi, 2007) contains at this moment more than 70000 single neuron reconstructions, but those cells lack information about their position. Similarly, the more recent Allen Institute neuron cell type database (<http://celltypes.brain-map.org/>) combines morphological, electrophysiological and transcriptomic layers of information, but still misses the link with topological or functional segregation. This is starting to be resolved through the latests efforts in mapping whole single neurons (including axonal projections), accounting for their position (Mouselight, <https://www.janelia.org/project-team/mouselight>), but until now only few have been completely traced.

Thus, a systematic characterization of neuromorphological properties while considering the topographical positioning of the neurons is required. In order to generalize the detailed knowledge obtained with single-neuron data, information obtained with immunostainings or transgenic population labeling could be used. For example, in the case of having a population

of labeled cells it would be informative to assess their density, or the dendritic density in a given layer. Such measurements could be a powerful tool to study within-class variability.

Given that the amount of neuromorphological variation along neuronal layers is generally unknown, there is a need for more comprehensive studies characterizing such inhomogeneities. To this end three aspects are necessary: first, the systematic study of neuronal morphology across single neuronal layers. Second, the development of population-based measurements able to account for within-class neuromorphological diversity. And third, a computational modeling framework that enables the exploration of their impact in the connectivity of neuronal circuits. The aim of this part of the Thesis is to assess those three aspects.

2.2. Methods

In this part of the Thesis, I combined histological experiments and classical techniques for neuronal reconstruction and cellularity estimations, with the development of a computational framework for population analysis and a generative model able to account for structural inhomogeneities along neuronal layers.

The first step was to characterize single-cell morphology in the hippocampus of healthy and perturbed scenarios such as those provided by DS mouse models. Those models might either show generalized abnormalities or, more interestingly, local alterations, providing additional information about the relevance of within-class variability. I first used classical single-cell injection and neuronal reconstruction methods to identify whether generalized abnormalities such as the differences found in the motor cortex in Chapter I are also present in dendritic tree architecture of pyramidal CA1 cells (*stratum radiatum*) of transgenic mice overexpressing *Dyrk1A* (TgDyrk1A; see Chapter I, **Section 1.2.1** and Altafaj et al., 2001) and their wild-type controls, the later defining the “healthy” structural features. To investigate whether pooling neuronal reconstructions from subtly different locations in neuronal layers could be hindering within-class variability, I accounted for the proximo-distal axis position in the analysis of morphological features.

In a second series of experiments, I used a genetic approach, crossing TgDyrk1A to a strain expressing yellow fluorescent protein (YFP) in a subset of pyramidal cells, to obtain population-based measurements accounting for cellular and dendritic density. Finally, I obtained cellular density measurements based both on the YFP transgenic labelling and NeuN stainings along the antero-posterior axis to feed a custom-developed computational framework that enables the study of neuronal network connectivity from a multi-scale data-driven perspective.

2.2.1. Single-cell analysis

For defining optimality in hippocampal CA1 pyramidal cells I performed single-cell analysis of CA1 pyramidal neurons of wild type and transgenic mice overexpressing *Dyrk1A* (TgDyrk1A) obtained as previously described (see Chapter I, **Section 1.2.1** and Altafaj et al.,

2001). All animal procedures were approved by the local ethical committee (CEEA-PRBB, MDS-08-1060P1 and JMC-07-1001P2-MDS), and met the guidelines of the local (Real Decreto 53/2013) and European regulations (EU directive 2010/63/EU and 2007/526/EC) and the Standards for Use of Laboratory Animals nº A5388-01 (NIH). The CRG is authorized to work with genetically modified organisms (A/ES/05/I-13 and A/ES/05/14).

Lucifer Yellow injections in TgDyrk1A mice in single CA1 pyramids

To compare dendritic tree architecture in the *stratum radiatum* of pyramidal CA1 cells between DS and control mice we performed Lucifer Yellow injections in manually selected single hippocampal CA1 pyramidal neurons and reconstructed in 3D their dendritic trees (collaboration with Inma Ballesteros, UCLM). Four wild-type and TgDyrk1A two-month-old mice (N=4) were perfused with 4% PFA, and 150 µm coronal sections were obtained with a vibratome. Intracellular injections of fluorescent Lucifer Yellow (LY) (described in detail in (Benavides-Piccione et al., 2005; M Dierssen et al., 2003) were performed by continuous current in CA1 pyramidal neurons. The injections were performed in the dorsal hippocampus according to the stereotaxic coordinates (Bregma, -1.34 to -2.34 mm; Paxinos & Franklin, 2004). Four to 12 neurons were injected in each section along the mediolateral axis of CA1, from which we selected those neurons that had a completely filled dendritic tree and with low background. The sections were counterstained with antibodies against LY. Sections were washed with PBS and 0.3 % PBS-T to make the cells permeable. To minimise the background staining, the slices were treated with 50 mM glycine (minimum 99 % TLC, Sigma-Aldrich,) in 0.3 % PBS-T for 20 min. After washing with 0.3 % PBS-T, the samples were treated for 2 h at room temperature with 3 % bovine serum albumin (BSA, Sigma-Aldrich) in 0.3 % PBS-T as a blocking agent and were incubated overnight at 4 °C in polyclonal rabbit IgG fraction anti-Lucifer yellow (1:500, Life Technologies, Thermo Fisher Scientific, Cat # A-5750) in 0.3 % PBS-T and 1 % BSA. After washing with 0.3 % PBS-T, they were incubated 2 h at room temperature in goat anti-rabbit IgG 488 (1:200, Invitrogen, Thermo Fisher Scientific, Cat # A11034) in 1 % BSA in 0.3 % PBS-T. Finally, sections were washed with 0.3 % PBS-T and PBS and were coverslipped using mowiol mounting medium.

Neuronal reconstruction

The preparations obtained as described in the previous section were used for neuronal reconstruction. To position the reconstructed neurons in CA1, I mapped their coordinates in a common reference space, between Bregma coordinates -1.34 and -2.34 mm (Mouse brain atlas, Paxinos et al., 2013). The mediolateral and dorsoventral axes were defined at low magnification (11.5x) images of the brain sections taking the dorsal tip of the 3rd ventricle as the origin. The low magnification images were obtained using a stereomicroscope MZ16F (Leica Microsystems, Wetzlar, Germany).

Single apical tree stacks were acquired with a confocal microscope (SP5 Upright; Leica Microsystems) with a 20x air objective and 0.347 μ m z steps (final voxel size of 0.296x0.296 μ m). Three stacks per sample were collected, aligned, and averaged to reduce noise. I used Leica Smart Gain in the Leica Application Suite software (<https://www.leica-microsystems.com/products/microscope-software/details/product/leica-application-suite/>) to adjust brightness, in order to equalize the fluorescence signal intensity in depth in the samples.

The signal to noise ratio was measured for each of the obtained stacks at 100 μ m depth to account for a representative dendritic segment and an equivalent area of the same depth containing only background. Images with SNR<1.2 were discarded for subsequent analysis. The stacks underwent 2 pixel wide 2D gaussian blurring, background subtraction (50 pixel sliding paraboloid without smoothing) and contrast enhancement (with 0.3% saturated pixels and using the stack histogram) in Fiji.

Dendritic trees of 20 neurons per genotype from 4 wild-type and 4 TgDyrk1A animals were reconstructed with NeuTube1.0 (Feng et al., 2015) (see Chapter I) given that the semi-automatic tracing of this software outperforms other open-source applications in processing time and usability, allowing neuronal reconstruction with minimal interaction.

Storage capacity estimation

Linear and non-linear storage capacity for each of the reconstructed single neurons was computed as described previously (**Equation 2**). These measures, account for ideal upper bounds to the amount of input-output functions that single trees could differentiate, based on n choose k combinatorics given by the number of synapses a tree (or a single dendrite) is receiving and the amount of presynaptic afferents (Poirazi & Mel, 2001). We assumed that dendrites sharing dorsoventral and anteroposterior location at the scale of a single axon (0.6 μm) would receive synapses from the same afferent axon (i.e. that axons project in straight lines on the medio-lateral direction). Synapses were assumed to be given by specified spine densities homogeneously throughout the trees. Self-developed MATLAB scripts using the Trees Toolbox to estimate the synaptic contacts and non-redundant afferents for each reconstruction can be found at (https://bitbucket.org/linusmg/2d_model_bitbucket/ in the folder single_tree_analysis/storage_capacity_estimation).

Statistics and principal component analysis

To analyze the reconstructed trees, I followed the procedure described in **Section 1.2.2** (Chapter I). Briefly, morphological metric statistics were obtained with the Trees Toolbox (Cuntz, Forstner, Borst, & Häusser, 2011) function *stats_tree*, a scaled PCA was performed in R, and wiring optimality was assessed by fitting a power law to the relation between total tree length and amount of branch points (see **Section 1.2.2** and Cuntz, Mathy, and Häusser 2012). In this case, the numbers of Sholl intersections were obtained using the *sholl_tree* function in the Trees Toolbox. In order to get a precise distribution of dendritic densities, I used a Sholl radius step of 1 μm .

In order to spare as many neurons as possible for my analysis, I used an unbalanced block design, which allows an unequal number of observations per groups (in our case, numbers of neurons reconstructed per genotype and areas). The neuromorphological metric distributions were compared among positions by fitting a mixed-effect linear model with the residual maximum likelihood (REML) method and blocking for biological replicates, the analysis was performed using R (version 3.4.1) and its package *lme4* (version 1.1-13). P-values were obtained from the adjusted denominator degrees of freedom for linear estimates and *t* distributions calculated using the Kenward-Roger approximation (*pblrtest* R package, version 0.4-7). Results were considered significant when $p < 0.05$.

2.2.2. Population-based analysis: morphological within-class variability of CA1 pyramidal neurons along the antero-posterior hippocampal axis in wild-type and TgDyrk1A

For population-based analysis, I required a systematic view of the cells along the whole structure that cannot be obtained through labour-intensive single-neuron injections, but are also not conveniently obtained through immunohistochemical techniques that would stain the whole population of cells making estimations more complicated. I thus generated double transgenic mice (Thy1-YFP/TgDyrk1A) by crossing TgDyrk1A male mice with *Thy1-Yellow Fluorescent Protein (YFP)* female mice (strain B6.Cg-Tg(Thy1-YFPH)2Jrs/J n°003782; The Jackson Laboratories), that expresses yellow fluorescent protein in a proportion of pyramidal cells driven by the Thy1 promoter and their non-transgenic littermates as controls. The Thy1-YFP line H has been reported to express the fluorescent protein in a large number of pyramidal neurons in several fields of the hippocampal formation. This model offers the advantage of having sparse YFP-stained pyramidal neurons that will also serve the purpose of population based analysis.

I first used classical stereology methods for unbiased “bona-fide” estimations of hippocampal CA1 volumes and neuronal density that thereafter served for validating a computational framework for population-based analysis that I developed to:

- 1) Estimate the spatial embedding by determining the volume of the specific hippocampal subregion (CA1); 2) estimate the number neurons; and 3) estimate dendritic densities.

Unbiased cellularity estimations along the antero-posterior axis of CA1 in TgDyrk1A

Given that stereological estimations of cell densities have to be done in consecutive planes, I decided to assess variations in cell-density along the antero-posterior axis. The relative importance of the intrinsic and extrinsic factors determining the variety of geometric shapes exhibited by dendritic trees remains unclear but important extrinsic determinants of dendritic shape are the spatial embedding and the cellularity, that constrain geometrical properties of dendritic trees. To this aim I investigated variations in the cellularity and the volume occupied by CA1 along the anteroposterior axis.

For the study of cellular and dendritic densities across CA1, two-month-old Thy1-YFP mice ($N=4$) were sacrificed and perfused intracardially with phosphate buffered saline (PBS), followed by chilled 4% paraformaldehyde (PFA; Sigma). The brains were removed from the skull, postfixed in the same fixative at 4°C overnight, and cryoprotected in 30% sucrose. One-hundred fifty μm coronal brain sections were obtained using a vibratome (VT1000S, Leica Microsystems), washed extensively with 0.1M PBS, and mounted and coverslipped with mowiol reagent.

Total neuronal densities were also analyzed using a NeuN staining in a similar setup with samples from TgDyrk1A and their wild-type littermates ($N=3$). To ensure the antibody penetration throughout the sample, forty μm coronal sections were obtained using a cryostat (CM3050 S, Leica Microsystems). Then, sections were permeabilized with 0.5 % Triton X-100 (Merck) in PBS (PBS-T 0.5 %) (3x15'), and blocked with 10% of Normal Goat Serum (NGS) for two hours at room temperature. Sections were incubated overnight at 4°C in mouse IgG anti-NeuN (1:500, Millipore, Cat # MAB377), PBS-T 0.5% and NGS 5 %. Slices were washed with PBS-T 0.5 % (3x15') and incubated for two hours at room temperature in 488 goat anti-mouse IgG (1:500, Invitrogen, Cat # A11001) antibodies in incubation buffer (PBS-T 0.5 % + NGS 5 %) and protected from light. Finally, sections were washed with 0.3 % PBS-T and PBS and were coverslipped using mowiol mounting medium.

Stereological estimations

I used design-based stereology methods for neuronal counting (Optical Disector; Harding, Halliday, & Cullen, 1994; Rosen & Harry, 1990) and volume estimation (Rosen & Harry, 1990). This method eliminates the need of information about the geometry of the objects to be counted, resulting in more robust and unbiased estimates of total neuron number, because potential sources of systematic errors in the calculations are eliminated. I used 150 μm Thy1-labeled and NeuN-stained coronal sections that are thick enough to allow many focal planes through the disector and to allow for guard zones. There must be multiple focal planes through the disector so that: one particle can be told apart from another; there will be a small leading edge that is detected; and there is room to focus up and down and make a good decision about whether the leading edge of the particle is contained in the disector or not.

I used a Leica DMI 6000B inverted microscope (Leica Microsystems, Wetzlar, Germany) equipped with a 20x air objective, a motorized scanning stage and a microcator and a digital camera connected to a PC to obtain microscopic captures. Images were analyzed with the newCAST™ software (Version: 5.3.0.1562, Visiopharm, Denmark) from Visiopharm Integrator System.

Volume estimation of the selected ROIs was calculated according to the Cavalieri principle. A specific point configuration was configured to ensure that more than 200 points in total were counted for every ROI across all the selected slices. 100% coverage of the area of each ROI was chosen for sampling. Volume estimation for the whole ROI and for every slice was calculated according to:

$$V_{ref} = T \cdot a(p) \cdot \sum P \quad (8)$$

Where T is the spacing between sections, $a(p)$ the area per point (dependent on each specific configuration), and $\sum P$ the sum of points inside the ROI.

To obtain Thy1+ cell densities, seven Thy1-labeled 150 µm thick consecutive slices (Bregma, -1.34 to -2.34 mm, mouse brain atlas; Paxinos et al., 2013) were quantified. NeuN quantifications, due to the thinner sectioning, were performed in every 4th slice, discarding 3 consecutive slices between quantifications. I used an Optical Disector and sampled 21-24 counting frames in each analyzed region of interest (ROI). I obtained an estimate of the real thickness of the planar sections (60µm) by measuring the z-axis distribution of the cell number and identifying the z extent having a uniform distribution of counts. Each counting frame covered 1% of field of view given by the 20x objective having the following dimensions: 58.1 x 58.1 x 60 µm. the optical plane was moved throughout the whole thickness of the preparation section to ensure correct cell identification. Cell densities (N_v) were calculated according to the following equation (Dorph-Petersen & Lewis, 2011):

$$N_v = \frac{\overline{t_Q}}{BA} \cdot \frac{\Sigma Q^-}{h \cdot (a/p) \cdot \Sigma P} \quad (9)$$

Where $\overline{t_Q}$ is the number-weighted mean section thickness, BA is the Block Advance (the cut thickness of the section on a calibrated cutting device), h the disector height, (a/p) : a is the area of the CF and p the number of points associated to the frame (1 - using the upper right

corner of the CF), and $\sum P$: is the sum of corner points hitting reference tissue.

The total number of cells (N) was estimated by the product of the cell density (N_v) and the volume (V_{ref}) obtained from Cavalieri estimations.

$$N = V_{ref} \cdot N_v \quad (10)$$

All the estimations were performed in one hemisphere, chosen at random as no differences are reported to exist between both hippocampal formations. Stereological estimations were performed in the CA1 pyramidal cell layer of the hippocampus. ROIs were manually delineated according to (Paxinos et al., 2013) mouse brain atlas.

2.2.3. Development of a customized pipeline for population-based analysis in histological sections

As described above, neuron morphologies capture some features of selected cell types, but they are hard to generalize to the whole cell population, given the inhomogeneities that have been reported. One bottleneck is that describing the shape of neurons requires quantitatively specifying many morphological features, examples of which are the length and branching patterns of neurites, and their spatial distribution. Another is that obtaining accurate 3D digital representations of neurons has traditionally been a slow, expensive, manual process. Here I developed a computational analysis pipeline to obtain population-based measurements semi-automatically and define dendritic and cellular density maps. Experimental data were obtained from Thy1-labeled mice in dorsal CA1 thus allowing the comparison with single-cell reconstructions and stereological.

Imaging and segmentation

Images of the dorsal hippocampus according to the stereotaxic coordinates Bregma, -1.34 to -2.34 mm, obtained from a mouse brain atlas (Paxinos et al., 2013) have been taken using a widefield microscope (Zeiss Cell Observer HS) with a 10x magnification objective with a field view of 895.26 x 670.80 μm and resolution of 0.643 $\mu\text{m}/\text{pixel}$. Using the *Panorama acquisition* module (ZEN blue edition, Zeiss) adjacent images with 5% overlapping edges were taken covering the whole brain section for each of the 6-8 brain sections analysed per animal.

Images covering the whole section were reconstructed using the ImageJ *Grid/Collection Stitching* plugin with 5% tile overlap, the *Linear Blending* fusion method and its default thresholds, a regression threshold of 0.30, an average displacement threshold of 2.50 and an absolute displacement threshold of 3.50. Stacks containing the whole section images of each animal were downsampled 20 times in the X-Y dimensions and aligned using the *RegisterVirtualStacks* plugin with the Rigid feature extraction and registration model and applying shrinkage constraint. The obtained transformations were multiplied by the downsampling factor and applied to the original large stacks.

Masks for the whole section and the left hemisphere regions CA1 and its somatic layer (*stratum pyramidale*; CA1-sp) were manually segmented according to the Allen P56 mouse brain Reference Atlas (Dong, 2008) using Fiji's *Segmentation Editor*. (Figure 24).

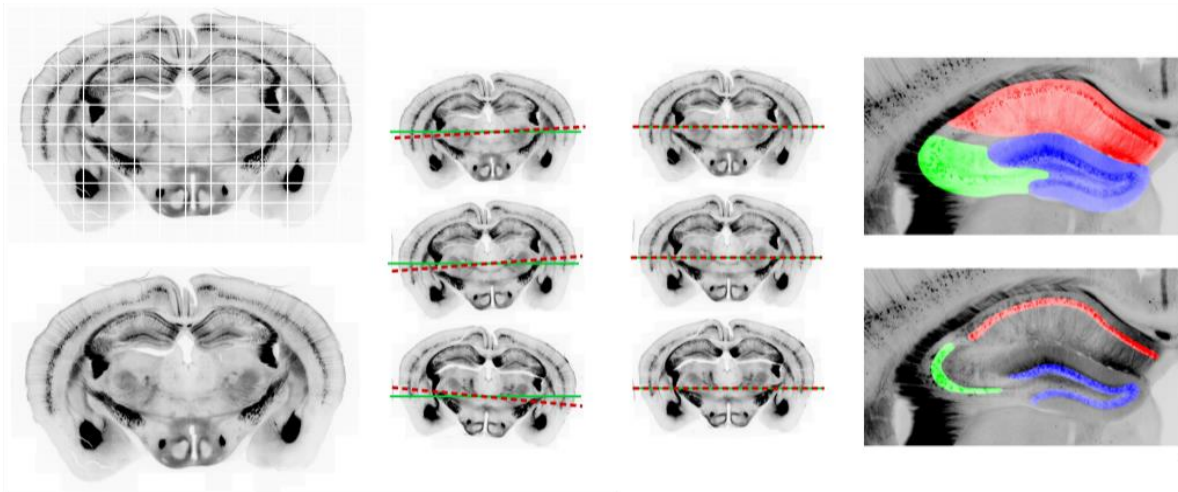


Figure 24 : Overview of the imaging, stitching, alignment and segmentation procedure. (Top left) Serial images covering the whole section were obtained with a 5% tile overlap. (Left) Stitching was performed using the ImageJ Grid/Collection Stitching plugin. (Middle) Consecutive sections were aligned using the RegisterVirtualStacks plugin. (Right) 2D segmentations for CA1 dendritic (top) and pyramidal (bottom) layers were manually delineated using the Fiji's Segmentation Editor and based on the Allen P56 mouse brain Reference Atlas.

In order to increase the extensibility of our approach I chose Fiji plugins as basic tools for our quantifications. I selected Fiji because it is an open source image processing package based on ImageJ with many bundled plugins. Fiji features an integrated updating system and provides a high number of users with a coherent menu structure, extensive documentation in the form of detailed algorithm descriptions and tutorials, and the ability to avoid the need to install multiple components from different sources.

For both cell and dendritic density mapping, the processing done in Fiji is aided by Matlab and Python scripts developed in-house that can be easily used in processing pipeline management tools. I first describe the examples of population metrics for which I have developed analysis algorithms and subsequently an interactive pipeline structure that allows a user-friendly application of our methods and their extension.

Cell density

A first requirement to obtain whole-CA1 cell density maps is to locate nuclei in the imaging datasets. An extensive literature on computational methods has tackled this challenge (Irshad, Veillard, Roux, & Racoceanu, 2014). Developing an optimal method to identify cells in microscopy imaging datasets is beyond the scope of this Thesis, but I aim to show that, by analyzing 2D datasets, I can obtain 3D cell density maps that are representative of the macroscopic scale properties of the tissue and give unprecedented detail and allow innovative analysis methods.

I wrote a Fiji macro that locates nuclei in segmented somatic layers of 2D microscopy images (CA1 stratum pyramidale in this case) and creates 2D cell density maps along them. The macro can either use Fiji's simplest method for identifying cells (2D maxima detection plugin) or can generate the density maps based on lists of cell coordinates provided by the user. It is important to note that the datasets used have been background subtracted with a rolling ball (radius = 15 μm) in order to highlight signal coming from somas and reduce signal intensity in thin neurites. The script needs as inputs the binary segmentation of the analyzed layer and either the original image or a list of 2D coordinates obtained with an alternative method. It first obtains the midline of the layer and subsequently quantifies the amount of identified cells in adjacent circular areas following the midline (**Figure 25**). The circles are located along the midline so that they are big enough to cover tenths of cells (radius = 160 μm in our datasets) and have some amount of overlap among them (distance = 130 μm in our datasets). In each circular area, a cell density (cells/ $10^7\mu\text{m}^3$) is calculated based on the measured cell quantity, the somatic layer area covered by the circle and the depth of the imaged sections. The $10^7\mu\text{m}^3$ scaling factor is introduced in order to obtain gray intensity values in the range of an 8-bit image. In the areas covered by overlapping circles, the cell density is set as the average of repeated measurements. Finally, the macro applies a gaussian blur (radius = 30 μm) and creates a 16-bit image expressing the cell density as the image intensity at each point. The resulting maps represent inhomogeneous cell body distributions along the analyzed layers (**Figure 25**).

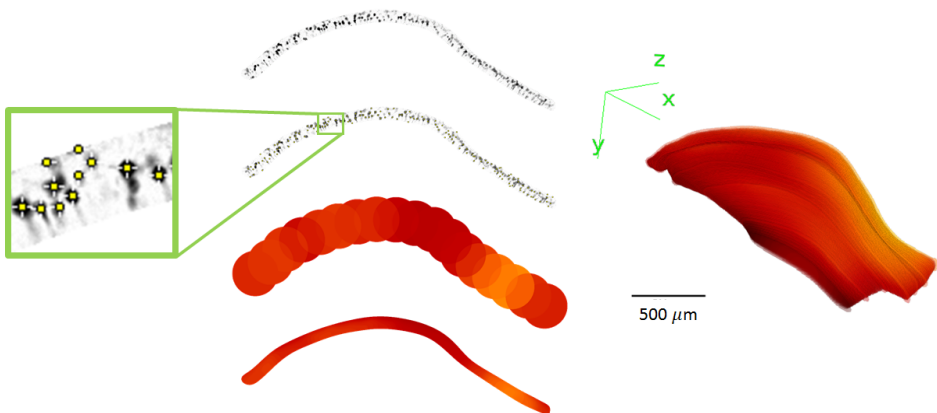


Figure 25: Overview of the cell density mapping procedure. A segmented somatic layer is preprocessed with a background subtraction of rolling ball radius = 15 μm in order to highlight somas. The amount of cells in equispaced (130 μm) circles (radius = 160 μm) is measured and shown as image intensity. A gaussian blur (radius=30 μm) is applied and the intensity map masked again. (Right) 3D rendering of an interpolated (see **Section 2.2.2**) cell density map for the CA1 pyramidal layer (Bregma from -1.34 to -2.34).

Dendritic density

While population-based labeling (Thy1-like) has been used to quantify cells and axonal projections, information related to dendritic complexity has been disregarded. I developed a novel method to quantify dendritic density that can be understood as an extension of the Sholl analysis for single neurons. In the classical single-cell version of the analysis, the amount of dendritic branches crossing concentric circles of increasing radius is quantified. The information obtained can be seen as a signature of dendritic tree architecture and has been studied in depth in neuronal cells from several organisms, brain regions and neuronal subtypes. In order to analyze similarly population-labeled 2D section microscopy images, I have developed a method to quantify the density of dendritic branches along the axis normal to any studied layer. I implemented it in a Fiji macro that computes the midline of a layer and uses it to scan the space surrounding it. A fluorescence intensity profile is obtained along the scanning line and local maxima accounting for dendritic segments are quantified. The quantification is subdivided in curved rectangles with height = 2 μm and length = 40 μm , allowing the detection of spatial inhomogeneities. In each curved rectangle, a 16-bit pixel intensity codes for the measured dendritic density (# dendrites/ $10^6 \mu\text{m}^3$). The $10^6 \mu\text{m}^3$ scaling factor is introduced in order to obtain gray intensity values in the range of a 16-bit image. Finally, a gaussian blur (radius = 30 μm) is applied and a smoothed image/stack containing the dendritic density map is created. The resulting maps represent dendritic density

accounting for both sublayer inhomogeneities (e.g. Stratum Oriens, Radiatum and Lacunosum in CA1) and variations along the somatic layer (e.g. Medio-Lateral axis in a coronal section). **Figure 26** shows an overview of this procedure.

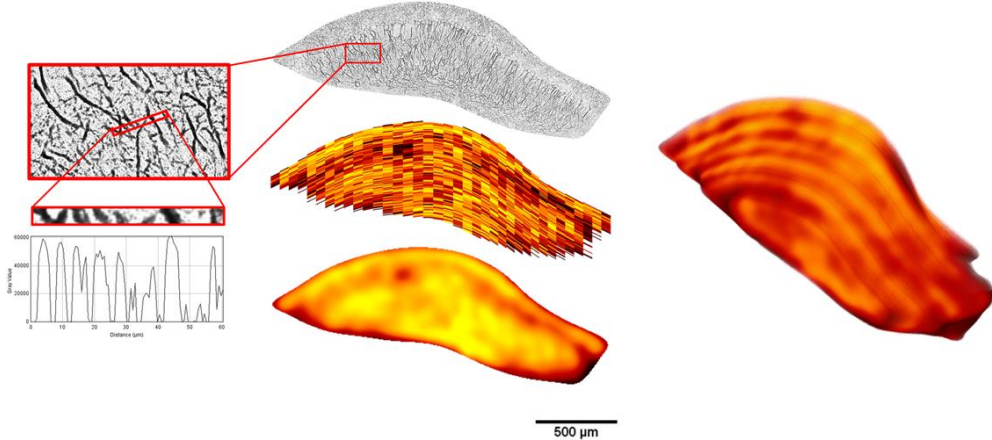


Figure 26: Overview of the dendritic density mapping procedure. A segmented somatic layer is preprocessed with a background subtraction of rolling ball radius = $2\mu\text{m}$ in order to highlight neurites. The amount of intersections in neighboring curved rectangles (height = $2\mu\text{m}$ and length = $40\mu\text{m}$) along lines parallel to the somatic layer is measured and shown as image intensity. A gaussian blur (radius= $30\mu\text{m}$) is applied and the intensity map masked again. (Right) 3D rendering of an interpolated (see **Section 2.2.2**) dendritic density map for the CA1 pyramidal layer (Bregma from -1.34 to -2.34).

Interpolation

The advantages of generating 3D maps are apparent when those are put in the context of a global analysis pipeline. However, usually researchers work with sparse histological sections. Thus the numerical values of the intermediate positions are not available, and for generating 3D maps I have to use interpolation methods to attain bona fide numerical values.

Intensity-based interpolation and triangulation methods could not generate satisfactory 3D masks, given that these methods lead to artifacts in the reconstructed morphology of thin structures. I explored the usage of contour information for constructing the interpolated masks. Even though methods based on distance transforms have been proposed to improve segmentation quality (Grevera & Udupa, 1996), they were not sufficient for the interpolation of thin somatic layers. Thus, I decided to use the information of the contour in order to guide the interpolation. To do so, I wrote an ImageJ macro that (1) obtains n equispaced points ordered along the contour of each of two consecutive slices, (2) linearly interpolates the X-Y positions of the obtained points for as many slices needed to fill the Z dimension and (3) creates the mask defined by the interpolated points in each of the interpolated slices.

The only additional requirement that the algorithm has is the definition of a starting point for each originally segmented slice that should lay on the same anatomical landmark of the reconstructed region (e.g. CA1 distal tip). Despite its simplicity, this algorithm has yielded optimal results in our analysis, recapitulating bona fide the results obtained by single-cell reconstruction.

Another caveat in the use of single-dimension intensity interpolation is the introduction of artifacts derived from inhomogeneous density maps, which may produce a mismatch when trying to interpolate values between section embedding structural displacements. In order to avoid those artifacts, I generalized the contour-informed interpolation method to generate 3D density maps. I developed a Fiji macro that obtains the contour of two consequent intensity map 2D slices. The basic algorithm evaluates the intensity signal at n points of each of the contours and generates an intermediate slice with interpolated coordinates and intensity. This is iteratively done for concentric contours until the whole area has been interpolated. The resulting 3D volumes show a qualitative improvement with respect to intensity- and triangulation-based interpolation methods. **Figure 27** shows a schematic representation of the interpolation procedure.

The developed source-code, a user-friendly ImageJ plugin and supplementary information can be found in <https://bitbucket.org/linusmg/nem4o-analysis>.

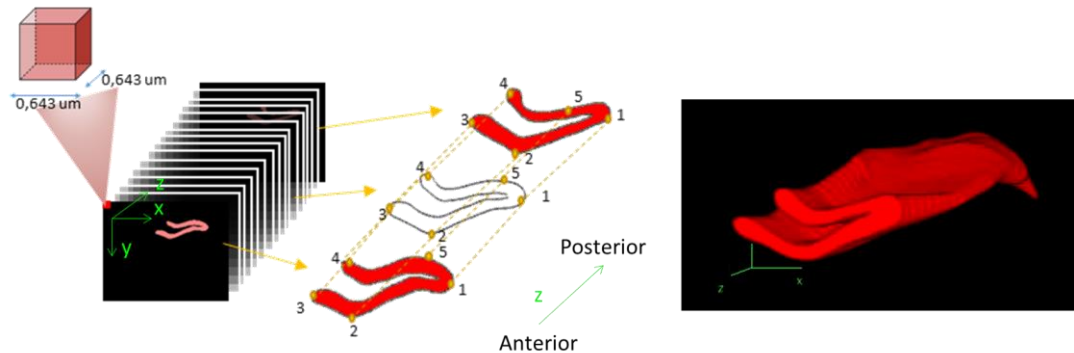


Figure 27 : Schematic representation of interpolation method developed. I show the third-dimension reconstruction of a dentate gyrus somatic layer as an example. (Left) Segmentations for each hippocampal region were defined manually on each of the consecutive slices, according to YFP labeling and mouse brain atlas. (Middle) Blank slices were interleaved in between each 2 slices in order to fill the spatial gaps, according to voxel size (the figure represents in detail the space between 2 specific slices). Coordinates of the sorted contour points of each pair of consecutive original segmentations were used to interpolate the coordinates for the contour of each in-between slice. In the image only 5 of the 1000 analogous points used to do the interpolation are shown. (Right) Resulting reconstructed volume for the region in-between two slices.

Voxel-based analysis of interpolated cellular and dendritic density maps

The analysis of Thy1-labeled mouse brain sections using the tools described above, assess cellular or dendritic densities at specific Bregma coordinates from a 2D perspective, interpolating missing values, and allowing to provide semi-generative 3D maps. I here developed a standardized 3D common coordinate framework and provided a simplified the statistical analysis to the application of already existing methods and software.

I took advantage of existing methods for MRI analyses and devised a pipeline that is based on three major steps: (1) the segmentation of the analysed ROIs and generation of sample group templates, (2) the generation of neuromorphological metric 3D maps and (3) the registration of maps to their templates and their voxel-based statistical analysis.

The segmentation of the ROIs is implemented as previously described. In order to generate group-specific templates, I used state-of-the-art methods based on minimum deformation averaging (Janke & Ullmann, 2015). MDA is the iterative registration of all the group samples to their average and the inverse registration of this average towards the original sample morphologies. The iterative procedure tends to zero deformation of the average, after some iterations (10-20) a template of the group is obtained. In the field of pediatric neuroimaging it has been proposed as a high accuracy method for obtaining templates of small groups of samples. I implemented it on our wild-type dorsal hippocampus segmentations by using the Nipype port of Volgenmodel. **Figure 28** shows a schematic representation of the template generation procedure.

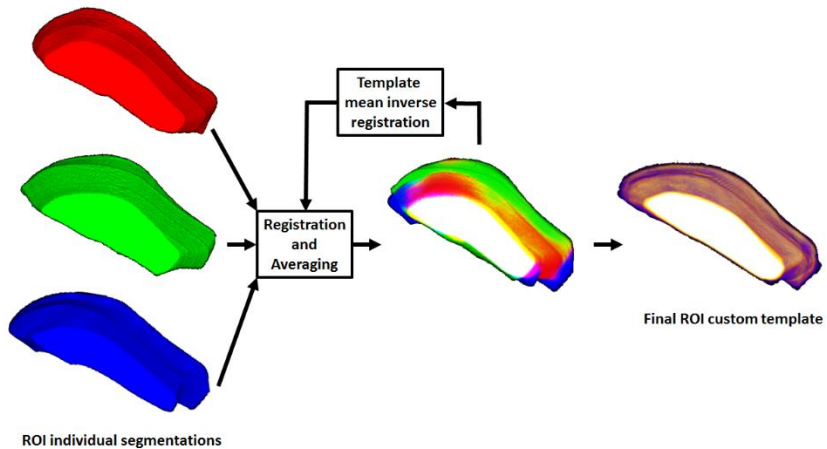


Figure 28: Schematic representation for the MDA procedure to the generation of anatomical templates. (Left) Three segmentations of CA1 dendritic field obtained from individual mouse brains. (Middle) First, an average of the three structures is obtained. All the samples are registered to the average and the transformations are used to perform an inverse registration from the average towards the original sample morphologies. The iterative procedure tends to zero deformation of the average, after some iterations (10-20) a template of the group is obtained.

Whole layer (CA1 dendritic field in this case) binary segmentations were registered to the wild-type template by automatic multiple step (rigid followed by non-linear) mutual information-based ANTs (Avants, Tustison, & Song, 2009) sample to template registration. In order to assess volumetric variability around the generated template, I saved displacement and volumetric change (Jacobian determinant) voxel-based maps of the non-linear registration. The transformations obtained with the binary masks were also applied to the 3D cellular and dendritic density maps. Finally, the registered 3D maps were compared statistically by using RMINC (<https://github.com/Mouse-Imaging-Centre/RMINC>), a versatile R package that facilitates fast fit of statistical models and false discovery rate (FDR) analysis in a voxel-based manner and user-friendly visual representation of the results.

2.3. Results

2.3.1. Morphological properties of TgDyrk1A CA1 pyramidal neurons

In order to assess whether single dendritic trees have optimal dendritic wiring in the dorsal hippocampus, I analyzed the morphology of apical trees from pyramidal CA1 neurons by comparing LY stained neurons from wild-type mice and also compared them with TgDyrk1A littermates (20 neurons from 4 animals across different positions for each genetic condition).

After obtaining the neuronal reconstructions, I analyzed the neuromorphological metrics for the two genotypes. The analysis revealed that the tip-to-soma path length distribution is skewed to larger values for the wild-type neurons (**Figure 30**), showing significant reduction of the number of short ($p_{len} < 120 \mu\text{m}$) and significant increases in intermediate-length ($260 \mu\text{m} < p_{len} < 310 \mu\text{m}$) and long branches. Conversely, the branch order distribution did not show differences among the two groups, indicating that the tree span, rather than the dendritic complexity pattern, is altered in the transgenic model.

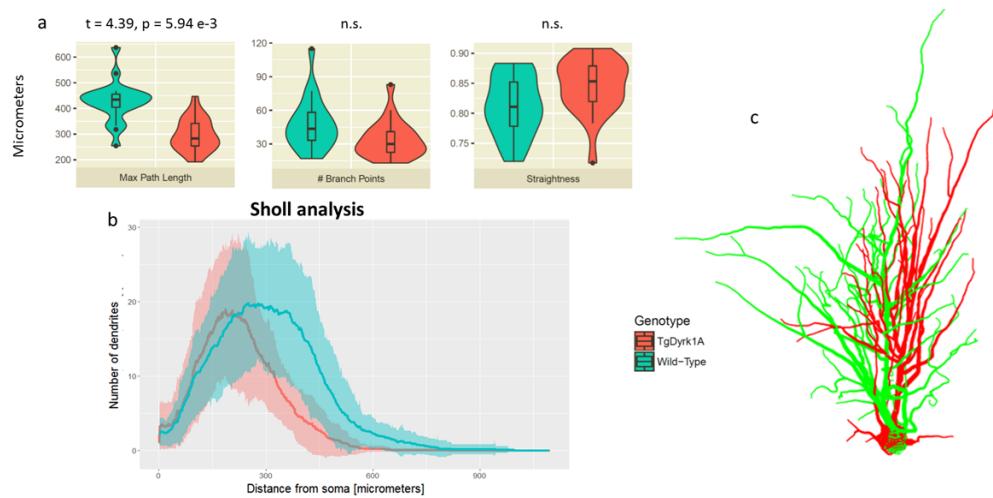


Figure 29: Genotype-dependent dendritic tree architectural modifications. (a) Box and violin plots showing the distributions of maximum path length, number of branch points and straightness of CA1 apical dendritic reconstructions from wild-type (blue) and TgDyrk1A (red) mice. (b) The thick line represents the mean number of branches for each genotype in function of the radius, the shaded region indicates the standard deviation around the mean values. (c) Representative reconstructions of wild-type and TgDyrk1A neurons.

The comparison of the maximum path length distributions shows a significant difference ($t=4.39$, $p=5.94e-3$, mixed effects linear model blocking for biological replicates) when comparing TgDyrk1A ($427 \pm 80 \mu\text{m}$) vs. wild-type ($298 \pm 63 \mu\text{m}$) neurons. Additionally, straightness does not show significant differences between both genotypes, indicating that the increase in path length is not a byproduct of higher tortuosity in dendritic branches.

The center of mass of the trees (see “Neuromorphological analysis” in Chapter 1), was displaced towards the pyramidal layer ($-100 \pm 28 \mu\text{m}$ vs. $-139 \pm 21 \mu\text{m}$; $t=-4.99$ $p=6.03e-3$) in the transgenic model, indicating shorter trees in this direction. Finally, the spanning volume shows a tendency ($2.17 \times 10^6 \pm 1.11 \times 10^6 \mu\text{m}^3$ vs. $5.31 \times 10^6 \pm 4.36 \times 10^6 \mu\text{m}^3$; $t=2.11$ $p=8.23e-2$) to be higher in the wild-type, also showing higher variance. These results are shown in **Supplementary Figure 1**.

Given that the branching order distribution is similar in the two genotypes (**Supplementary Figure 1**), I performed the Sholl analysis to check whether the distribution of branches along the dendritic trees is the same in both genotypes. The analysis shows that even though in both cases the trees reach maximum branching of about 20 branches per Sholl radius, in the case of the TgDyrk1A the distribution is skewed to smaller radii, reaching its maximum at $\sim 200 \mu\text{m}$ vs $\sim 300 \mu\text{m}$ in the case of the wild-type (**Figure 30 b**).

Principal component analysis

To identify metrics that explain the differences found in TgDyrk1A and account for the genotype-dependent neuromorphological variability, I performed a PCA with all the variables accounting for morphological aspects (**Figure 31 top**). The two first principal components explain 54.15% of the variance in the data. Principal Component 1 (PC1, 31.45% explained variance) is mainly contributed by measures that account for the size of the tree: the total length of the tree, the amount of branch points and the dendritic spanning volume. Principal Component 2 (PC2, 22.70% explained variance) is mainly contributed by measures that account for the symmetry of the trees (**Figure 31 bottom**): the center of mass in the dorso-ventral axis, followed by the mean path length, the mean branching asymmetry and the center of mass on the medio-lateral and antero-posterior axes. An overview provided by a 2D projection on those principal components shows that the neurons cluster by

genotype, and that the variables contributing more to the difference among groups are the maximum and mean path length, and the center of mass in the dorso-ventral axis, followed by the spanning volume.

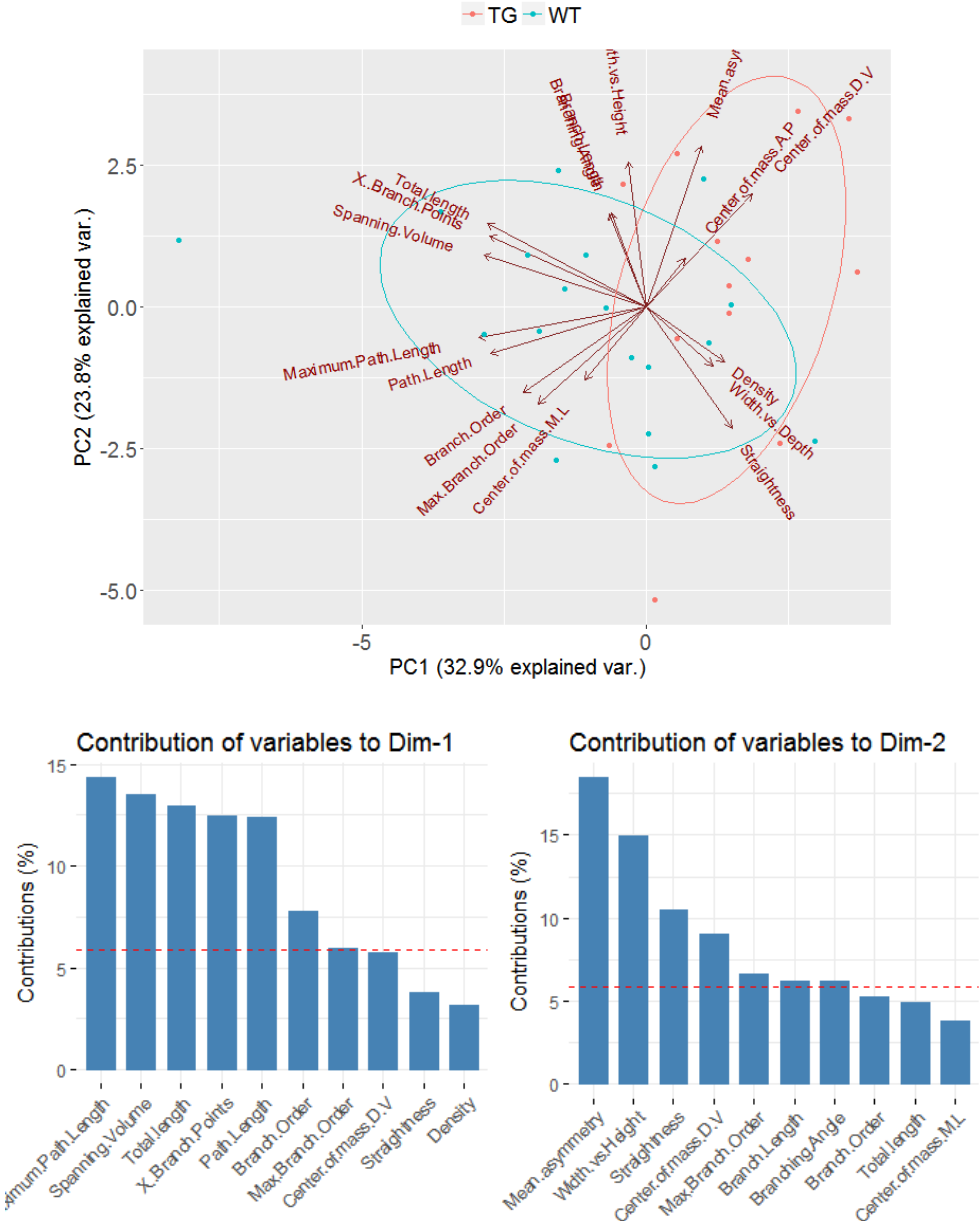


Figure 30: Principal component analysis (PCA) of the neuromorphological and geometric variables of the dendritic tree. PCA of the variables, where arrows represent the direction of each variable in the PCA space. Longer arrows belong to variables that are well represented by the two principal components. Each of the points represents one neuron, colored by the group they belong to. 68% confidence normal data ellipses for each group are drawn with solid lines. (Bottom) Bar plots showing the percentage of explained variance for each principal component. Bars represent the contribution (%) of each variable and the red dashed lines indicate the expected average contribution. The first principal component is a composite variable accounting for the dendritic tree size and the total dendrite length. The second principal component is a composite variable accounting for other morphological measurements, mainly the branching angle, the number of branch points and the horizontal center of mass and mean asymmetry.

Wiring optimality

Understanding the implication of these architectural abnormalities on the hippocampal circuit and its functional capacities is beyond the scope of this study. However, as for cortical neurons, I explored how optimal are the wild-type and TgDyrk1A dendritic trees. When comparing wild-type vs TgDyrk1A reconstructions and their scaling laws between total length and amount of branch points, I found that both wild-type and TgDyrk1A follow closely the $\frac{2}{3}$ optimal power found to be conserved among organisms and brain regions (exponent $b = 0.72 \pm 0.06$ and 0.66 ± 0.06 respectively; **Figure 31**). This result indicates that hippocampal transgenic neurons are as optimal as their wild-type counterparts for signal integration.

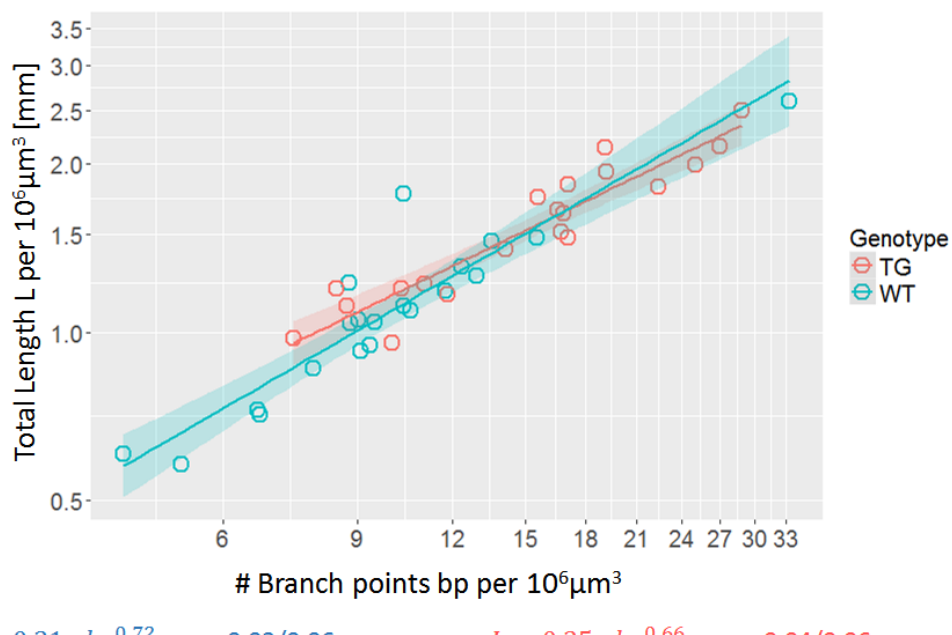


Figure 31: Power law relations between total dendritic length and branch number for layer II/III basal tree reconstructions of wild-type and TgDyrk1A neurons. The $\frac{2}{3}$ optimal power for 3D trees is followed by the control trees (power = 0.72 ± 0.06) and TgDyrk1A (0.66 ± 0.06). The number of branch points and total length was normalized by the dendritic surface ($S=10.000 \mu\text{m}^2$). Shaded regions indicate 95% confidence level interval of the power law fit.

Storage capacity estimation

Previous unpublished studies in the lab explored the morphology and distribution of spines in CA1 apical dendrites injected with LY. No differences between genotypes were detected in the total density of spines (**Figure 32 a, b and c**). However, while in wild-type apical dendrites most of the spines presented a mature mushroom-like protrusion phenotype, TgDyrk1A dendrites showed a higher proportion of thin and long immature spines, suggesting a in spine maturation impairment in TgDyrk1A.

In order to explore the possible implications of both dendritic architectural abnormalities and reduced mature spine densities on the formation of spatial memories, we measured the storage capacity at the single neuron level. We found that when taking into account only the dendritic tree morphology (using the same spine densities for both wild-type and TgDyrk1A), there were no differences regarding the upper bound for storage capacity. When taking into account only mature spines, the storage capacity estimation was shown to be significantly higher for wild-type than for TgDyrk1A neurons ($t=3.72$ $p=0.01$). Additionally, as observed in the spanning volume, wild-type dendritic trees show higher variance than transgenic ones for storage capacity (**Figure 32 d**).

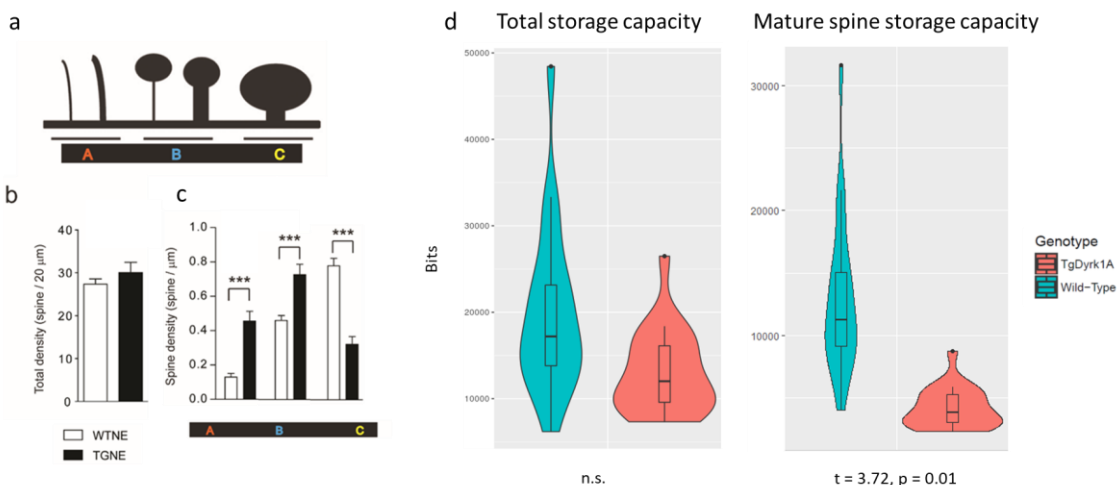


Figure 32: Storage capacity estimations for wild-type and TgDyrk1A CA1 apical dendritic trees. a) Schematic representation of dendritic spine morphologies (A thin, B immature, C mature mushroom-like). b) Spine density in 20 μm of dendrite. c) Density of each type of spine. Number of dendrites/animals analyzed: wild-type = 32/4; TgDyrk1A = 16/4. Data are expressed as mean + SEM. * $p<0.05$; ** $p<0.01$; *** $p<0.001$. d) Boxplots and violin plots for storage capacity estimations using total (left) and mature (right) densities of spines in the reconstructed trees.

Within-class CA1 pyramidal dendritic morphology variability along the proximal-distal axis

To address the question of within-class variability I selected CA1 pyramidal neurons positioned along the proximal-distal axis and analyzed whether their microstructural variability could be explained by their position along CA1 (**Figure 33**). I here grouped the reconstructed neurons in two subgroups depending on their position: distal and central. **Figure 34** shows boxplots of the mean path length and maximum branch order in neurons at distal and central positions along the proximal-distal axis of CA1. The analysis shows that in wild-type mice, there are subtle changes in the mean path length and branching, suggesting that CA1 pyramidal cells increase their dendritic length while decreasing their complexity from distal to central positions (path length: distal $185 \pm 25 \mu\text{m}$ vs. central $203 \pm 25 \mu\text{m}$; maximum branching order: distal 17.7 ± 3.3 vs. central 14.7 ± 3.8).

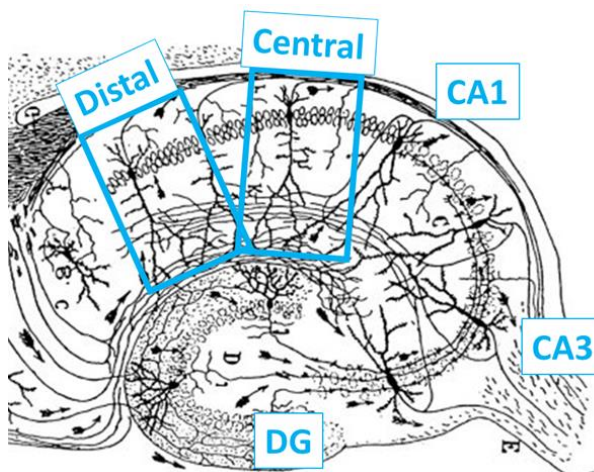


Figure 33: CA1 along the proximal-distal axis. Schematic representation of the hippocampus using a modified drawing by Ramon y Cajal showing orientative positions for the reconstructed and analyzed neurons in this section.

TgDyrk1A also show a similar positional dependency of their microstructure. However, even though the path length shows the same tendency to increase observed in wild-type (path length: distal $131 \pm 24 \mu\text{m}$ vs. central $150 \pm 22 \mu\text{m}$), complexity shows the opposite tendency, being increased in central positions (maximum branching order: distal 12.5 ± 4.0 vs. central 16.7 ± 4.9).

Regarding genotype-dependent differences, the mean path length shows a tendency to be lower in TgDyrk1A neurons vs wild-type for both distal ($131 \pm 24 \mu\text{m}$ vs. $185 \pm 25 \mu\text{m}$) and central ($150 \pm 22 \mu\text{m}$ vs. $203 \pm 25 \mu\text{m}$) positions ($t=3.35$, $p=0.057$; and $t=4.18$, $p=0.27$

respectively). However, the maximum branching order shows a tendency to be lower in distal TgDyrk1A neurons (12.5 ± 4.0 vs. 17.7 ± 3.3 ; $t=1.68$, $p=0.20$) while in central positions this tendency is lost (16.7 ± 4.9 vs. 14.7 ± 3.8 ; $t=-0.85$, $p=0.65$), leading to similar branch order distributions in the pooled analysis. Thus, TgDyrk1A neurons show stronger dysmorphology, with smaller and less complex neurons in distal CA1, while they show smaller trees with conserved dendritic complexity in the central region of the layer.

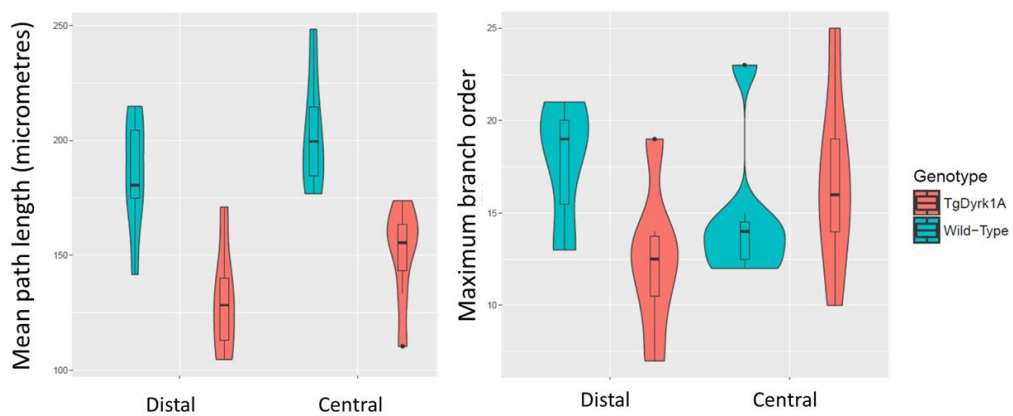


Figure 34: Genotype-dependent differences in neurite path length and branch order in TgDyrk1A. Box and violin plots representing mean path length (left) and maximum branch order (right) distributions for wild-type (blue) and TgDyrk1A (red) CA1 apical dendritic trees. The two labels in the x axis indicate the proximal-distal position along the pyramidal layer (see **Figure 33**).

2.3.2. Cellularity and volume variations along the antero-posterior axis of dorsal CA1 in TgDyrk1A

Stereological estimations

The representativeness of variations in neuromorphological properties that I have detected have to be considered in the scope of the volume and neuronal density of the layer. Specifically, Thy1 transgenic mice express fluorescent proteins in neuronal subpopulations but, even though its expression is seemingly consistent, quantitative studies estimating the percentage of fluorescent cells are lacking. To this aim, I obtained stereological volume and Thy1-labeled cell quantifications along the dorsal CA1 of wild-type and TgDyrk1A mice ($N=3$).

I first performed the same analysis using NeuN (a general marker of neurons) stained slices and found that neuronal densities show significant variation along the antero-posterior position, with an increase between Bregma -1.34 and -1.94 mm and a decrease between Bregma -1.94 and -2.34 mm ($3.78 \pm 0.68 \times 10^5$ cells/mm³, $5.64 \pm 0.63 \times 10^5$ mm³, $3.40 \pm 0.72 \times 10^5$ mm³ respectively; **Figure 35 right**), while the volume of the layer increases linearly (**Figure 35 left**). Conversely, TgDyrk1A mice show a slight tendency to decreased densities towards posterior Bregma, while the volume follows a similar increase in TgDyrk1A than in wild-type mice.

I compared the NeuN densities with the Thy1-labeled cell population in the wild-type (**Figure 35 middle**). Cell density increases from $0.89 \pm 0.27 \times 10^4$ cells/mm³ at Bregma -1.34 to a maximum at Bregma -1.94 ($1.66 \pm 0.94 \times 10^4$ cells/mm³), decreasing again towards Bregma -2.34 ($1.15 \pm 0.17 \times 10^4$ cells/mm³). Conversely, TgDyrk1A mice show a consistent increase in the amount of labeled cells ($1.45 \pm 0.68 \times 10^4$ cells/mm³, $1.97 \pm 0.91 \times 10^4$ cells/mm³, $2.39 \pm 0.77 \times 10^4$ cells/mm³; at Bregma -1.34, -1.94 and -2.34 respectively).

By comparing the Thy1 labeling with respect to NeuN positive cells, I found that the proportion of neurons labeled with Thy1 is in the range of 2-3%. Instead, TgDyrk1A mice show a constant Thy1+ neuronal density in all slices analyzed ($2.38 \pm 0.29 \times 10^5$ mm³, $2.56 \pm 0.34 \times 10^5$ mm³, $2.45 \pm 0.43 \times 10^5$ mm³; at Bregma -1.34, -1.94 and -2.34 respectively).

These results indicate that Thy1-labeled cells do not provide reliable estimates for neuronal density in the wild-type case, and suggest that Thy1-driven expression may be altered in TgDyrk1A.

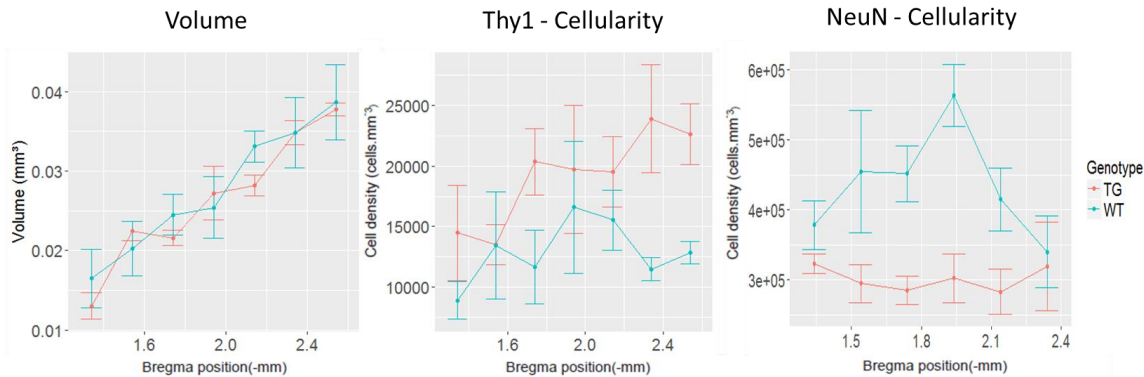


Figure 35: Stereological estimations for volume (left) and cellular density of Thy1-labeled (middle) and NeuN immunostained (right) neurons in CA1 pyramidal layer. Data are shown for wild-type (blue and black) and TgDyrk1A mice (red) estimated at increasing Bregma (in mm), as defined in Paxinos. Left panel: Volume estimations using Cavalieri. Note that increases linearly for both genotypes, with no genotype-dependent differences. Central panel: Thy1 labeled cellularity estimations obtained using the optical disector in newCAST. Thy1 estimations show a peak in cellularity at Bregma -1.94 in wild-type mice and a consistent increase in TgDyrk1A mice. Right panel: NeuN labeled cellularity estimations obtained using the optical disector in newCAST. Note that a maximum for NeuN stained neurons is detected in wild-type while no changes or even a slight decrease is detected in TgDyrk1A mice. Points indicate mean values and error bars standard deviations.

Population-based structural metrics through computational cellular and dendritic density mapping

In order to link the detailed information obtained by microscopy imaging of sliced histological samples with a population perspective, I have developed an analysis pipeline allowing 3D neuromorphological mapping in 2D sectioned brain.

I developed algorithms for obtaining 3D maps of the 2D population-based metrics (see **Section 2.2.2**): (1) the volume of neuronal layers, (2) the location and densities of cell bodies, and (3) the density of dendritic branches. Using the software I developed, I could obtain semi-automatic measures of the layer volume and cellular densities. Those semi-automatic quantifications broadly recapitulate the stereological measurements (**Figure 36**). Quantifications in the wild-type samples show again a convex curve along Bregma coordinates ($1.31 \pm 0.52 \times 10^4$ cells/mm³, $1.77 \pm 0.49 \times 10^4$ cells/mm³, $0.87 \pm 0.09 \times 10^4$ cells/mm³; at Bregma -1.34, -2.14 and -2.54 respectively), and TgDyrk1A show the consistent increase mentioned in the previous section ($1.22 \pm 0.89 \times 10^4$ cells/mm³, $2.61 \pm$

1.00×10^4 cells/mm³, $2.75 \pm 0.60 \times 10^4$ cells/mm³; at Bregma -1.34, -2.14 and -2.54 respectively).

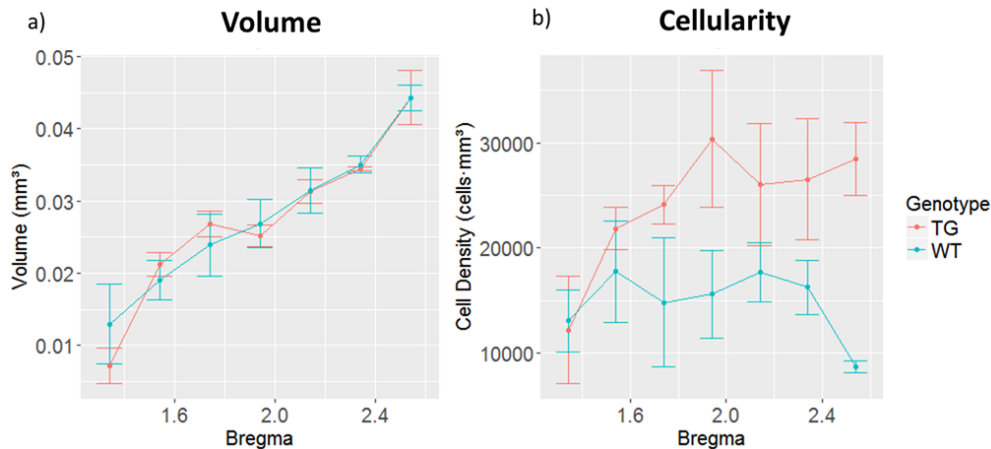


Figure 36: Volume and cellular density quantifications of CA1 pyramidal layer with the computational methods for population analysis. Volume shows a linear increase towards posterior Bregma for both wild-type (blue) and TgDyrk1A (red) mice. Cellular density in wild-type mice shows a plateau from Bregma -1.54 to -2.34, while in TgDyrk1A increases towards posterior positions. Points indicate mean values and error bars standard deviations.

In order to validate our computational method (**Section 2.2.2**), I obtained Bland-Altman plots for analyzing the agreement between our methods and the stereological quantifications of wild-type dorsal CA1 volume and cellularity. The mean and the difference between the two alternative measurements are obtained and plotted against each other. Also, lines showing the magnitude of 1.96 standard deviations with a 95% confidence interval are drawn in the plot (Altman & Bland, 1983).

The Bland-Altman plots of the pyramidal layer volume show (**Figure 37**) that differences between stereological and computational quantifications were distributed around 0, indicating that volumetric estimations were similar with both methods. Instead, the differences between stereological and computational cellularity estimations are distributed around ~ 3000 cells/mm³ difference, indicating that cellularity is systematically overestimated by our computational method.

It is important to note that for both volume and cellularity the variance is in the order of the smallest measurements and does not seem to depend on the magnitude of the volume and

cellularity values. Such high variance is found in both methods, as seen by the error bars (s.d. $\sim 0.5\text{--}1 \times 10^4$ cells/mm 3 ; **Figure 35** and **Figure 36**). This suggests that most probably the variance can be explained by the small size of our sample ($N=3$) rather than low precision in the measurements.

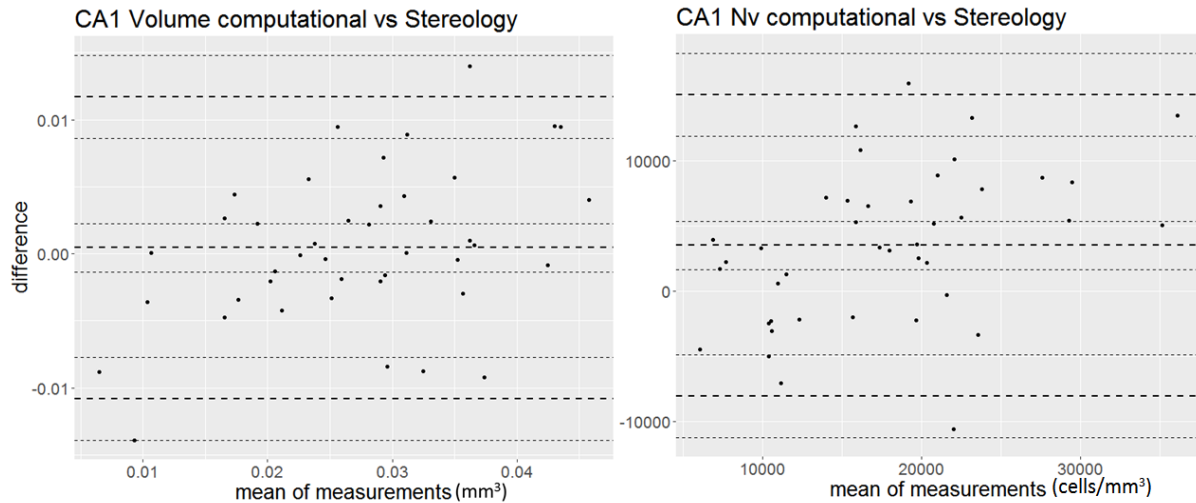


Figure 37: Bland-Altman plots of differences between the computational method and stereology vs. the mean of the two measurements. Plots for CA1 pyramidal layer volume (left) and cellular density (right) quantifications. Bold dashed lines in the centre of the plot represent the mean of the difference between the estimations while bold dashed lines in top and bottom of the plot represents 2 times the standard deviation of the mean value. Light dashed lines indicate the 95% confidence intervals around those quantities.

To assess whether our method is able to detect gross morphological properties with biological meaning, I compared the cellular and dendritic densities between hippocampal layers CA1 and CA3. The marked reduction in CA3 cell density (**Figure 38** left), along with the quantifications validated with stereology in CA1, show that our method captures relevant changes in cellular density. Similarly, to assess whether our method for dendritic density quantification is meaningful, I compared the dendritic occupancy ratio between CA1 and CA3 after normalizing the amount of measured dendrites by the amount of labeled cells. The ratio between CA3 and CA1 is 1.46, indicating higher dendritic occupancy as seen in previous estimations found in the literature.

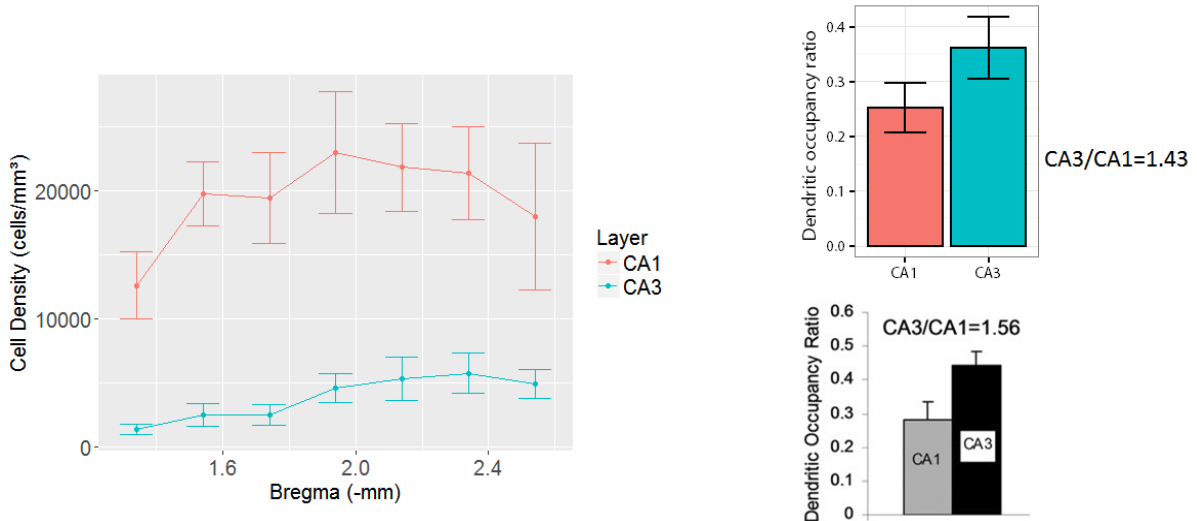


Figure 38: Cell density and dendritic occupancy in CA1 and CA3. (Left) Cellular density quantifications of CA1 (red) and CA3 (blue) pyramidal layers with the computational methods I developed. Points indicate mean values and error bars standard deviations. (Right) Dendritic occupancy ratio in CA1 and CA3 as calculated by our dendritic density measurements (up) and as estimated by Ropireddy, Bachus, and Ascoli 2012. Bars indicate mean values and error bars standard deviations.

In order to assess to what extent the population-based dendritic density maps are representative of single neuron dendritic tree morphology, I have compared measurements done with the classical Sholl analysis and our modified-Sholl method in synthetic 2D trees arranged in a homogeneous layer.

A 2D projection of a pyramidal neuron schematic representation was used as a proof-of-concept. The dendritic density distribution (Sholl analysis) of a binary bitmap of the image was quantified using the *Sholl Analysis* ImageJ plugin (Ferreira et al., 2014). The same bitmap image was analysed using the dendritic density quantification method I developed. In the latter, instead of quantifying the number of dendrites crossing concentric circles, I measure the quantity of branches crossing lines parallel to the somatic layer (see **Figure 39** left column). A population of cloned trees was obtained by generating copies of the 2D tree projection and arranging the trees along a straight line (see **Figure 39** left column, bottom row).

The analysis of synthetic 2D trees shows that both Sholl's and our method give comparable signatures ($k=1.62$, $int=-2.04$, $R^2=0.951$ for the Sholl analysis and $k=1.70$, $int=-1.64$,

$R^2=0.947$ for our method). When a population of cloned trees is analyzed with our method, the dendritic density signature is still clear ($k=1.77$, $\text{int}=-1.48$, $R^2=0.958$). Dendritic tree subregions can be appreciated in the modified-Sholl Linear fit (i.e. *stratum radiatum* and *lacunosum*; **Figure 39** middle column). These results indicate that the method I developed for measuring population-based dendritic density partially captures the morphology of the trees forming the layer.

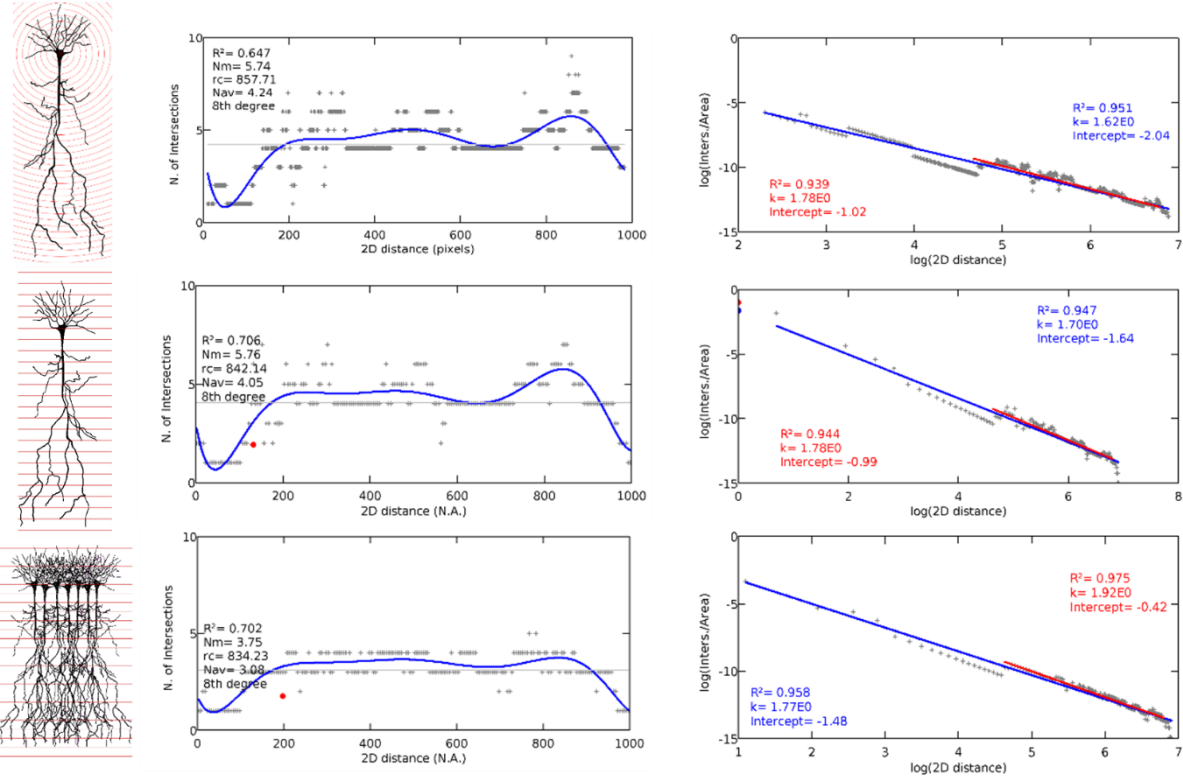


Figure 39: Comparison between single-cell and population-based Sholl analyses. (Left) Schematic representations of the analyses. (Middle) Linear Sholl plot of the number of intersections in function of the distance to the soma, a polynomial fit (blue and black parameters). (Right) Loglog Sholl analysis plot of the logarithm of the number of intersections per area versus the logarithm of the distance to the soma. In blue and red linear fit and parameters for a 95% of the data points and all points respectively. (Top) Single-cell default Sholl analysis. Analysis done only for the apical tree.

Voxel-based morphometry in dendritic density maps recapitulates single-neuron dendritic alterations

The neuronal reconstruction and stereological measurements obtained, highlight the fact that the percentage of cells labeled with Thy1 is very low and that there is a high within-cell variability. Thus, sampling small numbers of neurons is not representative for neurons throughout neuronal layers. To overcome this problem I here assumed that Thy1 labeling defines a Single-cell class.

To study their morphological properties from a population perspective, I use the computational methods I developed for quantifying cell and dendritic density (see **Section 2.2.2**) and generating 3D maps. As part of my method, I create a standardized spatial registration to a common coordinate framework for the analyzed samples, controlling for spatial variability and physical deformations that commonly arise during sample processing. The 3D mapping of those features is inspired in the field of neuroimaging, where statistical differences between groups of datasets are identified in a voxel-based manner. Thus, the generated maps allow neuroimaging-like 3D statistical comparisons among sample groups by the application of methods based on Voxel-Based-Morphometry (VBM) (N. S. White, Alkire, & Haier, 2003).

As a proof of concept, I used the analysis pipeline exposed in **Section 2.2.2** in two groups (wild-type vs TgDyrk1A; N=4) of Thy1-labeled samples to map cellular and dendritic densities across the dorsal CA1 (Bregma -1.34 to -2.34). Even though the statistical power of our analysis is too low to identify significant differences after the False Discovery Rate analysis, **Figure 40** shows the t-statistic of a voxel-wise linear model testing whether the genotype of the samples predicts (wild-type respect to TgDyrk1A; voxels with $t>0.83$, have a 20% probability of being false discoveries, **Table 7**) the measured dendritic density values of each voxel along the antero-posterior axis in dorsal CA1. A close-up at Bregma -1.94 shows a tendency to increased dendritic density in distal CA1 of wild-type mice and slightly decreased in proximal CA1. The results in distal CA1 are consistent with the lower dendritic complexity observed in our single-neuron reconstructions (**Figure 34**).

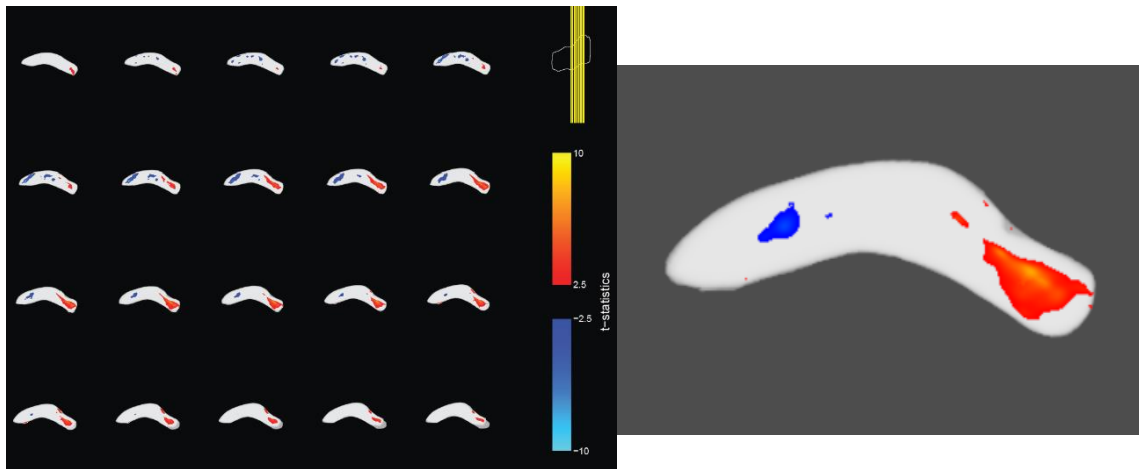


Figure 40: VBM analysis of dendritic density in CA1 from wild-type vs. TgDyrk1A mice. (Left) Series of coronal slices from Bregma -1.54 to -2.34. The colored scales show positive (red) and negative (blue) values for the t-statistic of the linear model applied to each voxel. (Right) Close-up visualization to a coronal CA1 slice at Bregma -1.94. Values $t < 4.83$ have been masked in the images.

Table 7: FDR analysis of the VBM dendritic density in CA1 comparison between wild-type vs. TgDyrk1A mice. The table summarizes the F-statistic, the t intercept and its value for various false discovery rates.

FDR	F-statistic	tvalue-(Intercept)	tvalue-ConditionWT
0.01	NA	3.401163	NA
0.05	NA	2.321877	NA
0.1	86.34038	1.867018	9.291953
0.15	65.49135	1.598359	8.092672
0.2	23.33567	1.401925	4.830701

Rewiring effects of environmental enrichment in CA1 apical dendritic trees: proof of concept

Thus, our population-based analysis can be used to identify dendritic complexity variations throughout neuronal layers. Here I used this analysis to assess whether environmental enrichment could be rewiring CA1 neuromorphology. By focusing on the distal region seen to have lower dendritic density in TgDyrk1A, I obtained “layer-Sholl” plots along the layer normal axis (from *stratum lacunosum*, through *stratum radiatum* until *stratum oriens*). Plotting the dendritic density obtained in the maps I generated, I can observe a dendritic signature characteristic from CA1 pyramidal neurons. Even though the tendencies are not significant ($N=3$), the plots show smaller and less complex *stratum radiatum* in TgDyrk1A mice compared to wild-types. Both TgDyrk1A and wild-type mice show an increase in dendritic complexity

in the *stratum radiatum* upon environmental enrichment. In the case of the environmentally enriched wild-types, the analysis shows a reduction of the span in *stratum lacunosum* and an increase in dendritic density in *stratum oriens* (**Figure 41**).

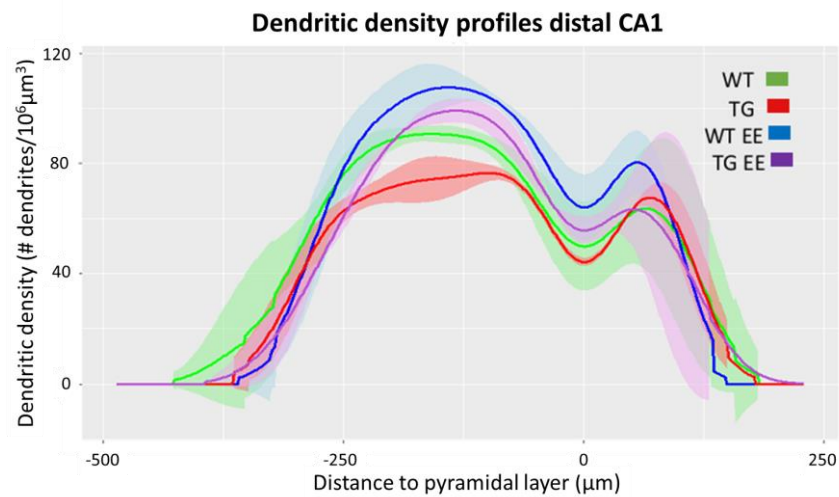


Figure 41: Dendritic density plot for distal CA1. Projection of the voxel values obtained from the CA1 dendritic density maps of wild-type (green), TgDyrk1A (red), and both groups upon environmental enrichment (blue and purple respectively). Mean (line) \pm S.E.M. (shade) is represented.

2.3.3. Development of computational tools for generative modeling of 3D neuronal circuits

To interrogate the organizational principles underlying the architecture of brain networks, I developed a customizable simulation environment (**Figure 42**) that allows to directly investigate how morphostructural features of brain circuits sculpt the emergent functional activity, and quantify the effects of targeted *in silico* perturbations. In that way, the model offers the unique opportunity to define the functional relevance of the network morphospace underlying the brain circuit of interest.

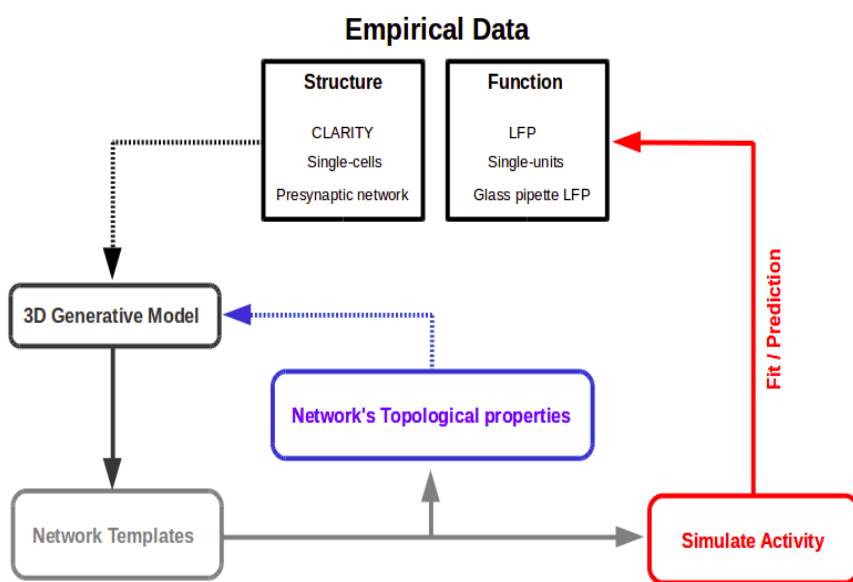


Figure 42: Our aim is to use population-based structural properties to parametrize a generative model leading to realistic network templates. These will be used to quantify topological properties of the network at an unprecedented level of detail, and enable posterior dynamical activity simulation. These properties depend on the morphostructural parameters used to generate the templates, which can be manipulated to obtain new templates showing desired topological characteristics, allowing to simulate network activity after targeted perturbation of the underlying topology.

My approach builds upon existing tools, supplying an easy-to-use and customizable unified toolkit to obtain, manipulate and visualize realistic 3D templates of network connectivity from population and single-cell structural data.

The model integrates self-developed MATLAB scripts and functionalities of the Trees Toolbox (Cuntz et al., 2011), and consists on a generative model of circuit connectivity in defined synthetic 3D Regions Of Interest (in our case, the layers of the hippocampal

trisynaptic circuit). This model can incorporate realistic neuromorphological features both at the single-cell and at the population level.

First, ROI segmentations are used to define a 3D synthetic space in Matlab. This space is formed by multi-resolution HDF5 3D matrices representing the simulated region. Regions of the space that can be occupied by somata, dendritic trees or axonal projections are labeled with integer indices. Using the HDF5 memory-mapped format allows to generate volumes as large as needed with on-the-fly compression, scalable and parallelizable access and processing of subvolumes.

I instantiated empty pyramidal layers using synthetic 3D ROIs of the layers of the hippocampal trisynaptic circuit, in Matlab (see methods). In this model I incorporated realistic neuromorphological features both at the single-cell and at the population level. Specifically, I used a parallel algorithm to locate spherical somata in the pyramidal layers (DG, CA3 and CA1 in our case) at a specified cell density obtained from our stereological countings. However, the cell density can be introduced either with a single homogeneous value, or by constraining it locally using cell density maps. Given that the soma location is done in local subvolumes, the local density can easily be adjusted in function of experimental 3D cellularity maps. Once each soma was located, its coordinates and the tangential angle to the dendritic layer boundary were saved for the posterior orientation and embedding of dendritic trees. At the same time, a supplementary HDF5 volume stored, in each voxel of the synthetic space, a neuronal identification number. Scanning for spatially close pairs of voxels belonging to different neurons allowed the generation of the connectivity matrix at the end of the instantiation.

Based on groups of single neuron *.swc experimental reconstructions obtained from wild type animals aligned along their principal axis, a 3D branch density cloud for a stereotypical morphology (e.g. CA1 dendritic or axonal tree) was generated with the *gdens_tree* function using the Trees Toolbox.

To obtain arbitrarily large neuronal populations, the dendritic density cloud was then used to generate clones. This was done by obtaining a subset of points in a 3D space. The probability of selecting a specific coordinate was given by the 3D branch density cloud. Thus,

coordinates in regions with high dendritic density have more probability to be chosen. Each new clone was generated using the obtained set of points and the *xMST_tree* function, which generates a minimum spanning tree connecting the selected points.

This procedure allowed not only to generate as many clones as needed to fill any neuronal layer, but also to modify the morphological properties of the trees by modulating the branch density clouds, the amount of points used to generate the trees and the options of the *xMST_tree* function. By scaling the branch density cloud with a population-based experimental dendritic density map obtained from either histological sections (see **Section 2.2.2**) or 3D imaging data (Chapter III), the tree embedding is constrained across neuronal layers, e.g. a thinner neuronal layer would imply smaller trees and a less intense dendritic density map, less complex trees.

Each neuron grows first an axon by translating (to the soma coordinates) and rotating (along the direction tangential to the layer) an axonal tree clone obtained as specified above. The translated and rotated tree is embedded by indexing free voxels in the HDF5 volume and taking into account the radius of the tree segments. An equivalent procedure is used to grow dendritic trees. When a tree segment intersects another, the minimum circumventing path is found by obtaining an obstacle distance map and performing a 3D fast marching between the two points of the tree that remain unconnected with the *perform_fmstar_3d* Matlab function.

Once axonal and dendritic trees were embedded, the HDF5 volume was visualized with Vaa3D. Finally, the populated synthetic space generated a connectivity matrix based on axon-dendrite, axon-soma, dendrite-dendrite and axon-axon pairs proximity (Stepanyants & Chklovskii, 2005) for all the synthetic cells. I introduced information about dendritic tree properties (such as cell type, branch order, distance from the soma, spine densities etc.) that could modulate synaptic contact probability.

Generation of realistic trisynaptic circuit templates

Even though I could not present here an exploration in the generative model I have developed, the developed software allows the synthetic instantiation of circuits I am interested in. **Figure 43** shows a snapshot of a 3D rendering of the trisynaptic circuit in dorsal CA1. The model allows to generate circuits based on minimal input: Dendritic, somatic and axonal layer segmentations, cellular density values, and a group of tree reconstructions.

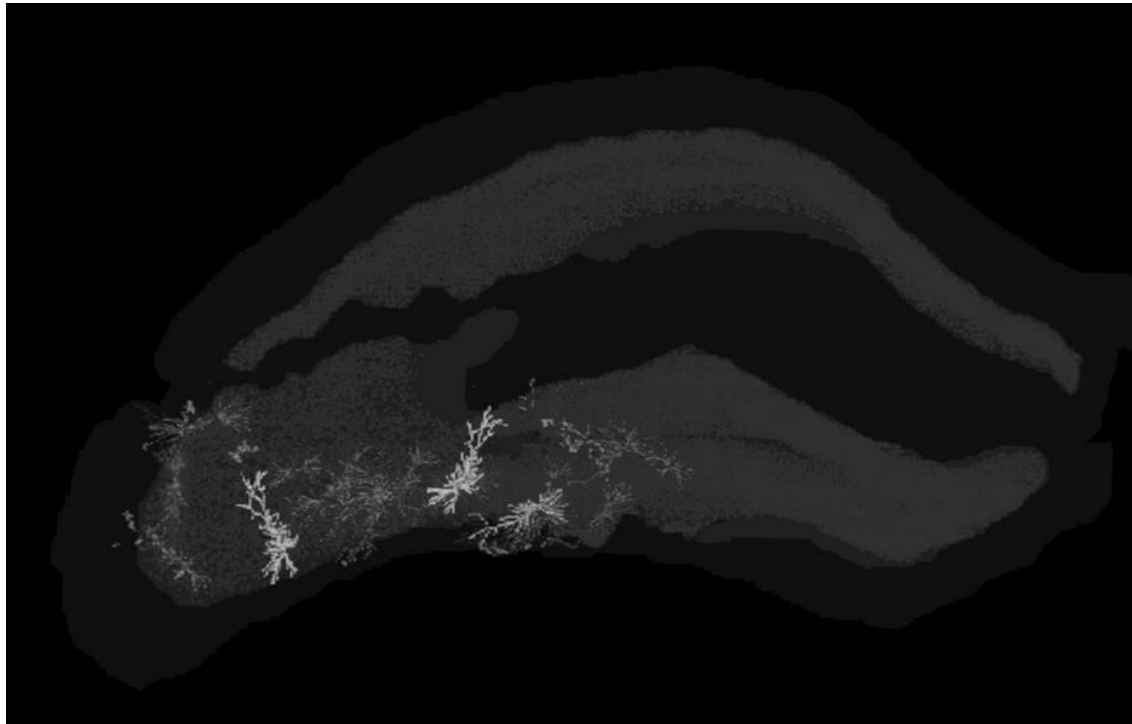


Figure 43: 3D model for the instantiation of biologically realistic neuronal circuitry. An overview of an instantiation of the hippocampus. The levels of grey indicate the layer segmentations and instantiated nuclei and, with increased brightness 10 embedded neurons.

Programming environment

The development of the computational modeling framework required Matlab (version 2014b) including the Trees and the Statistics Toolboxes. A repository with the source code and all the Matlab functions required for compilation can be found at (https://bitbucket.org/linusmg/nem4o-generative_model)

2.4. Discussion and conclusions

Overall, the work done in this Chapter contributes to two main aspects: first, the characterization of neuromorphological properties by taking into account within-class variability in wild-type and TgDyrk1A mice. Second, the development of computational methods to visualize, quantify and incorporate population-based neuromorphological quantification methods in a neuronal circuitry simulation framework.

Dendritic architecture of TgDyrk1A CA1 apical trees

The results presented in Chapter I suggest that DS mouse models have suboptimal dendritic architecture, both for the integration of synaptic signals and the storage of memories. One of the questions that arises in the study of complex phenotypes found in DS mouse models is to what extent the alterations found in a given cell-type or brain region can be generalized to the region or even the whole brain. To test whether the architectural alterations that could explain other behavioral impairments (such as reduced spatial and contextual learning and memory abilities) are the same as the alterations found in the cortex, I assessed whether the single-neuron architecture of CA1 apical dendritic trees has the same kind of suboptimal wiring than the cortical layer II/III basal trees.

I found that dendritic morphologies of both wild-type and TgDyrk1A mice follow almost exactly a 2/3 power law between the total length and the number of branch points. Indicating that their space filling and routing efficiency is optimal. However, TgDyrk1A neurons have smaller spanning volume, implying that their storage capacity is significantly reduced. Thus, these results support that a signal integration impairment does not exist and that TgDyrk1A CA1 neurons may have suboptimal architecture for storage capacity. Those results are supported by lower performance in the Morris water maze task for this DS mouse model (Pons-Espinal et al., 2013). However, discarding an impaired routing efficiency in such neurons is challenging. To my knowledge, neither behavioral tasks related to the processing speed in the retrieval of memories, nor electrophysiological studies assessing alterations of the rhythmicity in the TgDyrk1A CA1 layer have been done.

While I have not assessed yet the exploration of Pareto optimality with CA1 dendritic tree reconstructions, the morphological alterations found, and the estimation of a reduced storage capacity, point at a putative suboptimal architecture for storing memories.

Altogether, the dendritic tree alterations found suggest that there is no impairment in the signal integration efficiency of TgDyrk1A CA1 neurons, and that the transgenic mouse model could have an imbalance in the capacity for storing input-output patterns from afferent connections to the *stratum radiatum* and *stratum lacunosum* (including long-range incoming axons from CA3 and the Entorhinal Cortex, and short-range CA1 intrinsic modulation).

Morphological within-class variability of hippocampal neurons

Even though anatomical inhomogeneities across neuronal layers have been well known for decades (Ahmad & Henikoff, 2002; Jinno & Kosaka, 2009; Rihn & Claiborne, 1990) but largely overlooked in the study of neuronal circuits, assuming they are irrelevant for function. Recent evidence suggests that functional segregations is linked with such variations (Igarashi et al., 2014). My systematic study of dendritic trees in a small region of the dorsal hippocampus suggests that within-class variability depends on the neuron location along the proximal-distal axis. However, the power of our analysis is very low due to the small numbers of neurons per location. Thus, a completion (ongoing work) of the dataset is necessary to detect significant differences among positions, and dissect the variability of within-class neuromorphological properties along the proximal-distal and antero-posterior axes of dorsal CA1.

Nevertheless, interestingly, I found that dendritic tree span is reduced in the neurons of TgDyrk1A mice both in distal and central positions along the proximal-distal axis, while dendritic complexity is selectively reduced in the distal region of the dorsal CA1. Those differences are concomitant with a marked behavioral impairment in single object recognition tests (Pons-Espinal et al., 2013), and a mild impairment in spatial learning (Torre et al., 2014). Given the recent evidence for functional segregation between distal (contextual) and proximal (spatial) regions of CA1 (Igarashi et al., 2014), this suggests that the reduced

dendritic branching reaching the *stratum lacunosum* observed in TgDyrk1A neurons could be impairing the integration of sensory information provided by entorhinal cortex afferents.

Cellularity along the antero-posterior axis of CA1 in TgDyrk1A

Moreover, the stereological analysis of NeuN-immunostained neurons in dorsal CA1, indicates that gross morphological features, i.e. cellularity and volume, of the pyramidal layer tend to vary with antero-posterior coordinates at a local spatial scale ($\sim 500\mu\text{m}$). While cellularity variations along the septo-temporal axis of the hippocampus had been described at the scale of few millimetres (Gaarskjaer, 1978; Jinno & Kosaka, 2009), I show that those variations can be relevant at a shorter spatial range. Thus, the position-dependent variability is a confounding factor to take into account when analyzing the properties of neuronal populations even locally.

Computational methods for population-based analysis of cellular and dendritic density

To overcome the small number sampling issue, population based labelings (such as Thy1 induced fluorescent protein expression) can provide a holistic perspective to properties of neuronal layers, while tailoring the studies by constraining the analysis to specific cell classes. However, our stereological quantifications using NeuN and Thy1-labeled cells show that selecting a specific neuronal class as a representative set must be done carefully. In our study, cell density quantifications differ between the two labelings, and the Thy1 expression pattern in dorsal CA1 seems to be affected by the transgenic expression of Dyrk1A in the studied DS mouse model. Thus, a systematic validation and cautious interpretation of conclusions drawn from Thy1-dependent population-based labeling is needed.

In order to tackle the population-based measurements that can overcome the issue of small number samplings, and taking into account that stereological measurements have too low throughput for systematic detailed studies, I explored the development of population-based computational analysis tools. I developed algorithms for mapping cellular and dendritic density on Thy1-labeled neuronal populations. The obtained quantifications are consistent with the stereological measurements and our single-neuron morphology analysis. Thus, being sensitive enough to identify local variations. This unprecedented sensitivity suggests that the

developed tools, beyond the issues related to the Thy1 labeling, allow comparative morphological analysis with unprecedented detail that could help understanding functional segregation, explaining specific behavioral traits in the TgDyrk1A DS mouse model.

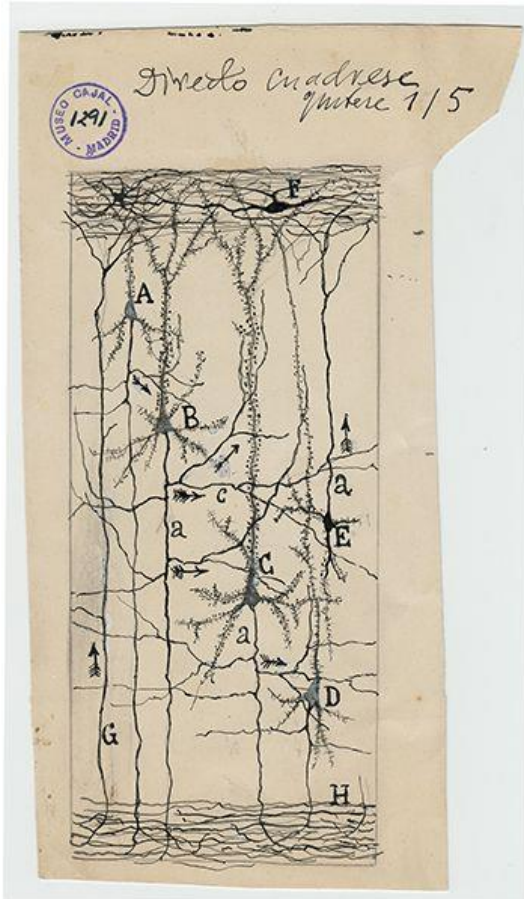
Previous studies have shown an increase in dendritic tree size and complexity in CA1 pyramidal neurons upon environmental enrichment in wild-type mice (Beauquis et al., 2010) I observed increased dendritic density in the *stratum radiatum* and *stratum lacunosum* fields. However, our data suggests that the span of the dendritic trees is smaller. Our results show a similar tendency in the case of TgDyrk1A mice. This recovery, mainly relevant for the *stratum lacunosum* region of the tree, could explain cognitive improvement in spatial memory tasks by environmental enrichment. Ongoing experiments to obtain single neuron reconstructions in environmental enrichment conditions will confirm the tendencies seen in the population-based analysis.

Generation of realistic trisynaptic circuits

Despite the extensive and ever-growing literature about the functional implications of topological properties of large-scale anatomical brain networks, the methodological limitations of the microscopic description of neuronal morphology have bounded the ability to analyze and characterize the topological organization of brain microcircuits from a systems perspective. Computational attempts to reproducing *in silico* the dynamical properties exhibited by different brain regions (Blue Brain Project, Markram 2006; Human Brain Project, Shepherd et al. 1998) do not provide the versatility needed to assess the impact of subtle neuromorphological alterations, neither the possibility of parameterizing the models with CLARITY experimental data. Thus, the neuroscientific community lacks a simple open-source extensible tool able to bridge this gap.

Even though our modeling framework has not been tested yet, our analysis in Chapter I suggests that interesting outcomes will be obtained once the model is instantiated, the morphospace explored, and the wild-type and TgDyrk1A cases parameterized based on experimental. I think that, together with the population-based computational analysis tools I developed, the studies enabled by the first steps presented here will be relevant for understanding functional segregation and, ultimately, the impact of subtle neuromorphological properties on the computations performed by specific neuronal layers.

3. CHAPTER III. RECONSTRUCTING AND MODELING THE TRANSPARENT WHOLE BRAIN



The “arrows” of Cajal. The drawing represents with arrows direction of information flow in cortical neurons. Courtesy of Instituto Cajal.

"To understand mental activity it is necessary to understand molecular modifications and changes in neuronal relationships. Of course one must know the complete and exact histology of cerebral centres, and their tracts, but that is not enough."

Santiago Ramón y Cajal

3.1. Introduction

Charting cellular localizations, projections, and network activity throughout the whole brain is a mandatory step to understand network properties, but the tools for combining these levels of description are not available yet. Many efforts in the Neuroscience field are devoted to build cellular-resolution, brain-wide neuroanatomical atlases of the mouse brain, but technical limitation to obtain whole brain structural information with microscopic resolution has hampered our capability of understanding micro-connectomics at a system level. I are usually faced with having either poor spatial scale (examining only a small part of a larger brain network) or poor spatial resolution (examining a large network but at the cost of understanding microstructure). Most experiments still involve slicing the brain into relatively thin sections (20-50 μm) before histological staining, imaging, and quantification. These techniques have yielded very good results for atlasing (e.g. Allen Brain Atlas) and are still being used in high-throughput mapping projects. For example, the MouseLight Project (<https://www.janelia.org/project-team/mouselight>) of Janelia that is mapping the complete axonal projections of individual neurons across the entire mouse brain (Figure 44). However, sectioning the brain has its own drawbacks. For instance, light continues to be scattered even within relatively thin brain sections (limiting axial resolution), sectioning may damage and/or distort the tissue, and much of the rich structural information may be lost in sectioned tissue, even if attempts are made to accurately reconstruct 3D images.

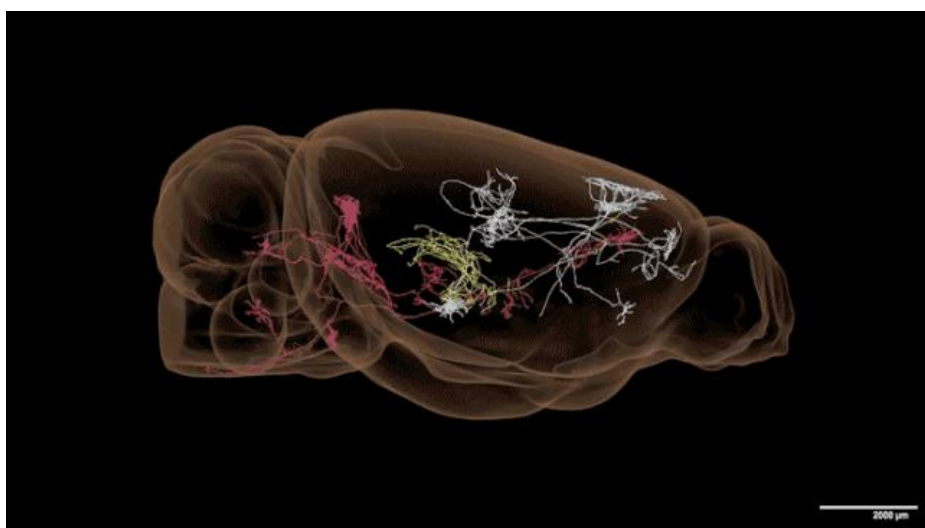


Figure 44: 3D structural analysis of whole mouse brains. A reconstruction of three neurons that span the mouse brain. [MOUSELIGHT PROJECT TEAM](#), Janelia Research Campus. Scale bar = 2000 μm .

A recent technique called CLARITY, allows rendering intact biological tissues transparent by lipid-exchange, by embedding the tissue in an anatomically rigid, imaging/immunostaining compatible, tissue hydrogel (Chung et al., 2013). The technique overcomes existing limitations to produce transparent tissue without quenching endogenous fluorescence, and this tissue can also be labeled via immunohistochemistry. This provides a unique opportunity to bridge anatomical scales from subcellular to whole brain. In the last years, a number of research groups have implemented new tissue clearing techniques (CLARITY, CUBIC, Lumos, STP, 3DISCO, Sca/e, or SeeDB) allowing comprehensive microscopic imaging of rodent whole brains. The power of these techniques relies on bridging *de facto* the macroscopic and microscopic scale descriptions of the system, allowing high-throughput imaging of whole brains with cellular resolution.

The CLARITY protocol was originally published by the Deisseroth lab (Chung et al. 2013; see **Figure 45**) and methods to optimize the imaging component subsequently added (Tomer, Ye, Hsueh, & Deisseroth, 2014). A modified CLARITY protocol, using only passive clearing techniques to avoid the possible tissue damage produced by electrophoretic current, was also recently described (Tomer et al., 2014; Yang et al., 2014; Zhang et al., 2014). However, to effectively take advantage of CLARITY, it is crucial to obtain brains that are highly transparent (for deep imaging) and rigid (to facilitate registration to a reference atlas). While passive clearing may produce transparent tissue, electrophoresis is necessary to achieve the full potential of CLARITY. The original protocol for CLARITY proposes FocusClear as a refractive index matching (RIM) medium for clear imaging, as well as a glycerol solution as an alternative (Chung et al., 2013). However, previous results in the lab show that the resolution decreases when trying to track axons on more than 3 mm in depth in the sample. Different media have been reported in order to improve the transparency and, so, the resolution in depth, such as a solution based on diatrizoic acid (M. J. Hawrylycz et al., 2012; Kim et al., 2015).

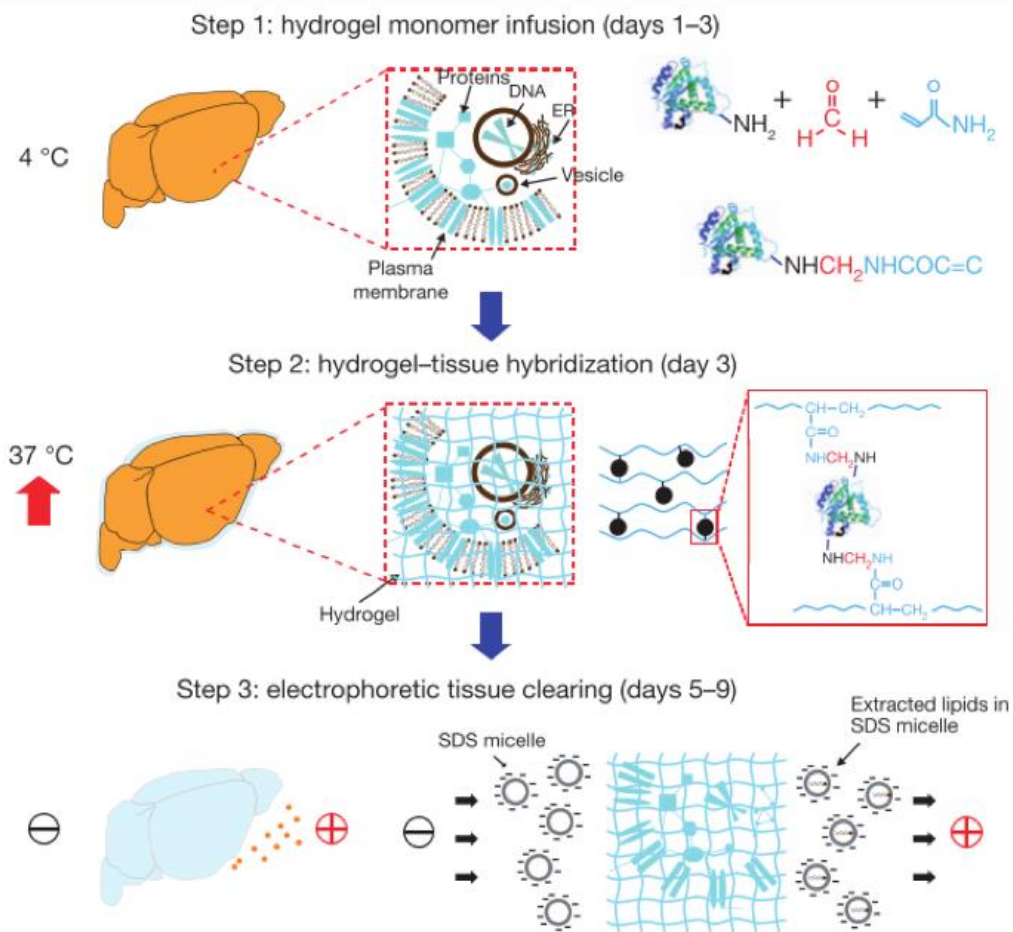


Figure 45: Schematic representation of CLARITY protocol basis. Tissue is crosslinked with formaldehyde (red) in the presence of hydrogel monomers (blue), covalently linking tissue elements to monomers that are then polymerized into a hydrogel mesh. Electric fields could be applied across the sample to actively transport ionic detergent micelles into the tissue, carrying the lipids out of the sample and leaving fine-structure and crosslinked biomolecules in place. Step 3 can also be done passively implying higher clearing time. Figure from (Chung et al., 2013).

Another limitation is that, up to date a relatively low effort has focused on developing standardized, extensible, and scalable analysis tools. Although whole brain imaging would enable multiscale and population-based analysis, at the moment many data arise from classical neuromorphological studies by histological sectioning. In order to avoid reductionist or homogeneity-assuming perspectives, this work aims to develop a computational toolset for multiscale and population-based characterization of brain regions by brain slices data reconstruction.

The aim of this part of my Thesis was to implement a new cost-efficient CLARITY protocol, and to start filling the analysis gap by developing a suite of unified software to construct multiscale structure-function maps from brain-clearing experiments, with specific

subworkflows for understanding topological dependencies on a brain-wide scale. The set of tools I propose are a first step towards a systems perspective description of neuronal circuits' microscopic structural and population-based properties. Such framework can help to link the extensive kinds of information available from cellular and molecular neuroscience with whole brain perspective studies. Besides, the proposed suite of tools can be used to bridge structural data with functional descriptions.

3.2. Methods

The aim of this chapter was to integrate the approaches and tools developed in chapters I and II in the scope of studying whole neuronal circuits in the mouse brain. To this end, a set of tools for imaging, analyzing and modeling whole brain data needed to be implemented. I first implemented and modified the CLARITY technique in our lab. To reach high quality whole mouse brain imaging I assessed existing alternatives for steps of the experimental protocol important for imaging quality and optimized them. Second, I searched, modified and gathered together a set of tools for the visualization and analysis of CLARITY datasets, setting up an analysis pipeline for whole brain imaging. Finally, I developed a 3D generative modeling platform for the instantiation of multi-scale neuronal networks, able to account for fine details in neuronal architecture, to be parameterized accounting CLARITY experimental data, and to simulate neuronal connectivity in arbitrarily large volumes.

3.2.1. Brain clearing technique (CLARITY)

To implement and optimize the CLARITY technique, I used the same Thy1-Yellow Fluorescent Protein (YFP) transgenic mice (strain B6.Cg-Tg(Thy1-YFPH)2Jrs/J n°003782; The Jackson Laboratories) used in Chapter II. Housing conditions, breeding and genotyping are described in the Methods Section of Chapter II. All animal procedures and housing conditions followed the guidelines of local and European regulations.

Brain sample obtention and clearing

For the clearing experiments I used eighteen 3-month-old adult wild-type mice. The mice were sacrificed and transcardially perfused with cold phosphate buffered saline (PBS), followed by cold CLARITY hydrogel solution, prepared as previously described (Chung, K.; Wallace et al., 2013). The brains were removed from the skull, immersed in 20 mL of hydrogel solution and stored at 4°C shielded from light. After 2-3 days at 4°C, hydrogel polymerization was induced by 3h incubation at 37°C. Contact with oxygen was prevented with a vegetal oil layer. Thereafter, the already polymerized surrounding hydrogel was removed. Entire brains were immersed in 50 mL of clearing solution (Chung, K.; Wallace et

al., 2013) and stored in a water bath at 45°C. Slices were arranged in a 48 well plate with 800 µL of clearing solution and stored in an incubator at 45°C. After 2 months of incubation in clearing solution for passive clearing, optical transparent brains were washed with 50 mL PBST (0.1% TritonX in 1X PBS) twice for 24 hours each, at 45°C. After that the samples were immersed in a Refractive Index Matching (RIM) medium for 2 days before imaging.

Refractive index matching (RIM) solution preparation and transparency evaluation

The first step was to optimize transparency in our samples. To this aim, I tested four RIM solutions: FocusClear, glycerol solution (Glycerol 87% + 2.5 mg/mL DABCO), diatrizoic acid solution (75 g diatrizoic acid, 70 g d-sorbitol and 23 g n-methyl-d-glucamine in 100 mL of water) and TDE solution (2,2-thiodiethanol 83% + 4 mg/mL n-methyl-d-glucamine). All reagents are from Sigma.

Transparency was evaluated on whole brain cleared samples under exposure to RIM media candidates. Four brain samples (N=4) were incubated with 50 mL of each RIM medium candidate during 4 days at 45°C. Transparency of the samples was assessed at days 2 and 4 after incubation by measuring the light transmittance. The samples were immersed in the corresponding medium in a Petri dish, which was situated on a white light source covered by a white paper with a printed grid. Images were taken by means of a stereomicroscope (LEICA MZ16F), using different sets of filters for increasing wavelengths: CFP (Cyan-Fluorescent Protein_excitation wavelengths (exc.) 426-446 nm, emission wavelengths (em.) 460-500 nm), GFP3 (Green-Fluorescent Protein 3_exc. 450-490 nm, em. 500-550 nm), DSR (DsRed_exc. 510-560 nm, em. 590-650 nm), Cy5 (exc. 590-650 nm, em. 663-738 nm). Also the total white light transmittance was evaluated by using no filter. Using ImageJ, the mean grey value was measured in the area occupied by the sample. This value was normalized by the mean grey value in the same area for the image taken, with the same filter and exposure conditions, when only the corresponding medium without the sample was in the Petri dish. Sharpness measurements were obtained by using the Matlab *sharpness* function (<https://es.mathworks.com/matlabcentral/fileexchange/32397-sharpness-estimation-from-image-gradients>). Sharpness is estimated by measuring the magnitude of intensity gradients in an image. The function was run on the images used for measuring the transmittance.

The deformation of the samples (Swelling Ratio) upon RIM incubation was assessed by measuring the linear expansion of the sample under exposure to each RIM media candidate. Measurements of pixel areas covered by the samples 2d and 4d after immersed in the RIM media candidates are normalized for pixel areas of images taken to the same samples at day 0 (0d) in PBS-T. The pixel area was measured by making polygonal selections around the brain contour were done using ImageJ tool.

Fluorescence signal to Noise Ratio

One of the possible problems in using specific RIM media is the loss of the sample fluorescence, and I had some problems with fluorescence loss after passive CLARITY. This is especially important for endogenous YFP, since I use transgenic mouse lines that express this fluorescent protein to visualize specific cell populations. Thus I aimed at finding optimum clearing protocol for genetically labeled neurons. In my experiments, I used cleared half brain coronal sections (1 mm) to assess the fluorescence signal under exposure to RIM media candidates. Four sections ($N=4$) of the same region were incubated in a 48 well plate with 800 μL of RIM media candidates at 45°C during 10 days. I assessed the fluorescence signal of the cleared sample at days 2 and 10. Stacks of 100 μm of depth with a step size of 2.98 μm were taken for each of the samples in the cortical area using a confocal microscope (Leica TCS SP5 CFS) with a 20x objective and the appropriate set of filter for YFP. All the imaging parameters were maintained constant for all the images. Z-projections at maximum intensity of the stacks were thresholded using Otsu's method (Otsu, 1979). Mean intensity and standard deviation were measured both in the thresholded zone and also in the background. These parameters were used to evaluate Contrast-to-Noise Ratio (CNR) as previously described (Magliaro et al., 2016).

3.2.2. CLARITY Whole-brain imaging and data preprocessing

I have developed a framework for visualization and analysis of 3D images of cleared brains. I combined existing open-source computational tools and self-developed scripts and developed simplified user interfaces for integrated processing, visualization, and analysis.

Imaging

Tissues cleared using the above methods were then imaged in 3D. Briefly, cleared whole brains were immersed in 50 mL of Diatrizoic Acid solution (DA; 75 g diatrizoic acid, 70 g d-sorbitol and 23 g n-methyl-d-glucamine in 100 mL of water) at 45°C for 48hr. After incubation in DA the samples were imaged in a custom-built Single Plane Illumination Microscopy (SPIM) set-up. SPIM is a fluorescence microscopy technique that uses a focused light-sheet to illuminate the specimen from the side. SPIM achieves excellent resolution at high penetration depths while being minimally invasive at the same time. SPIM offers a number of advantages over established techniques such as strongly reduced photo-bleaching, high dynamic range, and high acquisition speed. The idea behind SPIM and other light-sheet-based microscopy techniques is to illuminate the sample from the side in a well-defined volume around the focal plane of the detection optics. The microscope, built in James Sharpe's lab and used in collaboration with Jim Swoger, is designed to image 3D samples with sizes of about 1 cm. I used a detection lens with magnification 5x and a laser wavelength of 488 nm for fluorescence excitation. The sample is mounted to a micro-manipulation stage that allows translation in 3 dimensions and rotation about the vertical axis, to allow orientation for optimal imaging, inside a cuvette filled with 50 mL of RIM. The SPIM software has been written in Labview to control the instrument and automates scanning of samples that require up to 10s of thousands of individual images. Acquiring complete data sets covering a whole mouse brain hemisphere takes ~36h for a single-channel and generates ~0.5Tb, uncompressed data.

Tera-voxel sized dataset stitching

The most common format in which fluorescence microscopy data is obtained in neurobiology labs is adjacent image stacks covering the regions of interest. In case of being interested on features at the mesoscale or macroscale of the samples, the first necessary step is to stitch the tiled data obtaining a unique dataset for the whole system of interest (in our

case, the whole brain). The recently developed Terastitcher software allows this kind of preprocessing using small RAM amounts and by a user-friendly straightforward procedure that is compatible across platforms. Furthermore, it allows the export of the data in both the multi-resolution pyramid format used by Vaa3D Teramanager or single stacks in a variety of image formats that can then be used in any other image analysis software. This has been already assessed in Bria and Iannello, 2012.

Visualization

Once the dataset has been stitched a first visualization of the raw data is important in order to both check its quality and to allow the investigators to identify cues that can be informative of the analyzed samples and can orient subsequent analysis steps. As mentioned above there are currently two solutions for the visualization of teravoxel-sized imaging datasets, Vaa3D's TeraFly (Bria, Iannello, Onofri, & Peng, 2016) and Fiji's BigDataViewer (Pietzsch, Saalfeld, Preibisch, & Tomancak, 2015) plugins.

Segmentation

In the rodent brain case, the regions to be segmented are given by anatomical regions of the brain and are already well defined in atlases such as (Dong, 2008). However, the kind of processing performed here can also be compatible with self-generated compartmentalizations of any sample of interest.

Registration and template generation

As assessed in chapter II, the voxel-based statistical comparison of volumetric data requires both a reference space, and the spatial registration of the analyzed the datasets to the common reference. While the tools used in chapter II ANTs and Volgenmodel are the robust tools for spatial normalization and template generation, they are not devised to process teravoxel sized datasets. To overcome this problem I also used Fiji's BigWarp plugin (<https://imagej.net/BigWarp>), which allows landmark-based spatial registration of arbitrarily large datasets.

Mouse brain common coordinate framework

In order to instantiate our 3D generative model in a reference volume, I used the Allen Institute Common Coordinate Framework (CCF v3) of the adult (P56) mouse brain (M. Hawrylycz et al., 2011). The 10um precision volume with its segmentation labels was used. I

generated binary hippocampal reference volumes by isolating single labeled regions for DG (Molecular, granule cell and polymorph layers), CA3 (Stratum oriens, pyramidale and radiatum) and CA1 (Stratum oriens, pyramidale, radiatum and lacunosum) in Fiji. This was done by thresholding the original volume above and below the value of the label of interest. Multi-resolution copies of the obtained volumes were saved in the HDF5 format using Fiji (default parameters in the BigDataViewer plugin) as ready-to-use input files for the generative model.

Computational environment

A programming environment in a workstation running Ubuntu 16.04 was set in order to fulfill all necessary software and library dependencies, including: Python 2.7, Fiji (Schindelin et al., 2012), Vaa3D (Peng, Bria, Zhou, Iannello, & Long, 2014), Terastitcher (Bria & Iannello, 2012), MINC-TOOLS (Vincent et al., 2004), ANTS (Avants et al., 2009), nipype (Gorgolewski et al., 2011), Volgenmodel (Janke & Ullmann, 2015), R and RMINC. Additional Python wrappers and source-code can be found at (<https://bitbucket.org/linusmg/nem4o-analysis>). Big datasets were stored locally in a series of RAID system hard-drives (3x16GB WD MyBook Duo).

3.2.3. Statistical analysis

Data for transmittance, CNR and deformation were expressed as mean \pm S.E.M. Two-way analysis of variance (ANOVA) were performed using R commander package for Windows, version 3.1.1. In the case of transmittance, one ANOVA for each filter was performed, considering the factors medium and time. For both fluorescence and deformation, one ANOVA was done, considering the medium and the time as the factors. Effects for each factor were considered statistically significant when $p<0.05$. Bonferroni was used for post-hoc analysis when a significant, or a trend to, medium x time interaction was found ($p<0.09$).

Voxel-based comparisons of neuromorphological metric 3D maps were performed implementing the mixed-effect linear model in RMINC (version 1.4.2.1). Significance for observed relationships were assessed with a False Discovery Rate (FDR) analysis.

3.3. Results and discussion

3.3.1. Cost-effective optimization of tissue clearing techniques

I have implemented cost-effective optimizations in the CLARITY protocol achieving in-depth imaging quality improvement. Clearing of $\sim 2 \text{ cm}^3$ samples has been implemented in our lab on intact mouse brains achieving $> 5 \text{ mm}$ depth imaging with a custom-built Single Plane Illumination Microscope (SPIM).

Transparency

I tested brains cleared with the four candidate RIM media and compared their transparency as measured by light transmittance after two and four days of incubation, as compared to transmittance before incubation.

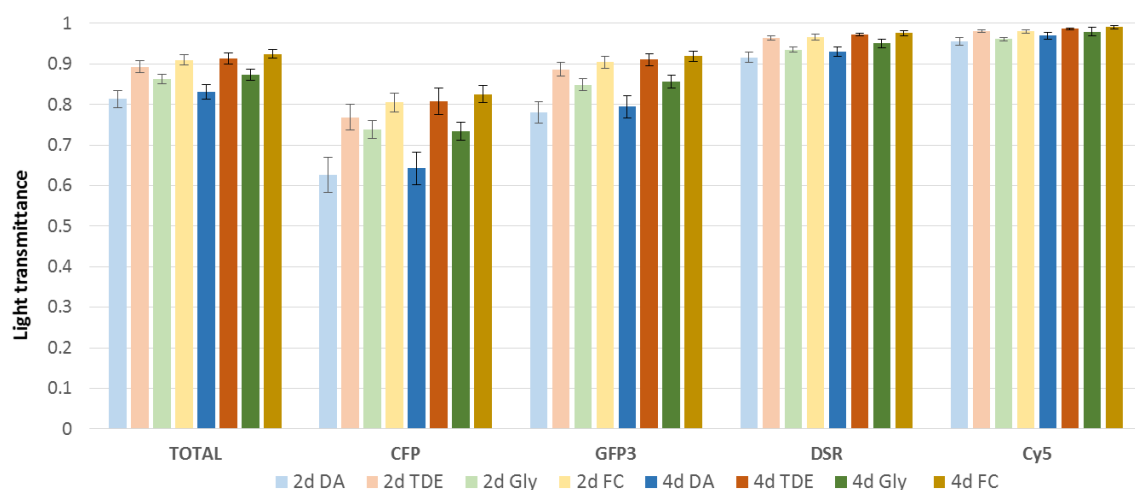


Figure 46: Comparison of transparency of RIM candidates. Light transmittance evaluated on different increasing wavelengths for the cleared samples under exposure to each of the four RIM media candidates (DA: diatrizoic acid based solution; FC: Focus Clear; Gly: glycerol-based solution; TDE: 2,2-thiodiethanol based solution). For each group the mean and the standard error are represented ($n=4$).

The results of the evaluation at different wavelengths reveals that samples exhibit better light transmittance at higher wavelengths and relative differences among media are maintained at different wavelengths (Figure 46). YFP has an excitation wavelength of 488-512 nm and an emission wavelength of 532-554 nm. In this regard, when imaging the endogenous fluorescence of the sample, values of transmittance will be considerably close to 1. Overall, it can be seen that 2'-Thiodiethanol (TDE) transparency is comparable to that of the original

proposed FocusClear (FC), being one of the best RIM medium regarding transmittance. The diatrizoic acid-based (DA) solution presents the lowest values of transmittance, and glycerol shows intermediate values. **Figure 48** shows a representative sample for each group before exposure to the RIM medium candidate. Quantitative measures are consistent with qualitative evaluation of the samples.

However, our observations when imaging whole brains in a SPIM setup were not consistent with these results, given that imaging in DA produced clear and sharp images through 6mm in depth in the samples (see **Figure 48** for a representative example). Thus, I revised the method for assessing transparency. Instead of using the transmittance, I measured the sharpness in the images. By normalizing this measure after RIM exposure to its value in PBS-T, I obtained a sharpness ratio with respect to the original conditions. The measurements obtained (**Figure 47**), shown that after 48hr incubations, 87%-Glycerol has the lowest sharpness ratio (1.09 ± 0.10), followed by DA (1.16 ± 0.03), while showing impressive results with 83%-TDE (1.41 ± 0.11). Unfortunately, due to its cost, I could not include FC in this experiment.

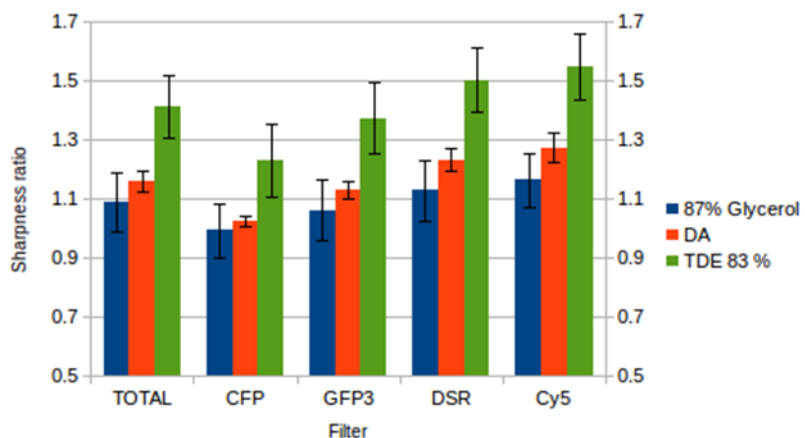


Figure 47: Comparison Sharpness ratio for RIM media candidates. Normalized sharpness evaluated on different increasing wavelengths for the cleared samples under exposure to three RIM media candidates (DA: diatrizoic acid based solution; Gly: glycerol-based solution; TDE: 2,2-thiodiethanol based solution). For each group the mean and the standard error are represented (n=4).

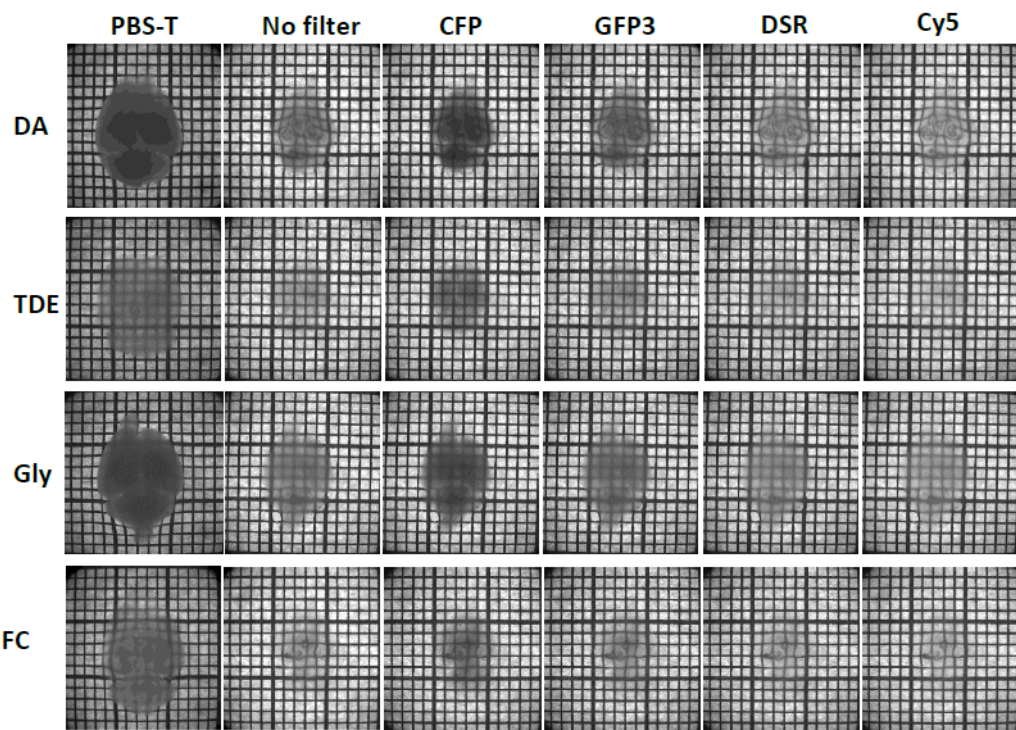


Figure 48: Stereomicroscope images for the assessment of sample transmittance under the different RIM media candidates. DA: diatrizoic acid based solution; FC: Focus Clear; Gly: glycerol-based solution; TDE: 2,2-thiodiethanol based solution. Samples are shown immersed in PBS-T at day 0 and after 2 days of incubation with the respective medium on day 2. Above the images the filters that were used to take the images on day 2 are indicated.

Fluorescence

Slices of the Thy1-YFP mouse brain were used to measure the signal quality after 2 and 10 days of immersion to RIM media candidates. Confocal microscope imaging shows that TDE causes a significant decrease in YFP signal after 2 days, being more evident after 10 days. TDE slices conserve the labelling in some regions of the cortex, although the intensity of the signal is decreased with respect to other media (**Figure 49**). Quantification of the signal quality by Contrast to Noise Ratio (CNR) (**Figure 50**) demonstrate that TDE caused complete quenching of the signal compared to the other media. In the case of TDE slices, images were taken in specific regions where labelling was found, so the CNR characterization is not a reliable measure for the signal quality in the whole brain. Measures for TDE after 10 days cannot be done because of lack of signal.

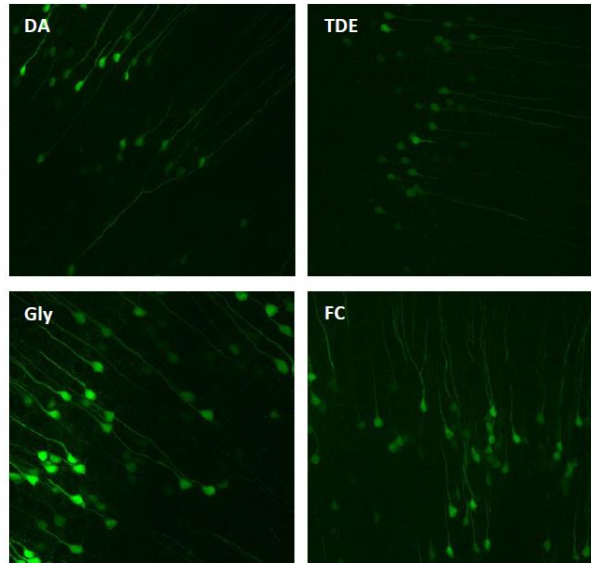


Figure 49: Comparison of fluorescence intensity in Thy1-YFP brain samples. Z-projection of the maximum intensity in a 100 μm stack of cortical region in Thy-YFP brain slices, after incubation of 2 days in RIM media candidates (DA, TDE83%, Glycerol87% and FocusClear).

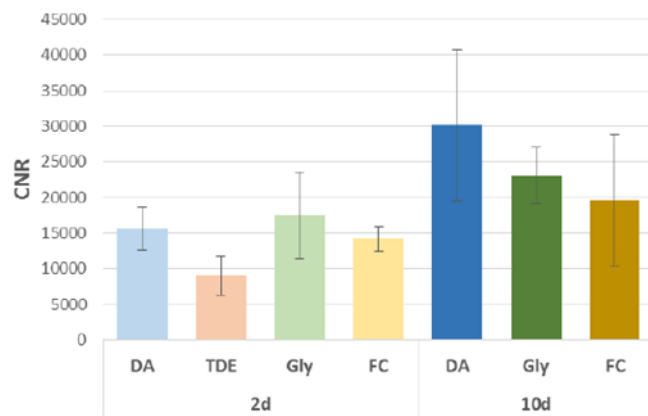


Figure 50: Contrast to Noise Ratio of the fluorescence microscope images obtained from slices under exposure to each of the four RIM media candidates. DA, TDE83%, Glycerol87% and FocusClear incubation during 2 days (2d) and 10 days (10d). Measure for 10 days for TDE is not available as no fluorescence was observed on the slices. For each group the mean and the standard error are represented ($n=4$).

Deformation

Deformation of the samples was assessed by measuring the variation of linear size of the brains immersed in the RIM candidate medium with respect to their initial expanded size in PBS-T. Taking into account that samples suffer an expansion when immersed in PBS-T, **Figure 51** represents the degree of recuperation of the original physiological size due to the incubation in RIM medium during 2 and 4 days. It can be seen that FocusClear is the best

one at reversing the expansion in a permanent way. Diatrizoic acid solution also presents a permanent effect, although it is no so hard. In any case, the qualitative evaluation of the samples evidence that no shrinkage with respect to the original size is caused. TDE 83% presents values similar to FocusClear, although the variability is higher and the effect not so durable, being at 4 days similar to diatrizoic acid solution values. Finally, glycerol presents a low recuperation of sample size, joined with high variability and low permanence of the results.

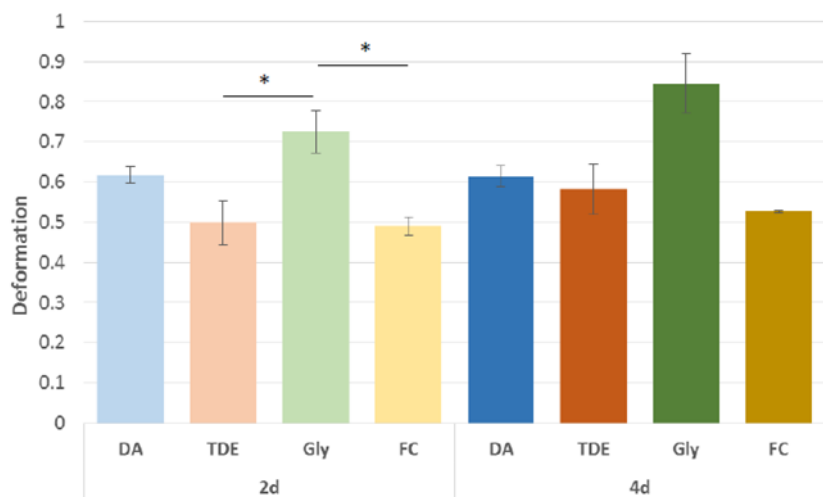


Figure 51: Deformation of the samples under 2 days (2d) and 4 days (4d) of incubation in RIM media candidates: Chung (diatrizoic acid solution), TDE83 (TDE 83% solution), Gly (glycerol 87% solution) and FC (FocusClear). The value is obtained by normalizing the area inside the brain contour in each medium by the same parameter of the brain immersed in PBS-T at day 0. For each group the mean and the standard error are represented (n=4). * p<0.05.

3.3.2. Computational pipeline for CLARITY based whole-brain structural interrogation

To establish and prove that our pipeline is suitable for the data analysis I aim to do implied a significant amount of time. Despite the fact that I cannot show a quantitative analysis comparing TgDyrk1A and wild-type mice, I have done a proof of concept of all the necessary steps. Nine brains have already been scanned. Three have undergone stitching and both multi-resolution datasets and subsets of the imaged volumes have been used for the proof of concept.

The stitching has been done using Terastitcher (**Section 3.2.2**). While the processing time is slow (~2d per sample), the procedure is reliable and the latest updates of the software allow doing the processing in a computing cluster. **Figure 52** shows a high-resolution maximum projection of a representative stitched imaging volume of a whole mouse hemisphere.

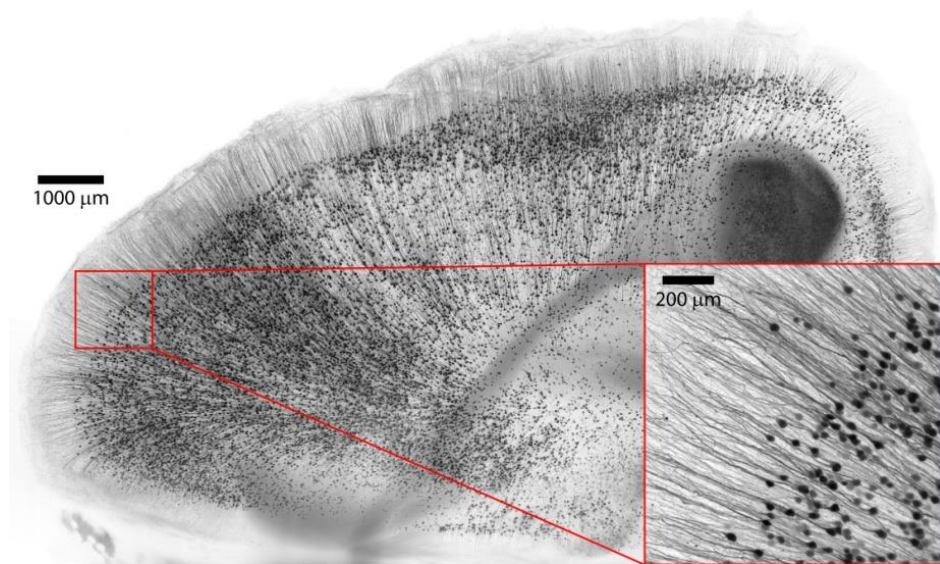


Figure 52: Maximum-value projections (inverted contrast) through one hemisphere of a B6.Cg-Tg(Thy1-YFP)HJrs/J mouse brain scanned at 5x magnification (scale bar = 1000μm). Close-up magnification of an unspecific region in the frontal cortex. Thy1-labeled cortical layer V nuclei and their apical dendrites can be appreciated (scalebar = 200μm).

Following our protocol optimizations, samples undergo passive clearing for 45 days to obtain high transparency and imaging quality, with adequate refractive index matching. **Figure 53** shows the qualitatively improvement reached with the the information of the experiments shown in **Section 3.3.1**.

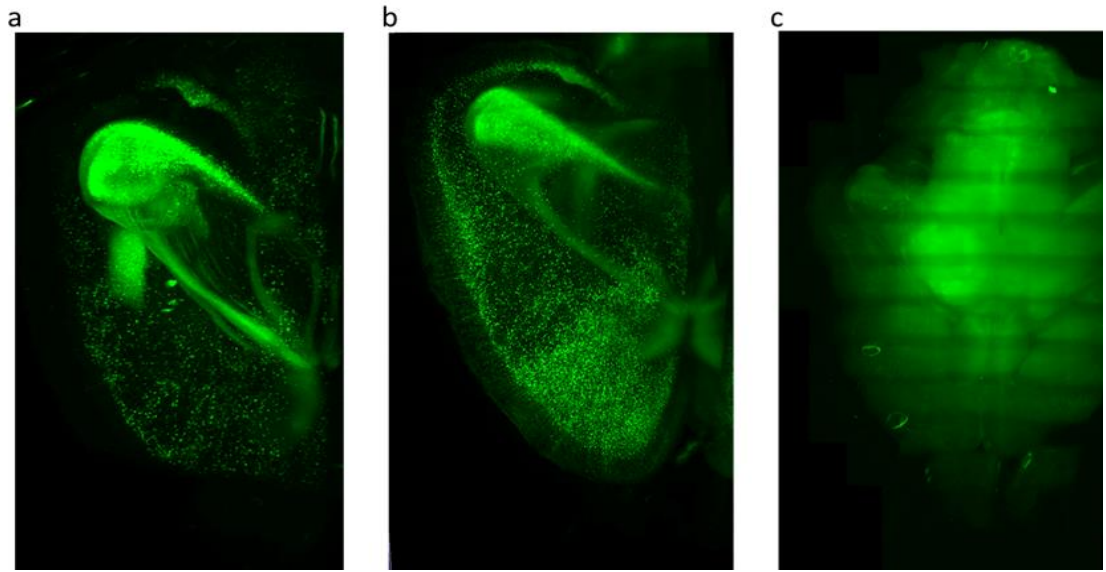


Figure 53: Snapshots of 3D views of whole brain imaging datasets in different imaging media. The three samples underwent 45 days-long passive clearing and were incubated in the imaging medium for 48hr previous to imaging. Note the difference in background fluorescence. The higher the signal to noise ratio, the less background can be appreciated in the 3D volume. Each sample was imaged in the following RIM: (a) diatrizoic acid solution, (b) 87% glycerol and (c) 87% TDE.

The stitched volumes were visualized in Vaa3D Terafly (see **Section 3.2.1**). The visualization was also tested in modest computers showing to be efficient and compatible across platforms. **Figure 54** (a,b,c) shows snapshots of the 3D visualization at different magnifications in the dataset. The improved imaging quality reached provides a high amount of detail, **Figure 54** (c) shows a high magnification maximum-value projection of the volume below cortical layer V. Axonal projections from layer V pyramidal neurons can be easily seen and tracked.

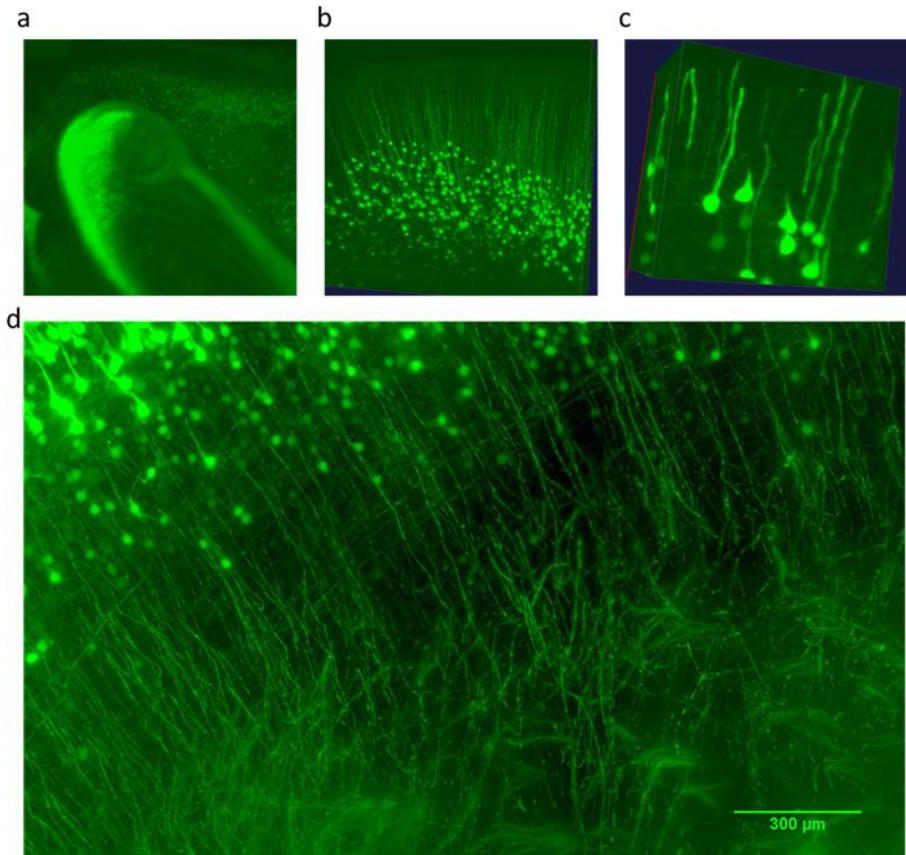


Figure 54: Multi-resolution imaging in a cleared whole mouse brain. (a,b,c) Snapshots of 3D views at different magnifications in a single dataset. (b) Maximum-value projection of an imaged volume showing partially layer V pyramidal neurons and their axonal projections.

Any quantitative analysis on volumetric data requires the previous step of the spatial registration to a common coordinate framework for all the analyzed samples. The basic step required for this procedure, is 3D spatial registration. I already developed a pipeline for mutual information-based spatial registration in **Section 2.2.3**. I here have adapted the procedure to teravoxel-sized datasets. To overcome the requirement of using the whole datasets, I have downsampled the whole brain volumes to an isotropic resolution of $10\mu\text{m}$ per voxel. The downscaled volumes can undergo all the procedures required for generating a common template and to spatially register each sample to this template. Once the transformations among the samples are known, it is applied to the coordinates of a set of markers (grid of points in the 3D space). The marker sets can then be scaled back to the original full resolution and can be used to warp the high resolution volume to a high resolution common coordinate space. **Figure 55** shows a sagittal view of an optical slice of

a whole hemisphere 3D dataset before (a) and after (b) mutual information-based registration to another sample.

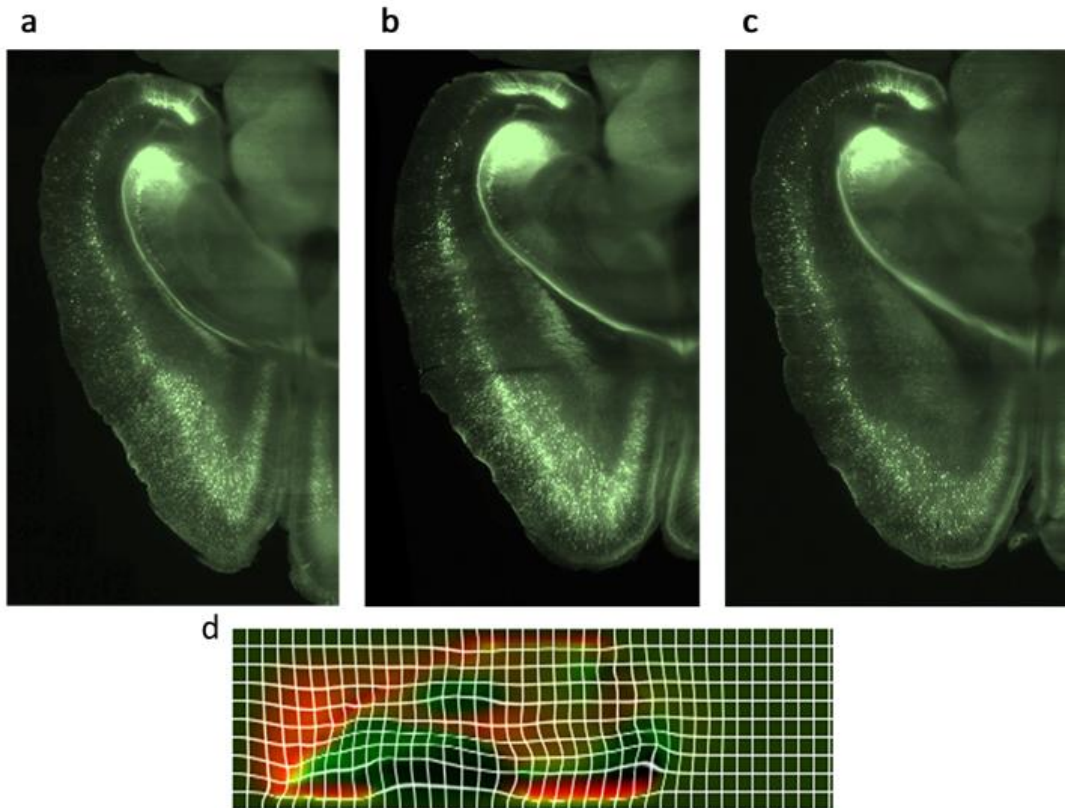


Figure 55: Deformation-based morphometry. (a,b,c) Sagittal view of a 2D slice of a whole hemisphere 3D dataset before (a) and after (b) mutual information-based registration to another sample. (d) 2D horizontal slice of deformation and compression maps obtained from a manually segmented CA1 volume nonlinear registration to a previously obtained MDA template of the region. In green, the Jacobian determinants of volumetric compression and in red displacements for each voxel in the image.

Proper definition and management of regions of interest (ROI) is needed at all levels of processing, visualization, and analysis. The 3D spatial registration is a basic step for further analysis because it allows automatic segmentation for posterior analysis. **Figure 56** shows a sagittal view of an optical slice of a whole hemisphere volume that has been manually registered (via landmark selection) to the segmentation of the Allen Institute Common Coordinate Framework (CCF v3) of the adult (P56) mouse brain. Thus, the high resolution annotated volume allows to choose ROI-specific processing. Manual segmentation is also possible the combination of our self-developed Fiji scripts, allowing high quality interpolation of thin structure segmentations.

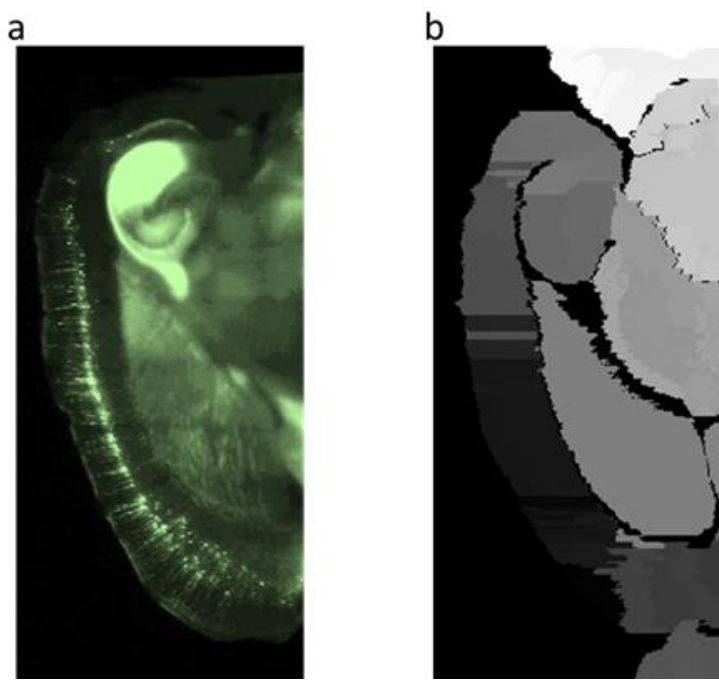


Figure 56: Registration to a common template for automatic segmentation. (a) Sagittal view of a 2D slice of a whole hemisphere 3D dataset after a landmark-based registration to the segmentation of the Allen Institute Common Coordinate Framework (CCF v3) of the adult (P56) mouse brain (b). Different shades of gray indicate standard delineated brain regions.

The steps until now, allow to obtain comparable whole brain volumes. To analyze them, I take advantage of the methods developed in Chapter II (**Section 2.2.2**). The multi-resolution structure of the data, allows to access small chunks and analyze them in parallel, generating small subvolumes containing cellular and dendritic density maps. I aim to generate python wrappers that will allow to apply any Fiji plugin throughout multi-resolution CLARITY datasets.

One of the great opportunities provided by whole brain imaging techniques, is the possibility of obtaining information about axonal projections with higher resolution than Diffusion Tensor Imaging (DTI). I propose to use the fluorescence structure tensor for large sample fluorescence microscopy datasets to study axonal pathways from densely labeled axonal projections of studied circuits (HC-mPFC in our case). I have developed Python code for obtaining and transforming multi-shell HARDI-like structure tensor datasets from CLARITY imaging datasets. This allows to generate Fibre Orientation Distribution (FOD) maps, robust FOD-based tractography and perform the structural connectomics and fixel-based analysis that MRtrix3 offers (**Figure 57**).

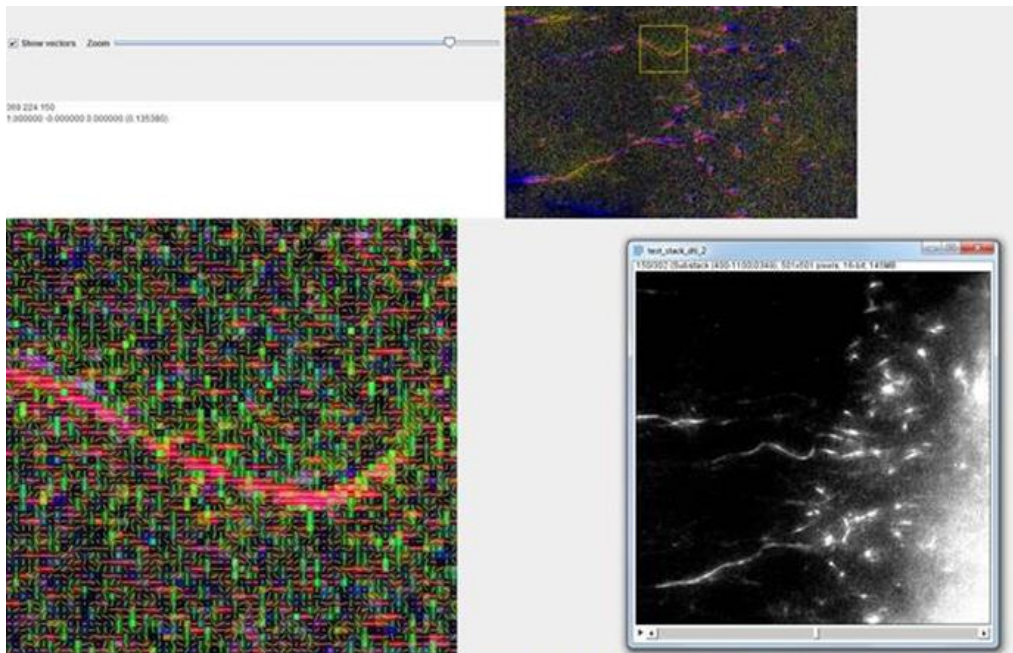


Figure 57: Structural tensor for axonal tracking. Snapshot showing an optical slice with representations of structural tensors in every voxel of the image (magnified in the lower left panel). The color indicates the orientation and white lines in each voxel represent the direction of maximum anisotropy of each tensor. The same optical slice in the original whole brain imaging dataset (lower right).

Altogether those tools allow the structural interrogation of whole brain datasets with a focus on a holistic perspective for the analysis of cellular, dendritic and axonal densities. But also provide a robust framework to elaborate on quantitative mapping that could be of interest for any particular application (e.g. analyzing patterns of genetic expression, or presence of specific proteins). Also, the direct link with the in-silico parametrization of neuronal networks in the generative model presented in Chapter II opens many possibilities for the interaction between experimental interrogation of whole brains and the simulation of neuronal circuits (**Figure 58**).

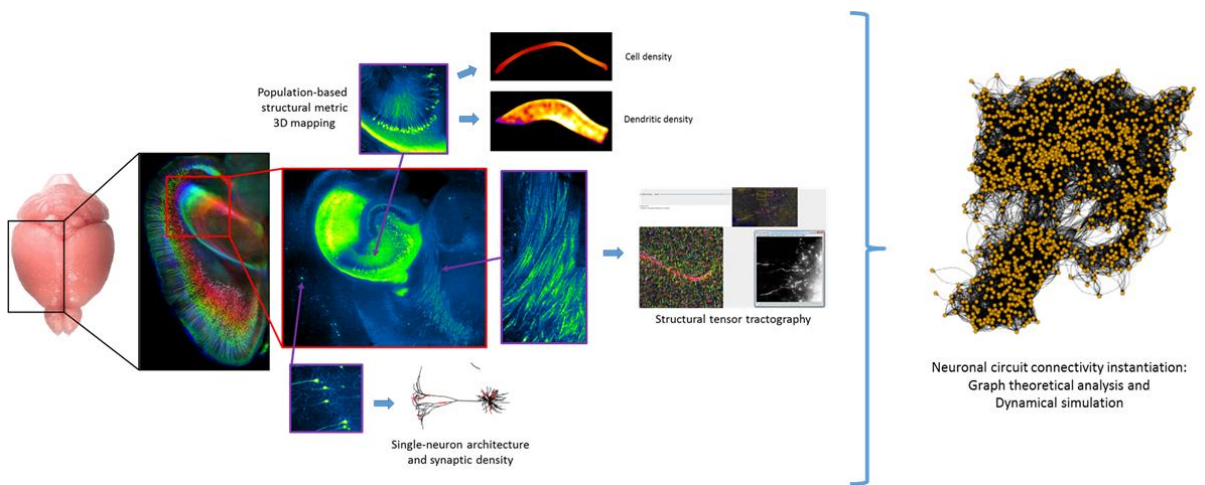


Figure 58: Overview of the whole-brain analysis and modeling workflow. I obtain structural experimental data from cleared brains which constrain computational modeling and analysis tools to explore neuronal circuit topology. Thus, providing a tool to investigate the organizational principles of mammalian neuronal networks.

3.4. Discussion and conclusions

CLARITY technique optimization

The development, refinement, and use of techniques that allow high-throughput imaging of whole brains with cellular resolution will help us understand the complex functions of the brain. Such techniques are crucial for the analysis of complete neuronal morphology— anatomical and functional—connectivity, and repeated molecular phenotyping. Recently developed tissue clearing protocols like Scale (Hama et al., 2011), CLARITY (Chung et al., 2013) or iDisco (Renier et al., 2014), together with the possibility of imaging whole brains at microscopic resolution in confocal or light-sheet fluorescence microscopes, allow virtually any neurobiology lab to obtain datasets that until now were only considered in the framework of big collaborative projects. However, many laboratories that try to use the techniques realize that the implementation of the clearing and labeling protocols is not straightforward and that many times the resulting imaging quality is not sufficient for the detailed microscopic analysis pursued. Thus, in the field of whole brain imaging, optimization of the protocols is a recurrent topic (Epp et al., 2015; H. Lee, Park, Seo, Park, & Kim, 2014). Our experiments modifying specific steps of the CLARITY technique have shown that the refractive index matching medium is crucial for imaging quality.

I have corroborated that FC is an optimal imaging medium regarding transparency, native fluorescence conservation, and deformation of the samples. Our results also point at DA as a good candidate, showing relatively high sharpness ratio and very stable fluorescence conservation (higher than in FC) while preserving sample size. This has been corroborated by our experience when imaging whole brains in SPIM. Nevertheless, the striking capacity of TDE to render cleared samples highly transparent, highlights its potentiality for whole brain imaging. The quenching effect I have observed, has also been observed in previous studies (Aoyagi, Kawakami, Osanai, Hibi, & Nemoto, 2015; Staudt, Lang, Medda, Engelhardt, & Hell, 2007), and it seems to be highly dependent on TDE concentration (Hasegawa et al., 2016). Our trials shown that adjusting to basic pH does not avoid quenching, and that in some cases, even at 83% concentration quenching does not occur (data not shown). This, together with the fact that the red fluorescent protein mutant (RFP) is not quenched by TDE (Staudt et al., 2007) suggests that the observed quenching must depend on very specific properties of GFP-like mutants (GFP, eGFP and eYFP). To

investigate this I have explored molecular dynamics simulations of the protein at different solvation concentrations of TDE (see **Annex II**).

It is worth mentioning, that our quantifications also highlighted the importance of a robust methodological framework and standardized measurements to compare the effectiveness of clearing protocols. I highlight the importance of normalization among measurements done in different samples and propose the sharpness ratio and CNR as consistent measures for transparency and fluorescence signal level.

Computational pipeline for whole-brain structural interrogation

The characterization done, allowed us to obtain high quality imaging datasets, that contain big amounts of structural information that characterizing neuronal circuitry in our mice. Whole rodent brain light-sheet imaging not only allow the generation of brain structural maps with unprecedented resolution, but also offer multiplexed molecular interrogation of the studied samples. Some efforts following the appearance of the first whole-brain microscopy imaging studies have generated basic tools needed to take advantage of the wealth of information they contain (atlas registration, fluorescence signal raw statistics (Renier et al., 2014), cell counting (Frasconi et al., 2014) and axonal projection density (Ye et al., 2016). However, except for axonal projection densities, those analyses still miss a link between the information at the microscopic level and a meaningful analysis for its implications on brain function. Specifically, in the samples I image, I choose the study of transgenically labelled neuronal subpopulations as sufficient to show how detailed microscopic properties and a whole-brain perspective can be linked.

The challenges that remain to be solved for any possible quantification in those datasets are two: (1) to determine which measures can be informative of populations of labeled cells or molecules and (2) to analyze those data taking into account the topographical information throughout the whole sample. The solution to those challenges has already been thoroughly explored in the neuroimaging field and has already been discussed in Chapter II. I have proposed novel methods for analyzing volumetric datasets and obtaining population-based cellular and dendritic density maps, and developed a computational generative model that will allow to assess the implications of multi-scale morphological properties on network topology.

Our proof of concept in this part of the Thesis, takes advantage of the framework developed for population-based analysis and modeling, and puts it in the context of whole brain imaging. By solving the spatial registration and generating wrappers that allow to perform common image analyses in whole brains by chunks, I open many possibilities for the analysis and development of neuromorphological metric mapping. Thus, in the framework presented here, I gathered together many existing tools that by being combined provide a powerful and extensible platform to study neuronal circuits from a systems perspective.

GENERAL DISCUSSION

GENERAL DISCUSSION

“If we want to understand the nature of memory as actually instantiated, we must take into account -and provide account of- both behavioral performance data and facts about the constraints imposed by the hardware of the brain”

Cohen and Eichenbaum “Memory, Amnesia, and the Hippocampal System”.

The work performed in this Thesis aims at uncover how the particular geometry of the dendritic arborization of neurons may influence our cognitive capabilities. This work stems at the interesting observation that impaired cognitive performance is usually accompanied by dendritic tree abnormalities, and that pro-cognitive therapies produce important dendritic remodelling. On the hypothesis that brain network organization has evolved by optimizing cost and efficiency, we predicted that reduced cognitive performance should be related to suboptimal cost efficiency of brain networks. To test this hypothesis, I took here an original approach: I used mouse models with similar behavioral and cognitive disturbances but slightly different dendritic perturbations, so that I could analyze the local “hardware” alterations knowing the behavioral impairments they present. I also compared two different mouse strains which can be considered as a template for a healthy mouse brain, but present strain-dependent differences at the behavioral and neuronal levels.

Interpreting wiring suboptimality at the single-cell and networks levels

My initial approximation was inspired by the wiring optimality defined by Cuntz et al. (Cuntz et al. 2012). This concept was interesting to me because the wiring optimality is assumed to be the same for all cell types, and thus I could explore to what extent the same class of neuron (pyramidal) in two brain regions that are very different between them in terms of computation (the cerebral cortex and the hippocampus) fulfilled such condition, and whether they deviated equally from optimality in mouse models of DS, with well-known neuromorphological alterations. The morphological analysis of the cortical pyramidal healthy and DS neurons in Chapter I confirmed previously published results (Dierssen et al. 2003). My the results showed approximately optimal wiring for the B6EiC3Sn (0.45 ± 0.13 power, to be compared with the optimal scaling law of Cuntz et al. - $1/2$ power for 2D trees-), slightly suboptimal wiring for the C57BL/6J-129Ola mixed background (0.65 ± 0.11 power), and clear deviations from optimality for both the trisomic (Ts65Dn) and the Dyrk1A+/- mouse

models (0.74 ± 0.15 and 0.75 ± 0.16 powers respectively). These results could be interpreted in light of the motor activity differences observed in these two mouse lines. However, the scaling between total length and tree radius showed contradictory results and suboptimal wiring for the B6EiC3Sn wild-type mice, highlighting a possibly misleading interpretation of (potentially inaccurate) power-law fits. Anyhow, this analysis could not capture the neuromorphological differences between Ts65Dn and Dyrk1A $^{+/-}$ mice, which show similar deviations from optimality in both strains (0.74 and 0.75 power, respectively) even though they present opposite behavioural phenotypes: hyper-active in trisomic mice (Coussons-Read & Crnic, 1996) and hypo-active in Dyrk1A $^{+/-}$ mice (Martínez de Lagrán et al., 2007). The next question was whether wiring suboptimality was specific of cortical layers, or was also present in the hippocampus of DS mouse models, given that this is a region strongly affected that presents clear dendritic abnormalities, but slightly different from those found in cortical pyramidal cells. Here I used single neuron CA1 apical dendritic tree reconstructions of a different mouse model, the TgDyrk1A model, as it recapitulates the morphological alterations and the cognitive phenotype of the Ts65Dn model. Given that the concept of dendritic wiring optimality (Cuntz et al., 2012) is applicable to all different types of neurons, I assumed that it also could be used for a specific part of the dendritic tree, and here I focused on apical trees of single-neuron reconstructions from the hippocampus of TgDyrk1A mice. Transgenic neurons showed smaller dendritic trees, which implies less number of spines and possibly reduced integration capacity. This, in fact, has been a long-standing argument to explain the altered visuo-spatial learning and memory phenotypes of these mice. However, when testing wiring optimality, transgenic neurons showed almost the same optimal scaling than their wild type littermates. These results may suggest that existing optimal wiring definitions can be missing aspects the impact of neuromorphology on cognitive function. However, since I only analyzed apical dendritic trees, we cannot discard that including the whole dendritic tree in the analysis we would have reached significant differences in optimality. Even so, the fact that TgDyrk1A mice have shown impaired acquisition of hippocampal-dependent spatial tasks (Altafaj et al., 2001), would support the involvement of storage capacity (that was significantly reduced in the transgenic model) in this function. In any case, discriminating the contribution of the reduced amount of contacts versus the contribution of other morphological aspects related to signal integration efficiency would require specific experimental confirmation.

To interpret the findings described above, I reasoned that probably the lack of discrimination power, was due to the fact that neurons should be optimized not only for space-filling. This assumption led me to explore other paradigms that could account for more functional aspects. To this aim, an interesting possibility was to use the approach used by Wen & Chklovskii (Wen & Chklovskii, 2008) to derive the total dendritic length versus tree radius scaling law (0.43 power), which allows to assess variations among cell-types through the trade-off between wiring cost and the maximization of the connectivity repertoire. However, here again the data were difficult to interpret. I found that B6EiC3Sn and C57BL/6J-129Ola mixed background wild-type mice and Ts65Dn mice deviate from optimality (0.20 ± 0.09 , -0.02 ± 0.25 and -0.63 ± 0.32 power respectively), while Dyrk1A $^{+/-}$ had optimal scaling (0.33 ± 0.16 power), in disagreement with what we found with the analysis of Cuntz et al. This disagreement could be due to the fact that Chklovskii uses the radius instead of branch number. Given that the radius has low variations within the experimental groups, this will reduce the statistical meaningfulness of the power-law fits.

Since neither of the methods tested could define an optimality that had discriminatory power between pathological and healthy state in neither brain region studied, added to the fact that adjusting their derivation to specific cell-types requires the assessment of a model-dependent cost function (Wen & Chklovskii, 2008), I reasoned that none of those combinations of factors is sufficient to account for a more broader concept of optimality.

I then decided to take a multi-objective (Pareto) perspective, inspired by the study of Avena-Koenigsberger et al. (Avena-Koenigsberger et al., 2014) who applied it to explore human brain MRI connectomes. The definition and quantification of Pareto optimality forces an assessment of the contribution of various aspects, specifically I used routing efficiency, and storage capacity, with regards to cost efficiency.

This allowed the quantitative analysis of optimality deviations for each individual neuron, thus avoiding the need of fitting scaling laws and increasing the statistical meaningfulness of the analysis. By defining signal integration efficiency and storage capacity based on morphological properties of dendritic trees (dendritic tree spanning area, density and straightness of dendritic branches) and by applying the Pareto optimality framework, I found that Ts65Dn pyramids show the lowest optimality for routing efficiency (highest distance to

the Pareto front; $dP = 0.15 \pm 0.13$). In contrast, Dyrk1A $^{+/-}$ neurons show a tendency to higher routing efficiency optimality ($dP = 0.05 \pm 0.16$), even though the difference with the Ts65Dn neurons is not significant. The wild-type controls of both groups show higher optimality for routing efficiency. However, subtle differences appeared so that the mixed background C57BL/6J-129Ola neurons ($dP = -0.07 \pm 0.15$) are not as optimal as the B6EiC3Sn group ($dP = -0.10 \pm 0.14$). At first glance this would be compatible with the slight behavioral differences in both strains. Surprisingly, while neurons of the mixed background C57BL/6J-129Ola are the closest to have an optimal architecture regarding storage capacity ($dP = 0.20 \pm 0.11$), B6EiC3Sn wild-types ($dP = 0.35 \pm 0.12$), Ts65Dn ($dP = 0.28 \pm 0.10$) and Dyrk1A $^{+/-}$ ($dP = 0.25 \pm 0.04$) neurons fall far from the obtained Pareto fronts.

While lacking statistical significance due to the small numbers of reconstructions, this analysis supported the results obtained when fitting the optimal wiring scaling law defined by Cuntz et al. (Cuntz et al., 2012), showing suboptimality for both DS models and an intermediate phenotype for the mixed-background mice. However, even though the discriminative power was still not very strong, using the multi-objective Pareto analysis I could define that while the architecture of Ts65Dn neurons deviates from optimality due to routing efficiency, Dyrk1A $^{+/-}$ neurons can have slightly higher optimality for routing efficiency. Additionally, I could assess how optimal the architecture of these groups of neurons is for storage capacity which is not considered in the optimality analysis of Cuntz et al.

To assess whether the morphological alterations found in single neurons can have an impact on the wiring of the networks in which they are embedded, I developed a computational model for instantiating the horizontal connectivity of cortical layer II/III, which allows to explicitly link single neuron properties to network topology, translating the Pareto optimality framework used at the single-cell level to the network level. We found that basal tree architecture in cortical layer II/III of Ts65Dn, TgDyrk1A and Dyrk1A $^{+/-}$ mouse models have slightly suboptimal network wiring. Specifically, Ts65Dn and Dyrk1A $^{+/-}$ mice show a similar phenotype with approximately 50 % reduction for both routing efficiency and storage capacity ($dP = 0.09$ and $dP = 0.10$ respectively) indicating suboptimal architecture. Instead, the TgDyrk1A networks show a lower (26%) reduction in storage capacity but similar (49 %) reduction in routing efficiency, and thus lie very close to optimality in the 2D Pareto front for storage capacity ($dP = 0.03$), while separating from it for routing efficiency ($dP = 0.12$).

Behavioral data in the cortical-dependent puzzle-box task could be the behavioral expression of the storage capacity reduction seen in TgDyrk1A networks. However, the fact that the same structural phenotype shows opposite behaviors (hyperactivity in the Ts65Dn and hypoactivity in the Dyrk1A^{+/−}), indicates that the dynamical aspects of those genetic conditions have to be taken into account (Martínez de Lagrán et al., 2007).

Altogether, the reductions in routing efficiency, at both the network and the single-cell levels, observed in both Ts65Dn and Dyrk1A^{+/−} neurons suggest dendritic integration disturbances that could alter the dynamics of cortical networks and lead to imbalanced patterns of activity and, ultimately, to the abnormal behavior observed in those mouse models. It would be interesting to test whether the routing efficiency alterations are more strongly related to the performance in the puzzle box task and hypo- and hyper-activity phenotypes, and whether storage capacity mostly accounts for impairments in tasks involving the consolidation of memories, which could be assessed using behavioral tasks that allow to finely separate behavioral subdomains, as for example, the touch-screen tests (Bussey et al., 2008). In this sense, the framework works as a “hypothesis pump”, which leads to simple predictions, but provides a promising scenario towards the study of complex networks. The comparative analysis of genetic mouse models in those tasks will allow testing such hypothesis.

The morphospace exploration performed allowed to disentangle and quantify the impact of specific morphological properties (dendritic tree size, its variability and synaptic contact probability) on the network topology, showing that subtle morphological changes can have a significant impact on the network topology. In this context, taking into account the radial dependency on synaptic contact probability increased small-worldness the network topology. Moreover, assessing how pro-cognitive treatments can modulate the network topology, I could predict that the therapeutic effect of pro-cognitive treatments depends on changes in dendritic tree size rather than on increases in synaptic density. Since most of the actual pro-cognitive therapies are based on targeting the synapse, it is important to notice that this concept is not against the notion that increased amounts of synaptic contacts should be beneficial for routing efficiency and storage capacity of the networks. However, the difference to the previous state of the art is that increasing dendritic tree size would have

higher impact, because that the amount of redundant synapses in the circuit would be reduced.

Neuromorphological within-class variability

A number of studies have demonstrated histological differences in CA1 in each of the dorsal-ventral, proximal-distal, and superficial-deep axes of the hippocampus. This are driven by within-class variability, which may be an important aspect of organizational principles of neuronal systems (Solstez, 2006). Moreover, Elston et al. (Elston et al., 1997) and Benavides-Piccione et al. (**Figure 59**; Benavides-Piccione et al. 2006) have shown that along the mouse cortex, the morphology of layer II/III cortical neurons varies, suggesting putatively differential computing needs for different processing approaches. Ballesteros et al. suggested that such morphological heterogeneity is not the result of a simple genetic expression gradient, indicating that functional heterogeneity is involved in shaping the morphological differences. In my analysis of apical dendritic tree architecture in dorsal CA1, I showed a quite marked within-class heterogeneity. Even though I cannot extrapolate that this variability could have an impact on the neuromorphological properties of the different hippocampal subregions, since I did not analyze ventral CA1 pyramids, the morphological variability observed in a functionally homogeneous area of the hippocampus (dorsal CA1) raises the question of whether it could be advantageous (or deleterious) for given neuronal computations. In my analysis, Distal CA1 dendritic trees show reduced span and dendritic complexity in the TgDyrk1A mouse model, while proximal transgenic CA1 pyramids show a reduction exclusively in dendritic span. Given that Igarashi et al. have found evidence that distal CA1 is preferentially involved in contextual learning while central CA1 processes spatial information (Igarashi et al., 2014), these results would be supportive of the stronger affection in contextual than spatial learning reported in transgenic mice (Pons-Espinal, de Lagran, & Dierssen, 2013; De La Torre et al., 2014).

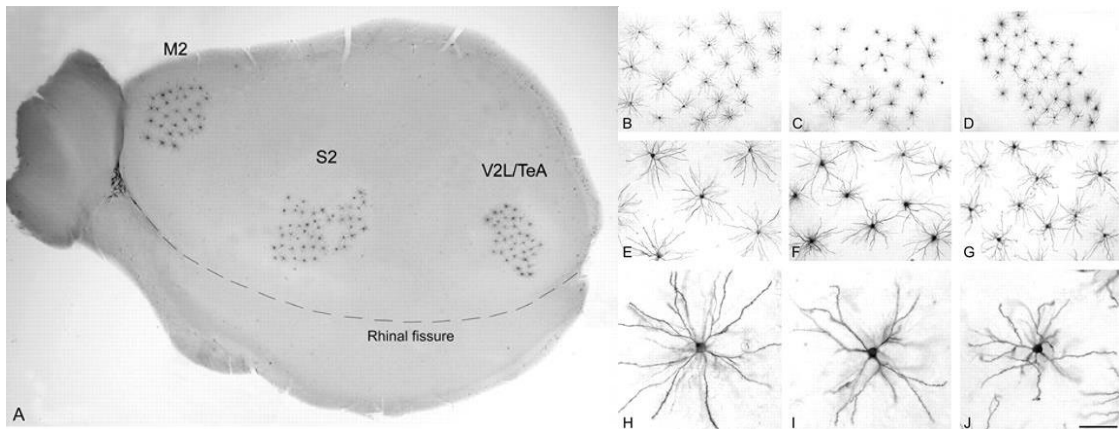


Figure 59. Dendritic architecture heterogeneity throughout cortical layer II/III. (A) Mouse cerebral cortex cut parallel to the cortical surface. Cells were injected with Lucifer yellow and reconstructed in areas approximately corresponding to M2, S2 and V2L/TeA of Franklin and Paxinos (1997). (B–J) Successive higher magnification photomicrographs showing pyramidal cells basal dendrites in M2 (B, E, H), S2 (C, F, I) and V2L/TeA (D, G, J) regions. Scale bar = 815 μm in A; 350 μm in B–D; 150 μm in E–G; 60 μm . Adapted from (Ruth Benavides-Piccione, Hamzei-Sichani, Ballesteros-Yáñez, DeFelipe, & Yuste, 2005).

It has been proposed that the processing of neuronal circuits has to be highly robust against noise from various sources and that sometimes neuronal networks take advantage of internal variability to perform computations (Faisal, Selen, & Wolpert, 2008). While such studies have generally focused on variability in dynamical activity, finding such a scenario for neuromorphological properties would support the same argument for the structural level, and to some extent, contradicts the notion that subtle changes in neuromorphology imply functional specializations. To what extent within-class variability is relevant for shaping the function of neuronal circuits or not remains to be elucidated, and opens questions such as: What is the amount of “morphological noise” that a given network architecture can hold while keeping its functionality? Do all the brain regions have the same amount of within-class morphological variability? Does morphological heterogeneity support specific network architectures or neuronal computations?

The verification of within-cell variability in my experiments made it very relevant to establish a method for population-based comparative analysis. To this aim we used a genetically labelled model: Thy1 transgenic labeling. The population-based labeling provided by the Thy1 transgenic expression of fluorescent proteins has to be interpreted cautiously, given that the proportion of labeled neurons is very low, as shown by cell density quantifications, which differ from NeuN immunostaining data. Even so, the robustness of this method is demonstrated by the fact that population based analysis confirmed the reduced dendritic

complexity of apical dendrites in distal CA1 pyramids on transgenic mice detected in single cell reconstructions. Being able to identify such variations with such a sparse labeling points at the fact that the amount of variation along CA1 could be much higher than detected in our analysis. While our exploration for dendritic tree size variability did not show any relevant effect in the routing efficiency or storage capacity of the cortical layer II/III, an assessment of the impact of such variations on the network topology remains to be done and the generative model developed in Chapter II will allow us to tackle those questions from a modelling perspective.

Towards a systems perspective

While the assessment of neuromorphological properties of single neurons is necessary to construct realistic generative models, the histological techniques used to obtain such information are not suitable for analyzing mesoscopic properties of neuronal layers, thus impeding the structural interrogation of brains from a systems perspective. The advent of clearing techniques was a step forward to obtain 3D structural maps. Such maps are crucial for a systematic population-based analysis of the brain regions affected in DS mouse models. Moreover, those maps will allow assessing the impact of neuronal microanatomic alterations on the network connectivity. In this thesis, we decided to undertake the development of the method both computationally and experimentally (Chapters II and III). On one hand, the population-based analysis methods and the 3D generative modelling platform are technical aspects needed for tackling the question of how neuromorphology modulates network connectivity in realistic scenarios. However, published clearing techniques do not provide a sufficient imaging quality for obtaining reliable analyses and this posed another technical challenge. The results obtained thanks to the optimization of the CLARITY technique, allowed us to obtain nine whole-brain imaging datasets with micrometric resolution throughout the whole brain volume. In the timeframe of my thesis, I could not push the analysis further, but given that the technical aspects regarding analysis and simulation of 3D brain circuits have been solved in parallel, we can now use the combination of both. Besides, taking advantage of population-based labeling will allow me to study neuronal circuits focusing on the mesoscopic scale not only locally in the brain regions affected in DS, but also accounting for the consequences of dendritic pathology at a more global level.

CONCLUSIONS

CONCLUSIONS

The work of this Thesis has revealed that the size and shape of dendritic trees are strong determinants of neuronal information processing because of their influence on the wiring optimality both at the single-cell and at the network levels, and that pathological perturbations of dendritic trees impair such optimality. I have also provided new computational tools to interrogate biological networks about the best strategy to rewire neuronal connectivity from a systems perspective.

1. The dendritic architecture abnormalities in cortical layer II/III basal trees of intellectual disability models (Ts65Dn, Dyrk1A+/- and C57BL/6J-129Ola) determines suboptimal target space filling. This possibly contributes to an impaired integration of afferent synapses and reduced storage capacity at the single-neuron level.
2. Within the neuromorphological parameters analyzed, dendritic tree size and synaptic contact probability of single pyramidal neurons are those that exert an influence the topology of modeled cortical layer II/III local networks. Network routing efficiency is mainly given by synaptic contact probability, while storage capacity, clustering and small-worldness ratio is mostly determined by dendritic tree size.
3. Introducing a distribution of synaptic contacts along dendritic trees extracted from experimental data modifies the topology of modeled networks, increasing the routing efficiency of the network for a given amount of contacts made by the neurons, and, to a lower extent, its small-worldness ratio, while slightly reducing its storage capacity.
4. Ts65Dn and Dyrk1A+/- Down syndrome mouse models show a 40-50% reduction in storage capacity and routing efficiency with respect to the wild type.
5. Environmental enrichment increases in 7% routing efficiency and storage capacity in Ts65Dn mice, suggesting that therapeutical approaches modifying dendritic tree size rather than synaptic contact probability could have stronger impact on the functionality of Down syndrome neuronal networks.
6. Mice overexpressing DYRK1A show dendritic abnormalities in dorsal CA1 *stratum radiatum* with reduced storage capacity (18%). However, differential architectural phenotypes are detected along the proximal-distal axis, being aberrations more marked in distal CA1.

7. The population-based neuromorphological analysis methods developed in this work presented a strategy towards the assessment of neuronal circuitry composition and architecture, providing a first step towards a holistic perspective in the study of neuronal networks at the cellular scale.
8. The multi-scale generative model for the instantiation of biologically realistic neuronal circuits allows the exploration of the morphospace impact on neuronal network topology based on multi-scale experimental data.
9. The analysis pipeline for population-based structural interrogation of whole brains allows population-based structural interrogation methods from a systems perspective.
10. Altogether, the analyses and tools developed in this Thesis constitute a methodological and conceptual framework that can now be used to explore a computational hypothesis generation - experimental testing feedback loop in the scope of comparative microconnectomics.

BIBLIOGRAPHY

BIBLIOGRAPHY

- Ahmad, K., & Henikoff, S. (2002). Epigenetic consequences of nucleosome dynamics. *Cell*, 111(3), 281–284.
- Ahn, K.-J., Jeong, H. K., Choi, H.-S., Ryoo, S.-R., Kim, Y. J., Goo, J.-S., ... Song, W.-J. (2006). DYRK1A BAC transgenic mice show altered synaptic plasticity with learning and memory defects. *Neurobiology of Disease*, 22(3), 463–472.
- Ahuja, R. K., Mehlhorn, K., Orlin, J., & Tarjan, R. E. (1990). Faster algorithms for the shortest path problem. *Journal of the ACM (JACM)*, 37(2), 213–223.
- Albert, R., & Barabási, A.-L. (2002). Statistical mechanics of complex networks. *Reviews of Modern Physics*, 74(1), 47.
- Altafaj, X., Dierssen, M., Baamonde, C., Martí, E., Visa, J., Guimerà, J., ... Others. (2001). Neurodevelopmental delay, motor abnormalities and cognitive deficits in transgenic mice overexpressing Dyrk1A (minibrain), a murine model of Down's syndrome. *Human Molecular Genetics*, 10(18), 1915–1923.
- Altman, D. G., & Bland, J. M. (1983). Measurement in medicine: the analysis of method comparison studies. *The Statistician*, 307–317.
- Amaral, D. G., Ishizuka, N., & Claiborne, B. (1990). Chapter Neurons, numbers and the hippocampal network. *Progress in Brain Research*, 83, 1–11.
- Amaral, D. G., & Witter, M. P. (1989). The three-dimensional organization of the hippocampal formation: a review of anatomical data. *Neuroscience*, 31(3), 571–591.
- Aoyagi, Y., Kawakami, R., Osanai, H., Hibi, T., & Nemoto, T. (2015). A rapid optical clearing protocol using 2, 2'-thiodiethanol for microscopic observation of fixed mouse brain. *Plos One*, 10(1), e0116280.
- Artola, A., Von Frijtag, J. C., Fermont, P. C. J., Gispen, W. H., Schrama, L. H., Kamal, A., & Spruijt, B. M. (2006). Long-lasting modulation of the induction of LTD and LTP in rat hippocampal CA1 by behavioural stress and environmental enrichment. *European Journal of Neuroscience*, 23(1), 261–272.
- Artzy-Randrup, Y., Fleishman, S. J., Ben-Tal, N., & Stone, L. (2004). Comment on “Network motifs: simple building blocks of complex networks” and “Superfamilies of evolved and designed networks.” *Science*, 305(5687), 1107.
- Ascoli, G. A., Donohue, D. E., & Halavi, M. (2007). NeuroMorpho.Org: A Central Resource for Neuronal Morphologies. *Journal of Neuroscience*, 27(35), 9247–9251. <https://doi.org/10.1523/JNEUROSCI.2055-07.2007>
- Avants, B. B., Tustison, N., & Song, G. (2009). Advanced normalization tools (ANTS). *Insight J*, 2, 1–35.
- Avena-Koenigsberger, A., Goñi, J., Solé, R., & Sporns, O. (2015). Network morphospace. *Journal of the Royal Society Interface*, 12(103), 20140881.
- Avena-Koenigsberger, A., Griffa, A., Hagmann, P., Thiran, J.-P., Sporns, O., Goñi, J., ... van den Heuvel, M. P. (2014). Using Pareto optimality to explore the topology and dynamics.
- Ballesteros-Yáñez, I., Benavides-Piccione, R., Elston, G. N., Yuste, R., & DeFelipe, J. (2006). Density and morphology of dendritic spines in mouse neocortex. *Neuroscience*, 138(2), 403–409.
- Barrett, K. E., & Others. (2010). Ganong's review of medical physiology. McGraw-Hill Medical New York, NY.
- Barthas, F., & Kwan, A. C. (2017). Secondary motor cortex: where sensory meets motor in the rodent frontal cortex. *Trends in Neurosciences*, 40(3), 181–193.

- Bartoletti, A., Medini, P., Berardi, N., & Maffei, L. (2004). Environmental enrichment prevents effects of dark-rearing in the rat visual cortex. *Nature Neuroscience*, 7(3), 215–216.
- Bassett, D. S., & Bullmore, E. D. (2006). Small-world brain networks. *The Neuroscientist*, 12(6), 512–523.
- Beauquis, J., Roig, P., De Nicola, A. F., & Saravia, F. (2010). Short-term environmental enrichment enhances adult neurogenesis, vascular network and dendritic complexity in the hippocampus of type 1 diabetic mice. *PLoS One*, 5(11), e13993.
- Belichenko, P. V., Kleschevnikov, A. M., Masliah, E., Wu, C., Takimoto-Kimura, R., Salehi, A., & Mobley, W. C. (2009). Excitatory-inhibitory relationship in the fascia dentata in the Ts65Dn mouse model of Down syndrome. *Journal of Comparative Neurology*, 512(4), 453–466.
- Benavides-Piccione, R., Dierssen, M., Ballesteros-Yáñez, I., de Lagrán, M. M., Arbones, M. L., Fotaki, V., ... Elston, G. N. (2005). Alterations in the phenotype of neocortical pyramidal cells in the Dyrk1A+/- mouse. *Neurobiology of Disease*, 20(1), 115–122.
- Benavides-Piccione, R., Hamzei-Sichani, F., Ballesteros-Yáñez, I., DeFelipe, J., & Yuste, R. (2005). Dendritic size of pyramidal neurons differs among mouse cortical regions. *Cerebral Cortex*, 16(7), 990–1001.
- Bernard, A., Lubbers, L. S., Tanis, K. Q., Luo, R., Podtelezhnikov, A. A., Finney, E. M., ... Others. (2012). Transcriptional architecture of the primate neocortex. *Neuron*, 73(6), 1083–1099.
- Bernard, C., & Wheal, H. V. (1994). Model of local connectivity patterns in CA3 and CA1 areas of the hippocampus. *Hippocampus*, 4(5), 497–529.
- Brejc, K., Sixma, T. K., Kitts, P. A., Kain, S. R., Tsien, R. Y., Ormö, M., & Remington, S. J. (1997). Structural basis for dual excitation and photoisomerization of the Aequorea victoria green fluorescent protein. *Proceedings of the National Academy of Sciences*, 94(6), 2306–2311.
- Bria, A., & Iannello, G. (2012). TeraStitcher-a tool for fast automatic 3D-stitching of teravoxel-sized microscopy images. *BMC Bioinformatics*, 13(1), 316.
- Bria, A., Iannello, G., Onofri, L., & Peng, H. (2016). TeraFly: real-time three-dimensional visualization and annotation of terabytes of multidimensional volumetric images. *Nature Methods*, 13(3), 192–194.
- Bullmore, E., & Sporns, O. (2009). Complex brain networks: graph theoretical analysis of structural and functional systems. *Nature Reviews Neuroscience*, 10(3), 186–198.
- Bussey, T. J., Padain, T. L., Skillings, E. A., Winters, B. D., Morton, A. J., & Saksida, L. M. (2008). The touchscreen cognitive testing method for rodents: how to get the best out of your rat. *Learning & Memory*, 15(7), 516–523.
- Carandini, M. (2004). Amplification of trial-to-trial response variability by neurons in visual cortex. *PLoS Biology*, 2(9), e264.
- Cauller, L. J., Clancy, B., & Connors, B. W. (1998). Backward cortical projections to primary somatosensory cortex in rats extend long horizontal axons in layer I. *Journal of Comparative Neurology*, 390(2), 297–310.
- Cembrowski, M. S., Bachman, J. L., Wang, L., Sugino, K., Shields, B. C., & Spruston, N. (2016). Spatial gene-expression gradients underlie prominent heterogeneity of CA1 pyramidal neurons. *Neuron*, 89(2), 351–368.
- Chklovskii, D. B., Schikorski, T., & Stevens, C. F. (2002). Wiring optimization in cortical circuits. *Neuron*, 34(3), 341–347.

- Chung, K., Wallace, J., Kim, S.-Y., Kalyanasundaram, S., Andelman, A. S., Davidson, T. J., ... Others. (2013). Structural and molecular interrogation of intact biological systems. *Nature*, 497(7449), 332–337.
- Conel, J. L. (1941). *The postnatal development of the human cerebral cortex: The cortex of the one-month infant*.
- Conel, J. L. (1947). *The postnatal development of the human cerebral cortex: the cortex of the three-month infant*.
- Conel, J. L. (1955). *The Postnatal Development of the Human Cerebral Cortex: The Cortex of the Fifteen-month Infant*.
- Conel, J. L. (1959). *The Postnatal Development of the Human Cerebral Cortex: The Cortex of the Twenty-four-month Infant*.
- Conel, J. L. (1963). *The Postnatal Development of the Human Cerebral Cortex, V. 7: The Cortex of the Four-year Child*. Harvard University Press.
- Conel, J. L. (1967). The Postnatal Development of the Human Cerebral Cortex: Vol. VIII. The cortex of six-year child. *Harvard University Press*.
- Cossette, M., Lecomte, F., & Parent, A. (2005). Morphology and distribution of dopaminergic neurons intrinsic to the human striatum. *Journal of Chemical Neuroanatomy*, 29(1), 1–11.
- Coussons-Read, M. E., & Crnic, L. S. (1996). Behavioral assessment of the Ts65Dn mouse, a model for Down syndrome: altered behavior in the elevated plus maze and open field. *Behavior Genetics*, 26(1), 7–13.
- Cuntz, H., Forstner, F., Borst, A., & Häusser, M. (2010). One rule to grow them all: a general theory of neuronal branching and its practical application. *PLoS Computational Biology*, 6(8), e1000877.
- Cuntz, H., Forstner, F., Borst, A., & Häusser, M. (2011). The TREES toolbox probing the basis of axonal and dendritic branching. *Neuroinformatics*, 9(1), 91–96.
- Cuntz, H., Mathy, A., & Häusser, M. (2012). A scaling law derived from optimal dendritic wiring. *Proceedings of the National Academy of Sciences*, 109(27), 11014–11018.
- de Nö, R. (1934). Studies on the structure of the cerebral cortex. II. Continuation of the study of the ammonic system. *Journal Für Psychologie Und Neurologie*.
- Defelipe, J., González-Albo, M. C., Del Río, M. R., & Elston, G. N. (1999). Distribution and patterns of connectivity of interneurons containing calbindin, calretinin, and parvalbumin in visual areas of the occipital and temporal lobes of the macaque monkey. *Journal of Comparative Neurology*, 412(3), 515–526.
- Demas, G. E., Nelson, R. J., Krueger, B. K., & Yarowsky, P. J. (1998). Impaired spatial working and reference memory in segmental trisomy (Ts65Dn) mice. *Behavioural Brain Research*, 90(2), 199–201.
- Diamond, M. C., Krech, D., & Rosenzweig, M. R. (1964). The effects of an enriched environment on the histology of the rat cerebral cortex. *Journal of Comparative Neurology*, 123(1), 111–119.
- Dierssen, M., Benavides-Piccione, R., Martinez-Cue, C., Estivill, X., Florez, J., Elston, G. N., & DeFelipe, J. (2003). Alterations of neocortical pyramidal cell phenotype in the Ts65Dn mouse model of Down syndrome: effects of environmental enrichment. *Cerebral Cortex*, 13(7), 758–764.
- Dierssen, M., Herault, Y., & Estivill, X. (2009). Aneuploidy: from a physiological mechanism of variance to Down syndrome. *Physiological Reviews*, 89(3), 887–920.
- Dolinsky, T. J., Nielsen, J. E., McCammon, J. A., & Baker, N. A. (2004). PDB2PQR: an automated pipeline for the setup of Poisson–Boltzmann electrostatics calculations. *Nucleic Acids Research*, 32(suppl_2), W665–W667.

- Dolorfo, C. L., & Amaral, D. G. (1998). Entorhinal cortex of the rat: topographic organization of the cells of origin of the perforant path projection to the dentate gyrus. *Journal of Comparative Neurology*, 398(1), 25–48.
- Dong, H. W. (2008). *The Allen reference atlas: A digital color brain atlas of the C57Bl/6J male mouse*. John Wiley & Sons Inc.
- Dorph-Petersen, K.-A., & Lewis, D. A. (2011). Stereological approaches to identifying neuropathology in psychosis. *Biological Psychiatry*, 69(2), 113–126.
- Dougherty, K. A., Islam, T., & Johnston, D. (2012). Intrinsic excitability of CA1 pyramidal neurones from the rat dorsal and ventral hippocampus. *The Journal of Physiology*, 590(22), 5707–5722.
- Dougherty, K. A., Nicholson, D. A., Diaz, L., Buss, E. W., Neuman, K. M., Chetkovich, D. M., & Johnston, D. (2013). Differential expression of HCN subunits alters voltage-dependent gating of h-channels in CA1 pyramidal neurons from dorsal and ventral hippocampus. *Journal of Neurophysiology*, 109(7), 1940–1953.
- Dudman, J. T., Tsay, D., & Siegelbaum, S. A. (2007). A role for synaptic inputs at distal dendrites: instructive signals for hippocampal long-term plasticity. *Neuron*, 56(5), 866–879.
- Duffy, S. N., Craddock, K. J., Abel, T., & Nguyen, P. V. (2001). Environmental enrichment modifies the PKA-dependence of hippocampal LTP and improves hippocampus-dependent memory. *Learning & Memory*, 8(1), 26–34.
- Ecker, A. S., Berens, P., Cotton, R. J., Subramanyan, M., Denfield, G. H., Cadwell, C. R., ... Tolias, A. S. (2014). State dependence of noise correlations in macaque primary visual cortex. *Neuron*, 82(1), 235–248.
- Elston, G. N. (2002). Cortical heterogeneity: implications for visual processing and polysensory integration. *Journal of Neurocytology*, 31(3–5), 317–335.
- Elston, G. N., Benavides-Piccione, R., & DeFelipe, J. (2001). The pyramidal cell in cognition: a comparative study in human and monkey. *Journal of Neuroscience*, 21(17).
- Elston, G. N., & Rosa, M. G. (1997). The occipitoparietal pathway of the macaque monkey: comparison of pyramidal cell morphology in layer III of functionally related cortical visual areas. *Cerebral Cortex (New York, NY: 1991)*, 7(5), 432–452.
- Epp, J. R., Niibori, Y., Hsiang, H.-L. L., Mercaldo, V., Deisseroth, K., Josselyn, S. A., & Frankland, P. W. (2015). Optimization of CLARITY for clearing whole-brain and other intact organs. *eNeuro*, 2(3), ENEURO----0022.
- Escorihuela, R. M., Fernández-Teruel, A., Vallina, I. F., Baamonde, C., Lumbreiras, M. A., Dierssen, M., ... Flórez, J. (1995). A behavioral assessment of Ts65Dn mice: a putative Down syndrome model. *Neuroscience Letters*, 199(2), 143–146.
- Escorihuela, R. M., Fernández-Teruel, A., Tobena, A., Vivas, N. M., Marmol, F., Badia, A., & Dierssen, M. (1995). Early environmental stimulation produces long-lasting changes on β-adrenoceptor transduction system. *Neurobiology of Learning and Memory*, 64(1), 49–57.
- Eyal, G., Mansvelder, H. D., de Kock, C. P. J., & Segev, I. (2014). Dendrites impact the encoding capabilities of the axon. *Journal of Neuroscience*, 34(24), 8063–8071.
- Faisal, A. A., Selen, L. P. J., & Wolpert, D. M. (2008). Noise in the nervous system. *Nature Reviews Neuroscience*, 9(4), 292–303.
- Fanselow, M. S., & Dong, H.-W. (2010). Are the dorsal and ventral hippocampus functionally distinct structures? *Neuron*, 65(1), 7–19.
- Feldt, S., Bonifazi, P., & Cossart, R. (2011). Dissecting functional connectivity of neuronal microcircuits: experimental and theoretical insights. *Trends in Neurosciences*, 34(5), 225–236.

- Feng, L., Zhao, T., & Kim, J. (2015). neuTube 1.0: A New Design for Efficient Neuron Reconstruction Software Based on the SWC Format. *eNeuro*, 2(1).
<https://doi.org/10.1523/ENEURO.0049-14.2014>
- Ferreira, T. A., Blackman, A. V., Oyrer, J., Jayabal, S., Chung, A. J., Watt, A. J., ... Van Meyel, D. J. (2014). Neuronal morphometry directly from bitmap images. *Nature Methods*, 11(10), 982–984.
- Foster, T. C., & Dumas, T. C. (2001). Mechanism for increased hippocampal synaptic strength following differential experience. *Journal of Neurophysiology*, 85(4), 1377–1383.
- Fotaki, V., Martinez De Lagran, M., Estivill, X., Arbones, M., & Dierssen, M. (2004). Haploinsufficiency of Dyrk1A in mice leads to specific alterations in the development and regulation of motor activity. *Behavioral Neuroscience*, 118(4), 815.
- Frasconi, P., Silvestri, L., Soda, P., Cortini, R., Pavone, F. S., & Iannello, G. (2014). Large-scale automated identification of mouse brain cells in confocal light sheet microscopy images. *Bioinformatics*, 30(17), i587---i593.
- Freese, J. L., & Amaral, D. G. (2005). The organization of projections from the amygdala to visual cortical areas TE and V1 in the macaque monkey. *Journal of Comparative Neurology*, 486(4), 295–317.
- Gaarskjaer, F. B. (1978). Organization of the mossy fiber system of the rat studied in extended hippocampi. I. Terminal area related to number of granule and pyramidal cells. *Journal of Comparative Neurology*, 178(1), 49–71.
- Gibble, K. L., Kishi, G. T., & Peake, J. W. (2006). Method, system, and program for moving data among storage units. Google Patents.
- Girvan, M., & Newman, M. E. J. (2002). Community structure in social and biological networks. *Proceedings of the National Academy of Sciences*, 99(12), 7821–7826.
- Goñi, J., van den Heuvel, M. P., Avena-Koenigsberger, A., de Mendizabal, N. V., Betzel, R. F., Griffa, A., ... Sporns, O. (2014). Resting-brain functional connectivity predicted by analytic measures of network communication. *Proceedings of the National Academy of Sciences*, 111(2), 833–838.
- Gorgolewski, K., Burns, C. D., Madison, C., Clark, D., Halchenko, Y. O., Waskom, M. L., & Ghosh, S. S. (2011). NiPy: a flexible, lightweight and extensible neuroimaging data processing framework in python. *Frontiers in Neuroinformatics*, 5.
- Goris, R. L. T., Movshon, J. A., & Simoncelli, E. P. (2014). Partitioning neuronal variability. *Nature Neuroscience*, 17(6), 858–865.
- Gough, B. (2009). *GNU scientific library reference manual*. Network Theory Ltd.
- Graves, A. R., Moore, S. J., Bloss, E. B., Mensh, B. D., Kath, W. L., & Spruston, N. (2012). Hippocampal pyramidal neurons comprise two distinct cell types that are countermodulated by metabotropic receptors. *Neuron*, 76(4), 776–789.
- Gray, J. A. (1982). On mapping anxiety. *Behavioral and Brain Sciences*, 5(3), 506–534.
- Grevera, G. J., & Udupa, J. K. (1996). Shape-based interpolation of multidimensional grey-level images. *IEEE Transactions on Medical Imaging*, 15(6), 881–892.
- Grillner, S. (2015). Action: The Role of Motor Cortex Challenged. *Current Biology*, 25(12), R508-- R511. <https://doi.org/https://doi.org/10.1016/j.cub.2015.04.023>
- Groenewegen, H. J., te der Zee, E., Te Kortschot, A., & Witter, M. P. (1987). Organization of the projections from the subiculum to the ventral striatum in the rat. A study using anterograde transport of Phaseolus vulgaris leucoagglutinin. *Neuroscience*, 23(1), 103–120.
- Hama, H., Kurokawa, H., Kawano, H., Ando, R., Shimogori, T., Noda, H., ... Miyawaki, A. (2011). Scale: a chemical approach for fluorescence imaging and reconstruction of transparent mouse brain. *Nature Neuroscience*, 14(11), 1481–1488.

- Harding, A. J., Halliday, G. M., & Cullen, K. (1994). Practical considerations for the use of the optical disector in estimating neuronal number. *Journal of Neuroscience Methods*, 51(1), 83–89.
- Hasegawa, J., Sakamoto, Y., Nakagami, S., Aida, M., Sawa, S., & Matsunaga, S. (2016). Three-dimensional imaging of plant organs using a simple and rapid transparency technique. *Plant and Cell Physiology*, 57(3), 462–472.
- Hasselmo, M. E., & Schnell, E. (1994). Laminar selectivity of the cholinergic suppression of synaptic transmission in rat hippocampal region CA1: computational modeling and brain slice physiology. *Journal of Neuroscience*, 14(6), 3898–3914.
- Hasselmo, M. E., Schnell, E., & Barkai, E. (1995). Dynamics of learning and recall at excitatory recurrent synapses and cholinergic modulation in rat hippocampal region CA3. *Journal of Neuroscience*, 15(7), 5249–5262.
- Hasselmo, M. E., & Wyble, B. P. (1997). Free recall and recognition in a network model of the hippocampus: simulating effects of scopolamine on human memory function. *Behavioural Brain Research*, 89(1), 1–34.
- Hawrylycz, M., Baldoock, R. A., Burger, A., Hashikawa, T., Johnson, G. A., Martone, M., ... Others. (2011). Digital atlasing and standardization in the mouse brain. *PLoS Computational Biology*, 7(2), e1001065.
- Hawrylycz, M. J., Lein, E. S., Guillozet-Bongaarts, A. L., Shen, E. H., Ng, L., Miller, J. A., ... Others. (2012). An anatomically comprehensive atlas of the adult human brain transcriptome. *Nature*, 489(7416), 391–399.
- Herculano-Houzel, S. (2009). The human brain in numbers: a linearly scaled-up primate brain. *Frontiers in Human Neuroscience*, 3.
- Hilgetag, C. C., & Kaiser, M. (2004). Clustered organization of cortical connectivity. *Neuroinformatics*, 2(3), 353–360.
- Hill, S. L., Wang, Y., Riachi, I., Schürmann, F., & Markram, H. (2012). Statistical connectivity provides a sufficient foundation for specific functional connectivity in neocortical neural microcircuits. *Proceedings of the National Academy of Sciences*, 109(42), E2885–E2894.
- Hodgkin, A. L., & Huxley, A. F. (1952). A quantitative description of membrane current and its application to conduction and excitation in nerve. *The Journal of Physiology*, 117(4), 500–544.
- Hunter, C. L., Bimonte, H. A., & Granholm, A.-C. E. (2003). Behavioral comparison of 4 and 6 month-old Ts65Dn mice: Age-related impairments in working and reference memory. *Behavioural Brain Research*, 138(2), 121–131.
- Igarashi, K. M., Ito, H. T., Moser, E. I., & Moser, M.-B. (2014). Functional diversity along the transverse axis of hippocampal area CA1. *FEBS Letters*, 588(15), 2470–2476.
- Ilin, V., Malyshev, A., Wolf, F., & Volgshev, M. (2013). Fast computations in cortical ensembles require rapid initiation of action potentials. *Journal of Neuroscience*, 33(6), 2281–2292.
- Insausti, A. M., Megías, M., Crespo, D., Cruz-Orive, L. M., Dierssen, M., Vallina, T. F., ... Florez, J. (1998). Hippocampal volume and neuronal number in Ts65Dn mice: a murine model of Down syndrome. *Neuroscience Letters*, 253(3), 175–178.
- Irshad, H., Veillard, A., Roux, L., & Racocceanu, D. (2014). Methods for nuclei detection, segmentation, and classification in digital histopathology: a review current status and future potential. *IEEE Reviews in Biomedical Engineering*, 7, 97–114.
- Irvine, G. I., & Abraham, W. C. (2005). Enriched environment exposure alters the input-output dynamics of synaptic transmission in area CA1 of freely moving rats. *Neuroscience Letters*, 391(1), 32–37.

- Janke, A. L., & Ullmann, J. F. P. (2015). Robust methods to create ex vivo minimum deformation atlases for brain mapping. *Methods*, 73, 18–26.
- Jarsky, T., Mady, R., Kennedy, B., & Spruston, N. (2008). Distribution of bursting neurons in the CA1 region and the subiculum of the rat hippocampus. *Journal of Comparative Neurology*, 506(4), 535–547.
- Jinno, S., & Kosaka, T. (2009). Neuronal circuit-dependent alterations in expression of two isoforms of glutamic acid decarboxylase in the hippocampus following electroconvulsive shock: A stereology-based study. *Hippocampus*, 19(11), 1130–1141.
- Kida, E., Rabe, A., Walus, M., Albertini, G., & Golabek, A. A. (2013). Long-term running alleviates some behavioral and molecular abnormalities in Down syndrome mouse model Ts65Dn. *Experimental Neurology*, 240, 178–189.
- Kim, S.-Y., Cho, J. H., Murray, E., Bakh, N., Choi, H., Ohn, K., ... others. (2015). Stochastic electrotransport selectively enhances the transport of highly electromobile molecules. *Proceedings of the National Academy of Sciences*, 112(46), E6274–E6283.
- Kohn, A., & Smith, M. A. (2005). Stimulus dependence of neuronal correlation in primary visual cortex of the macaque. *Journal of Neuroscience*, 25(14), 3661–3673.
- Kolb, B., & Gibb, R. (1991). Environmental enrichment and cortical injury: behavioral and anatomical consequences of frontal cortex lesions. *Cerebral Cortex*, 1(2), 189–198.
- Komulainen, E., Zdrojewska, J., Freemantle, E., Mohammad, H., Kulevskaya, N., Deshpande, P., ... Others. (2014). JNK1 controls dendritic field size in L2/3 and L5 of the motor cortex, constrains soma size, and influences fine motor coordination. *Frontiers in Cellular Neuroscience*, 8.
- Kondo, H., Hashikawa, T., Tanaka, K., & Jones, E. G. (1994). Neurochemical gradient along the monkey occipito-temporal cortical pathway. *Neuroreport*, 5(5), 613–616.
- Kurt, M. A., Davies, D. C., Kidd, M., Dierssen, M., & Flórez, J. (2000). Synaptic deficit in the temporal cortex of partial trisomy 16 (Ts65Dn) mice. *Brain Research*, 858(1), 191–197.
- Kurt, M. A., Kafa, M. I., Dierssen, M., & Davies, D. C. (2004). Deficits of neuronal density in CA1 and synaptic density in the dentate gyrus, CA3 and CA1, in a mouse model of Down syndrome. *Brain Research*, 1022(1), 101–109.
- Lapicque, L. (1907). Recherches quantitatives sur l'excitation électrique des nerfs traitée comme polarisation. *J. Physiol. Pathol. Gen.*, 9, 620–635.
- Lee, H., Park, J.-H., Seo, I., Park, S.-H., & Kim, S. (2014). Improved application of the electrophoretic tissue clearing technology, CLARITY, to intact solid organs including brain, pancreas, liver, kidney, lung, and intestine. *BMC Developmental Biology*, 14(1), 48.
- Lee, S.-H., Marchionni, I., Bezaire, M., Varga, C., Danielson, N., Lovett-Barron, M., ... Soltesz, I. (2014). Parvalbumin-positive basket cells differentiate among hippocampal pyramidal cells. *Neuron*, 82(5), 1129–1144.
- Leggio, M. G., Mandolesi, L., Federico, F., Spirito, F., Ricci, B., Gelfo, F., & Petrosini, L. (2005). Environmental enrichment promotes improved spatial abilities and enhanced dendritic growth in the rat. *Behavioural Brain Research*, 163(1), 78–90.
- London, M., & Häusser, M. (2005). Dendritic computation. *Annu. Rev. Neurosci.*, 28, 503–532.
- Longair, M. H., Baker, D. A., & Armstrong, J. D. (2011). Simple Neurite Tracer: open source software for reconstruction, visualization and analysis of neuronal processes. *Bioinformatics*, 27(17), 2453–2454.

- Lübke, J., Markram, H., Frotscher, M., & Sakmann, B. (1996). Frequency and dendritic distribution of autapses established by layer 5 pyramidal neurons in the developing rat neocortex: comparison with synaptic innervation of adjacent neurons of the same class. *Journal of Neuroscience*, 16(10), 3209–3218.
- Magliaro, C., Callara, A. L., Mattei, G., Morcinelli, M., Viaggi, C., Vaglini, F., & Ahluwalia, A. (2016). Clarifying CLARITY: quantitative optimization of the diffusion based delipidation protocol for genetically labeled tissue. *Frontiers in Neuroscience*, 10.
- Mai, J. K., & Paxinos, G. (2011). *The human nervous system*. Academic Press.
- Mainen, Z. F., Sejnowski, T. J., & Others. (1996). Influence of dendritic structure on firing pattern in model neocortical neurons. *Nature*, 382(6589), 363–366.
- Malik, R., Dougherty, K. A., Parikh, K., Byrne, C., & Johnston, D. (2016). Mapping the electrophysiological and morphological properties of CA1 pyramidal neurons along the longitudinal hippocampal axis. *Hippocampus*, 26(3), 341–361.
- Manita, S., Suzuki, T., Homma, C., Matsumoto, T., Odagawa, M., Yamada, K., ... Others. (2015). A top-down cortical circuit for accurate sensory perception. *Neuron*, 86(5), 1304–1316.
- Markram, H. (2006). The blue brain project. *Nature Reviews Neuroscience*, 7(2), 153–160.
- Marr, D., Willshaw, D., & McNaughton, B. (1991). Simple memory: a theory for archicortex. In *From the Retina to the Neocortex* (pp. 59–128). Springer.
- Martínez-Cué, C., Rueda, N., García, E., Davisson, M. T., Schmidt, C., & Flórez, J. (2005). Behavioral, cognitive and biochemical responses to different environmental conditions in male Ts65Dn mice, a model of Down syndrome. *Behavioural Brain Research*, 163(2), 174–185.
- Martínez de Lagrán, M., Altafaj, X., Gallego, X., Martí, E., Estivill, X., Sahun, I., ... Dierssen, M. (2004). Motor phenotypic alterations in TgDyrk1a transgenic mice implicate DYRK1A in Down syndrome motor dysfunction. *Neurobiology of Disease*, 15(1), 132–142.
- Martínez de Lagrán, M., Benavides-Piccione, R., Ballesteros-Yáñez, I., Calvo, M., Morales, M., Fillat, C., ... Dierssen, M. (2012). Dyrk1A influences neuronal morphogenesis through regulation of cytoskeletal dynamics in mammalian cortical neurons. *Cerebral Cortex*, 22(12), 2867–2877.
- Martínez de Lagrán, M., Bortolozzi, A., Millan, O., Gispert, J. D., Gonzalez, J. R., Arbones, M. L., ... Dierssen, M. (2007). Dopaminergic deficiency in mice with reduced levels of the dual-specificity tyrosine-phosphorylated and regulated kinase 1A, Dyrk1A+/. *Genes, Brain and Behavior*, 6(6), 569–578.
- Mason, A., & Larkman, A. (1990). Correlations between morphology and electrophysiology of pyramidal neurons in slices of rat visual cortex. II. Electrophysiology. *Journal of Neuroscience*, 10(5), 1415–1428.
- McNaughton, B. L., & Morris, R. G. M. (1987). Hippocampal synaptic enhancement and information storage within a distributed memory system. *Trends in Neurosciences*, 10(10), 408–415.
- Mizuseki, K., Diba, K., Pastalkova, E., & Buzsáki, G. (2011). Hippocampal CA1 pyramidal cells form functionally distinct sublayers. *Nature Neuroscience*, 14(9), 1174–1181.
- Moreno-Bote, R., Beck, J., Kanitscheider, I., Pitkow, X., Latham, P., & Pouget, A. (2014). Information-limiting correlations. *Nature Neuroscience*, 17(10), 1410–1417.
- Morris, C., & Lecar, H. (1981). Voltage oscillations in the barnacle giant muscle fiber. *Biophysical Journal*, 35(1), 193–213.
- Moser, M.-B., & Moser, E. I. (1998). Functional differentiation in the hippocampus. *Hippocampus*, 8(6), 608–619.

- Musielak, T. J., Slane, D., Liebig, C., & Bayer, M. (2016). A Versatile Optical Clearing Protocol for Deep Tissue Imaging of Fluorescent Proteins in *Arabidopsis thaliana*. *PloS One*, 11(8), e0161107.
- Nambu, J. R., Lewis, J. O., Wharton, K. A., & Crews, S. T. (1991). The *Drosophila* single-minded gene encodes a helix-loop-helix protein that acts as a master regulator of CNS midline development. *Cell*, 67(6), 1157–1167.
- Norman, K. A., & O’reilly, R. C. (2003). Modeling hippocampal and neocortical contributions to recognition memory: a complementary-learning-systems approach. *Psychological Review*, 110(4), 611.
- O’Connor, A. M., Burton, T. J., Leamey, C. A., & Sawatari, A. (2014). The Use of the Puzzle Box as a Means of Assessing the Efficacy of Environmental Enrichment. *Journal of Visualized Experiments: JoVE*, (94).
- O’reilly, R. C., & McClelland, J. L. (1994). Hippocampal conjunctive encoding, storage, and recall: avoiding a trade-off. *Hippocampus*, 4(6), 661–682.
- Orlandi, J. G., Soriano, J., Alvarez-Lacalle, E., Teller, S., & Casademunt, J. (2013). Noise focusing and the emergence of coherent activity in neuronal cultures. *Nature Physics*, 9(9), 582–590.
- Otsu, N. (1979). A threshold selection method from gray-level histograms. *IEEE Transactions on Systems, Man, and Cybernetics*, 9(1), 62–66.
- Pareto, V. (1963). *The mind and society: A treatise on general sociology* (Vol. 3). Dover Publications.
- Parrish, R. M., Burns, L. A., Smith, D. G. A., Simmonett, A. C., DePrince, A. E., Hohenstein, E. G., ... others. (2017). Psi4 1.1: An Open-Source Electronic Structure Program Emphasizing Automation, Advanced Libraries, and Interoperability. *Journal of Chemical Theory and Computation*.
- Paxinos, G. (2014). *The rat nervous system*. Academic press.
- Paxinos, G., & Franklin, K. B. J. (2004). *The mouse brain in stereotaxic coordinates*. Gulf Professional Publishing.
- Paxinos, G., & Others. (2013). *Paxinos and Franklin’s the mouse brain in stereotaxic coordinates*. Academic Press.
- Peng, H., Bria, A., Zhou, Z., Iannello, G., & Long, F. (2014). Extensible visualization and analysis for multidimensional images using Vaa3D. *Nature Protocols*, 9(1), 193–208.
- Pennington, B. F., Moon, J., Edgin, J., Stedron, J., & Nadel, L. (2003). The neuropsychology of Down syndrome: evidence for hippocampal dysfunction. *Child Development*, 74(1), 75–93.
- Pietzsch, T., Saalfeld, S., Preibisch, S., & Tomancak, P. (2015). BigDataViewer: visualization and processing for large image data sets. *Nature Methods*, 12(6), 481–483.
- Poirazi, P., & Mel, B. W. (2001). Impact of active dendrites and structural plasticity on the memory capacity of neural tissue. *Neuron*, 29(3), 779–796.
- Pons-Espinal, M., de Lagran, M. M., & Dierssen, M. (2013). Environmental enrichment rescues DYRK1A activity and hippocampal adult neurogenesis in TgDyrk1A. *Neurobiology of Disease*, 60, 18–31.
- Ramón, F., Moore, J. W., Joyner, R. W., & Westerfield, M. (1976). Squid giant axons. A model for the neuron soma? *Biophysical Journal*, 16(8), 953–963.
- Ramón y Cajal, S. (1995). *Histology of the nervous system of man and vertebrates* (Vol. 1). Oxford University Press, USA.
- Reimann, M. W., Nolte, M., Scolamiero, M., Turner, K., Perin, R., Chindemi, G., ... Markram, H. (2017). Cliques of Neurons Bound into Cavities Provide a Missing Link between Structure and Function. *Frontiers in Computational Neuroscience*, 11, 48.

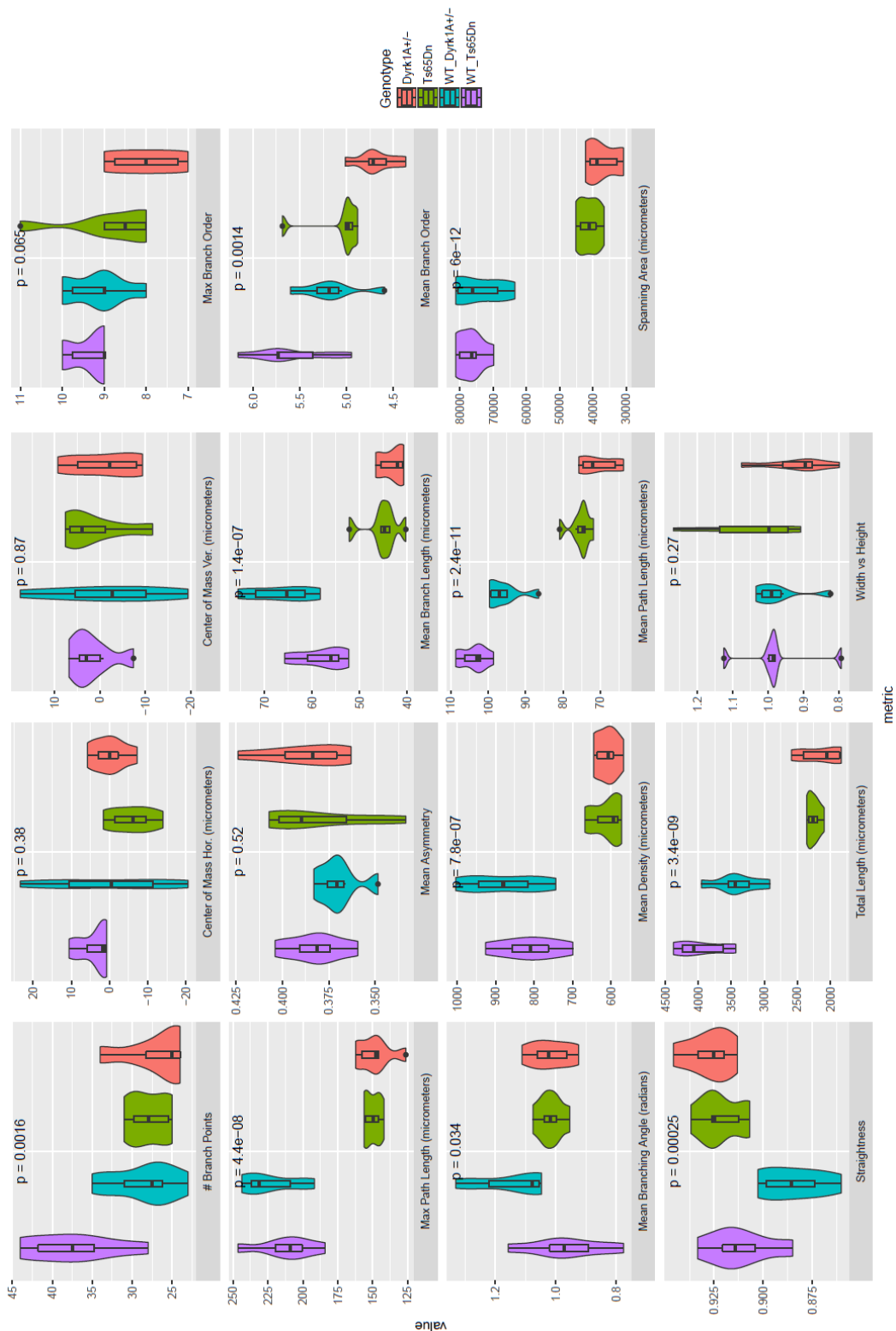
- Renier, N., Wu, Z., Simon, D. J., Yang, J., Ariel, P., & Tessier-Lavigne, M. (2014). iDISCO: a simple, rapid method to immunolabel large tissue samples for volume imaging. *Cell*, *159*(4), 896–910.
- Rihm, L. L., & Claiborne, B. J. (1990). Dendritic growth and regression in rat dentate granule cells during late postnatal development. *Developmental Brain Research*, *54*(1), 115–124.
- Risold, P. Y., & Swanson, L. W. (1996). Structural evidence for functional domains in the rat hippocampus. *Science*, *272*(5267), 1484.
- Ropireddy, D., Bachus, S. E., & Ascoli, G. A. (2012). Non-homogeneous stereological properties of the rat hippocampus from high-resolution 3D serial reconstruction of thin histological sections. *Neuroscience*, *205*, 91–111.
- Rosen, G. D., & Harry, J. D. (1990). Brain volume estimation from serial section measurements: a comparison of methodologies. *Journal of Neuroscience Methods*, *35*(2), 115–124.
- Royle, S. J., Collins, F. C., Rupniak, H. T., Barnes, J. C., & Anderson, R. (1999). Behavioural analysis and susceptibility to CNS injury of four inbred strains of mice. *Brain Research*, *816*(2), 337–349.
- Ruiz-Mejias, M., de Lagran, M. M., Mattia, M., Castano-Prat, P., Perez-Mendez, L., Ciria-Suarez, L., ... others. (2016). Overexpression of Dyrk1A, a down syndrome candidate, decreases excitability and impairs gamma oscillations in the prefrontal cortex. *Journal of Neuroscience*, *36*(13), 3648–3659.
- Sago, H., Carlson, E. J., Smith, D. J., Kilbridge, J., Rubin, E. M., Mobley, W. C., ... Huang, T.-T. (1998). Ts1Cje, a partial trisomy 16 mouse model for Down syndrome, exhibits learning and behavioral abnormalities. *Proceedings of the National Academy of Sciences*, *95*(11), 6256–6261.
- Sanchez-Vives, M. V., & Garcia-Ojalvo, J. (2016). Collective stochastic coherence in recurrent neuronal networks. *Nature Physics*, *12*(9), 881–887.
- Sansom, S. N., & Livesey, F. J. (2009). Gradients in the brain: the control of the development of form and function in the cerebral cortex. *Cold Spring Harbor Perspectives in Biology*, *1*(2), a002519.
- Sasaki, T., Matsuki, N., & Ikegaya, Y. (2012). Effects of axonal topology on the somatic modulation of synaptic outputs. *Journal of Neuroscience*, *32*(8), 2868–2876.
- Schindelin, J., Arganda-Carreras, I., Frise, E., Kaynig, V., Longair, M., Pietzsch, T., ... Others. (2012). Fiji: an open-source platform for biological-image analysis. *Nature Methods*, *9*(7), 676–682.
- Schröter, M., Paulsen, O., & Bullmore, E. T. (2017). Micro-connectomics: probing the organization of neuronal networks at the cellular scale. *Nature Reviews Neuroscience*, *18*(3), 131–146.
- Shadlen, M. N., & Newsome, W. T. (1998). The variable discharge of cortical neurons: implications for connectivity, computation, and information coding. *Journal of Neuroscience*, *18*(10), 3870–3896.
- Shepherd, G. M., Mirsky, J. S., Healy, M. D., Singer, M. S., Skoufos, E., Hines, M. S., ... Miller, P. L. (1998). The Human Brain Project: neuroinformatics tools for integrating, searching and modeling multidisciplinary neuroscience data. *Trends in Neurosciences*, *21*(11), 460–468.
- Siarey, R. J., Carlson, E. J., Epstein, C. J., Balbo, A., Rapoport, S. I., & Galdzicki, Z. (1999). Increased synaptic depression in the Ts65Dn mouse, a model for mental retardation in Down syndrome. *Neuropharmacology*, *38*(12), 1917–1920.

- Siarey, R. J., Stoll, J., Rapoport, S. I., & Galdzicki, Z. (1997). Altered long-term potentiation in the young and old Ts65Dn mouse, a model for Down Syndrome. *Neuropharmacology*, 36(11), 1549–1554.
- Siek, J. G., Lee, L.-Q., & Lumsdaine, A. (2001). *The Boost Graph Library: User Guide and Reference Manual, Portable Documents*. Pearson Education.
- Slomianka, L., Amrein, I., Knuesel, I., Sørensen, J. C., & Wolfer, D. P. (2011). Hippocampal pyramidal cells: the reemergence of cortical lamination. *Brain Structure and Function*, 216(4), 301.
- Smith, D. O. (1977). Ultrastructural basis of impulse propagation failure in a nonbranching axon. *Journal of Comparative Neurology*, 176(4), 659–669.
- Solstze, I. (2006). *Diversity in the Neuronal Machine: Order and Variability in Interneuronal Microcircuits*.
- Sporns, O., Chialvo, D. R., Kaiser, M., & Hilgetag, C. C. (2004). Organization, development and function of complex brain networks. *Trends in Cognitive Sciences*, 8(9), 418–425.
- Stasko, M. R., & Costa, A. C. S. (2004). Experimental parameters affecting the Morris water maze performance of a mouse model of Down syndrome. *Behavioural Brain Research*, 154(1), 1–17.
- Staudt, T., Lang, M. C., Medda, R., Engelhardt, J., & Hell, S. W. (2007). 2, 2'-thiodiethanol: a new water soluble mounting medium for high resolution optical microscopy. *Microscopy Research and Technique*, 70(1), 1–9.
- Stepanyants, A., & Chklovskii, D. B. (2005). Neurogeometry and potential synaptic connectivity. *Trends in Neurosciences*, 28(7), 387–394.
- Stoner-Ma, D., Jaye, A. A., Matousek, P., Towrie, M., Meech, S. R., & Tonge, P. J. (2005). Observation of excited-state proton transfer in green fluorescent protein using ultrafast vibrational spectroscopy. *Journal of the American Chemical Society*, 127(9), 2864–2865.
- Strange, B. A., Witter, M. P., Lein, E. S., & Moser, E. I. (2014). Functional organization of the hippocampal longitudinal axis. *Nature Reviews Neuroscience*, 15(10), 655–669.
- Szigeti, B., Gleeson, P., Vella, M., Khayrulin, S., Palyanov, A., Hokanson, J., ... Larson, S. (2014). OpenWorm: an open-science approach to modeling *Caenorhabditis elegans*. *Frontiers in Computational Neuroscience*, 8.
- Tolhurst, D. J., Movshon, J. A., & Dean, A. F. (1983). The statistical reliability of signals in single neurons in cat and monkey visual cortex. *Vision Research*, 23(8), 775–785.
- Tomer, R., Ye, L., Hsueh, B., & Deisseroth, K. (2014). Advanced CLARITY for rapid and high-resolution imaging of intact tissues. *Nature Protocols*, 9(7), 1682–1697.
- Torre, R., Sola, S., Pons, M., Duchon, A., Lagran, M. M., Farré, M., ... Others. (2014). Epigallocatechin-3-gallate, a DYRK1A inhibitor, rescues cognitive deficits in Down syndrome mouse models and in humans. *Molecular Nutrition & Food Research*, 58(2), 278–288.
- Treves, A., & Rolls, E. T. (1992). Computational constraints suggest the need for two distinct input systems to the hippocampal CA3 network. *Hippocampus*, 2(2), 189–199.
- Treves, A., & Rolls, E. T. (1994). Computational analysis of the role of the hippocampus in memory. *Hippocampus*, 4(3), 374–391.
- van Elburg, R. A. J., & van Ooyen, A. (2010). Impact of dendritic size and dendritic topology on burst firing in pyramidal cells. *PLoS Computational Biology*, 6(5), e1000781.
- Vegue, M., Perin, R., & Roxin, A. (2017). On the structure of cortical micro-circuits inferred from small sample sizes. *bioRxiv*, 118471.

- Vincent, R. D., Janke, A., Sled, J. G., Baghdadi, L., Neelin, P., & Evans, A. C. (2004). MINC 2.0: a modality independent format for multidimensional medical images. In *10th Annual Meeting of the Organization for Human Brain Mapping* (Vol. 2003, p. 2003).
- Voges, N., Schüz, A., Aertsen, A., & Rotter, S. (2010). A modeler's view on the spatial structure of intrinsic horizontal connectivity in the neocortex. *Progress in Neurobiology*, 92(3), 277–292.
- Volkmar, F. R., & Greenough, W. T. (1972). Rearing complexity affects branching of dendrites in the visual cortex of the rat. *Science*, 176(4042), 1445–1447.
- Wen, Q., & Chklovskii, D. B. (2005). Segregation of the brain into gray and white matter: a design minimizing conduction delays. *PLoS Computational Biology*, 1(7), e78.
- Wen, Q., Stepanyants, A., Elston, G. N., Grosberg, A. Y., & Chklovskii, D. B. (2009). Maximization of the connectivity repertoire as a statistical principle governing the shapes of dendritic arbors. *Proceedings of the National Academy of Sciences*, 106(30), 12536–12541.
- White, J. G., Southgate, E., Thomson, J. N., & Brenner, S. (1986). The structure of the nervous system of the nematode *Caenorhabditis elegans*: the mind of a worm. *Phil. Trans. R. Soc. Lond.*, 314, 1–340.
- White, N. S., Alkire, M. T., & Haier, R. J. (2003). A voxel-based morphometric study of nondemented adults with Down Syndrome. *Neuroimage*, 20(1), 393–403.
- Wold, S., Esbensen, K., & Geladi, P. (1987). Principal component analysis. *Chemometrics and Intelligent Laboratory Systems*, 2(1–3), 37–52.
- Xu, L., Tanigawa, H., & Fujita, I. (2003). Distribution of α -amino-3-hydroxy-5-methyl-4-isoxazolepropionate-type glutamate receptor subunits (GluR2/3) along the ventral visual pathway in the monkey. *Journal of Comparative Neurology*, 456(4), 396–407.
- Yang, B., Treweek, J. B., Kulkarni, R. P., Deverman, B. E., Chen, C.-K., Lubeck, E., ... Gradinaru, V. (2014). Single-cell phenotyping within transparent intact tissue through whole-body clearing. *Cell*, 158(4), 945–958.
- Ye, L., Allen, W. E., Thompson, K. R., Tian, Q., Hsueh, B., Ramakrishnan, C., ... Others. (2016). Wiring and molecular features of prefrontal ensembles representing distinct experiences. *Cell*, 165(7), 1776–1788.
- Zador, A. M., Agmon-Snir, H., & Segev, I. (1995). The morphoelectrotomographic transform: a graphical approach to dendritic function. *Journal of Neuroscience*, 15(3), 1669–1682.
- Zhang, M.-D., Tortoriello, G., Hsueh, B., Tomer, R., Ye, L., Mitsios, N., ... Others. (2014). Neuronal calcium-binding proteins 1/2 localize to dorsal root ganglia and excitatory spinal neurons and are regulated by nerve injury. *Proceedings of the National Academy of Sciences*, 111(12), E1149–E1158.
- Zheng, Z., Lauritzen, J. S., Perlman, E., Robinson, C. G., Nichols, M., Milkie, D., ... Bock, D. D. (2017). A Complete Electron Microscopy Volume Of The Brain Of Adult *Drosophila melanogaster*. *bioRxiv*. <https://doi.org/10.1101/140905>

ANNEX

ANNEX I: Supplementary Figure

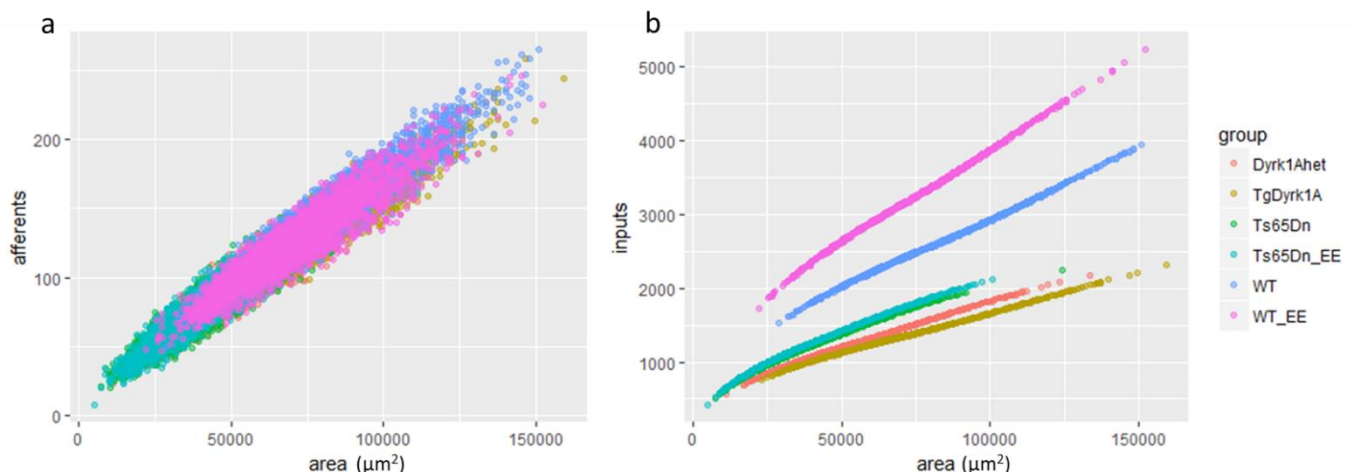


Supplementary Figure 1. Boxplots and violin plots of single-neuron morphological metrics. Each panel shows violin and boxplots for metrics having significant differences in one-way ANOVA tests between the Ts65Dn, Dyrk1A^{+/−} and their respective controls, the p-value of the test is shown on top of each panel. Each metric units are specified in the panel label. Each colored box/violin plot represents the distribution of the metric for each group.

ANNEX II: Number of afferents and dendritic tree area correlation

Based on the network building method in the cortical layer II/III model, it can be expected that the amount of afferents neurons connecting to a given neuron is proportional to the spanning area of the postsynaptic neuron. The instantiation of the cortical layer II/III model (Chapter I) allows to assess whether these variables correlate (**Supplementary Figure 2**). In order to obtain the numbers of afferents for single neurons in the Pareto optimality exploration of 2D neuronal reconstructions, all the data points were fitted with a linear model using the *lm* function in R. The coefficients of the fit were:

	Estimate	Std. Error	t value	Pr(> t)
(Intercept)	1.500e+01	1.991e-01	75.35	<2e-16 ***
area	1.546e-03	3.030e-06	510.33	<2e-16 ***



Supplementary Figure 2. Scatterplots of the numbers of afferents and numbers of inputs to all the neurons in the cortical layer II/III model. a) The number of afferents is proportional to the dendritic tree spanning area regardless of the parameterization used (indicated by the color). b) The number of inputs, even though correlates with the area, is model dependent in function of the parameterization used.

ANNEX III: Computational and experimental approaches for optimizing cleared whole-brain fluorescence microscopy imaging

INTRODUCTION

In recent decades, the advent of tissue clearing techniques has made possible the imaging of relatively big volumes (1 cm^3) in intact biological samples at the microscopic scale. The parallel development of fluorescent proteins and laser scanning microscopy techniques that can achieve deep tissue imaging of fluorescently labeled tissues has opened new opportunities for the application of these tools. However, the application of these novel techniques still requires the refinement of technical aspects. Most of the methods present problems that include degradation of the fluorescent signal, swelling of the samples, and reduced transparency, which strongly limit their applicability. Given the high amount of work done in models with genetically encoded fluorescent proteins (FPs), which is extremely helpful for tracking neuronal morphology in fixed, cleared tissue, this fluorescence quenching driven by the use of a solvent-based clearing procedure, sometimes needed for lipid removal, is very limiting. Even in well-cleared tissue, FPs can be imaged if the signal is strong, but FPs expressed at endogenous levels may not be bright enough to be detected over background. The selection of media is usually done by essay-error, which is labor-intensive, and not cost-effective. In fact, many laboratories find difficulties reaching the imaging quality needed. Having a computational framework to provide predictions on the efficacy of candidate imaging media could accelerate this research by scaling up the quantity of compound that could be screened and providing optimal solutions.

In my work I faced the problems mentioned above. As shown in Chapter III, there is high variability on the clearing quality depending on the choice of the imaging medium. While the original protocol suggests using 87% glycerol or FocusClear (a commercial imaging medium), the use of either media led to suboptimal imaging quality in my experiments. Thus, I tried using a diatrizoic acid solution that was recently proposed by Kim et al. (Kim et al., 2015). However, despite it is the best candidate regarding transparency, fluorescence preservation and swelling of the samples, it still shows some drawbacks. The other candidate that would improve those aspects and that also has shown very high transparency is thioldiethanol (TDE). However, its main problem is fluorescence quenching.

While studying tissue transparency and swelling from a computational perspective would require modeling frameworks developed from scratch, fluorescence quenching can be assessed by using molecular dynamics (MD) computational modeling existing tools. Here I aimed to propose a hypothesis-based method to select the best clearing media. Even though the method could be used to investigate the quenching produced by any reagent used in a tissue clearing protocol, I have focused on the mechanistic explanation of eYFP quenching in high concentration of TDE. The reasons for this choice are: (1) the high transparency and low swelling shown by TDE (see Chapter III) are of high interest for the imaging of CLARITY-treated whole brains, and (2) the eYFP quenching by TDE that we observed is known to happen specifically in YFP and GFP mutants, but not in RFP (Staudt et al., 2007) and (3) the quenching is highly dependent on TDE concentration (Musielak, Slane, Liebig, & Bayer, 2016).

I reasoned that since FPs require an aqueous medium to fluoresce, the interference with the presence of this water molecule inside the protein barrel could explain the TDE quenching. This has been investigated from a mechanistic point of view based on X-ray crystallography and molecular dynamics simulations. Brejc et al. (Brejc et al., 1997) found that GFP has a proton tunnel that connects the fluorescent chromophore with the bulk medium at the surface of the protein that allows the transport of the proton released in the excited state proton transfer (which is a required process for FP fluorescence). This connection is performed via a water molecule that is in the close vicinity of the OH atom of the phenolic ring found in the GFP chromophore and thus its presence is required for fluorescence to occur. The fact that the released proton is transported through the water molecule in the vicinity of the chromophore has been corroborated by time-resolved infrared vibrational spectroscopy (Stoner-Ma et al., 2005).

In my work, I assayed the use of molecular dynamics computational modeling techniques to investigate the presence of water in the vicinity of the GFP chromophore, its dependence on TDE concentration and to predict reagents that could help avoiding the quenching. I chose to study eYFP and RFP because eYFP is the fluorescent protein expressed in the Thy1 transgenic mouse line used in Chapter II and III and because RFP shows lower quenching upon incubation in high TDE concentration. To model computationally the presence of water in the Chromophore pocket, I obtained crystallographic structures of the eYFP and

RFP mutants from the Protein Data Bank (PDB). Subsequently, I analyzed the structural differences in the channels through the barrel in both mutants. By performing molecular dynamics simulations I assessed the presence of water in the vicinity of the chromophore depending on the TDE concentration. Finally, I performed high-throughput docking simulations on the eYFP protein structure screening commercial compounds that could promote the formation of the proton channel by having high affinity for the surface of the channel and high hydrophilicity and, thus, promoting the presence of water in the vicinity of the barrel channel.

METHODS

Identification of barrel channels that could exchange the chromophor water molecule

In order to check whether structural differences in the channels of the barrel that allow the presence of the water molecule needed for the proton transfer, I obtained the crystallographic structures for fluorescent protein mutants with a ~2A resolution were obtained from PDB: eYFP-3V3D, RFP-2VAD. The MolAxis standalone version 1.0 was used in order to identify the barrel holes that allow proton exchange and chromophore resonance. The obtained channels were visualized with the open-source software Visual Molecular Dynamics (VMD).

Molecular dynamics simulations to explore the formation of the proton tunnel

In order to visually inspect the structural properties of the eYFP and RFP proteins, Pymol (<https://pymol.org>) was used to obtain net charge, hydrophobicity and Van der Waals surfaces. All the molecular dynamics system building and simulations were performed using the programmable environment High-Throughput Molecular Dynamics (HTMD).

Prior to simulating the dynamics of any system (formed by all the atoms constituting the studied molecules), it has to be equilibrated, avoiding any net charge, missing atoms, mismatched protonation states or tuning the structure so that hydrogen bond networks are as stable as possible. Thus, the original PDB files were automatically prepared with *proteinprepare*, including the titration of the protonation states using the software *PROPKA 3.1* (<http://propka.org/>), addition of missing atoms and overall optimization of the H-network using *PDB2PQR 2.1* (Dolinsky, Nielsen, McCammon, & Baker, 2004).

To simulate molecular dynamics, information about their structure (topology) and their mechanics (parameters) are needed. Those are available for the residues and structures most commonly found in nature. However, for small compounds they have to be estimated. Topology and parameter files for small molecules of interest (TDE) in the CHARMM format were obtained with the *parameterize* tool. This HTMD subroutine optimizes the parametrization including minimization and Quantum Mechanics (QM) calculations. Default full QM calculations were used with the PSI4 open-source engine (Parrish et al., 2017).

The system formed by the protein and solvent molecules was built with the parametrized TDE molecules at 63% and 83% concentrations in water using periodic cell boundaries and equilibrated for 40ns at 310K. 20ns (310K) simulations were run in high throughput using

HTMD's adaptive sampling (the source code used can be found at https://bitbucket.org/linusmg/md_simulations). Water densities around the chromophore were measured using HTMD's *MetricShell* module with a radius of 10 angstroms, which includes the region where the water molecule needed for the proton transfer is found.

Identification of high affinity ligands using molecular docking

Affinity between ligands and molecules can be computationally assessed using molecular docking simulations, in which ligands are located close to the molecule of interest, and conformations that could minimize the free energy of the ligand+molecule system are explored. To screen candidate molecules that could have high affinity for the region of the channel in eYFP, a molecule library was generated from the ZINC15 database, which is formed by ready-to-dock 3D mol2 format structures for compounds. I selected hydrophilic compounds ($\log P \leq 0$), having mid-reference pHs, all the available sizes (from 200 to >500 Daltons) and charge between -2 and +2. To define a docking volume surrounding previously identified holes in the fluorescent protein barrel, the biggest compound of the library was used in the rDock cavity generation functionality. A high-throughput exhaustive docking with 50 runs per molecule was performed in a computing cluster.

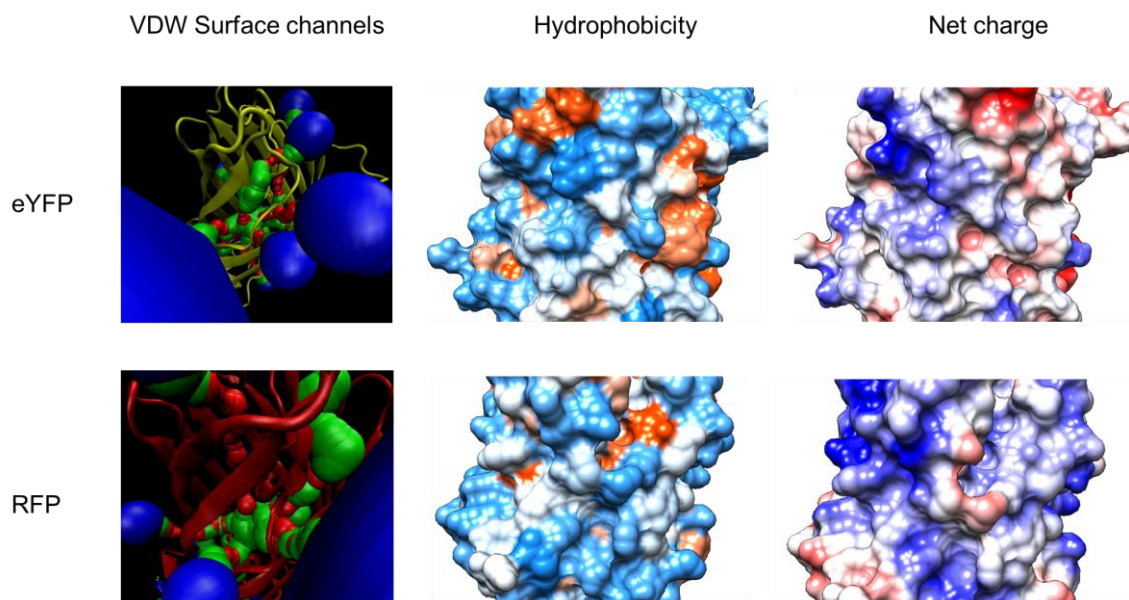
Computational resources

The workstation used to run all the HTMD simulations has been described previously ([HP-Z620](#) equipped with an Nvidia Quadro K4000 graphics card). Additionally, the ligand parametrization and docking was run on a high performance computing cluster (3,020 Linux cores, 200 computing nodes and a total storage capacity of 5 PB).

RESULTS

RFP has higher number and thickness of channels in the barrel

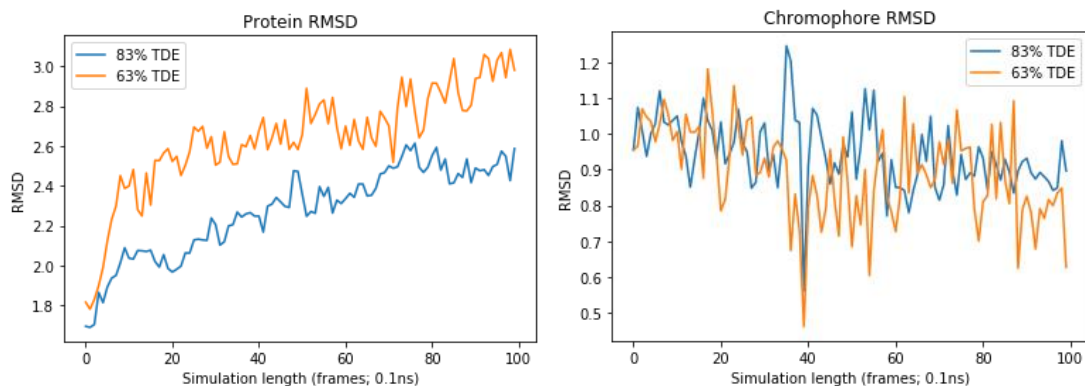
I first aimed at identifying channels in the fluorescent proteins and differences among mutants. I specifically explored the presence of channels connecting the chromophore to the β -barrel exterior. An analysis of channel sizes and paths using MolAxis in both mutants (e-YFP and RFP) shows that RFP has more and thicker channels ($n_{RFP}=4$, $n_{eYFP}=3$, $r_{max,RFP}=1.2$, $r_{max,eYFP}=0.7$ Å) (**Supplementary Figure 3** left column). Additionally, when plotting hydrophobicity (**Supplementary Figure 3** middle column) and net charge (**Supplementary Figure 3** right column) on the protein surface around the channels necessary for the water tunnel formation, it can be qualitatively observed that those properties have different spatial distributions. In particular, hydrophobicity has a strong influence on interactions with the substrate, the differences in the surface region where the channels are located point at the possibility of variations in the formation of the water tunnel.



Supplementary Figure 3: Structural exploration of eYFP and RFP. 3D rendering snapshots of the eYFP (upper row) and RFP (lower row) crystallographic structures with visualizations in VMD of the channels identified by MolAxis (left column). Pymol visualizations of the protein surface are coloured on the Kyte-Doolittle scale for hydrophobicity (middle column) or based on the electrostatic potential (right column).

Absence of protein denaturation or direct interaction between solvent molecules and the chromophore

I investigated whether molecular dynamics simulations could explain the highly specific fluorescent protein quenching upon immersion in TDE at high concentration. E-YFP and RFP crystallographic structures were solvated (pure H₂O, 63% TDE and 83% TDE) and their molecular dynamics simulated at 310K for 20 ns. The simulations shown that the Root-Mean-Square Deviation of the chromophore coordinates was low ($\sim 1 \pm 0.3 \text{ \AA}$) and almost the same for the tested solvating media, indicating that TDE quenching is not caused by direct interaction with the chromophore (**Supplementary Figure 4** right). Similarly, the whole protein RMSD was similar in the studied solutions and in water ($\sim 2.5 \pm 0.5 \text{ \AA}$), pointing that at the simulated timescales the protein is not undergoing denaturation (**Supplementary Figure 4** left).

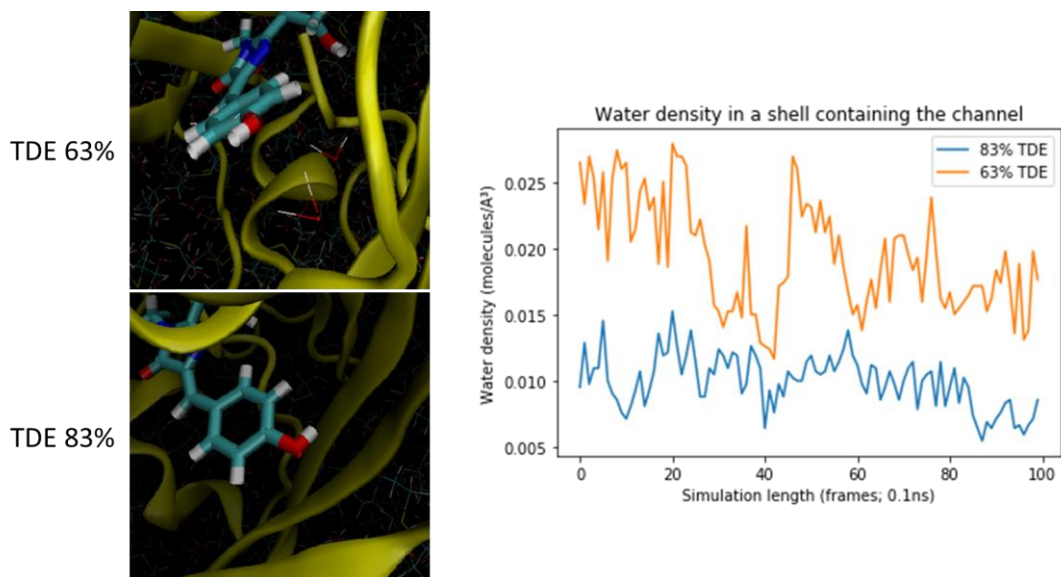


Supplementary figure 4: Root Mean-Square Deviation of the atom locations for the whole protein and the chromophore. RMSD for the locations of the eYFP atoms along 10 ns of simulation time. In the left panel the RMSD of all the atoms of the protein was quantified, showing slightly higher quantities for the solvation at 63% TDE concentration (orange curve) than in 83% TDE concentration (blue curve). The right panel shows the RMSD of the atoms forming the chromophore, both concentrations show similar fluctuation levels.

Water density around the fluorophore is solvent concentration-dependent

In order to check whether the water tunnel between the eYFP chromophore and the bulk necessary for protonation and fluorescence is formed, I measured the water density in a shell containing the chromophore and the channel. Our simulations show that the amount of water molecules is significantly reduced in 83% TDE versus 63% TDE or H₂O solvation (**Supplementary Figure 5**), as expected by the reduction of water molecules in the solution.

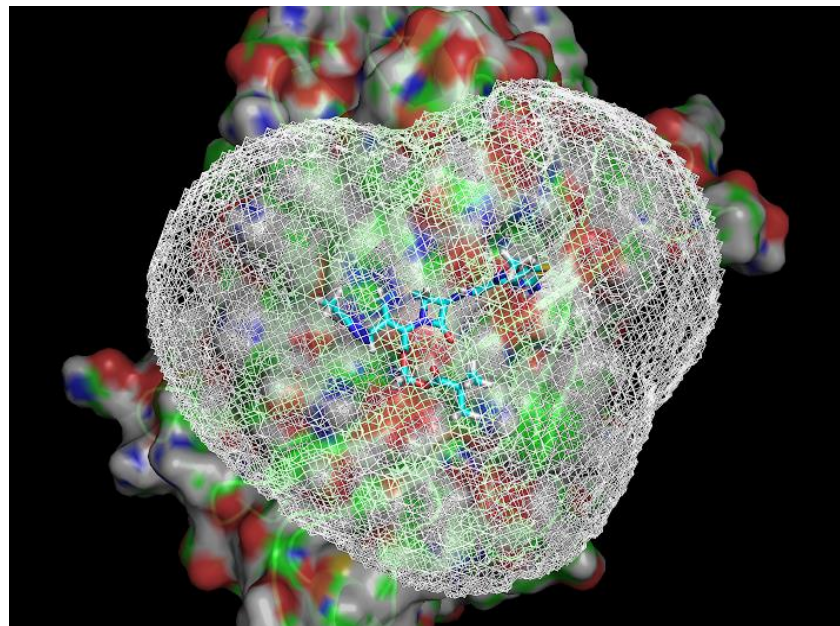
The lower density of waters implies that the pocket between the barrel and the chromophore is not occupied by the water molecule necessary for the proton transfer.



Supplementary Figure 5: Water density in the vicinity of the chromophore is reduced at 83% TDE. (Left) 3D rendering snapshots of molecular dynamics simulations of eYFP solvated at 63% (top) and 83% (bottom) TDE concentrations visualized in VMD. (Right) Quantification of the density of water molecules in a shell with a radius of 10 angstroms.

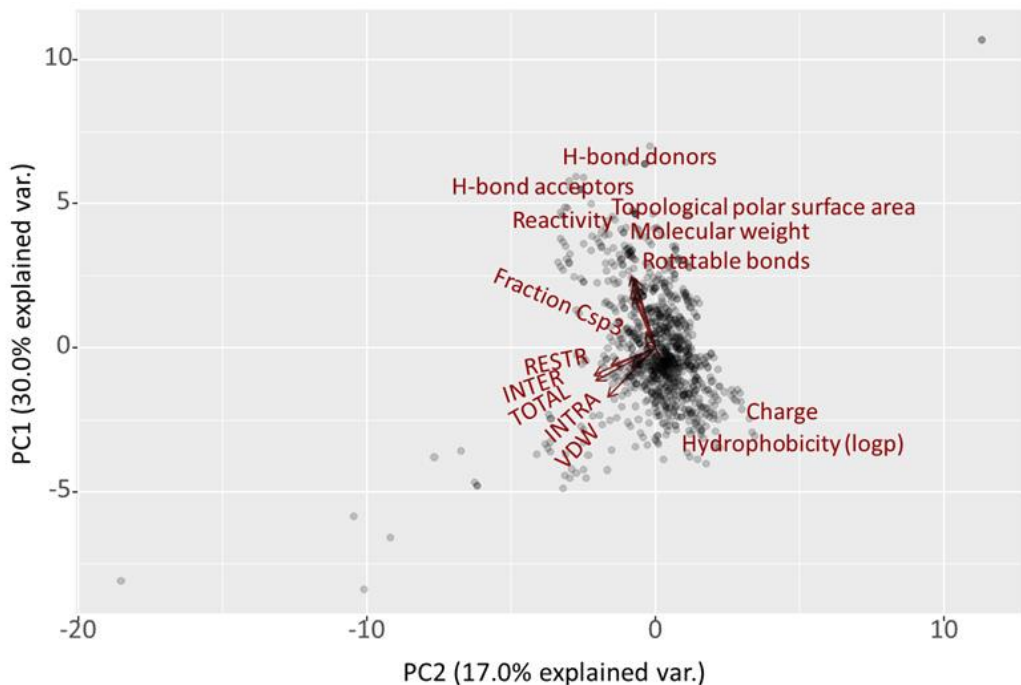
Small molecules to increase water density in the fluorophore

Those observations, together with the fact that TDE is significantly more hydrophobic than the other solvents, point at the possibility of avoiding e-YFP quenching by the addition of highly hydrophilic small molecules with high affinity for the protein surface region around the channel. In order to find those anti-quenching candidates, I have screened all the hydrophilic, commercially available, small molecules in the ZINC15 database. In order to assess their affinity for the surface around the channels, I obtained 3D representations of those molecules and used rDock to run high throughput docking simulations (**Supplementary Figure 6**).

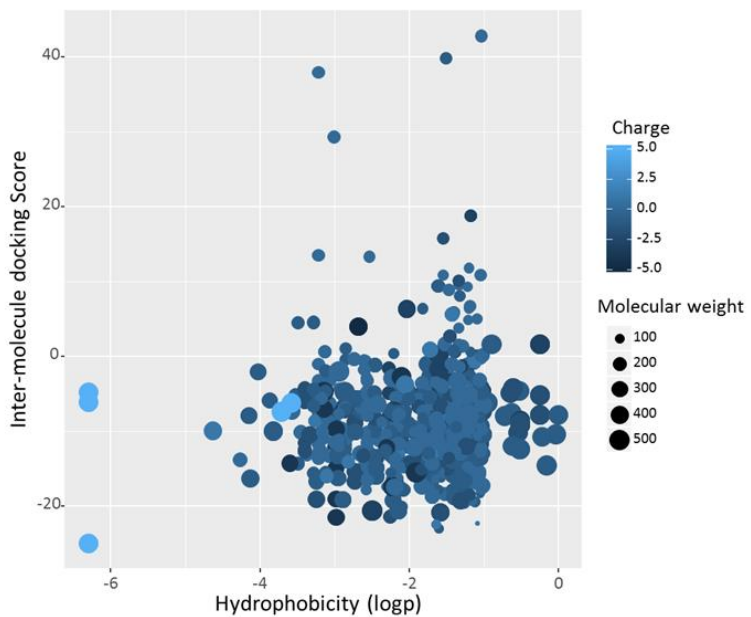


Supplementary Figure 6: Compound docking in a pocket surrounding the water channel of eYFP. Snapshot of a 3D rendering showing the crystallographic structure of eYFP (green), its surface electrostatic potential (grey, red and blue), the pocket in which the high-throughput docking simulations were performed and a docked molecule of GDP visualized in Pymol.

Finally, I aimed to find an optimal candidate for imaging and to introduce possible optimizations based on this computational pipeline I selected. A PCA combining the available annotated information of the molecules and the docking scores obtained, shows that the physico-chemical properties of the molecules do not correlate with docking scores, meaning that those are not reliable proxies for pinpointing candidates with high affinity for the protein surface around the channel (**Supplementary Figure 7**). **Supplementary Figure 8** shows all the screened molecules that are commercially available, I selected two candidates based on their docking score and hydrophilicity: Guanosine 5'-DiPhosphate and D-Fructose.



Supplementary Figure 7: Principal component analysis. PCA of the variables annotated in the ZINC15 database and docking scores obtained after high-throughput docking simulations. Arrows represent the direction of each variable in the PCA space. Longer arrows belong to variables that are well represented by the two principal components. Each of the points represents one compound. The first principal component is mainly contributed by the physico-chemical properties of the compounds. The second principal component is mainly contributed by the docking scores.



Supplementary Figure 8: Scatter plot of high-throughput docking simulations. Each point represents a commercially available compound. The position in the x axis is given by the hydrophobicity of each compound. The position in the y axis is given by the inter-molecule score of the docking simulations. The darkness of the color indicates the net charge of the molecules. The size of the dots represents the molecular weight of the compounds. Molecules having low hidrophobicity and low docking score are selected as suitable candidates for preserving eYFP fluorescence in high TDE concentrations.

CONCLUSIONS AND FUTURE PLANS

The channel identification results presented suggest that structural differences in the β -barrel of the eYFP and RFP mutants (i.e. number and thickness of channels) could account for the differences in the quenching produced by high TDE concentrations. The molecular dynamics simulations performed indicate that high concentration (above 80%) of TDE quenches eYFP fluorescence by avoiding the presence of a water molecule in the chromophore pocket of the protein and the formation of the proton tunnel needed for excited state proton transfer. The high throughput docking simulations allowed me to pinpoint specific compounds as candidates for preserving eYFP fluorescence in high concentrations of TDE.

While the analysis shown here does not allow to conclude that the candidates for preserving fluorescence in high concentration TDE solutions, it constitutes a proof-of-concept including all the needed tools to deepen in its analysis. The approach not only can provide computational predictions in regards of the water tunnel formation, but also is an enriching environment for the study of variations among FP mutants and upon solvation conditions that can improve technical aspects of FP imaging, but also shed some light in quenching phenomena that are not completely understood.

To finalize the study shown here I plan to:

- Quantify the amount of time that water molecules are present in the chromophore pocket
- Simulate the dynamics of eYFP in 83% TDE concentration with small quantities of the selected anti-quenching molecules
- Simulate the solvation of RFP at 63% and 83% TDE concentration
- Corroborate experimentally that TDE is not denaturating the proteins
- Test experimentally fluorescence preservation upon the introduction of the compounds predicted to avoid the fluorescence quenching
- Perform molecular dynamics simulations with 87% glycerol and diatrizoic acid solutions and assess the existence of the proton tunnel

The expected outcomes of this parallel work are both (1) obtaining an anti-quenching agent for allowing the usage of TDE as a refractive index matching medium for the mouse brains with Thy1-eYFP labeling used in our laboratory, and (2) proposing an innovative approach to imaging medium selection and adjustment.

ANNEX IV: Publications of this Thesis

Where environment meets cognition: a focus on two developmental intellectual disability disorders.

De Toma I., Manubens-Gil L., Ossowski S., and Dierssen M. Neural Plasticity, 2016

Articles in preparation:

Exploration of the morphospace in a minimal model of local cortical layer II/III: neuromorphological alterations in DS mouse models and their impact on computational capacities. Manubens-Gil L., Garcia-Ojalvo J. and Dierssen M., in preparation.

Environmental enrichment effects on neuromorphological alterations in the tgDyrk1A DS mouse model and its mesoscopic implications on the trisynaptic circuit. Pons-Espinal M.*[,] Manubens-Gil L.* et al., in preparation (Co-first author).

CLARITY technique optimization through fluorescent protein molecular dynamics and docking simulations. Manubens-Gil L., Swoger J., Sharpe J., Garcia-Ojalvo J. and Dierssen M., in preparation.

Systems-perspective analysis pipeline for whole-organ fluorescence microscopy teravoxel-sized datasets

Manubens-Gil L., García Ojalvo, J. and Dierssen M. in preparation

Multi-scale morphological effects on neuronal network contact topology: Pareto optimality in the tgDyrk1A DS mouse model

Manubens-Gil L., García Ojalvo, J. and Dierssen M.

